© 2010 Rui Wang

INCORPORATION OF FEED-NETWORK AND CIRCUIT MODELING INTO THE TIME-DOMAIN FINITE ELEMENT ANALYSIS OF ANTENNA ARRAYS AND MICROWAVE CIRCUITS

BY

RUI WANG

DISSERTATION

Submitted in partial fulfillment of the requirements
for the degree of Doctor of Philosophy in Electrical and Computer Engineering
in the Graduate College of the
University of Illinois at Urbana-Champaign, 2010

Urbana, Illinois

Doctoral Committee:

Professor Jianming Jin, Chair
Professor Andreas C. Cangellaris
Professor Milton Feng
Professor José E. Schutt-Ainé

ABSTRACT

In this dissertation, accurate and efficient numerical algorithms are developed to incorporate the feed-network and circuit modeling into the time-domain finite element analysis of antenna arrays and microwave circuits. First, simulation of an antenna system requires accurate modeling of interactions between the radiating elements and the associated feeding network. In this work, a feed network is represented in terms of its scattering matrix in a rational function form in the frequency domain that enables its interfacing with the time-domain finite element modeling of the antenna elements through a fast recursive time-convolution algorithm. The exchange of information between the antenna elements and the feed network occurs through the incident and reflected modal voltages/currents at properly defined port interfaces. The proposed numerical scheme allows a full utilization of the advanced antenna simulation techniques, and significantly extends the current antenna modeling capability to the system level. Second, a hybrid field-circuit solver that combines the capabilities of the time-domain finite element method and a lumped circuit analysis is developed for accurate and efficient characterization of complicated microwave circuits that include both distributive and lumped-circuit components. The distributive portion of the device is modeled by the time-domain finite element method to generate a finite element subsystem, while the lumped circuits are analyzed by a SPICE-like circuit solver to generate a circuit subsystem. A global system for both the finite-element and circuit unknowns is established by combining the two subsystems through coupling matrices to model their interactions. For simulations of even more complicated mixed-scale circuit systems that contain pre-characterized blocks of discrete circuit elements, the hybrid field-circuit analysis implemented a systematic and efficient algorithm to incorporate multiport lumped networks in terms of frequency-dependent admittance matrices. Other advanced features in the hybrid field-circuit solver include application of the tree-cotree splitting algorithm and introduction of a flexible time-stepping scheme. Various numerical examples are presented to validate the implementation and demonstrate the accuracy, efficiency, and applications of the proposed numerical algorithms.

To Jiawei and our parents

ACKNOWLEDGMENTS

On the completion of this dissertation, I would like, first of all, to express my cordial thanks to my graduate adviser, Professor Jian-Ming Jin, who has provided me with much guidance, support, advice, help, and encouragement, without which I would not have been able to complete this work. All I have learned during my study and research under Professor Jin’s direction will continue to be of great benefit to every aspect of my future career and the rest of my life.

My sincere thanks also go to Professor Andreas C. Cangellaris, Professor Milton Feng, and Professor José E. Schutt-Ainé for serving as members of my doctoral committee and for their valuable time and important suggestions. I would like to thank every current and former member in Professor Jin’s research group and the Center for Computational Electromagnetics (CCEM) at the University of Illinois at Urbana-Champaign for their helpful discussions and suggestions. I specially want to thank Dr. Zheng Lou for his pioneering work in the time-domain finite element method and for his valuable help when I first started on this topic. I would also like to thank Dr. Douglas J. Riley and Dr. Hong Wu who collaborated with us on research projects and Professor Ali Yilmaz for interesting discussions on the hybrid field-circuit simulation.

Finally, I want to give my sincere gratitude to my wife, Jiawei Tan, and our parents for their dedication and their continued love and support.

TABLE OF CONTENTS

CHAPTER 1 INTRODUCTION 1

1.1 Time-Domain Finite Element Method 1
1.2 Incorporation of Feed-Network Modeling Into Array Analysis 3
1.3 Hybrid Field-Circuit Simulation 5
1.4 Application of Tree-Cotree Splitting Technique 8
1.5 Outline of the Dissertation 9

CHAPTER 2 FINITE ELEMENT FORMULATION IN THE TIME DOMAIN 12
2.1 Introduction 12
2.2 Single-Field TDFEM Formulation 13
2.2.1 Spatial Discretization and Basis Functions 14
2.2.2 Temporal Discretization and Newmark-Beta Method 17
2.2.3 Absorbing Boundary Condition 19
2.2.4 Waveguide Port Boundary Condition 20
2.3 DFDD TDFEM Formulation 22
2.4 Figures 26

CHAPTER 3 INCORPORATION OF FEED-NETWORK MODELING INTO THE TDFEM ANALYSIS OF ANTENNA ARRAYS 29
3.1 Formulation 30
3.1.1 Port Interfaces and Coupling Scheme 30
3.1.2 The Single-Field TDFEM/WPBC Formulation 32
3.1.3 Feed-Network Macromodel and Time Convolution 34
3.1.4 Coupled Time-Marching Scheme 37
3.2 Extension to the Dual-Field Formulation 37
3.3 Discussion on Stability 39
3.4 Numerical Results 41
3.4.1 Feed Network 41
3.4.2 Monopole Array 42
3.4.3 8×1 Vivaldi Array 43
3.4.4 4×4 and 8×8 Vivaldi Arrays 45
3.5 Summary 46
3.6 Figures and Tables 48

CHAPTER 4 A HYBRID FIELD-CIRCUIT SIMULATOR BASED ON THE EXTENDED TDFEM 74

4.1 Introduction 74
4.2 Formulation 77
  4.2.1 Construction of the FEM Subsystem 77
  4.2.2 Stamping Technique 78
  4.2.3 Construction of the Circuit Subsystem 81
  4.2.4 Coupling Scheme and Global System of Equations 82
  4.2.5 Solution Algorithm 85
4.3 Numerical Results 88
  4.3.1 A Terminated Coaxial Cable 89
  4.3.2 Microwave Amplifier 90
  4.3.3 Shielded Amplifier 92
4.4 A Flexible Time-Stepping Scheme 93
  4.4.1 Global Time Stepping vs. Local Time Stepping 93
  4.4.2 A Generalized Coupling Scheme 96
  4.4.3 Validations and Applications 99
4.5 Summary 102
4.6 Figures and Tables 104

CHAPTER 5 INCORPORATION OF MULTIPORT LUMPED NETWORKS INTO THE HYBRID FIELD-CIRCUIT ANALYSIS 120
5.1 Introduction 120
5.2 Formulation 122
  5.2.1 Mathematical Representation 122
  5.2.2 Coupling to the FEM Subsystem 124
  5.2.3 Coupling to the Circuit Subsystem 126
  5.2.4 Global System of Equations 126
5.3 Numerical Results 129
5.4 Summary 131
5.5 Figures 133

CHAPTER 6 APPLICATION OF THE TREE-COTREE SPLITTING TECHNIQUE TO THE TDFEM ANALYSIS 140
6.1 Constraint on the Time-Step Size of the TDFEM 140
6.2 Methodology 142
  6.2.1 The TCS Algorithm 142
  6.2.2 Inclusion of the Time-Domain WPBC 145
  6.2.3 Inclusion of Lumped Port Interfaces 147

6.2.4 Diagonal Scaling 148
6.3 Numerical Results 149
6.3.1 Performance Tests 149
6.3.2 Practical Examples 152
6.3.3 Suppression of the Late-Time Linear Drift and Instability 154
6.4 Summary 155
6.5 Figures and Tables 157

CHAPTER 7 CONCLUSIONS AND FUTURE WORK 169

APPENDIX A DERIVATION OF THE UPDATING EQUATIONS 174

APPENDIX B DERIVATION AND PROOF OF VALIDITY OF THE SOLUTION ALGORITHM 177

REFERENCES 180

AUTHOR’S BIOGRAPHY 190

CHAPTER 1
INTRODUCTION

1.1 Time-Domain Finite Element Method

The core purpose of computational electromagnetics is the transformation of governing physical equations of a given boundary-value problem into the corresponding linear systems of equations that can be solved numerically on a digital computer. With the advent of modern high-performance computers, numerical simulation has become an indispensable tool for the design and optimization of complex antenna systems and microwave circuits [1], [2].

Among various existing numerical simulation tools, three most important methods are the method of moments (MoM) [3], the finite-difference time-domain (FDTD) method [4], and the finite element method (FEM) [1], [2]. The MoM uses appropriate Green's functions that accurately account for the Somerfield radiation condition, which is very suitable for open-region radiation and scattering problems. When a surface integral equation is applied, the discretization and thus the degrees of freedom are confined only on the surface of the region of interest, which results in a typically small (compared to that from the finite element discretization) but fully populated impedance matrix whose computation and solution involve high computational complexity. Moreover, Green's functions need to be formulated for each specific problem. For complex antennas and microwave circuits designed with highly inhomogeneous or anisotropic material, the process becomes extremely complicated, if not impossible. In contrast, the FDTD method and the FEM solve the partial differential equation directly. The entire computational domain needs to be discretized into small grids/elements, resulting in typically large number of unknowns. When applied for open-region problems, appropriate absorbing boundary conditions also need to be implemented to truncate the computational domain. On the other hand, these two methods are very suitable for dealing with material anisotropy and inhomogeneity.

First proposed in the 1940s [5], the FEM has been formulated and applied to a wide range of mathematical and engineering problems including those in the field of microwave engineering and electromagnetics. The FEM itself can be formulated in both the frequency and time domains, and the one that solves Maxwell's equations or the second-order wave equations directly in the time domain is known as the time-domain FEM or TDFEM. Compared to its frequency-domain counterpart, the unique strength of TDFEM lies in its capabilities for conducting efficient broadband analysis and modeling nonlinear components, devices and media. Compared to the FDTD method that usually uses rectangular grids, the TDFEM has inherent attributes of modeling versatility by utilizing unstructured grids as well as curvilinear triangles and tetrahedrons, which is obviously more appropriate for modeling curved surfaces and complicated fine structures. More importantly, the TDFEM can be formulated to be unconditionally stable so that the time-step size does not need to be reduced even when very small finite elements are present [1], [2]. These favorable features make the TDFEM very suitable for broadband analysis of antennas and other electromagnetic devices of high geometric and material complexity and possibly involving nonlinearity. Through various developments and applications, the TDFEM has recently been demonstrated as a powerful and versatile candidate for the transient analysis of electromagnetic devices including various types of antennas and antenna arrays [6]-[13].

One of the recent important developments in applying the TDFEM to the simulation of antennas and microwave devices is the time-domain waveguide port boundary condition (WPBC) [10]. Based on a multimodal expansion of the fields on the port interface, this highly stable and accurate time-domain port model can effectively absorb reflected waves and excite incident waves on waveguide ports. The TDFEM with the time-domain WPBC has been applied successfully to the simulation of a variety of microwave devices as well as broadband antennas [11]. Another important development is the dual-field domain-decomposition (DFDD) TDFEM [12]. This novel domain-decomposition scheme solves the dual-field, second-order vector wave equations in each subdomain and relates the solutions in adjacent subdomains explicitly using equivalent surface currents on the subdomain interfaces. The accuracy, efficiency, and capability of this method have been demonstrated through applications to complex electromagnetic problems, including large finite antenna arrays [13]. Such problems are very challenging for the conventional TDFEM, which has to solve a linear system involving millions of unknowns. Besides, the capability of TDFEM has been further extended when combined with other numerical methods, such as the FDTD method for facilitated incorporation of perfectly matched layers [14], and the time-domain surface integral equation method for accurate and efficient simulation of antennas installed on a large platform [15]. More details on the formulations and recent development of the TDFEM are included in [1], [16], [17]. Readers are also referred to [2] for the most complete, up-to-date coverage of the frequency- and time-domain finite element analysis and modeling of antennas and arrays.

1.2 Incorporation of Feed-Network Modeling Into Array Analysis

In an advanced antenna system, multiple antenna elements are usually arranged into a certain array configuration, driven through a feed network whose major function is to distribute the input signal from the signal generator to the radiating elements and combine the signals received by the antenna elements. Built on a combination of power dividers and phase shifters, a typical design of a feed network consists of complex waveguiding structures, passive components, and waveguide junctions. For large and complex antenna arrays, the associated feed network could be very complicated, depending on the number of antenna elements, the desired amplitude and/or phase distribution between these elements, and various requirements on beam steering. Complicated interactions could occur between the antennas and the feed network, which affect the overall performances of the entire radiation system. A well-designed feed network with good control over the signal distribution enables the antenna system to have desired radiation characteristics such as the beamwidth, sidelobe level, and steered main beam. However, multiple interactions resulting from signals traveling back and forth between radiating and feed structures could lead to undesired mutual couplings and give rise to secondary radiations that deteriorate the system performance. Consequently, accurate modeling of the interactions between the antennas and the feed network is essential and must be taken into consideration for optimizing the performance of the antenna system.

For the case of planar antenna arrays etched on a single substrate, such as series- and corporate-fed microstrip antenna-arrays, the antennas and the feed network can be analyzed simultaneously using a single numerical method, such as the moment method in conjunction with the discrete complex image method [18]-[20]. For more complex array designs, the antennas and the feed network are often separated physically, with their connection or coupling enabled via waveguiding structures or apertures. For such structures, modeling of the antennas and the feed network simultaneously becomes much more cumbersome. Because of this complexity, it is often the case that the antennas and the feed network are designed and modeled separately and then combined with the hope that the resulting antenna array system will perform according to the specifications. In some commercial software [21], this idea has been realized in the following way. After all the components are analyzed independently from each other, subsequent simulations for system-level performance assessment are then carried out by means of general-purpose, network analysis-oriented circuit simulators, making use of the multiport network parameter (such as scattering parameter) matrices of the feed network and the antenna array. However, such simulations do not lend themselves to expedient antenna array design iteration, since the physical attributes of the array structure are not accessible in the electromagnetic model. Furthermore, such network analysis simulation does not lend itself to direct prediction of antenna array radiation pattern performance. This is especially true in the case where nonlinear elements are embedded directly in the antenna array for the purposes of enhancement of element radiation and overall antenna array performance. For such cases, not only is an electromagnetic field model required for the antenna structure, but also the electromagnetic analysis must be carried out in the time domain to account for the nonlinearity of the embedded circuit elements.

In this dissertation work, an accurate and efficient numerical scheme is proposed for incorporating the feed-network modeling into the TDFEM analysis of antenna arrays and thus accounting for the impact of the interactions between the radiating elements and the feed network on the performance of antenna system. To the best of the author’s knowledge, this is the first time that such an accurate hybrid technique, which combines the state-of-the-art modeling capabilities (such as the WPBC, the DFDD formulation, and incorporation of a macromodel) to simulate a complete antenna system, has appeared in the literature.

This algorithm is fundamentally different from the insertion of lumped circuit elements into time-domain electromagnetic field solvers which results in various hybrid field-circuit simulators including the one proposed later in this dissertation. Hybrid field-circuit implementations tend to emphasize those cases where the embedded circuit elements are electrical models of electrically small electronic components. The small electrical size of such components allows for the current and voltage quantities used for the interfacing of the lumped circuit model with the electromagnetic field solver to be associated, respectively, with an electric field and a magnetic field node in the field solver, without any modeling accuracy issues. However, the systematic handling of those cases where a multiport network model description of an electrically large, distributed structure is to be interfaced with a time-domain electromagnetic field solver is less obvious and more prone to errors in the modeling of the wave interactions between the multiport networks with the rest of the structure. Clearly, the interfacing of the multiport network model of a feed network with an electromagnetic model of the antenna array is a most representative example of this class of modeling cases that are of significant practical interest. The algorithm proposed in this thesis work is a systematic methodology for making such an interfacing possible and accurate.

1.3 Hybrid Field-Circuit Simulation

As mentioned in the preceding section, circuit modeling can be incorporated into the full-wave analysis by including lumped circuits (in the form of isolated elements as well as lumped circuitry) into electromagnetic field solvers for those cases where the embedded circuit elements are models for electrically small components. Actually, the hybridization of lumped-circuit modeling with an electromagnetic field solver is a natural result due to the fact that individual components in a typical modern electronic system exhibit significant disparity in the electrical size of their geometrical features. As microwave circuits become more complex with multifunctional capabilities, higher operating frequency, and increased integration scale, any successful design must take into account the electromagnetic effects resulting from undesired radiations and mutual coupling of electronic devices. This requirement necessitates the application of full-wave solvers in the early stage of the design cycle to ensure accurate prediction of the electromagnetic responses of the integrated and packaged components and systems. Meanwhile, since microwave circuit design is moving toward highly integrated systems, more active and/or passive devices are integrated on circuit boards. The interactions between these devices and the electromagnetic fields significantly affect the performance of the system. Therefore, a hybrid field-circuit solver that combines the capabilities of a full-wave analysis and a lumped circuit simulation is of great interest because of its ability to account for the presence of lumped components in complicated and mixed-scale electromagnetic devices.

The hybrid field-circuit solver proposed in this dissertation is based on the hybridization of the TDFEM algorithm with a general-purpose circuit simulation technique, resulting in a coupled FEM-circuit global system which enables a concurrent solution of the FEM and circuit unknowns. In contrast to some other hybrid solvers of its kind (more complete literature review and comparison are given in Chapter 4), the proposed algorithm preserves the symmetry of the mutual coupling and that of the global system matrix. This is important for a time-domain hybrid solver because the symmetry is a general requirement for achieving unconditional stability in a coupled time-marching solution. Moreover, the proposed TDFEM-based hybrid solver inherits the modeling versatility and capability of the TDFEM, and also preserves the efficiency and flexibility of a SPICE-like circuit simulation technique in the analysis of arbitrary circuit topology and devices. The hybrid formulation minimizes extra matrix manipulations so that an existing TDFEM solver can be easily extended to a hybrid field-circuit solver.

This TDFEM-based field-circuit solver employs a system-wide global time-step size and thus samples and couples the signals of all the subsystems in a strict synchronous manner. Such a global time-stepping scheme is a natural choice when all the subsystems in a hybrid system have a similar requirement on their time-step sizes. This, however, is not necessarily the case in many realistic applications, where signals in subsystems have quite distinct temporal variations and require different signal-sampling rates. Therefore, a more flexible time-stepping scheme that allows local, subsystem-wide time-step sizes is of great interest. This dissertation proposes such a flexible time-stepping scheme which enables a multirate feature in the hybrid field-circuit simulation. Different time-step sizes have been adopted for fast- and slow-varying subsystems, which are coupled through a generalized coupling scheme in the time-marching process. Because of the ability of allowing different sampling rates for different subsystems, the flexible time-stepping scheme can significantly improve the computational efficiency of this TDFEM-based hybrid field-circuit solver, especially when the computational cost associated with the slow subsystems is much higher than that associated with the fast subsystems.

The capability of the hybrid field-circuit solver can be further enhanced by incorporating the more advanced macromodeling technique into the framework. In the hybrid analysis, lumped circuits are described in detail in terms of discrete circuit elements such that a SPICE-like circuit solver can be directly applied. However, in some applications, lumped circuit subsystems might have been predesigned and characterized compactly in terms of frequency-dependent multiport network matrices usually referred to as *lumped networks*. The hybrid field-circuit analysis implements a systematic, efficient algorithm to incorporate multiport lumped networks in terms of admittance matrices into the hybrid field-circuit solver. The Laplace-domain admittance matrices are cast into the time-domain stepping equations for port voltages and currents to form a lumped-network subsystem which is then interfaced with the FEM and circuit subsystems through shared ports. While the port voltages of the lumped-network subsystem are determined by the FEM and circuit subsystems, its port currents are treated as external current excitations for the finite-element and circuit subsystems. All the lumped-network port variables are then eliminated from the final expressions to form a global system for only the finite-element and circuit unknowns. The proposed algorithm further extends the capability and improves the efficiency of the existing field-circuit solver to model more complex and mixed-scale electronic systems.

1.4 Application of Tree-Cotree Splitting Technique

The TDFEM formulation adopted in this dissertation models electromagnetic phenomena by solving the second-order vector wave equation for electric fields using vector edge basis functions, which can be viewed as an extension of the frequency-domain FEM to the time domain. As an implicit scheme, the resulting TDFEM system is solved at each time step using either a direct solver or an iterative solver. For large-scale electromagnetic problems, preconditioned iterative solvers are usually preferred for their efficiency and low memory cost as compared to direct solvers. It is well known that such a formulation results in an unconditionally stable time-marching scheme. So, ideally, with this unconditional stability the time-step size can be chosen based entirely on the maximum frequency in the frequency band of interest instead of being constrained by the smallest finite elements required for modeling fine structures. However, since the time-step size has a significant effect on the property of the TDFEM system matrix, the actual choice of the time-step size is not only limited by the maximum frequency, but also constrained by the speed of convergence at each time step when an iterative solver is applied to solve the TDFEM system. It is observed that as the time-step size increases, a typical TDFEM system matrix becomes more ill-conditioned, and thus the number of iterations needed to solve such a system at each time step increases drastically. The situation becomes more severe when the geometry of the problem imposes further challenges in the simulation, for example, when very small elements are required in the finite element discretization or when the disparity in the geometrical size of individual components leads to an extremely nonuniform mesh. In practical applications, these situations are quite common and cannot be avoided. As a result, in the TDFEM analysis the time-step size usually has to be much smaller than required by the temporal sampling rate for achieving certain temporal discretization accuracy. Moreover, when the input signal contains relatively slow-varying (low-frequency) components, such a small time-step size will lead to an unacceptably long simulation time during which the solutions can respond to the slow-varying signal and finally reach a steady state.

In this dissertation, a so-called tree-cotree splitting algorithm is applied to the TDFEM to alleviate the constraint on the time-step size and to improve the convergence of iterative solutions at each time step. A simplified algorithm of finding a spanning tree over a graph is applied to the edge set of a three-dimensional finite element mesh, splitting finite element edges into tree and cotree edges. Based on this splitting, both pure gradient and curl-conforming basis functions are formed to expand the electric field. Through Galerkin's procedure and Newmark-beta time integration, a time-marching system with a modified TDFEM system matrix is constructed. It is shown that after special care is taken, the use of the TCS algorithm is compatible with the recent advanced features in the TDFEM such as the time-domain WPBC and lumped port interfaces for hybrid field-circuit analysis. Compared with the conventional TDFEM, application of the tree-cotree splitting algorithm maintains the accuracy of the TDFEM solution but significantly reduces the number of iterations per time step for a preconditioned iterative solver to converge when the time-step size becomes relatively large. This desirable feature allows us to adopt a larger time-step size within the requirement of the temporal sampling rate to achieve faster time-marching with marginal additional cost. This is most beneficial when the input signal contains slow-varying (low-frequency) components or when a highly nonuniform mesh of simulated objects imposes a practical constraint on the time-step size due to the ill-conditioned system matrix. In addition, because the null space of the curl operator is now represented by the pure gradient basis functions, the formulation is naturally free of late-time linear drift.

1.5 Outline of the Dissertation

The remaining chapters of this dissertation are organized as follows:

Chapter 2 reviews details about finite element formulations in the time domain, including the conventional single-field formulation and the highly efficient DFDD formulation, along with descriptions of boundary conditions that properly truncate the finite element meshes in free space as well as at the waveguide ports.

Chapter 3 describes an accurate and efficient numerical algorithm for incorporating the feed-network modeling into the TDFEM analysis of antenna arrays. A coupled time-marching scheme is presented based on the traveling-wave decomposition on the port interfaces that separate the feed network and antennas. The proposed scheme works seamlessly with the single-field TDFEM/WPBC formulation, and is extended to a dual-field formulation which is compatible with the DFDD TDFEM. Discussion of the stability issue is provided. Simulation examples are presented to validate the proposed methodology and demonstrate its application.

Chapter 4 begins with a review of various hybrid field-circuit simulators that are currently available in the literature and then highlights the unique features of the one proposed in this work. The construction of the FEM and circuit subsystems is then described in detail, followed by the coupling scheme to hybridize these two subsystems and a discussion of solution algorithms to efficiently solve the resulting global system. The proposed hybrid field-circuit solver is validated and its application and performance are demonstrated through numerical examples. Its capability and flexibility are further enhanced by a flexible time-stepping scheme described at the end of the chapter.

Chapter 5 presents a systematic and efficient algorithm for incorporating multiport lumped networks in terms of admittance matrices into the hybrid field-circuit solver. After a brief introduction and literature review, the mathematical representation of a lumped network is described. The formulation for incorporating multiport lumped networks into the hybrid time-domain finite element solver comes next, followed by a discussion about reducing the computational cost of time-stepping equations derived from admittance matrices. Numerical examples are presented to validate the proposed methodology and demonstrate its application and performance.

Chapter 6 presents the application of the tree-cotree splitting algorithm to the TDFEM analysis of electromagnetic problems to accelerate the time-marching process. It begins with a discussion of the problem of slow convergence associated with a TDFEM system when the time-step size is relatively large. The tree-cotree splitting algorithm is then described in detail, and based on the splitting of finite element edges into tree and cotree edges, two sets of basis functions are formed to expand the electric field and construct the time-marching system. Inclusion of the time-domain waveguide port boundary condition and lumped port interfaces is also described briefly, and numerical results are presented at the end.

Conclusions and proposed future work are given in Chapter 7.

CHAPTER 2

FINITE ELEMENT FORMULATION IN THE TIME DOMAIN

2.1 Introduction

The formulations of the TDFEM presented in this chapter form the foundation for the latter chapters. In the existing literature, there are generally two approaches to formulate the FEM in the time domain. The first approach is based on modeling the electromagnetic phenomena by directly solving two time-dependent first-order Maxwell's equations, i.e., Ampère’s and Faraday’s laws [22]. If a traditional leapfog method is adopted through the use of central differences, the resulting time-marching algorithm can be viewed as the generalization of the conventional FDTD method for unstructured grids. Actually, it has been shown that for rectangular brick elements, the elemental matrices associated with this finite element formulation can be reduced to an equivalent representation to the conventional FDTD method when those matrices are constructed using trapezoidal integration [2]. Also similar to the conventional FDTD method, this TDFEM formulation is conditionally stable in the sense that the time-step size is limited by the finest spatial discretization in the computational domain.

In the second approach, the TDFEM is formulated based on the second-order wave equation for the electric field. This approach leads to a fully implicit formulation because numerical solution at the current time step is implicitly related to those at previous time steps and a linear system of equations needs to be solved at each time step. Although computationally more expensive in each time step than the explicit methods, the implicit formulation based on the second-order wave equation has gained a lot of popularity. One of its favorable properties is the unconditional stability achieved by use of the Newmark-beta time-integration scheme [23]. Therefore, the choice of time-step sizes is independent of the finite element discretization. In addition, since the frequency-domain FEM is also formulated based on the second-order wave equation, the extension of many well-developed frequency-domain techniques, such as high-order basis functions, eigenfunction expansion, absorbing boundary conditions and waveguide port boundary conditions, to the time domain becomes straightforward due to the similarities shared by these two formulations. For these reasons, the TDFEM formulations in this dissertation are based on the second approach.

The following sections detail the TDFEM formulations. First, the single-field formulation for solving transient electric fields is described in Section 2.2. By applying Galerkin's method, the second-order electric wave equation along with proper boundary conditions is cast into its weak-form representation. A finite element solution is then obtained after performing appropriate spatial and temporal discretizations. The rest of this section is devoted to boundary conditions in order to properly truncate the finite element meshes in the free space as well as at the waveguide ports. The DFDD TDFEM formulation [12], [13] is reviewed in Section 2.3 as a highly efficient domain-decomposition technique for transient simulation of large antennas and arrays.

2.2 Single-Field TDFEM Formulation

In the following, a TDFEM formulation for solving the transient electric field will be presented. The TDFEM formulation for solving the transient magnetic field can be derived similarly. Since the formulation in this section uses only the electric field as the working variable, it is referred to here as the single-field formulation in contrast to the dual-field formulation in Section 2.3 where both the electric and magnetic fields are solved.

Assume the electromagnetic boundary value problem under consideration is within the volume *V* which is bounded by outer boundary *S*. The electromagnetic field inside volume *V* is satisfied by the following Maxwell's equations:

$$\nabla \times \mathbf{E} = -\frac{\partial \mathbf{B}}{\partial t} \qquad \text{(Faraday's law)} \qquad (2.1)$$

$$\nabla \times \mathbf{H} = \frac{\partial \mathbf{D}}{\partial t} + \mathbf{J} = \frac{\partial \mathbf{D}}{\partial t} + \sigma \mathbf{E} + \mathbf{J}^{\mathrm{im}} \qquad \text{(Maxwell-Ampère law)} \qquad (2.2)$$

By invoking the constitutive relations [22] and eliminating the magnetic field **H** from the above equations, the electric field **E** inside V satisfies the following second-order differential equation as

$$\nabla \times \frac{1}{\mu_r} \nabla \times \mathbf{E} + \mu_0 \sigma \frac{\partial \mathbf{E}}{\partial t} + \frac{\varepsilon_r}{c_0^2} \frac{\partial^2 \mathbf{E}}{\partial t^2} = -\mu_0 \frac{\partial \mathbf{J}^{\mathrm{im}}}{\partial t} \tag{2.3}$$

where $\mathbf{J}^{\mathrm{im}}$ represents the impressed current excitation in the computational domain. The boundary surface S is assumed to be a union of three kinds of surfaces satisfying three different types of boundary conditions, respectively, as

$$\hat{n} \times \mathbf{E} = 0 \qquad \text{on } S_1 \tag{2.4}$$

$$\hat{n} \times (\nabla \times \mathbf{E}) = 0 \qquad \text{on } S_2 \tag{2.5}$$

$$\hat{n} \times \left(\frac{1}{\mu_r} \nabla \times \mathbf{E} \right) + P(\mathbf{E}) = \mathbf{U} \qquad \text{on } S_3 \tag{2.6}$$

where $\hat{n}$ is the outward unit vector normal to S. Equation (2.4) is a Dirichlet boundary condition to model perfect electric conducting (PEC) surfaces, and (2.5) is a Neumann boundary condition to model perfect magnetic conducting (PMC) surfaces. While (2.5) is naturally satisfied in finite element formulation, the boundary condition in (2.4) needs to be enforced explicitly following the procedure in [1]. The boundary condition in (2.6) is often referred to as a generalized impedance boundary condition, where $P(\cdot)$ is a known operator of both time and position and **U** is a known vector quantity representing the excitation from the exterior region.

To apply Galerkin's method, we test (2.3) with vector testing function $\mathbf{N}_i$ and make use of (2.4)-(2.6); we can then obtain the following weak-form representation of the wave equation:

$$\begin{aligned} &\iiint_V \left[\frac{1}{\mu_r} (\nabla \times \mathbf{N}_i) \cdot (\nabla \times \mathbf{E}) + \frac{\varepsilon_r}{c_0^2} \mathbf{N}_i \cdot \frac{\partial^2 \mathbf{E}}{\partial t^2} + \mu_0 \sigma \mathbf{N}_i \cdot \frac{\partial \mathbf{E}}{\partial t} \right] dV \\ &- \iint_{S_3} \mathbf{N}_i \cdot P(\mathbf{E}) dS = - \iint_{S_3} \mathbf{N}_i \cdot \mathbf{U} dS - \mu_0 \iiint_V \mathbf{N}_i \cdot \frac{\partial \mathbf{J}^{\mathrm{im}}}{\partial t} dV. \end{aligned} \tag{2.7}$$

2.2.1 Spatial Discretization and Basis Functions

To seek the finite element solution of (2.7), we need to perform spatial discretization, which involves two steps. First, the three-dimensional computational domain (volume V) is partitioned into small tetrahedral elements. Second, the electric field **E** is expanded in terms of basis functions inside each element.

It is well known that if the scalar (node-based) basis functions are employed to present electromagnetic field vectors, spurious solutions will occur, which is due to the lack of enforcement of the divergence condition as inherent in the weak-form formulation. Therefore, the electric field **E** is expanded using vector basis functions. For the case of tetrahedral elements, the vector basis function associated with the *i*th edge is given by [1]

$$\mathbf{N}_i^e = \left(L_{i_1}^e \nabla L_{i_2}^e - L_{i_2}^e \nabla L_{i_1}^e \right) l_i^e \tag{2.8}$$

where i_1 and i_2 denote the two vertices associated with the *i*th edge and l_i^e is the length of the *i*th edge. Furthermore, L_k^e $(k = 1,2,3,4)$ are the nodal basis functions associated with the four vertices of the tetrahedron. Figure 2.1 shows one of the six lowest-order vector basis functions for a tetrahedral element. For the case of triangular elements (patches), the basis functions take the same form as in (2.8) while L_k^e $(k = 1,2,3)$ are the area coordinates of the element. It can easily be verified that $\mathbf{N}_i^e$ automatically satisfies the divergence condition. Thus, the solutions obtained by using these vector basis functions are free of spurious solutions. In addition, vector basis functions can be used easily to impose boundary conditions at material interfaces and conducting surfaces and to model sharp tips and corners.

The vector basis functions defined in (2.8) are of the lowest order. To achieve better interpolation accuracy, higher order basis functions are introduced and employed. There are two types of higher-order vector elements. The first type is interpolatory basis functions [24], which are defined on a set of points on the element, such that each basis function vanishes at all the points except for one. Interpolatory basis functions of a given order are totally different from those of lower orders. The second type is hierarchical basis functions [25], which are adopted in this work. In contrast to interpolatory basis functions, the higher-order hierarchical basis functions are not defined on a set of points, but rather are formed by adding new functions to the lower ones, which permits the use of different orders in one problem; therefore, these functions can be employed for p–adaption, i.e., iterative increase of the element orders in different regions of the problem until convergence of the field to a specified accuracy is achieved. Take three dimensional tetrahedral elements for examples. Let V_p be the space of all three-dimensional vector functions on this element. Any function in V_p can be expressed as the sum of functions from the 11 subspaces, i.e.,

$$V_p = V_p^{(v)} \oplus 4V_p^{(f)} \oplus 6V_p^{(e)} \tag{2.9}$$

where $V_p^{(e)}$ is the space of all one-dimensional vector functions associated with one specific edge, called edge functions; $V_p^{(f)}$ is the space consisting of face functions with vanishing tangential component an all three edges of one specific face; and $V_p^{(v)}$ is the space consisting of volume functions with vanishing tangential component an all four faces of the tetrahedron. Each of the three spaces above can be divided into two subspaces, respectively: one presenting gradient (irrotational) functions with zero curl, and one presenting rotational functions with nonzero curl. For instance,

$$V_p^{(e)} = G_p^{(e)} \oplus W_1^{(e)}, \tag{2.10}$$

and suitable formulas for functions in $G_p^{(e)}$ and $W_1^{(e)}$ are

$$G_p^{(e)} = \nabla(\varsigma_1\varsigma_2(\varsigma_1 - \varsigma_2)^{p-1}), \qquad p \geq 1 \tag{2.11}$$

$$W_1^{(e)} = \varsigma_1 \nabla \varsigma_2 - \varsigma_2 \nabla \varsigma_1 \tag{2.12}$$

where ς_1, ς_2 are one-dimensional simplex coordinates. The detailed formulas and discussions for edge, face and volume basis functions can be found in [25]. As a consequence of the separation of gradient and rotational subspaces, a general higher-order element is characterized by a pair of indices (r, g), where r is the order of rotational subspace and g is the order of the gradient subspace.

Once the basis functions are determined, the electric field can be expanded using curl-conforming basis functions. Specifically, within each tetrahedral element, we expand the transient electric field as

$$\mathbf{E}^e(\mathbf{r},t)=\sum_{i=1}^{n^e} e_j^e(t)\mathbf{N}_j^e(\mathbf{r}) \tag{2.13}$$

where n^e denotes the number of degrees of freedom associated with each element. The superscript of e will be ignored for the sake of simplicity. By substituting (2.13) into (2.7), the spatial discretization yields a semidiscrete system, i.e., an ordinary differential equation with respect to time t. To illustrate the semidiscrete system, we further assume that the linear operator $P(\cdot)$ is a product of a linear time operator $P^t(\cdot)$ and a linear position operator $P^{\mathbf{r}}(\cdot)$, and thus

$$P(\mathbf{E}^e)=\sum_j P^{\mathbf{r}}(\mathbf{N}_j^e(\mathbf{r}))P^t(e_j^e(t)). \tag{2.14}$$

Therefore, the semidiscrete system can be writen as

$$\left[S\right]\{e\}+\frac{1}{c_0^2}\left[M\right]\frac{\partial^2\{e\}}{\partial t^2}+\frac{1}{c_0}\left[G\right]\frac{\partial\{e\}}{\partial t}+\left[P^{\mathbf{r}}\right]P^t\left(\{e\}\right)=\{b^{\mathbf{U}}\}+\frac{Z_0}{c_0}\frac{\partial\{b^{\mathrm{im}}\}}{\partial t}. \tag{2.15}$$

The matrix entries in (2.15) are given by

$$S_{ij}=\iiint_V \frac{1}{\mu_r}(\nabla\times\mathbf{N}_i)\cdot(\nabla\times\mathbf{N}_j)dV \tag{2.16}$$

$$M_{ij}=\iiint_V \varepsilon_r\mathbf{N}_i\cdot\mathbf{N}_j dV \tag{2.17}$$

$$G_{ij}=Z_0\iiint_V \sigma\mathbf{N}_i\cdot\mathbf{N}_j dV \tag{2.18}$$

$$P_{ij}^{\mathbf{r}}=-\iint_{S_3}\mathbf{N}_i\cdot P^{\mathbf{r}}(\mathbf{N}_j)dS \tag{2.19}$$

$$b_i^{\mathbf{U}}=-\iint_{S_3}\mathbf{N}_i\cdot\mathbf{U}dS \tag{2.20}$$

$$b_i^{\mathrm{im}}=-\iiint_V \mathbf{N}_i\cdot\mathbf{J}^{\mathrm{im}}dV \tag{2.21}$$

where $Z_0=\sqrt{\mu_0/\varepsilon_0}$ is the free-space wave impedance.

2.2.2 Temporal Discretization and Newmark-Beta Method

After spatial discretization, the weak-form representation in (2.7) has been cast into an ordinary differential equation (2.15) with respect to time. Such an equation can be solved numerically using various time integration techniques or a finite difference method. For this purpose, the time axis is first divided uniformly into a number of small time intervals (steps) and the size of each interval, denoted as Δt, is called the time-step size.

Generally, choice of Δt depends on the upper bound of the frequency band of interest (at least to satisfy the Nyquist criterion), accuracy requirement of time discretization, and sometimes the minimum spatial discretization if the adopted time-marching scheme is not unconditionally stable. Furthermore, choice of Δt affects the properties of the final linear system of equations and thus is inevitably related to the convergence of iterative linear solvers. In the context of a system of mixed linear and nonlinear equations like that in Chapter 4, choice of Δt also affects the convergence of a Newton-Raphson iteration because of the use of the converged solution at the previous time step as an initial guess of the nonlinear solution for the current time step.

After the division of the time axis, the time variable t can be written as $t = n\Delta t$, where $n = 0,1,2,\cdots$ is an integer called the time index. Given any time-dependent continuous function $u(t)$, the values of $u(t)$ evaluated at discrete time points $t = n\Delta t, \quad n = 0,1,2,\cdots$, yield a discrete sequence $u(n\Delta t)$, denoted here as u^n for the sake of simplicity. Next, the continuous time derivatives need to be approximated by a finite difference scheme.

A simple finite difference scheme (forward, backward, or central difference) may not be a good option in this case because of either loss of the unconditional stability or lack of the second-order accuracy in time. A much preferred choice is the Newmark-beta method, which was first introduced by Newmark [23] to solve structural dynamics problems. Originally with two parameters γ and β, the most useful version of this method is the one with $\gamma = 1/2$, and it has been shown that when $\beta \geq 1/4$, this method results in an unconditionally stable time-marching process while preserving the second-order accuracy with respect to temporal discretization [26]-[28]. The resulting finite differencing formula is equivalent to using central differencing for the first- and second-order time derivatives and a weighted average for the terms without differentiation at $t = n\Delta t$ as

$$\frac{d\{u(t)\}}{dt} = \frac{u^{n+1} - u^{n-1}}{2\Delta t} \tag{2.22}$$

$$\frac{d^2\{u(t)\}}{dt^2} = \frac{u^{n+1} - 2u^n + u^{n-1}}{(\Delta t)^2} \tag{2.23}$$

$$u(t) = \beta u^{n+1} + (1-2\beta)u^n + \beta u^{n-1}. \tag{2.24}$$

When $\beta = 0$, the formulas above reduce those of the central difference. A typical value for β is $1/4$. Substituting (2.22)~(2.24) with $\beta = 1/4$ into (2.15) yields

$$\begin{aligned}
&c_0^2\Delta t^2\left[S\right]\left(\frac{1}{4}\{e\}^{n+1} + \frac{1}{2}\{e\}^n + \frac{1}{4}\{e\}^{n-1}\right) + \left[M\right]\left(\{e\}^{n+1} - 2\{e\}^n + \{e\}^{n-1}\right) \\
&+ \frac{c_0\Delta t}{2}\left[G\right]\left(\{e\}^{n+1} - \{e\}^{n-1}\right) + c_0^2\Delta t^2\left[P^{\mathbf{r}}\right]\tilde{P}^{\Delta t}\left(\{e\}^0, \cdots, \{e\}^n, \{e\}^{n+1}\right) \\
&= c_0^2\Delta t^2\left(\frac{1}{4}\{b^{\mathbf{U}}\}^{n+1} + \frac{1}{2}\{b^{\mathbf{U}}\}^n + \frac{1}{4}\{b^{\mathbf{U}}\}^{n-1}\right) + \frac{c_0\Delta t Z_0}{2}\left(\{b^{\mathrm{im}}\}^{n+1} - \{b^{\mathrm{im}}\}^{n-1}\right)
\end{aligned} \tag{2.25}$$

where $\tilde{P}^{\Delta t}\left(\{e\}^0, \cdots, \{e\}^n, \{e\}^{n+1}\right)$ denotes a discretized version of $P^t\left(\{e(t)\}\right)$, which will be specified later. Therefore, at any time index *n*, assuming $\{e\}^n$ and $\{e\}^{n-1}$ are known, $\{e\}^{n+1}$ can be computed by invoking (2.25). This process is called time marching.

2.2.3 Absorbing Boundary Condition

Numerical simulation of open-region electromagnetic problems using the FEM in both the frequency and time domains requires a proper artificial truncation boundary in order to truncate the infinite region exterior to the objects. Such a boundary condition should minimize the nonphysical reflection and behave as transparently as possible to the scattered or radiated field. Various types of truncation boundary conditions for the FEM are available and can be categorized roughly into two classes. One class includes the boundary integral equations and eigenfunction expansions, which lead to globalized relations between boundary fields. The other class is called absorbing boundary conditions (ABCs) including perfectly matched layers, which only relates local boundary fields and thus keeps the sparsity of the FEM system matrix. Detailed descriptions of the formulations and implementations of boundary integral equations and perfectly matched layers as truncation boundary conditions for the TDFEM are included in [15] and [11], respectively.

The first-order ABC in the form of an impedance boundary condition is widely used because of its simplicity. In the frequency domain, the first-order ABC relates the tangential electric and magnetic fields on the boundary as

$$\hat{n} \times \left(\nabla \times \mathbf{E} \right) + jk \left(\hat{n} \times \hat{n} \times \mathbf{E} \right) = 0 \tag{2.26}$$

where $\hat{n}$ is the outward unit vector normal to the truncation boundary. When transformed to the time domain via Fourier transform, (2.26) becomes

$$\hat{n} \times \left(\frac{1}{\mu_r} \nabla \times \mathbf{E} \right) + \frac{Y_r}{c_0} \frac{\partial}{\partial t} \left(\hat{n} \times \hat{n} \times \mathbf{E} \right) = 0 \tag{2.27}$$

where $Y_r = \sqrt{\varepsilon_r / \mu_r}$ and ε_r and μ_r is the relative permittivity and permeability of the infinite medium. For free space, $\varepsilon_r = \mu_r = 1$. The first-order ABC can be easily incorporated into the TDFEM system. In fact, by comparing (2.27) with (2.6), we can identify that the ABC is simply a special case of (2.6) with $\mathbf{U} = 0$, and $P(\mathbf{E}) = \left(Y_r / c_0 \right) \partial \left(\hat{n} \times \hat{n} \times \mathbf{E} \right) / \partial t$. Consequently, in (2.14), $P^t(\cdot) = \partial(\cdot) / \partial t$ and $P^{\mathbf{r}}(\cdot) = \left(Y_r / c_0 \right) \hat{n} \times \hat{n} \times (\cdot)$. Thus, in the fully discrete system (2.25), if we denoted the ABC-related matrix as $[A]$,

$$P_{ij}^{\mathbf{r}} = A_{ij} = \frac{Y_r}{c_0} \iint_{S_3} (\hat{n} \times \mathbf{N}_i) \cdot (\hat{n} \times \mathbf{N}_j) dS \tag{2.28}$$

$$\tilde{P}^{\Delta t} \left(\{e\}^0, \cdots, \{e\}^n, \{e\}^{n+1} \right) = \frac{1}{2\Delta t} \left(\{e\}^{n+1} - \{e\}^{n-1} \right). \tag{2.29}$$

2.2.4 Waveguide Port Boundary Condition

Based on a multimodal expansion of the fields on the port interface, the waveguide port boundary condition (WPBC) was first proposed in [1] in the frequency domain as an accurate and efficient antenna feed model. The WPBC is capable of perfectly absorbing both propagating and evanescent modes incident on a waveguide port surface with an arbitrary cross section, and, at the same time launching an incident wave into the waveguide. This allows the truncation boundary to be placed as close as possible to antennas in order to reduce the size of the computation domain.

While successfully applied to the frequency-domain analysis of a variety of microwave waveguide devices [29], the WPBC for a homogeneous waveguide port has recently been extended into the time domain, leading to a highly stable and accurate time-domain port model [10] for simulation of broadband antennas [11]. As shown in Fig. 2.2, on the port surface, $\mathbf{S}_p$, $p = 1, 2, \cdots, N$, the time-domain WPBC is given in the following unified format similar to that in (2.6):

$$\hat{n} \times (\nabla \times \mathbf{E}) + P_p(\mathbf{E}) = \mathbf{U}_p^{\text{inc}}(\mathbf{E}_p^{\text{inc}}) \tag{2.30}$$

where

$$\begin{aligned} P_p\left(\mathbf{E}\right) = &-\mathbf{e}_{p0}^{\text{TEM}} \iint_{\mathbf{S}_p} \mathbf{e}_{p0}^{\text{TEM}} \cdot \frac{1}{c}\frac{\partial}{\partial t}\mathbf{E}\, dS - \sum_{m=1}^{\infty} \mathbf{e}_{pm}^{\text{TE}} \iint_{\mathbf{S}_p} \mathbf{e}_{pm}^{\text{TE}} \left(\frac{1}{c}\frac{\partial}{\partial t}\mathbf{E} + h_{pm}(t) * \mathbf{E} \right) dS \\ &- \sum_{m=1}^{\infty} \mathbf{e}_{tpm}^{\text{TM}} \iint_{\mathbf{S}_p} \mathbf{e}_{tpm}^{\text{TM}} \left(\frac{1}{c}\frac{\partial}{\partial t}\mathbf{E} + g_{pm}(t) * \mathbf{E} \right) dS \end{aligned} \tag{2.31}$$

and

$$\begin{aligned} \mathbf{U}_p^{\text{inc}}(\mathbf{E}_p^{\text{inc}}) = \hat{n} \times \left(\nabla \times \mathbf{E}_p^{\text{inc}} \right) &- \mathbf{e}_{p0}^{\text{TEM}} \iint_{\mathbf{S}_p} \mathbf{e}_{p0}^{\text{TEM}} \frac{1}{c}\frac{\partial}{\partial t}\mathbf{E}_p^{\text{inc}}\, dS \\ &- \sum_{m=1}^{\infty} \mathbf{e}_{pm}^{\text{TE}} \iint_{\mathbf{S}_p} \mathbf{e}_{pm}^{\text{TE}} \left(\frac{1}{c}\frac{\partial}{\partial t}\mathbf{E}_p^{\text{inc}} + h_{pm}(t) * \mathbf{E}_p^{\text{inc}} \right) dS \\ &- \sum_{m=1}^{\infty} \mathbf{e}_{tpm}^{\text{TM}} \iint_{\mathbf{S}_p} \mathbf{e}_{tpm}^{\text{TM}} \left(\frac{1}{c}\frac{\partial}{\partial t}\mathbf{E}_p^{\text{inc}} + g_{pm}(t) * \mathbf{E}_p^{\text{inc}} \right) dS. \end{aligned} \tag{2.32}$$

In the above, $\mathbf{E}_p^{\text{inc}}$ denotes an incident wave onto the antenna domain (from the feed network) through the *p*th port interface and "$*$" denotes a time convolution. If the incident wave consists of only dominant modes, the expression for $\mathbf{U}_p^{\text{inc}}(\mathbf{E}_p^{\text{inc}})$ will be greatly simplified. The expressions for $h_{pm}(t)$ and $g_{pm}(t)$ can be found analytically [10] as

$$h_{pm}(t) = \frac{k_{pm}}{t} J_1(k_{pm}ct)u(t) \tag{2.33}$$

$$g_{pm}(t)=\frac{k_{pm}}{t}J_1(k_{pm}ct)u(t)-k_{pm}^2cJ_0(k_{pm}ct)u(t) \tag{2.34}$$

where k_{pm} is the cutoff wavenumber of the *m*th modes at the *p*th port surface. The terms $\mathbf{e}_{p0}^{\mathrm{TEM}}$, $\mathbf{e}_{pm}^{\mathrm{TE}}$, and $\mathbf{e}_{tpm}^{\mathrm{TM}}$ are, respectively, the TEM, the *m*th TE, and the transverse component of the *m*th TM modal electric fields at the *p*th port interface. These modal fields and their related propagation constants can be computed using the two-dimensional FEM [1]. Alternatively, for regular coaxial, rectangular, and circular waveguides, analytical expressions for modal fields are also available in [2].

Finally, by substituting (2.30)-(2.32) into (2.6), the time-domain WPBC can readily be incorporated into the weak-form representation (2.7), which can then be converted into a fully discrete system after spatial and temporal discretization. The derivation of the fully discrete TDFEM system with the time-domain WPBC is described in detail in Chapter 3, where the time-domain WPBC is used as an interface between the antenna and feed-network domains.

2.3 DFDD TDFEM Formulation

The single-field TDFEM formulation described in the previous section has been demonstrated as a powerful and versatile simulation tool for transient analysis. However, one problem that restricts its application to the simulation of large-scale problems such as large and complex antennas and antenna arrays is the necessity of solving a matrix equation in every time step. Although the involved FEM matrix is time-invariant and thus requires only one-time factorization or preconditioning before time marching, the computational cost is still quite prohibitive for problems with a large number of unknowns. Much research effort has been devoted into this aspect, and available solutions include matrix-lumping techniques [27] and the use of orthogonal vector basis functions [30], [31].

One important recent development in TDFEM is the dual-field domain-decomposition (DFDD) TDFEM [12], which is a highly efficient domain-decomposition implementation of the TDFEM. This novel domain-decomposition scheme solves the dual-field (i.e., both the electric and magnetic fields) second-order vector wave equations in each subdomain and relates the solutions in adjacent subdomains explicitly using equivalent surface currents on the subdomain interfaces. Specifically, in each subdomain, the electric field is calculated at integer time indices and the magnetic field is calculated at half integer time indices, which enables a leapfrogging time-marching scheme to update the equivalent surface currents on the subdomain interfaces. Once those currents are known, the electric and magnetic fields inside each subdomain can be solved independently using a direct solver with the local prefactored matrix of much smaller size than an original global FEM matrix. The accuracy, efficiency, and capability of this method have been demonstrated through applications to complex electromagnetic problems, including large finite antenna arrays [13]. Such problems are very challenging for the conventional TDFEM, which has to solve a linear system involving millions of unknowns. In this section, a few important aspects about this algorithm are highlighted.

The computational domain Ω is partitioned into a number of nonoverlapping subdomains Ω^s, $s = 1, 2, \cdots, N^s$, where N^s is the number of subdomains. Inside Ω^s, solution of the electric wave equation (2.3) for the electric field $\mathbf{E}^s$ can be formulated following the procedure described in Section 2.2. The only difference is that, at the subdomain interface, denoted as Γ^s, a boundary condition for $\mathbf{E}^s$ needs to be specified. As shown in Fig. 2.3(a), assuming the surface electric current density $\mathbf{J}_S^s$ on Γ^s is known and applying Maxwell's equation, a Neumann-type boundary condition for $\mathbf{E}^s$ is given as

$$\hat{n}^s \times \frac{1}{\mu_r} \nabla \times \mathbf{E}^s = -\mu_0 \frac{\partial \mathbf{J}_S^s}{\partial t}. \tag{2.35}$$

Equation (2.35) can easily be included into (2.7) through (2.6) by adding the term $\mu_0 \iint_{\Gamma^s} \hat{n} \times \mathbf{N}_i \cdot \hat{n} \times \left(\partial \mathbf{J}_S^s / \partial t \right) dS$ to the right-hand side of (2.7). Note that $\mathbf{E}^s$ is discretized on integer time indices, $n = 0, 1, 2, \cdots$. Therefore, once $\left(\partial \mathbf{J}_S^s / \partial t \right)^n$ is known, $\left\{ \mathbf{E}^s \right\}^{n+1}$ can be computed independently from the other subdomains.

Similarly, the solution of the magnetic wave equation for the magnetic field $\mathbf{H}^s$ inside Ω^s

can be formulated. As shown in Fig. 2.3(a), at the subdomain interface Γ^s, assuming the surface magnetic current density $\mathbf{M}_S^s$ is known, a Neumann-type boundary condition for $\mathbf{H}^s$ is given as

$$\hat{n}^s \times \frac{1}{\varepsilon_r} \nabla \times \mathbf{H}^s = -\varepsilon_0 \frac{\partial \mathbf{M}_S^s}{\partial t} \tag{2.36}$$

which can be cast into $\varepsilon_0 \iint_{\Gamma^s} \hat{n} \times \mathbf{N}_i \cdot \hat{n} \times \left(\partial \mathbf{M}_S^s / \partial t \right) dS$ and added in the weak-form representation. Unlike the electric field, $\mathbf{H}^s$ is discretized on half-integer time indices $n + 1/2$, $n = 0, 1, 2, \cdots$, and once $\left(\partial \mathbf{M}_S^s / \partial t \right)^{n+1/2}$ is known, $\left(\mathbf{H}^s \right)^{n+3/2}$ can also be computed.

We further assume that the subdomain interface Γ^s is shared by Ω^s and its neighbor Ω^{ns}, and the electric and magnetic fields in Ω^{ns} are denoted as $\mathbf{E}^{ns}$ and $\mathbf{H}^{ns}$, respectively. As shown in Fig. 2.3(b), the quantity $\left(\partial \mathbf{J}_S^s / \partial t \right)^n$ can now be computed from the tangential component of $\mathbf{H}^{ns}$ on Γ^s as

$$\left(\partial \mathbf{J}_S^s / \partial t \right)^n = \frac{\hat{n} \times \left(\mathbf{H}^{ns} \right)^{n+1/2} - \hat{n} \times \left(\mathbf{H}^{ns} \right)^{n-1/2}}{\Delta t}. \tag{2.37}$$

Dually, as shown in Fig. 2.3(b), $\left(\partial \mathbf{M}_S^s / \partial t \right)^{n+1/2}$ is computed from the tangential component of $\mathbf{E}^{ns}$ as

$$\left(\partial \mathbf{M}_S^s / \partial t \right)^{n+1/2} = \frac{\left(\mathbf{E}^{ns} \right)^{n+1} \times \hat{n} - \left(\mathbf{E}^{ns} \right)^n \times \hat{n}}{\Delta t}. \tag{2.38}$$

As a result, the electric and magnetic fields in Ω^s can be updated in a leapfrogging fashion: at any time step *n*, $\left(\partial \mathbf{J}_S^s / \partial t \right)^n$ is first computed using (2.37), and $\left\{ \mathbf{E}^s \right\}^{n+1}$ can be updated next. Once this is done, $\left(\partial \mathbf{M}_S^s / \partial t \right)^{n+1/2}$ is available from the computation of (2.38), which then enables the calculation of $\left(\mathbf{H}^s \right)^{n+3/2}$.

Finally, for finite array simulation, an important attribute of this method is that it allows us to fully exploit the geometrical redundancy of the array-type structures to significantly speed up the simulation and reduce the memory requirement [13]. Geometrically, since all the array elements have identical geometry (as shown in Fig. 2.4(a)), the entire array can be characterized by a single array element, named a unit cell. In DFDD TDFEM, each array element is considered as an individual subdomain and identical spatial discretizations are applied to all of them. Therefore, the FEM matrices for all subdomains are the same except for the array elements on the four corners and four edges. Figure 2.4(b) shows the partition of a typical two-dimensional array into nine unit regions: a central region, four edge regions, and four corner regions. A two-dimensional array can be fully characterized by these nine unit regions. For large arrays, this algorithm can lead to a significant reduction in the total memory usage and factorization time. This feature has been utilized in Chapter 3 when simulating large antenna arrays.

2.4 Figures

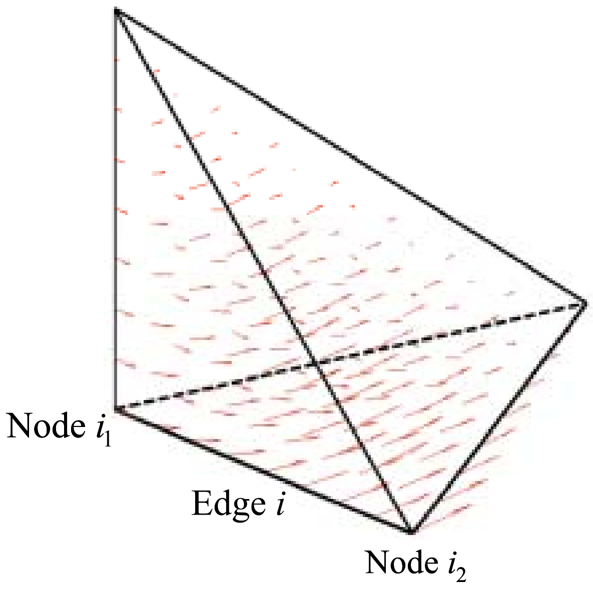
Node i_1
Edge i
Node i_2

Figure 2.1: The lowest-order vector basis function associated with the *i*th edge for a tetrahedral element.

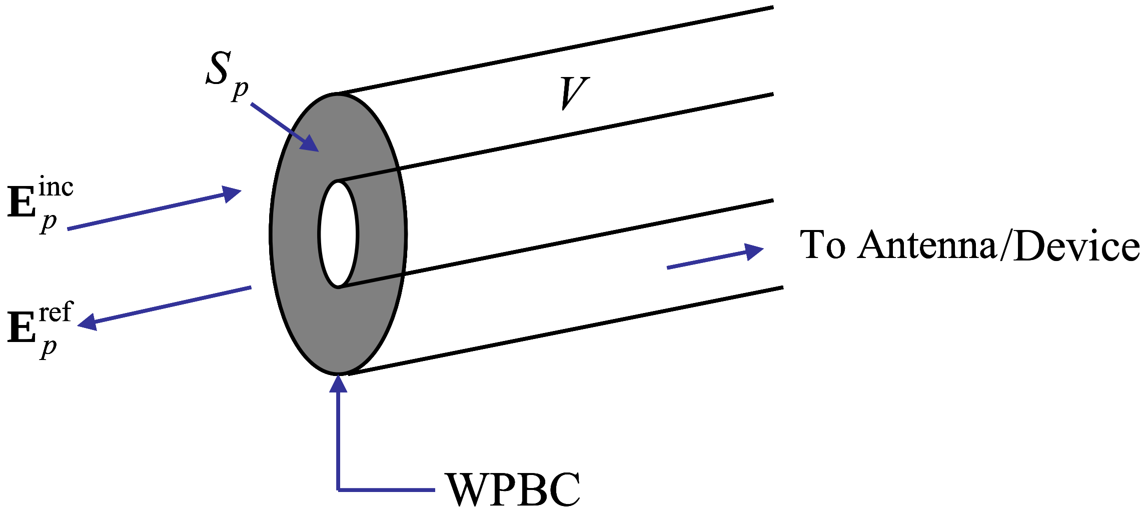
S_p
V
$\mathbf{E}_p^{\text{inc}}$
$\mathbf{E}_p^{\text{ref}}$
To Antenna/Device
WPBC

Figure 2.2: One of the coaxial waveguide ports for antennas or microwave devices.

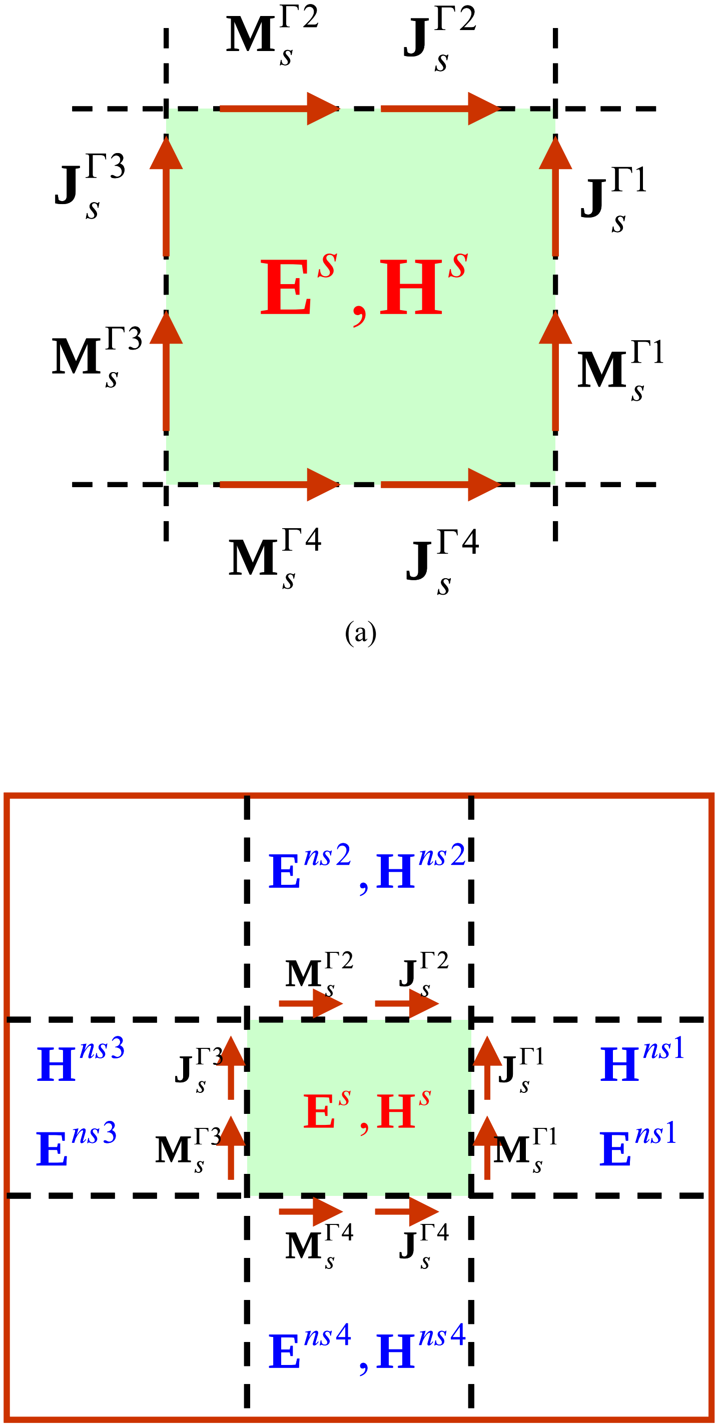
$\mathbf{M}_s^{\Gamma 2}$
$\mathbf{J}_s^{\Gamma 2}$
$\mathbf{J}_s^{\Gamma 3}$
$\mathbf{J}_s^{\Gamma 1}$
$\mathbf{E}^s, \mathbf{H}^s$
$\mathbf{M}_s^{\Gamma 3}$
$\mathbf{M}_s^{\Gamma 1}$
$\mathbf{M}_s^{\Gamma 4}$
$\mathbf{J}_s^{\Gamma 4}$
$\mathbf{E}^{ns2}, \mathbf{H}^{ns2}$
$\mathbf{H}^{ns3}$
$\mathbf{E}^{ns3}$
$\mathbf{H}^{ns1}$
$\mathbf{E}^{ns1}$
$\mathbf{E}^{ns4}, \mathbf{H}^{ns4}$

(a)

(b)

Figure 2.3: The dual-field scheme for subdomain *s* in DFDD TDFEM.

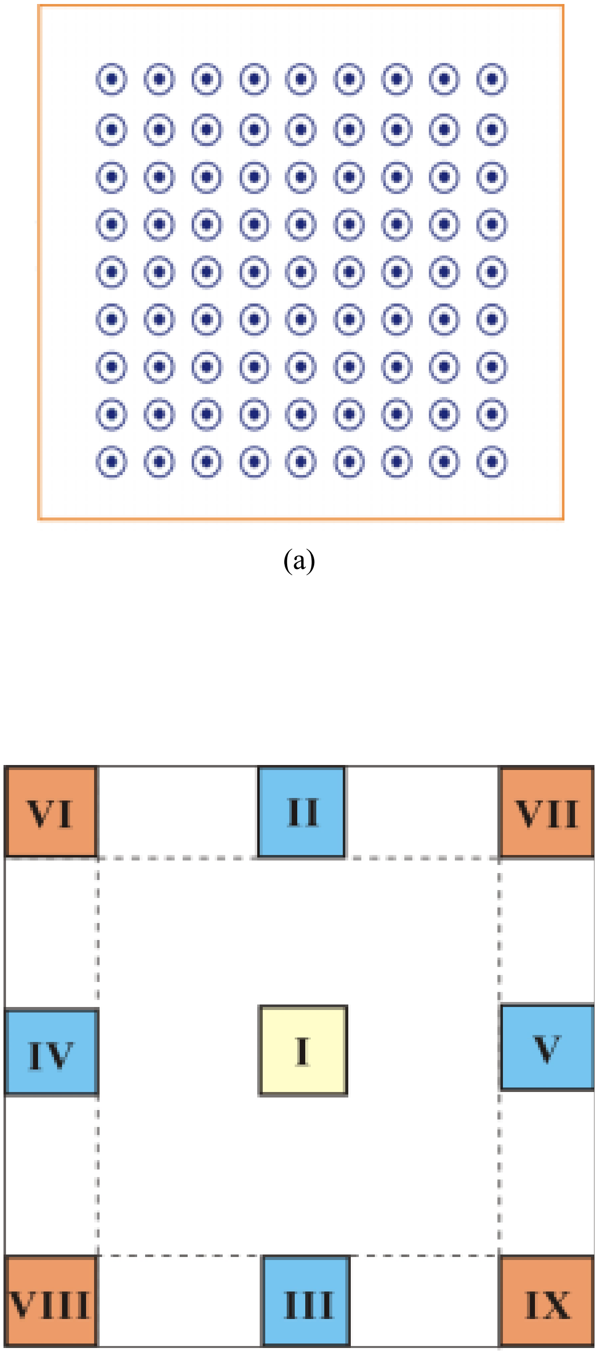
VI
II
VII
IV
I
V
VIII
III
IX

(a)

(b)

Figure 2.4: A two-dimensional array (a) can be fully characterized by nine unit regions (b).

CHAPTER 3

INCORPORATION OF FEED-NETWORK MODELING INTO THE TDFEM ANALYSIS OF ANTENNA ARRAYS

In this chapter, an accurate and efficient numerical scheme is presented for incorporating the feed-network modeling into the TDFEM analysis of antennas and antenna arrays and thus accounting for the impact of the interactions between the radiating elements and the feed network on the performance of antenna systems. In the proposed approach, a feed network is considered as a linear, passive, multiport electromagnetic device, which is connected to the source and the antennas solely through electromagnetic ports associated with the cross section of either an electromagnetic waveguide or an aperture, and characterized in terms of its frequency-dependent S-matrix over a wide frequency band. The extraction of the S-matrix relies upon the application of an electromagnetic field solver that calculates the S-parameters over the desirable frequency bandwidth [32]-[34]. A macromodel of the S-matrix is then derived in terms of rational function interpolation of the discrete frequency data using the vector-fitting (VECTFIT) algorithm [35]. This macromodel, which captures the important characteristics of the original feed network, is interfaced with the TDFEM solver through an efficient time-domain convolution scheme. The proposed approach works seamlessly with the conventional single-field TDFEM/WPBC and is extended to be compatible with the dual-field formulation to utilize the capability of the DFDD TDFEM for simulating large, complex structures. This approach not only significantly simplifies the simulation of an entire antenna system, but also allows one to fully utilize the power of the state-of-the-art TDFEM techniques to deal with large and complex antenna arrays.

The remainder of this chapter is organized as follows. In Section 3.1, we first present the coupling scheme based on the traveling-wave decomposition of the fields on the port interfaces that separate the feed-network domain from the antenna domain and the source. Next, we describe the single-field TDFEM/WPBC formulation to incorporate the macromodeling of the feed network into the antenna simulation and present a coupled time-marching scheme, which combines the modeling of the antenna and the feed-network domains. We then extend the proposed scheme to a dual-field formulation in Section 3.2, which is compatible with the DFDD-TDFEM. The stability of the coupled time-marching scheme is discussed in Section 3.3. The simulation examples in Section 3.4 validate the proposed methodology and demonstrate its application to the modeling of one- and two-dimensional antenna arrays fed by various types of feed networks. Finally, concluding remarks are given in Section 3.5

3.1 Formulation

3.1.1 Port Interfaces and Coupling Scheme

The feed network is considered as a multiport, linear, passive system, which is connected to the source and the antennas solely through a set of port interfaces $\mathbf{S}_p$, $p = 0,1,2,\cdots,N$, as illustrated in Fig. 3.1. These port interfaces separate the feed-network domain from the antenna domain and the source.

At the *p*th port interface, the total transverse electric field $\mathbf{E}_p$ and magnetic field $\mathbf{H}_p$ can be decomposed into two traveling waves as

$$\mathbf{E}_p(\mathbf{r},s) = \mathbf{E}_p^{(+)}(\mathbf{r},s) + \mathbf{E}_p^{(-)}(\mathbf{r},s) \tag{3.1}$$

$$\mathbf{H}_p(\mathbf{r},s) = \mathbf{H}_p^{(+)}(\mathbf{r},s) + \mathbf{H}_p^{(-)}(\mathbf{r},s) \tag{3.2}$$

where $s = j\omega$ is the complex frequency, and $\mathbf{r}$ denotes the position vector on the port surface. Referring to Fig. 3.1, the (+) sign is used to label the waves traveling from the antenna domain (or the source) to the feed-network domain through the port interface, while the (–) sign is used to label the waves traveling from the feed-network domain to the antenna domain (or the source) through the port interface. The (+) and (–) notations will be used throughout this chapter. Next, we assume that each port interface is associated with the cross section of a homogeneous, isotropic, and lossless electromagnetic waveguide, whose dominant mode is the transverse electromagnetic (TEM) and is independent of frequency. This assumption is valid for feed networks made of coaxial lines or shielded striplines; however, the formulation can be extended to those whose dominant modes are either TE or TM modes. With the assumption of TEM-mode propagation, the traveling-wave decompositions in (3.1) and (3.2) are also applicable to the modal coefficients

$$V_p(s) = V_p^{(+)}(s) + V_p^{(-)}(s) \tag{3.3}$$

$$I_p(s) = I_p^{(+)}(s) - I_p^{(-)}(s) \tag{3.4}$$

where "*V*" and "*I*" denote the modal coefficients of the dominant TEM electric and magnetic modal fields, respectively, which are also known as the modal voltages and the modal currents. The time-domain counterparts of (3.3) and (3.4) are simply given by

$$V_p(t) = V_p^{(+)}(t) + V_p^{(-)}(t) \tag{3.5}$$

$$I_p(t) = I_p^{(+)}(t) - I_p^{(-)}(t)\,. \tag{3.6}$$

Based on the decompositions above, the interactions between the feed network and the antennas can be simulated in the time domain through the following scheme. First, the feed network takes $V_p^{(+)}(t)$ $\left(\text{or}\, I_p^{(+)}(t)\right)$, $p = 0,1,2,\cdots,N,$ as the incident fields and produces the output signals (which can be termed as reflections of the feed network) $V_p^{(-)}(t)$ $\left(\text{or}\, I_p^{(-)}(t)\right)$, $p = 0,1,2,\cdots,N.$ The quantities $V_p^{(+)}(t)$ $\left(\text{or}\, I_p^{(+)}(t)\right)$ and $V_p^{(-)}(t)$ $\left(\text{or}\, I_p^{(-)}(t)\right)$, $p = 0,1,2,\cdots,N,$ are related by the S-matrix of the feed network. Then, the reflections of the feed network, $V_p^{(-)}(t)$ $\left(\text{or}\, I_p^{(-)}(t)\right)$, $p = 0,1,2,\cdots,N,$ are considered as the excitations for the antennas at the port interfaces. When the antenna domain is modeled by the TDFEM, the time-domain WPBC applied at the port interfaces can take $V_p^{(-)}(t)$ $\left(\text{or}\, I_p^{(-)}(t)\right)$, $p = 0,1,2,\cdots,N,$ as the port incident fields and calculate any reflections from the antennas. These reflections from the antennas becomes $V_p^{(+)}(t)$ $\left(\text{or}\, I_p^{(+)}(t)\right)$, $p = 0,1,2,\cdots,N,$ which again become the incident fields for the feed network across the port interfaces. Therefore, the interactions of the feed-network domain and the antenna domain are carried out by exchanging their incident and reflected modal voltages (currents) through the port interfaces that connect them.

Note that a similar bidirectional decomposition approach has also been adopted in [36] for interfacing the FDTD method with embedded circuit networks based on the multiconductor transmission-line theory.

3.1.2 The Single-Field TDFEM/WPBC Formulation

As shown in Fig. 3.2, the antenna domain denoted by V is modeled by the single-field TDFEM with the time-domain WPBC applied on the port interfaces $\mathbf{S}_p$, $p = 1, 2, \cdots, N$. The time-domain WPBC, based on a multimodal expansion, is given by

$$\hat{n} \times (\nabla \times \mathbf{E}) + P_p(\mathbf{E}) = \mathbf{U}_p^{\mathrm{inc}}(\mathbf{E}_p^{(-)}) \tag{3.7}$$

where $P_p(\mathbf{E})$ and $\mathbf{U}_p^{\mathrm{inc}}(\mathbf{E}_p^{(-)})$ are defined in (2.31) and (2.32), respectively. $\mathbf{E}_p^{(-)}$ denotes an incident wave onto the antenna domain (from the feed network) through the pth port interface.

Making use of the time-domain WPBC on all the port interfaces, we obtain the following weak form of the wave equation:

$$\begin{aligned}&\iiint_V \left[\frac{1}{\mu_r}(\nabla \times \mathbf{N}_i) \cdot (\nabla \times \mathbf{E}) + \frac{\varepsilon_r}{c_0^2}\mathbf{N}_i \cdot \frac{\partial^2 \mathbf{E}}{\partial t^2} + \mu_0 \sigma \mathbf{N}_i \cdot \frac{\partial \mathbf{E}}{\partial t} \right] dV \\ &- \sum_{p=1}^{N} \iint_{\mathbf{S}_p} \frac{1}{\mu_r} \mathbf{N}_i \cdot P_p(\mathbf{E}) dS = -\sum_{p=1}^{N} \iint_{\mathbf{S}_p} \frac{1}{\mu_r} \mathbf{N}_i \cdot \mathbf{U}_p^{\mathrm{inc}}(\mathbf{E}_p^{(-)}) dS.\end{aligned} \tag{3.8}$$

For simplicity in the discussion that follows, in the equation above we have not included terms associated with any excitations inside the antenna domain and terms associated with other possible boundary conditions such as the ABC. After spatial discretization, (3.8) yields the following semi-discrete system:

$$[S]\{e\} + \frac{1}{c_0^2}[M]\frac{\partial^2 \{e\}}{\partial t^2} + \frac{1}{c_0}\big([G] + [P]\big)\frac{\partial \{e\}}{\partial t} + \sum_{p=1}^{N}\sum_{m=1}^{\infty}[Q^{pm}]\{u_{pm}\} + \sum_{p=1}^{N}\sum_{m=1}^{\infty}[R^{pm}]\{v_{pm}\} = \{b\}\,. \tag{3.9}$$

The expressions for the matrix entries in $\left[S\right]$, $\left[M\right]$, and $\left[G\right]$ are given in (2.16)-(2.18), respectively, and those in $\left[P\right]$, $\left[Q^{pm}\right]$, and $\left[R^{pm}\right]$ are given by

$$P_{ij} = \sum_{p=1}^{N} \frac{1}{\mu_r c} \left(\Phi_{ip0}^{\text{TEM}} \cdot \Phi_{jp0}^{\text{TEM}} + \sum_{m=1}^{\infty} \Phi_{ipm}^{\text{TE}} \cdot \Phi_{jpm}^{\text{TE}} + \sum_{m=1}^{\infty} \Phi_{ipm}^{\text{TM}} \cdot \Phi_{jpm}^{\text{TM}} \right) \tag{3.10}$$

$$Q_{ij}^{pm} = \Phi_{ipm}^{\text{TE}} \cdot \Phi_{jpm}^{\text{TE}} \tag{3.11}$$

$$R_{ij}^{pm} = \Phi_{ipm}^{\text{TM}} \cdot \Phi_{jpm}^{\text{TM}} \tag{3.12}$$

where $\eta_0 = \sqrt{\mu_0 / \varepsilon_0}$ and $\Phi_{ipm}^{\text{TEM/TE/TM}}$ is defined as the projection of the modal field onto the basis function $\mathbf{N}_i$ over the port surface

$$\Phi_{ipm}^{\text{TEM/TE/TM}} = \iint_{\text{S}_p} \mathbf{N}_i \cdot \mathbf{e}_{(t)pm}^{\text{TEM/TE/TM}} \, dS \, . \tag{3.13}$$

Furthermore, $\{u_{pm}\}$ and $\{v_{pm}\}$ denote the following convolution vectors:

$$\{u_{pm}\} = h_{pm} * \{e\} \tag{3.14}$$

$$\{v_{pm}\} = g_{pm} * \{e\} \, . \tag{3.15}$$

The inclusion of enough higher-order modes in the WPBC is important for accurate truncation of the antenna domain. The number of modes to be included is problem-dependent and the typical number used in the simulations of this work is 4~5. As far as the excitation of the structure is concerned, in view of our assumption that, for the purposes of this work, only the dominant TEM mode is propagating in the feed network, the expressions for $\mathbf{U}_p^{\text{inc}}$ and $\left\{b\right\}$ are greatly simplified as

$$\mathbf{U}_p^{\text{inc}}(\mathbf{E}_p^{(-)}) = \mathbf{U}_p^{\text{inc}}(V_p^{(-)}(t)\mathbf{e}_{p0}^{\text{TEM}}) = -2\,\mathbf{e}_{p0}^{\text{TEM}} \frac{1}{c} \frac{\mathrm{d}}{\mathrm{d}t}[V_p^{(-)}(t)] \tag{3.16}$$

$$b_i = \frac{2}{\mu_r c} \sum_{p=1}^{N} \Phi_{ip0}^{\text{TEM}} \frac{\mathrm{d}}{\mathrm{d}t}[V_p^{(-)}(t)] \, . \tag{3.17}$$

Next, (3.9) is discretized in the time domain using the Newmark-beta method with $\beta = 1/4$, which yields

$$
\begin{aligned}
& c_0^2\Delta t^2[S]\left(\frac{1}{4}\{e\}^{n+1}+\frac{1}{2}\{e\}^{n}+\frac{1}{4}\{e\}^{n-1}\right)+[M]\left(\{e\}^{n+1}-2\{e\}^{n}+\{e\}^{n-1}\right)\\
&\quad+\frac{c_0\Delta t}{2}\left([G]+[P]\right)\left(\{e\}^{n+1}-\{e\}^{n-1}\right)\\
&\quad+\sum_{p=1}^{N}\sum_{m=1}^{\infty}\left[Q^{pm}\right]\left(\frac{1}{4}\{u_{pm}\}^{n+1}+\frac{1}{2}\{u_{pm}\}^{n}+\frac{1}{4}\{u_{pm}\}^{n-1}\right)\\
&\quad+\sum_{p=1}^{N}\sum_{m=1}^{\infty}\left[R^{pm}\right]\left(\frac{1}{4}\{v_{pm}\}^{n+1}+\frac{1}{2}\{v_{pm}\}^{n}+\frac{1}{4}\{v_{pm}\}^{n-1}\right)\\
&\quad=\frac{c_0^2\Delta t}{\mu_r c}\sum_{p=1}^{N}\left(V_p^{(-)}(n+1)-V_p^{(-)}(n-1)\right)\left\{\Phi_{p0}^{\mathrm{TEM}}\right\}.
\end{aligned}
\tag{3.18}
$$

In the equation above, $V_p^{(-)}$, $p=1,2,\cdots,N$, are provided by the feed network and assumed to be known for time index ($n+1$) and ($n-1$); therefore, we can solve for $\{e\}^{n+1}$ in a time-marching fashion. At the *p*th port interface, whenever the unknown vector $\{e\}$ is solved for, the total modal voltage V_p can be calculated by

$$V_p=\sum_i e_i\Phi_{ip0}^{\mathrm{TEM}} \tag{3.19}$$

and the reflected modal voltage $V_p^{(+)}$ from the antennas at that time index can be extracted by invoking (3.5), yielding

$$V_p^{(+)}=V_p-V_p^{(-)}. \tag{3.20}$$

3.1.3 Feed-Network Macromodel and Time Convolution

With the feed network considered as a linear, passive, multiport device, we are able to explore the relations between modal voltages and currents at the port interfaces and thus represent the feed network by various types of network parameter matrices, such as impedance matrix, admittance matrix, or S-matrix. As described before, a feed-network model should take the port reflections from the antennas as its incident fields and provide proper reflections (outputs) as the port excitations for the antennas. In this context, we choose to characterize the feed network by its broadband S-matrix, which directly relates the incident and reflected modal voltages at the port interfaces over a wide frequency band as

$$\begin{bmatrix} V_0^{(-)}(s)/\sqrt{Z_0} \\ V_1^{(-)}(s)/\sqrt{Z_1} \\ \vdots \\ V_N^{(-)}(s)/\sqrt{Z_N} \end{bmatrix} = \begin{bmatrix} S_{00}(s) & S_{01}(s) & \cdots & S_{0N}(s) \\ S_{10}(s) & S_{11}(s) & \cdots & S_{1N}(s) \\ \vdots & \vdots & \ddots & \vdots \\ S_{N0}(s) & S_{N1}(s) & \cdots & S_{NN}(s) \end{bmatrix} \begin{bmatrix} V_0^{(+)}(s)/\sqrt{Z_0} \\ V_1^{(+)}(s)/\sqrt{Z_1} \\ \vdots \\ V_N^{(+)}(s)/\sqrt{Z_N} \end{bmatrix} \tag{3.21}$$

where Z_p, $p = 0,\cdots,N$, is the port impedance of the *p*th port. Such a broadband S-matrix can be efficiently computed, either by a fast circuit solver such as HSPICE [37] or Agilent Advanced Design System (ADS) [38] for those cases for which a circuit diagram of the feed network is available, or by a broadband electromagnetic field solver when the physical layout of the feed network is available. In both cases, the calculated S-parameters are in terms of a set of values calculated at a set of discrete frequencies spanning the bandwidth of interest. In this form the data is not easily interfaced with the numerical scheme used for the integration of (3.18). A preferable and computationally efficient alternative to the discrete data is a rational function interpolation over the bandwidth of interest, since it lends itself to a recursive scheme for the expedient calculation of the convolution operations in (3.18). The VECTFIT technique for the rational function interpolation of network functions is well known for its robustness, accuracy and efficiency. Thus, we choose the VECTFIT scheme for the rational function interpolation of the discrete data [35].

Using VECTFIT each entry $S_{ij}(s)$, $i, j = 0,1,\cdots,N$, of the S-matrix can be approximated as

$$S_{ij}(s) \approx \tilde{S}_{ij}(s) = \sum_{k=1}^{N_k} \frac{c_{ij,k}}{s - a_k} + d_{ij}\,. \tag{3.22}$$

In the above expression, a_k, $k = 1,2,\cdots,N_k$, is the set of common poles used for all the entries in the S-matrix, while $c_{ij,k}$ denotes the residue of $\tilde{S}_{ij}(s)$ associated with the pole a_k. The variables a_k and $c_{ij,k}$ are either real or in the form of complex conjugate pairs, and d_{ij} is an optional real constant. This rational function approximation of the S-matrix is referred to as the macromodel of the feed network.

By invoking the rational approximations in (3.22), the matrix representation in (3.21) can be easily transformed into the time domain as

$$\begin{bmatrix} V_0^{(-)}(t)\big/\sqrt{Z_0} \\ V_1^{(-)}(t)\big/\sqrt{Z_1} \\ \vdots \\ V_N^{(-)}(t)\big/\sqrt{Z_N} \end{bmatrix} = \begin{bmatrix} \tilde{S}_{00}(t) & \tilde{S}_{01}(t) & \cdots & \tilde{S}_{0N}(t) \\ \tilde{S}_{10}(t) & \tilde{S}_{11}(t) & \cdots & \tilde{S}_{1N}(t) \\ \vdots & \vdots & \ddots & \vdots \\ \tilde{S}_{N0}(t) & \tilde{S}_{N1}(t) & \cdots & \tilde{S}_{NN}(t) \end{bmatrix} * \begin{bmatrix} V_0^{(+)}(t)\big/\sqrt{Z_0} \\ V_1^{(+)}(t)\big/\sqrt{Z_1} \\ \vdots \\ V_N^{(+)}(t)\big/\sqrt{Z_N} \end{bmatrix} \tag{3.23}$$

where "*" denotes a time convolution. It is well known that the elements of the time-domain S-matrix are in terms of exponential functions. Therefore, the convolutions in the discrete form of (3.23) can be recursively evaluated with a computationally efficient algorithm of O($T_{\max}$) complexity, where $T_{\max}$ is the number of time steps in the transient simulation. This recursive convolution process, in a compact matrix form, can be described in terms of the following updating equations:

$$\left\{\mathbf{T}_{\mathrm{V}}\right\}^{n+1} = \overline{\mathbf{E}}_1 \cdot \left\{\mathbf{T}_{\mathrm{V}}\right\}^{n} + \overline{\mathbf{E}}_2 \cdot \overline{\mathbf{B}} \cdot \left\{\mathbf{V}^{(+)}\right\}^{n} \tag{3.24}$$

$$\left\{\mathbf{V}^{(-)}\right\}^{n+1} = \overline{\mathbf{C}} \cdot \left\{\mathbf{T}_{\mathrm{V}}\right\}^{n+1} + \overline{\mathbf{D}} \cdot \left\{\mathbf{V}^{(+)}\right\}^{n}. \tag{3.25}$$

In the equations above, $\left\{\mathbf{V}^{(+)}\right\}^{n}$ = [$V_0^{(+)}(n)\big/Z_0, V_1^{(+)}(n)\big/Z_1, \cdots, V_N^{(+)}(n)\big/Z_N$]^{T} and $\left\{\mathbf{V}^{(-)}\right\}^{n+1}$ = [$V_0^{(-)}(n+1)\big/Z_0, V_1^{(-)}(n+1)\big/Z_1, \cdots, V_N^{(-)}(n+1)\big/Z_N$]^{T}, and $n = 0, 1, \cdots, T_{\max}$, is the time index. The vector $\left\{\mathbf{T}_{\mathrm{V}}\right\}^{n+1}$ is an intermediate time-dependent vector whose entries can be computed recursively using (3.24). The matrices $\overline{\mathbf{E}}_1$, $\overline{\mathbf{E}}_2$, $\overline{\mathbf{B}}$, $\overline{\mathbf{C}}$ and $\overline{\mathbf{D}}$ are independent of time, and their entries are only dependent on the coefficients of the rational function representations of the entries of the S-matrix shown in (3.22) and the time step Δt. The derivations of the expressions for the elements of the vectors and matrices in (3.24) and (3.25) are given in the Appendix A.

If Port 0 is assumed connected to the matched voltage source, as illustrated in Fig. 3.1, $V_0^{(+)}$ is then specified at all time indices. Based on Thévenin's theorem, we can simply model this source as a single voltage generator with a single series resistor of value Z_0, the port impedance of Port 0.

3.1.4 Coupled Time-Marching Scheme

The coupled time-marching scheme which combines the TDFEM time-marching process of the antenna domain and the time-convolution process in the feed network domain are summarized here.

Before the time marching starts, the macromodel of the feed network is precalculated and stored in terms of its pole-residue form of the rational approximation of its S-matrix. This is called preprocessing and is illustrated in Fig. 3.3(a).

During the time marching, at time index n:

Step 1: Antenna domain: Compute $V_1(n),\ V_2(n),\ \cdots,\ V_N(n)$ from $\{e\}^n$ using (3.19).

Step 2: Antenna domain: Calculate $V_1^{(+)}(n),\ V_2^{(+)}(n),\ \cdots,\ V_N^{(+)}(n)$ from $V_1^{(-)}(n),\ V_2^{(-)}(n),\ \cdots,\ V_N^{(-)}(n)$ and $V_1(n),\ V_2(n),\ \cdots,\ V_N(n)$ using (3.20).

Step 3: Feed network domain: Update $\{\mathbf{V}^{(-)}\}^{n+1}$ based on $\{\mathbf{V}^{(+)}\}^n$ ($V_0^{(+)}(n)$ from the source) using (3.24) and (3.25).

Step 4: Antenna domain: Update $\{e\}^{n+1}$ using (3.18).

The coupled time-marching scheme described above is illustrated in Fig. 3.3(b).

3.2 Extension to the Dual-Field Formulation

The DFDD TDFEM is a highly efficient domain-decomposition implementation of the TDFEM based on the dual-field second-order vector wave equations [12]-[13]. In each subdomain, the electric field is calculated at integer time indices and the magnetic field is calculated at half integer time indices, which enables a leapfrog time-marching scheme to update the equivalent surface currents on the subdomain interfaces. Once those currents are known, the electric and magnetic fields inside each subdomain can be updated independently. Since the

DFDD TDFEM is a desired method to model large and complex antenna arrays, it is necessary to extend the proposed coupled time-marching scheme to make it compatible with the dual-field formulation.

To solve the electric field equations in each subdomain, the feed network and the antennas interact with each other in the same fashion as described in the previous sections. The only difference is that the exchange of incident and reflected modal voltages is now between the feed network and the specific antenna subdomain to which the port interface belongs. To solve the magnetic field equations with time-domain magnetic-field WPBC in each subdomain, we need to establish a dual scheme for exchanging the incident and reflected modal currents. Fortunately, the S-matrix in (3.23) also relates the incident and reflected modal currents at the port interfaces as

$$\begin{bmatrix} \sqrt{Z_0} I_0^{(-)}(t) \\ \sqrt{Z_1} I_1^{(-)}(t) \\ \vdots \\ \sqrt{Z_N} I_N^{(-)}(t) \end{bmatrix} = \begin{bmatrix} \tilde{S}_{00}(t) & \tilde{S}_{01}(t) & \cdots & \tilde{S}_{0N}(t) \\ \tilde{S}_{10}(t) & \tilde{S}_{11}(t) & \cdots & \tilde{S}_{1N}(t) \\ \vdots & \vdots & \ddots & \vdots \\ \tilde{S}_{N0}(t) & \tilde{S}_{N1}(t) & \cdots & \tilde{S}_{NN}(t) \end{bmatrix} * \begin{bmatrix} \sqrt{Z_0} I_0^{(+)}(t) \\ \sqrt{Z_1} I_1^{(+)}(t) \\ \vdots \\ \sqrt{Z_N} I_N^{(+)}(t) \end{bmatrix}. \tag{3.26}$$

Dual to (3.24) and (3.25), the following recursive convolution process exists for (3.26), but on half integer time indices:

$$\left\{\mathbf{T}_{\mathrm{I}}\right\}^{n+\frac{3}{2}} = \overline{\mathbf{E}}_1 \cdot \left\{\mathbf{T}_{\mathrm{I}}\right\}^{n+\frac{3}{2}} + \overline{\mathbf{E}}_2 \cdot \overline{\mathbf{B}} \cdot \left\{\mathbf{I}^{(+)}\right\}^{n+\frac{1}{2}} \tag{3.27}$$

$$\left\{\mathbf{I}^{(-)}\right\}^{n+\frac{3}{2}} = \overline{\mathbf{C}} \cdot \left\{\mathbf{T}_{\mathrm{I}}\right\}^{n+\frac{1}{2}} + \overline{\mathbf{D}} \cdot \left\{\mathbf{I}^{(+)}\right\}^{n+\frac{1}{2}}. \tag{3.28}$$

The vector $\left\{\mathbf{T}_{\mathrm{I}}\right\}^{n+\frac{3}{2}}$ is another intermediate time-dependent vector, dual to $\left\{\mathbf{T}_{\mathrm{V}}\right\}^{n+1}$. Again, if Port 0 is assumed to connect to the source, $I_0^{(+)}$ is known at all half integer time indices. To find $I_0^{(+)}$ we can invoke Norton's theorem (dual to Thévenin's theorem) and model the source part as a single equivalent current generator with the value $V_0^{(+)}/\mathrm{R}$ in parallel with a single resistor whose value R is equal to Z_0.

Based on the description above, a dual coupled time-marching scheme to solve for the magnetic field can be easily established. The scheme is very similar to steps 1 to 4 in the previous section, but for modal currents which are all in half integer time indices.

The above extension to the dual-field formulation involves two time convolutions, one for updating modal voltages and the other for updating modal currents. This treatment indicates that any computational cost associated with time convolution is doubled, compared to the single-field formulation, which is not desired, especially when the array size gets larger and the feed-network model becomes more complex. However, for the dominant TEM mode, the second convolution for updating modal currents can be avoided when we utilize the relation between the incident modal voltage and the incident modal current for antennas at each port interface. More specifically, instead of computing $\frac{\mathrm{d}}{\mathrm{d}t}[I_p^{(-)}(t)]$ at time index $(n+1/2)$ by a central difference formula involving $I_p^{(-)}(n+3/2)$ and $I_p^{(-)}(n+1/2)$, the relation $V_p^{(-)}(t)=Z_p I_p^{(-)}(t)$ can be utilized so that

$$\left.\frac{\mathrm{d}}{\mathrm{d}t}[I_p^{(-)}(t)]\right|_{t=(n+1/2)\Delta t}=\frac{1}{Z_p\Delta t}\Big(V_p^{(-)}(n+1)-V_p^{(-)}(n)\Big). \tag{3.29}$$

Therefore, once $V_p^{(-)}$ at integer time indices is known, $\frac{\mathrm{d}}{\mathrm{d}t}[I_p^{(-)}(t)]$ at half integer time indices can be directly computed, thus avoiding the extra time convolution.

3.3 Discussion on Stability

It is well known that an implicit TDFEM system employing the Newmark-beta scheme with $\beta\geq 1/4$ is unconditionally stable [26]-[28]. It has also been shown that the introduction of the WPBC does not affect the overall stability [10], but the DFDD TDFEM is conditionally stable with the stability condition depending on the spatial discretization immediately next to the subdomain interfaces [12]. Since the proposed approach combines the single-/dual-field TDFEM time-marching process with a time convolution involving the feed-network macromodel, it is important to investigate whether the incorporation of the feed-network model introduces any instability into the overall TDFEM system. The development of a strict proof of the stability of such a hybrid scheme is not straightforward. Rather, we limit ourselves to providing the following guidelines for ensuring its stability of the proposed hybrid scheme.

First, the frequency range of validity of the macromodel for the feed network should be larger than the frequency bandwidth for the antenna simulation. This provides better accuracy when the macromodel is converted into the time domain and, thus, stricter control of the numerical errors in time convolution. Based on numerical experiments, it is found that the upper bound of the frequency range of the macromodel should be four to five times that of the frequency bandwidth pertinent to the antenna simulation. Second, although the VECTFIT rational function fitting process assures that all the poles of a macromodel are strictly stable, i.e., on the left half of the complex plane, the passivity of the macromodel cannot always be guaranteed. Passivity, which dictates that a system is incapable of generating energy, is a critical factor for a stable time-domain simulation, since a stable but non-passive system may become unstable when interacting with other stable systems in the transient simulation. Provided that the discrete data for the S-parameters are not erroneous (erroneous data may result, for example, from errors in the numerical technique used for their calculation or, in the case of measured data, from measurement errors), violations of passivity tend to be rather minor. Often, passivity violation may be induced by the rational function fitting process itself. For example, this may occur when an unnecessarily large number of poles are prescribed by the user for the fitting. Fortunately, passivity violations can be precisely identified from the model parameters via the model Hamiltonian matrix, and small violations can be corrected without deteriorating the accuracy of the macromodel either via a perturbation of the Hamiltonian matrix [39] or by enforcing passivity through a quadratic programming algorithm [40].

When the above two issues are properly addressed, the combined modeling of the antennas and the feed network does not exhibit any instability in the coupled single-/dual-field time-marching scheme.

3.4 Numerical Results

This section presents several numerical examples using the proposed hybrid schemes to calculate radiation from one- and two-dimensional antenna arrays fed by various feed networks. The purpose of these examples is to validate the proposed algorithm and demonstrate its accuracy, efficiency, and stability. For the finite element modeling of the arrays, the open space is terminated using the first-order ABC for efficiency. All the examples in this section are calculated on a single SGI Altix 350 machine that uses Intel Itanium II 1.5 GHz processors.

3.4.1 Feed Network

The feed networks used in the subsequent simulations are described as follows. As shown in Fig. 3.4, a generic feed network consists of power dividers and phase shifters. Power dividers receive power from the source, and split the power into several paths. They also interact with any reflections from antenna elements and allow the signals to travel back and forth between antennas and the feed network. Figures 3.5(a)-(c) illustrate three different types of eight-way, equal-split power dividers. In these figures, Port 0 is assumed to connect to the source, while all the other ports are assumed to connect to antenna elements. The dividers in Figs. 3.5(a) and (b) are assembled from segments of lossless transmission lines of $\lambda/4$ electrical length at the operating frequency. The one in Fig. 3.5(a), referred to as the single-stage divider, contains only one lossless 1-to-8 junction so that the power from the source (left) is equally split into eight paths in one stage. In contrast, the divider in Fig. 3.5(b) is called the multistage divider. It consists of several lossless T-junctions that are arranged in multiple stages. In these two types, the transmission lines of the *i*th stage, $i = 1, 2, \cdots$, share the same characteristic impedance Z_i. Fig. 3.5(c) shows a typical eight-way Wilkinson divider, which is well known for its perfect isolations between the output ports at a designated frequency. The parameters of the Wilkinson divider, such as the impedances and the electrical lengths of transmission lines and the resistor values, can be found in [41].

Phase shifters are also an important part of a feed network, since they control the phase shifts of excitations for individual antenna elements in order to obtain desired radiation patterns. In time-domain simulations, phase shifters are considered as time-delay units, which are modeled as transmission lines of properly selected lengths to provide the appropriate delay. The combination of the phase shifters with the above three different types of power dividers results in three different feeding schemes for antenna arrays, denoted, respectively, as single-stage feeding, multistage feeding and Wilkinson-divider feeding.

As mentioned in the previous section, stable poles and passivity of a feed-network macromodel are essential for a stable time-marching process. Figure 3.6 shows the pole distribution of the macromodels for two Wilkinson-divider feed networks. One is of 30 poles for the broadside case, and the other is of 50 poles for the case where the mainbeam is steered to 45°. It is clear that all the poles from the VECTFIT process are real or in conjugated pairs and all have a negative real part (on the left-hand side of the complex plane) and thus are stable poles. Furthermore, the passivity of the marcomodels can be verified via the model parameters of the model Hamiltonian matrix and any violation of passivity should be removed. The passivity condition requires that the eigenvalues $\lambda_i(\omega)$ of the real part of the Y-matrix are nonnegative, or equivalently, that all the singular values $\sigma_i(\omega)$ of the S-matrix are bounded by one at all frequencies. Therefore, just to illustrate the satisfaction of the passivity condition, Figs. 3.7 and 3.8 plot the singular values $\sigma_i(\omega)$ of the S-matrix and the eigenvalues $\lambda_i(\omega)$ of the real part of the Y-matrix calculated from the macromodels for the above two cases, respectively, with 200 frequency samples from dc up to 20 GHz.

3.4.2 Monopole Array

For the purposes of validating the proposed hybrid scheme we consider, first, an 8×1 monopole array radiating over an infinite ground plane. The monopole is formed by extending the central conductor of the coaxial cable 10 cm above the ground plane. The coaxial cable has an inner radius of 1 cm and an outer radius of 2.3 cm. The unit cell and the front and top views of the array configuration are shown in Fig. 3.9. We apply both the single-field and the dual-field formulations of the proposed approach to analyze this antenna array fed by the Wilkinson-divider feed network. The dual-field formulation is compatible with the DFDD TDFEM when the antenna domain is decomposed into 30 subdomains, sketched in Fig. 3.9(c). The total number of unknowns for the entire problem is about 80,000. We compare the results obtained using the single-field and dual-field formulations in the proposed hybrid scheme with the case when each antenna is fed individually without any feed network (denoted as "individual feeding"). At 750 MHz, the Wilkinson divider is designed to have perfect isolations between all eight output ports. Since there is no crosstalk between the antenna elements through the feed network, the Wilkinson divider feeding scheme behaves just like the individual feeding scheme at this frequency. The normalized radiation patterns in the *xy*-plane cut are computed at 750 MHz and shown in Fig. 3.10. It is clear that both the single-field and dual-field formulations accurately capture the behavior of the Wilkinson divider and give results identical to those of the individual feeding case. Figure 3.11 shows that the single-field and dual-field formulations result in the same time-domain profiles for the modal voltages recorded at Ports 1 and 4.

3.4.3 8×1 Vivaldi Array

The proposed hybrid scheme is applied to the modeling of large arrays. Since the DFDD TDFEM is most efficient for the simulation of large antenna arrays, it is the method used in the simulations in this and the next sections. An important attribute of the method is that it allows us to fully exploit the geometrical redundancy of the array-type structures to speed up the simulation and reduce the memory requirement.

The next example is an 8×1 linear array of Vivaldi antennas, which are considered as ultra wide-band (UWB) antennas, fed by the above three feed networks. The dimensions and parameters of a single Vivaldi antenna are given in Fig. 3.12(a), while the array configuration is shown in Fig. 3.12(b). This design of the Vivaldi antenna is based on a conducting patch printed on one side of the substrate, which stands vertically above an infinite ground plane. A gradually flared notch cut in the middle of the conducting patch provides smooth impedance transition to free space, while a hollow circle cut on the conducting patch serves as a wide-band open circuit. The shielded stripline input at the bottom is modeled as a TEM port. The spacing between array elements is 40 mm in the x-direction, which corresponds to one half of a wavelength at 3.75 GHz. Again, the computational domain of the antenna array is partitioned into 30 subdomains. Each subdomain contains about 20,000 unknowns, with the total number of unknowns for the entire problem being approximately 600,000. Table 3.1 lists the computational information when incorporating the above three feed networks into this antenna simulation. Clearly, the extra computational cost brought by the incorporation of the feed-network modeling into the time marching of TDFEM is very marginal.

The calculated E-plane radiation patterns at 3.75 GHz for the broadside case and the case of the E-plane scan angle $\theta_s = 45^{\circ}$ are shown in Figs. 3.13–3.15, when the array is fed by the three different types of feed networks described previously. It is clear that, for the Wilkinson-divider feeding (designed at 3.75 GHz), the computed radiation patterns are identical to those with the individual feeding. However, for the single-stage and multistage feeding cases (shown in Figs. 3.14 and 3.15, respectively), although the maximum radiation direction remains almost unchanged, the beamwidth, the location of nulls and side-lobes, and the level of side-lobes are all different, due to multiple interactions between the feed network and the antenna array. These multiple interactions come from the properties of the single- and multistage power dividers. The poor isolation between their output ports allows crosstalk between antenna elements through the feed network, and the reflections from the antennas are bounced back and forth between the junctions of the divider and antennas, resulting in a series of secondary radiations. This phenomenon is clearly seen in the time domain, as depicted in Fig. 3.16 in the plots of the time profile of the magnitude of the modal voltage at the leftmost port. In the cases of the single- and multistage feeding, it takes a much longer time for the time-domain solutions to decay to a negligible level, compared to the case of the individual feeding. This is particularly true for the multistage feeding, since there are more junctions in this type of feed network, resulting in more complicated and longer multiple reflections. In contrast, the time-domain magnitude of the modal voltage in the case of the Wilkinson-divider feeding is at the same level as that in the case of the individual feeding, since in both cases the reflections from the antennas are immediately absorbed and dissipated.

The proposed approach also facilitates the calculation of the power dissipated in the feed network. The time-dependent modal voltages in (3.23) are recorded at each time step and can be converted back into the frequency domain. If we assume that Port 0 is connected to the source, the total power delivered to the feed network, denoted as P_{A+F}, is

$$P_{A+F} = \left(V_0^{(+)}\right)^2 \Big/ (2Z_0) - \left(V_0^{(-)}\right)^2 \Big/ (2Z_0)\,. \tag{3.30}$$

The total power delivered to the antennas, denoted as P_A, is

$$P_A = \sum_{p=1}^{N} \frac{\left(V_p^{(-)}\right)^2}{2Z_p} - \sum_{p=1}^{N} \frac{\left(V_p^{(+)}\right)^2}{2Z_p}\,. \tag{3.31}$$

The power dissipated in the feed network, denoted as P_F, is then

$$P_F = P_{A+F} - P_A\,. \tag{3.32}$$

In contrast to the other two lossless feed networks we considered, the Wilkinson divider feed network is lossy because of the imbedded resistors shown in Fig. 3.5(c). By using (3.30)–(3.32), the power dissipated in the Wilkinson divider feed network in the broadside radiation case is calculated and shown in Fig. 3.17.

3.4.4 4×4 and 8×8 Vivaldi Arrays

Two two-dimensional Vivaldi arrays fed by multistage feed networks are analyzed using the proposed method. The sizes of the arrays are 4×4 and 8×8, respectively, with the same unit cell as in the previous example. Their array configurations and the associated feed networks are shown in Figs. 3.18 and 3.19, respectively. Their corporate feed networks are built by following the same approach as for the multistage feed network in Fig. 3.5(b) and using 4 and 6 stages, respectively. The computed radiation patterns are shown in Figs. 3.20–3.25, all compared with the case of the individual feeding. For the simulation of the 4×4 array, approximately 800,000 unknowns are involved, and for that of the 8×8 array, the total number of unknowns exceeds 2.3 million. The computational information is given in Tables 3.2 and 3.3, which again show that the incorporation of the feed-network modeling only requires a small increase in both the memory requirement and solution time.

3.5 Summary

This chapter presented an accurate and efficient algorithm for incorporating the feed-network modeling into the time-domain finite element analysis of antenna-arrays. The feed network and the antennas are separated by a set of port interfaces. The antennas are simulated by the TDFEM combined with the time-domain WPBC, while the feed network is modeled as a linear, passive, multiport electromagnetic device, whose frequency-domain scattering matrix is represented in terms of a rational function macromodel. The feed-network macromodel is then incorporated into the transient analysis through a computationally efficient, recursive convolution scheme. Antennas and the feed network interact with each other through a coupled time-marching scheme by exchanging their incident and reflected modal voltages and/or currents through the port interfaces. The proposed approach is extended to a domain decomposition formulation to enable the simulation of large and complex antenna arrays. No instability is introduced in this coupled analysis provided that the frequency range of validity of the feed-network macromodel is properly selected and its passivity over the frequency bandwidth of interest is enforced. Finally, the validity, efficiency, and capability of the proposed method were demonstrated through its application to the modeling of several linear and planar antenna arrays fed by various feed networks. The proposed approach allows a full utilization of the recently developed techniques for the TDFEM simulations of antennas, including the time-domain WPBC and the dual-field domain-decomposition scheme. By efficiently hybridizing the antenna simulation and the feed network macromodel, the proposed approach significantly extends the current antenna modeling capability to the system level, making it possible to account for the important interactions between the antenna elements and the feed network without significantly complicating the simulation of the entire antenna system. This method has the potential for wide application in the synthesis and optimization of large antenna array systems with complicated feed structures.

3.6 Figures and Tables

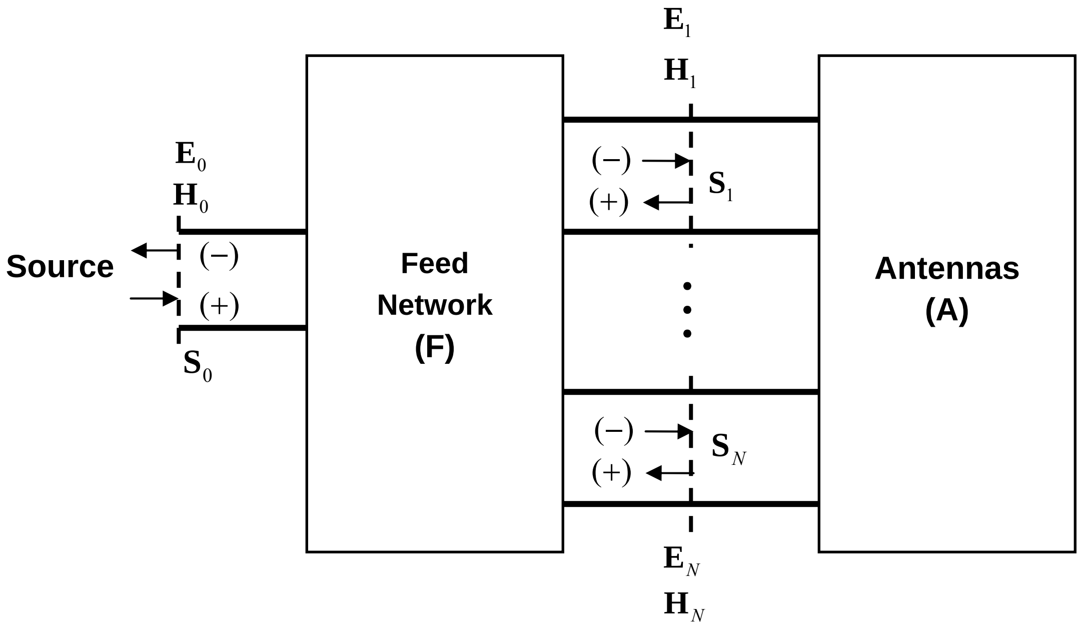

$\mathbf{E}_1$
$\mathbf{H}_1$
$\mathbf{E}_0$
$\mathbf{H}_0$
Source
(−)
(+)
$\mathbf{S}_0$
Feed
Network
(F)
(−)
(+)
$\mathbf{S}_1$
(−)
(+)
$\mathbf{S}_N$
$\mathbf{E}_N$
$\mathbf{H}_N$
Antennas
(A)

Figure 3.1: Port interfaces and the separation of the feed network, the antennas, and the source.

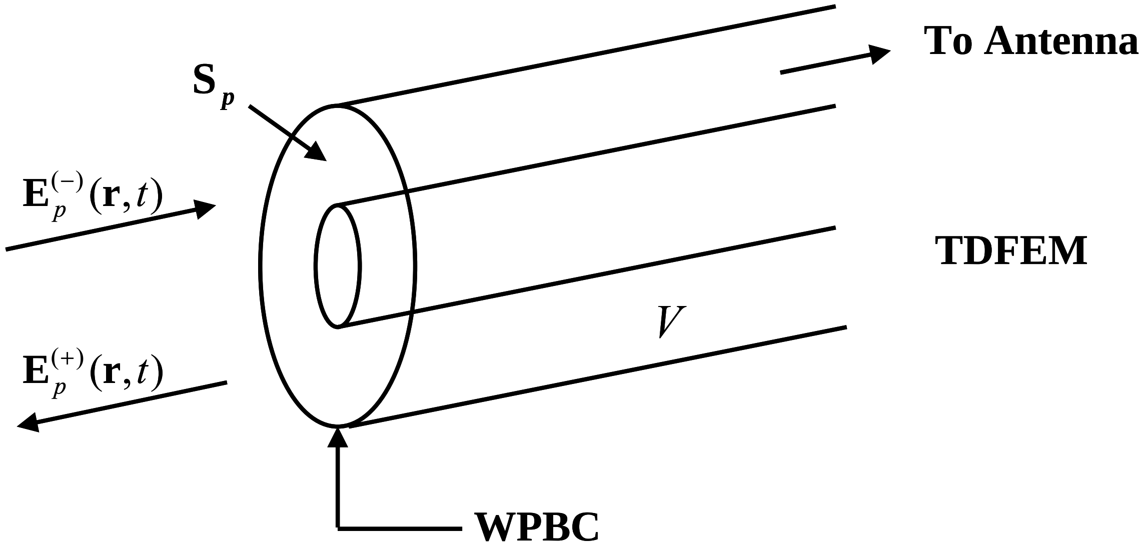

$\mathbf{S}_p$
To Antenna
$\mathbf{E}_p^{(-)}(\mathbf{r},t)$
TDFEM
V
$\mathbf{E}_p^{(+)}(\mathbf{r},t)$
WPBC

Figure 3.2: The TDFEM/WPBC modeling of the antenna domain.

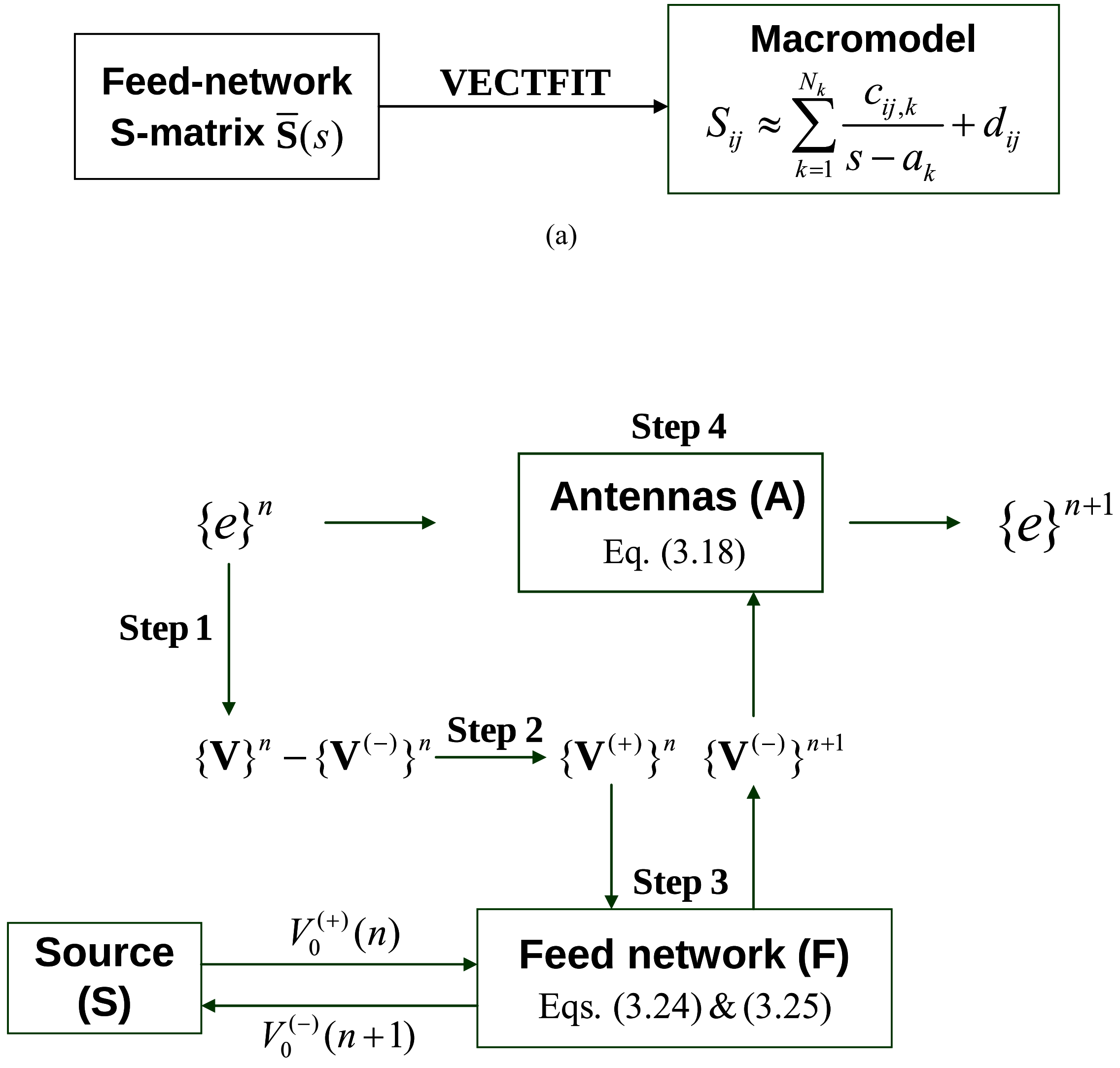
Feed-network
S-matrix $\overline{\mathrm{S}}(s)$
VECTFIT
Macromodel
$S_{ij} \approx \sum_{k=1}^{N_k} \frac{c_{ij,k}}{s-a_k} + d_{ij}$
Step 4
$\{e\}^n$
Antennas (A)
Eq. (3.18)
$\{e\}^{n+1}$
Step 1
$\{\mathbf{V}\}^n - \{\mathbf{V}^{(-)}\}^n$
Step 2
$\{\mathbf{V}^{(+)}\}^n$
$\{\mathbf{V}^{(-)}\}^{n+1}$
Step 3
Source
(S)
$V_0^{(+)}(n)$
$V_0^{(-)}(n+1)$
Feed network (F)
Eqs. (3.24) & (3.25)

(a)

(b)

Figure 3.3: Algorithm flowchart. (a) Pre-processing of the feed network. (b) Coupled time-marching scheme.

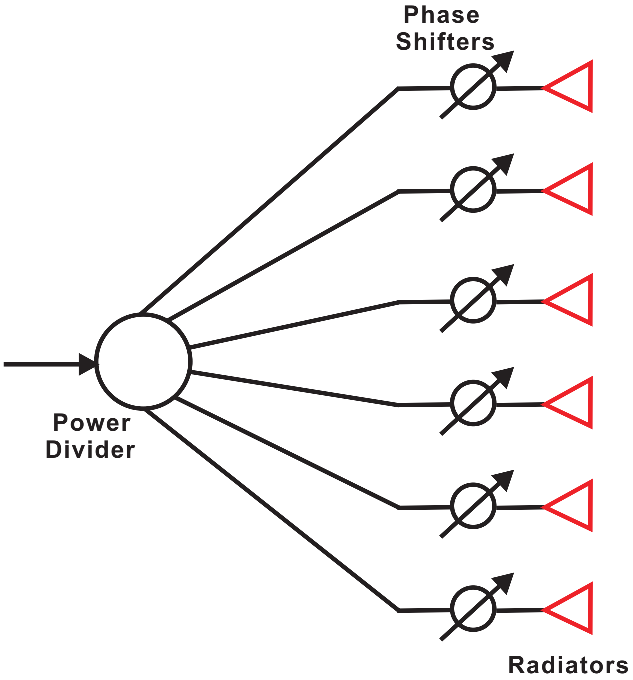
Phase
Shifters
Power
Divider
Radiators

Figure 3.4: A generic feed network.

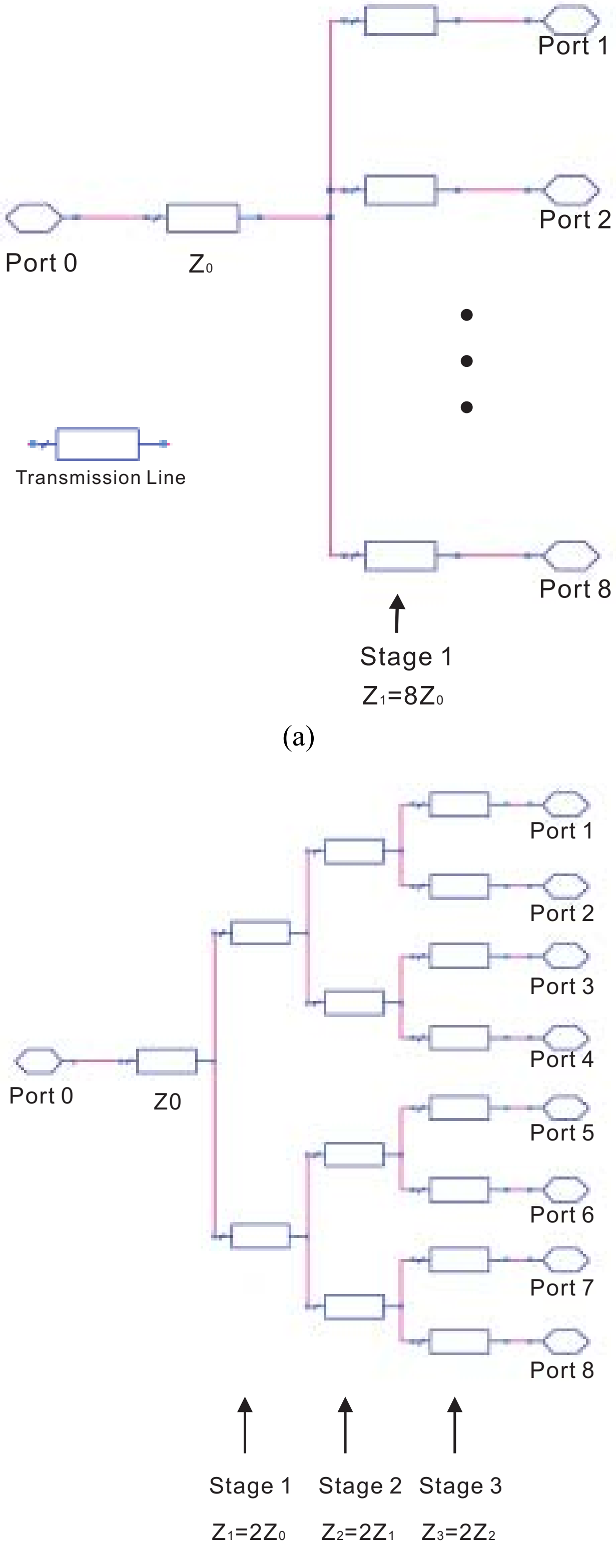
Port 0
Z_0
Port 1
Port 2
Port 8
Transmission Line
Stage 1
$Z_1=8Z_0$
Port 0
Z0
Port 1
Port 2
Port 3
Port 4
Port 5
Port 6
Port 7
Port 8
Stage 1
Stage 2
Stage 3
$Z_1=2Z_0$
$Z_2=2Z_1$
$Z_3=2Z_2$

(a)

(b)

Figure 3.5: Three types of power dividers. (a) Single-stage divider. (b) Multistage divider. (c) Wilkinson divider [41].

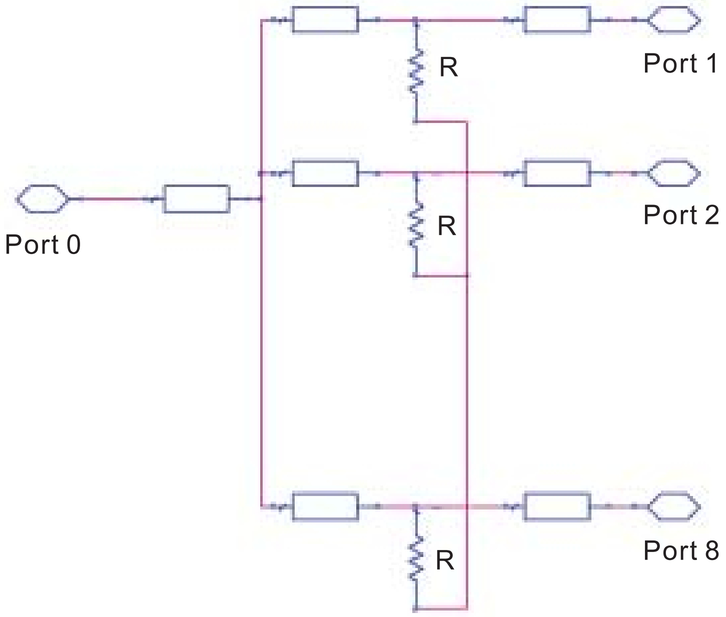
R
Port 1
R
Port 2
Port 0
R
Port 8

(c)

Figure 3.5: Continued.

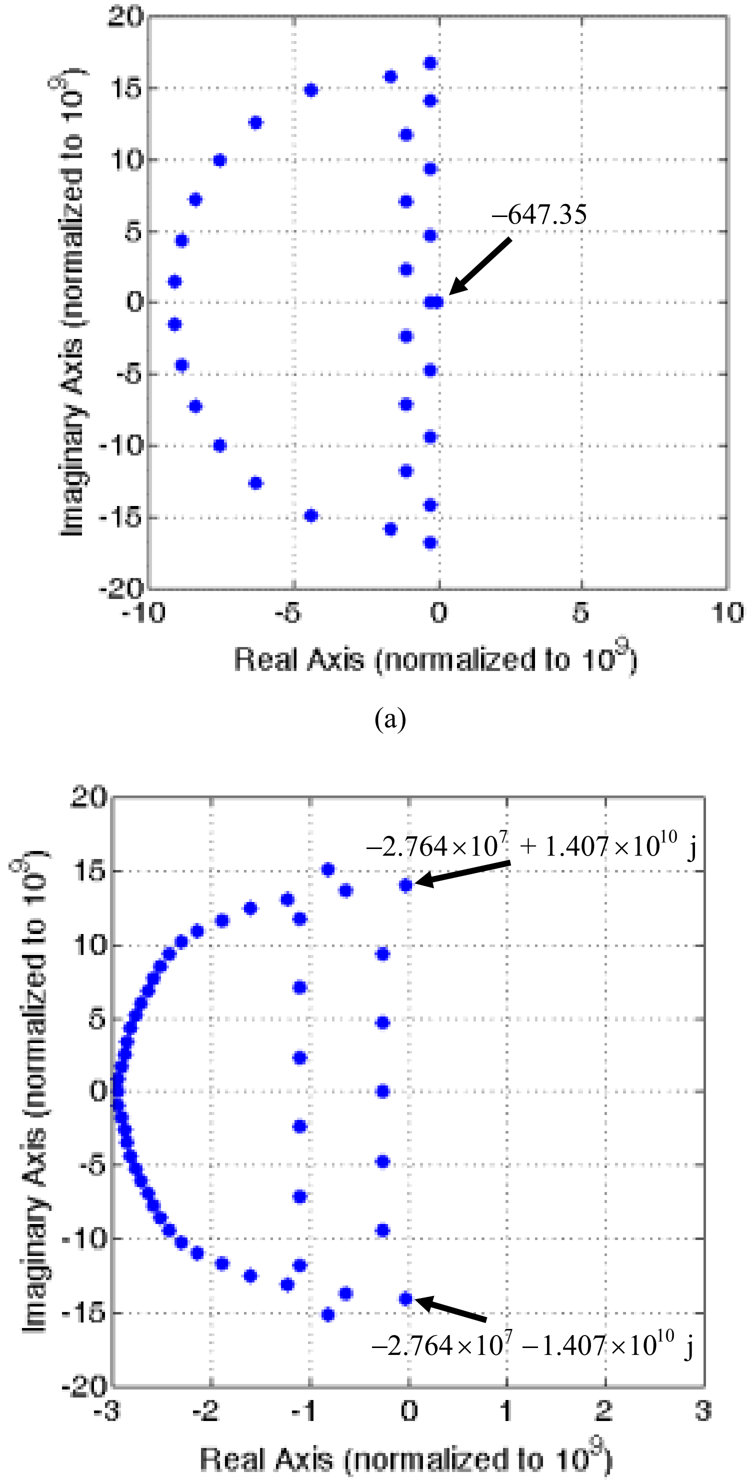

-647.35

(a)

$-2.764\times10^{7}+1.407\times10^{10}\ j$

$-2.764\times10^{7}-1.407\times10^{10}\ j$

(b)

Figure 3.6: Pole distribution of the macromodels for two Wilkinson-divider feed networks. (a) The broadside case (30 poles). (b) The case where the mainbeam is steered to 45° (50 poles).

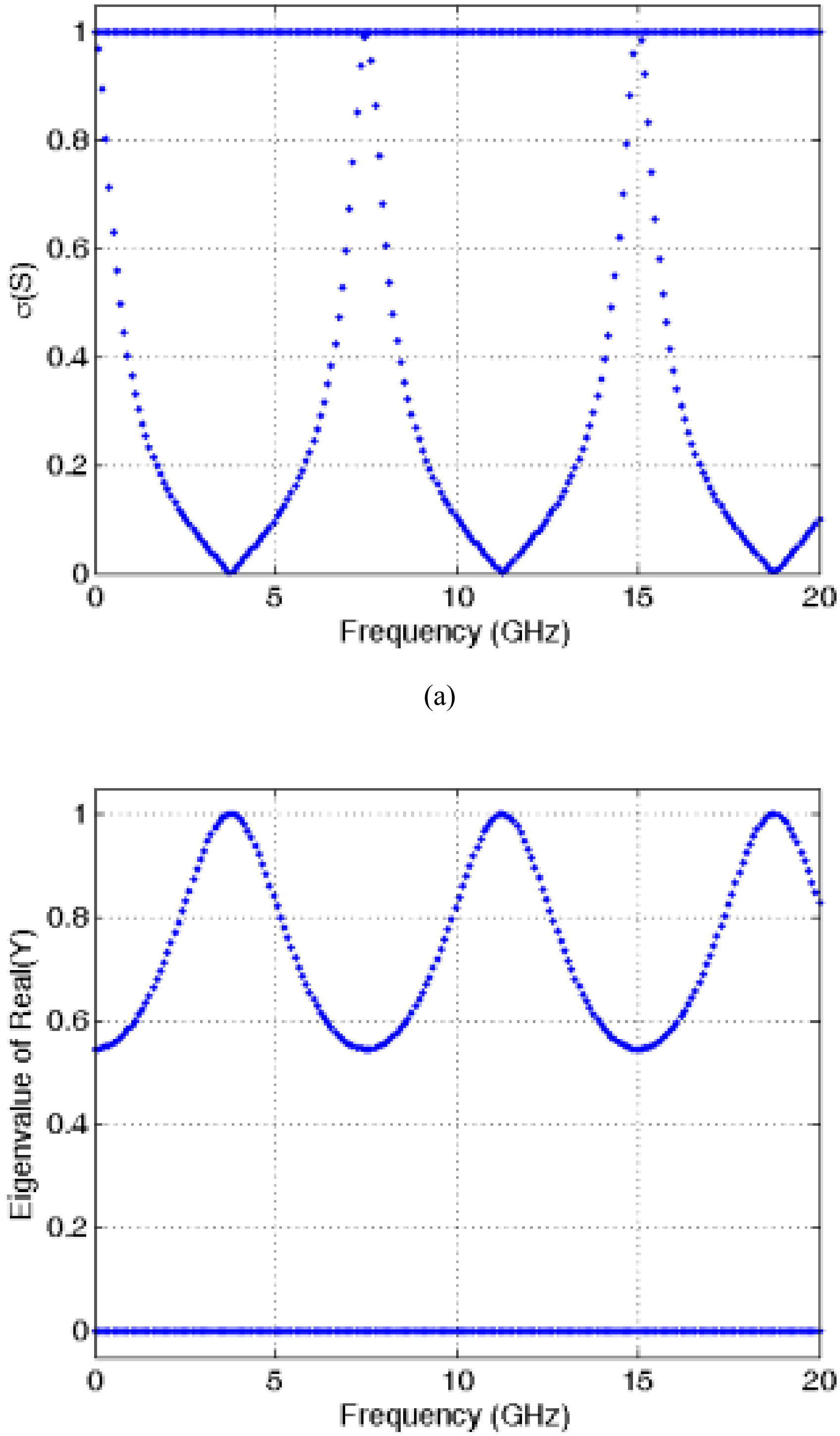

(a)

(b)

Figure 3.7: (a) The singular values $\sigma_i(\omega)$ of the S-matrix and (b) the eigenvalues $\lambda_i(\omega)$ of the real part of the Y-matrix calculated from the macromodel for the broadside case.

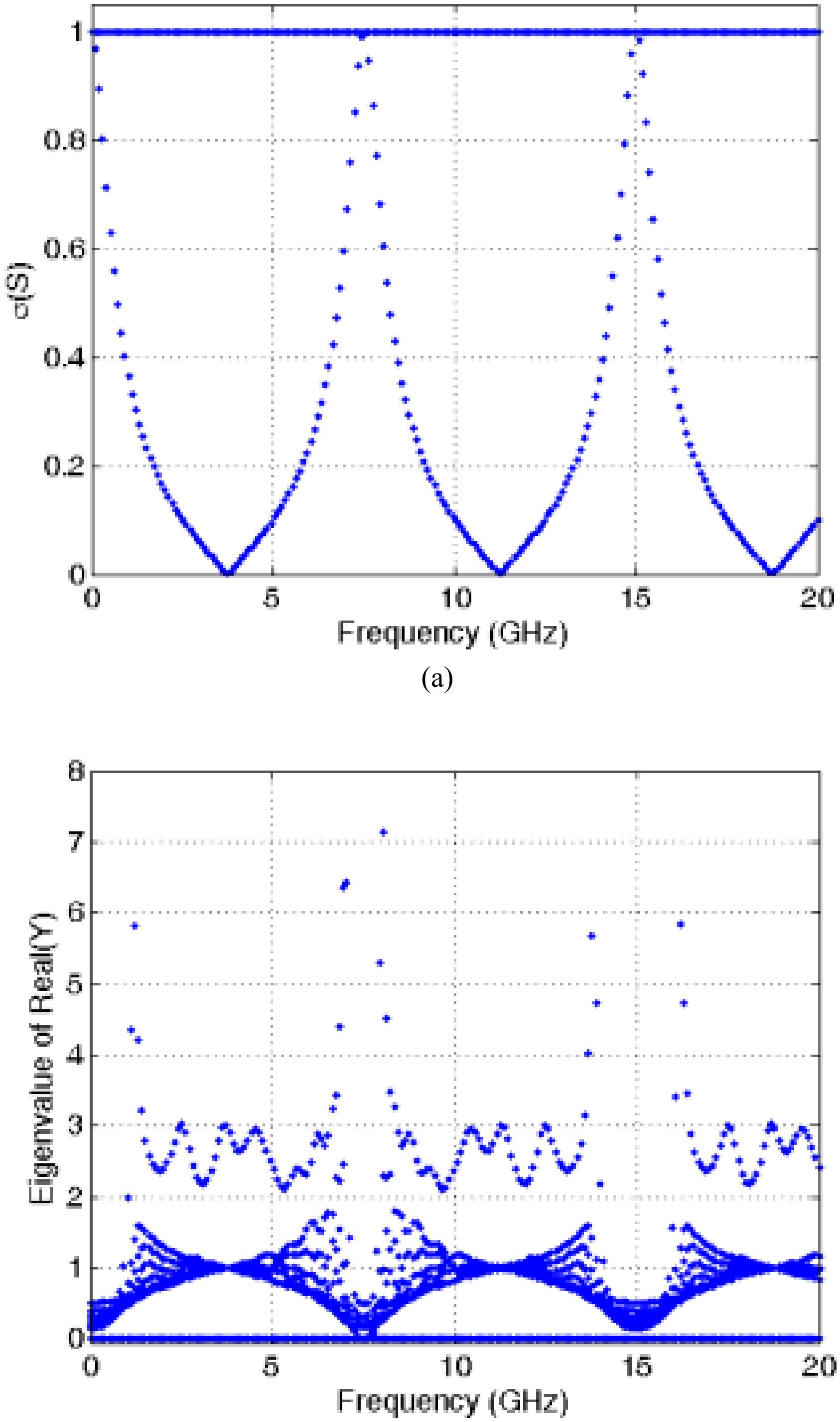

(a)

(b)

Figure 3.8: (a) The singular values $\sigma_i(\omega)$ of the S-matrix and (b) the eigenvalues $\lambda_i(\omega)$ of the real part of the Y-matrix calculated from the macromodel for the mainbeam-steered case.

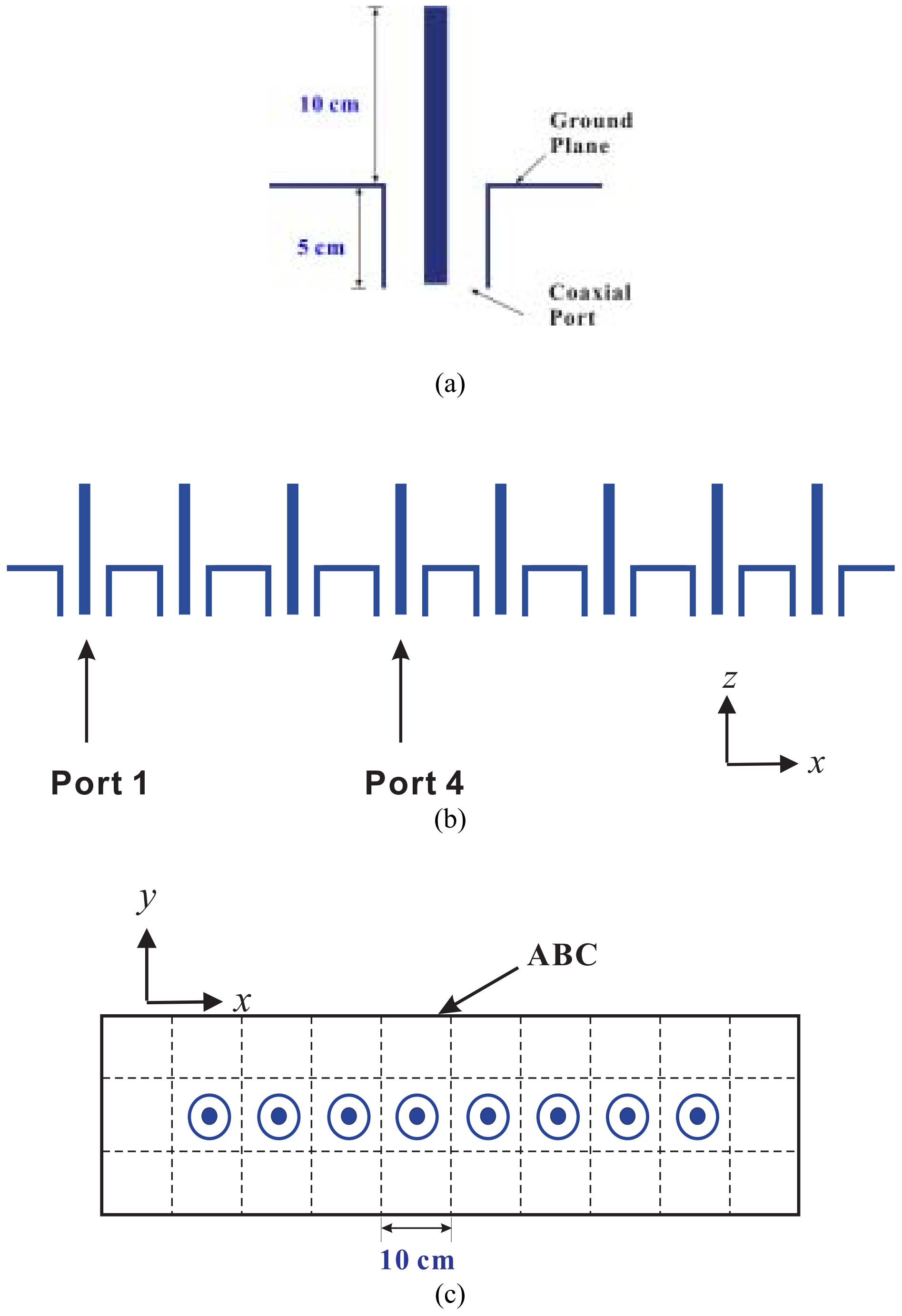
10 cm
5 cm
Ground Plane
Coaxial Port
Port 1
Port 4
z
x
y
x
ABC
10 cm

(a)

(b)

(c)

Figure 3.9: (a) Unit cell, (b) front view, and (c) top view of the 8×1 monopole array.

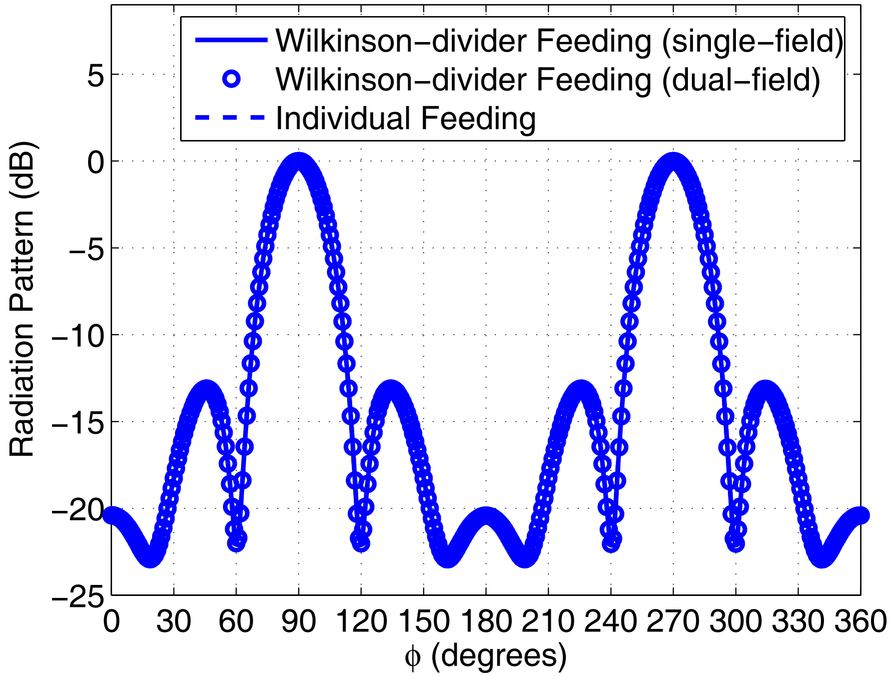

(a)

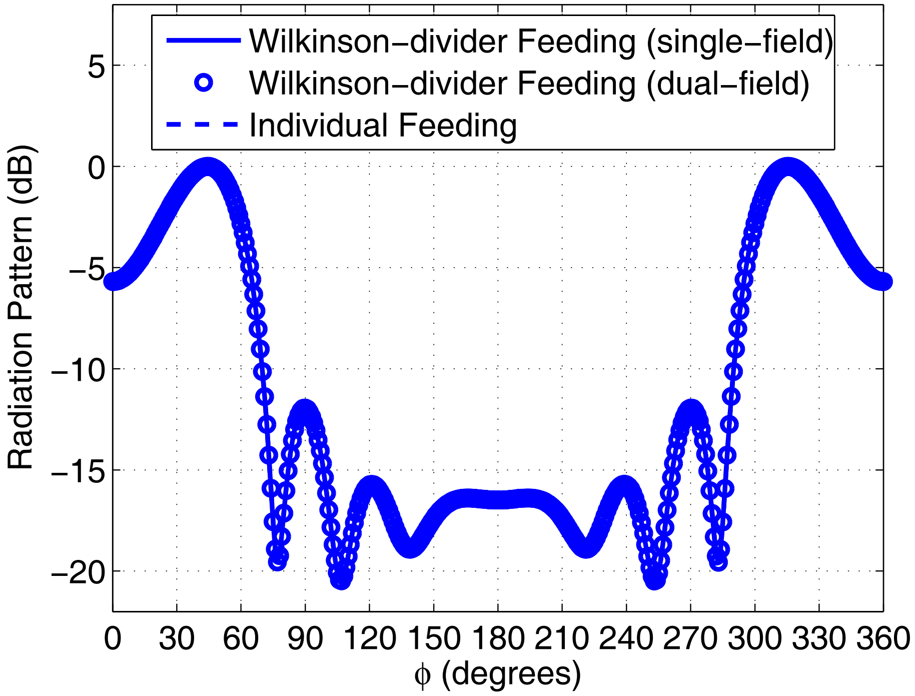

(b)

Figure 3.10: Radiation patterns (*xy*-plane cut) for the 8×1 monopole array. (a) Broadside. (b) Mainbeam steered to 45°.

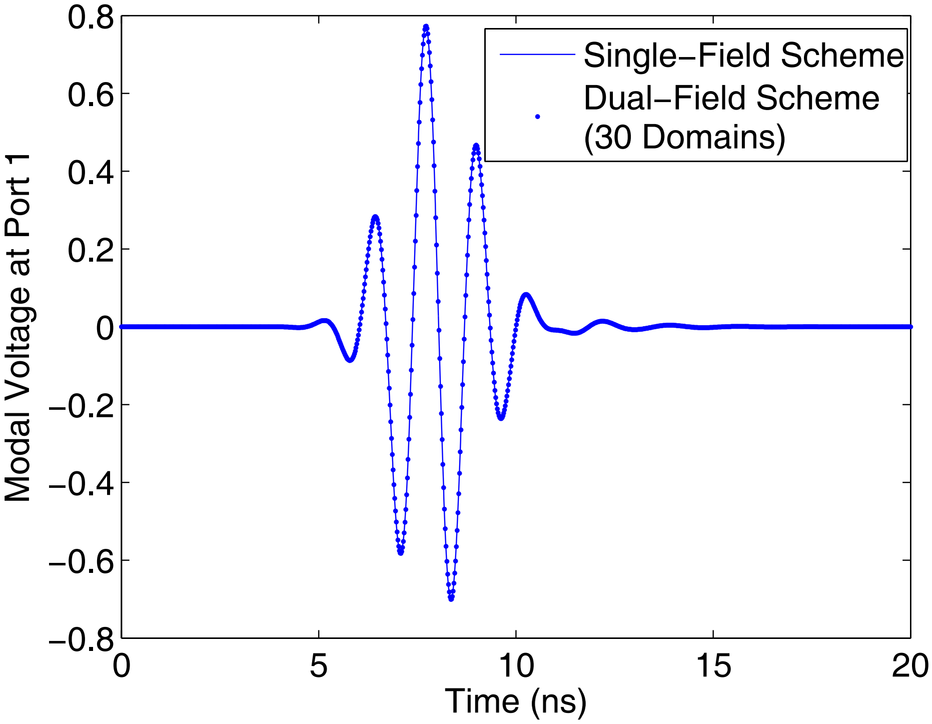

(a)

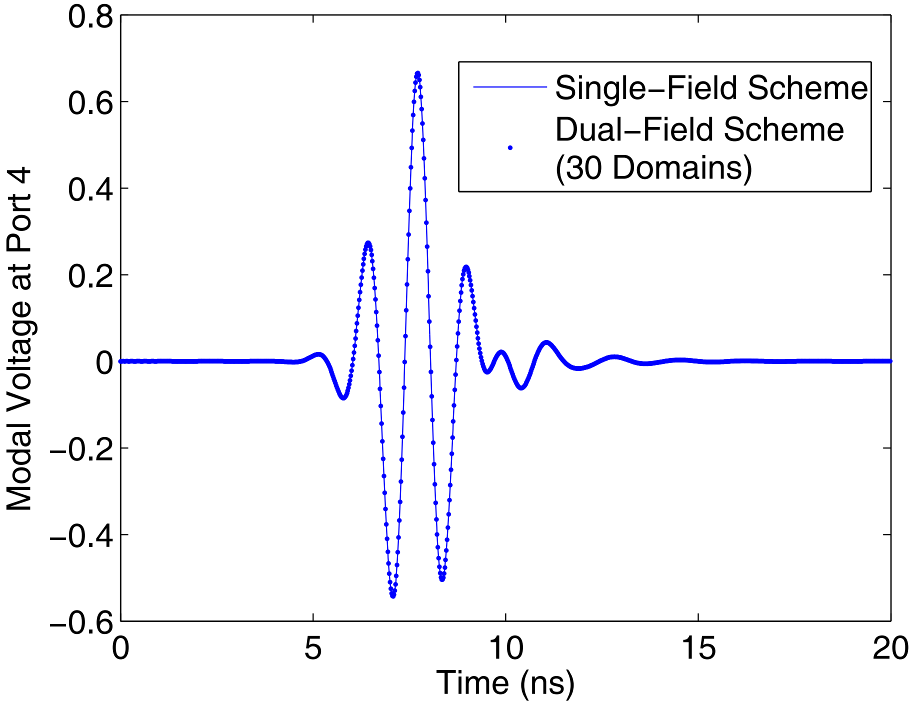

(b)

Figure 3.11: Amplitude of the time-domain modal voltage for the electrical field at (a) Port 1 and (b) Port 4 for the broadside case ($\Delta t = 0.01$ ns).

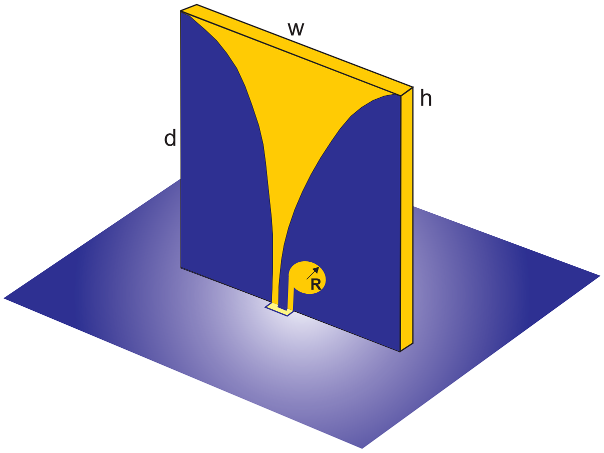

(a)

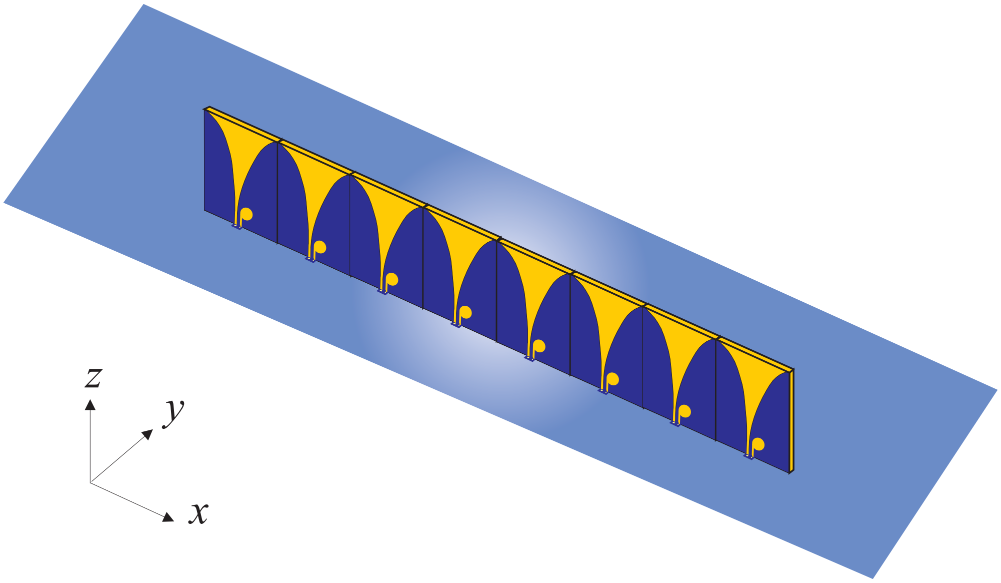

(b)

Figure 3.12: (a) Geometry of a single Vivaldi antenna. Dimensions: w = 40 mm, d = 55 mm, R = 5 mm, h = 1.5 mm. The relative permittivity of the stub is 3.0. Stripline width τ_s = 2 mm. (b) An 8×1 linear array configuration.

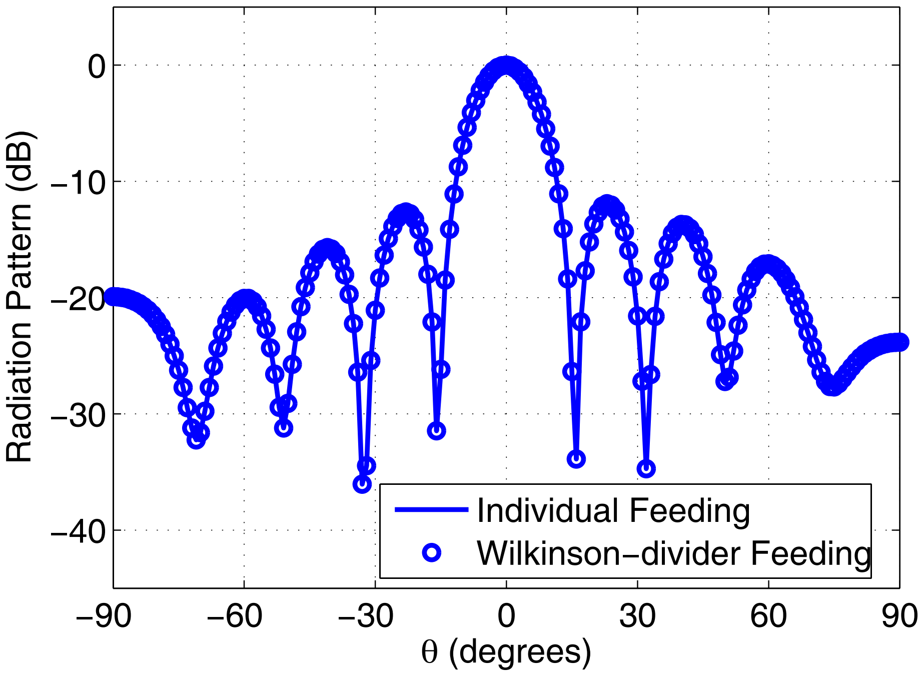

(a)

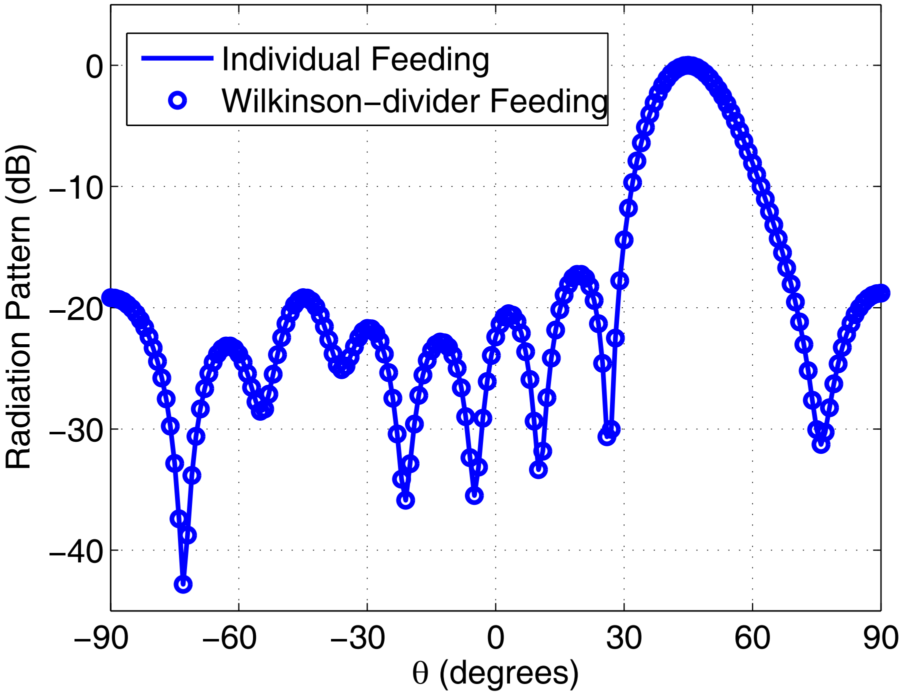

(b)

Figure 3.13: E-plane radiation patterns using the Wilkinson-divider feed network compared to those of the individual feeding case. (a) Broadside. (b) Main-beam steered to 45° .

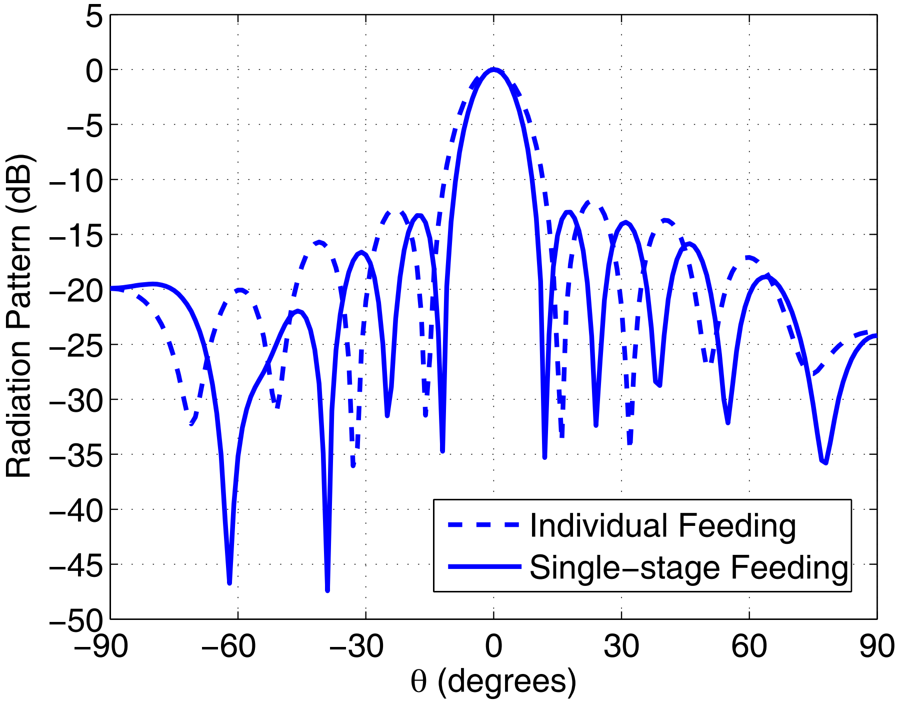

(a)

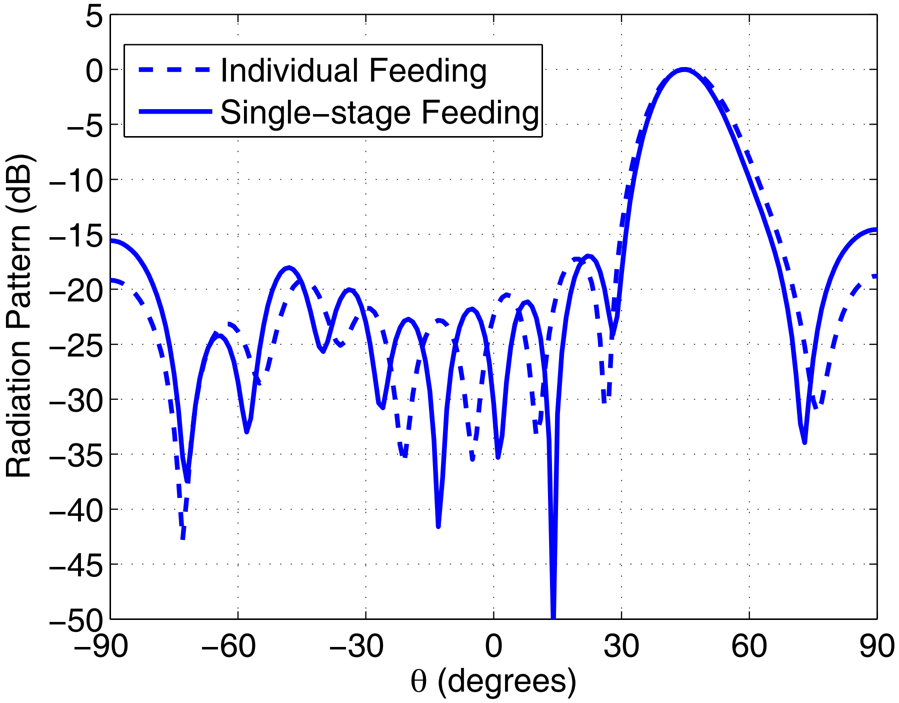

(b)

Figure 3.14: E-plane radiation patterns using the single-stage feed network compared to those of the individual feeding case. (a) Broadside. (b) Main-beam steered to 45°.

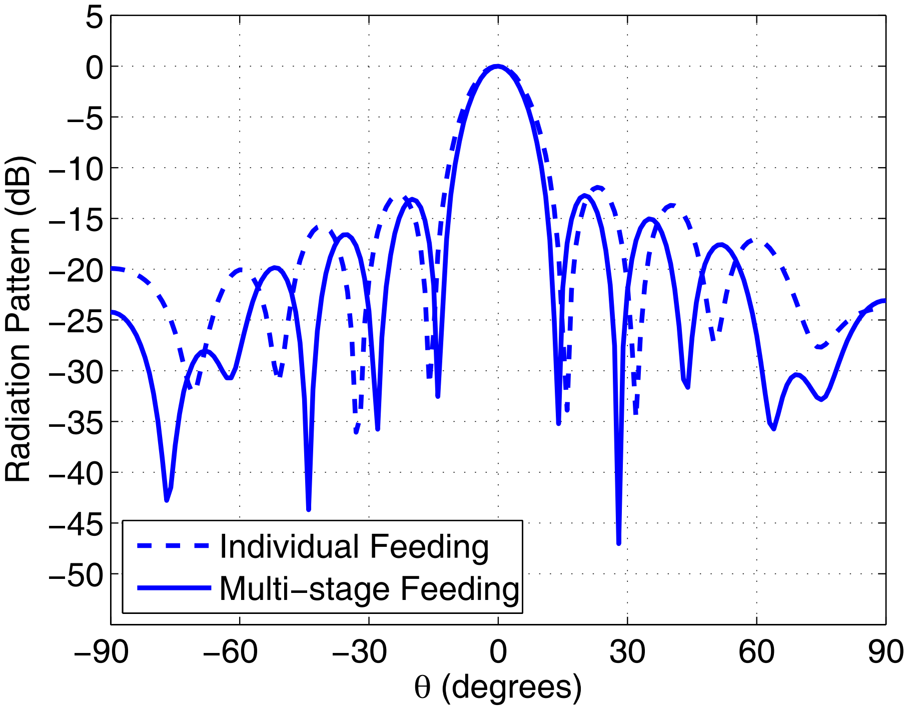

(a)

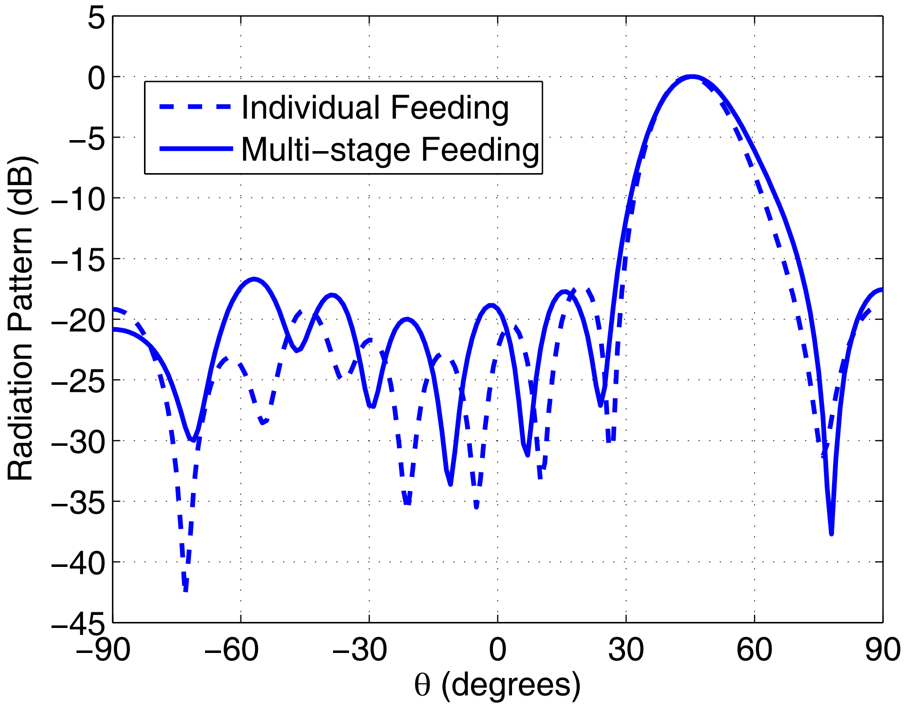

(b)

Figure 3.15: E-plane radiation patterns using the multistage feed network compared to those of the individual feeding case. (a) Broadside. (b) Main-beam steered to 45°.

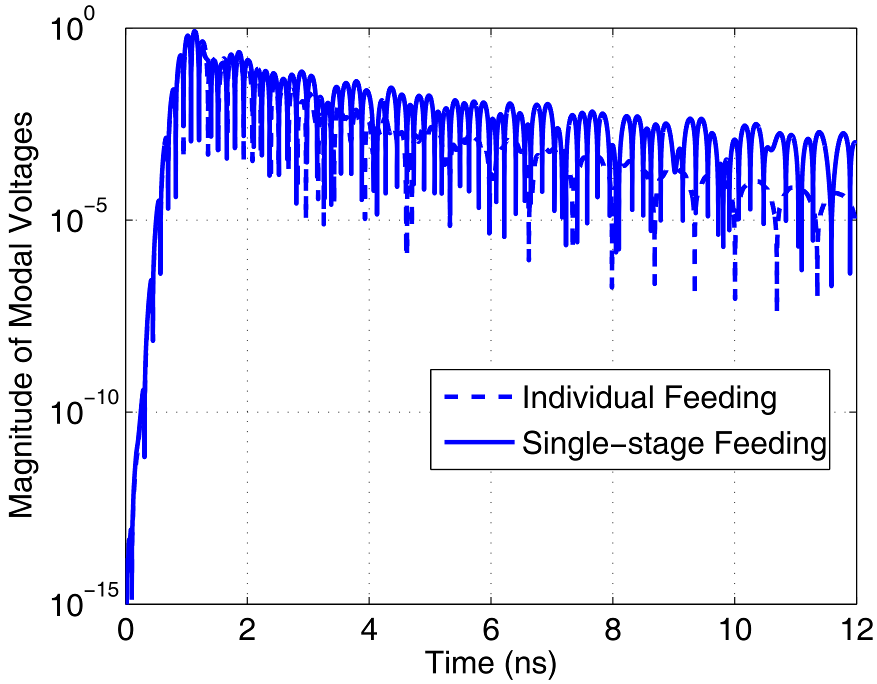

(a)

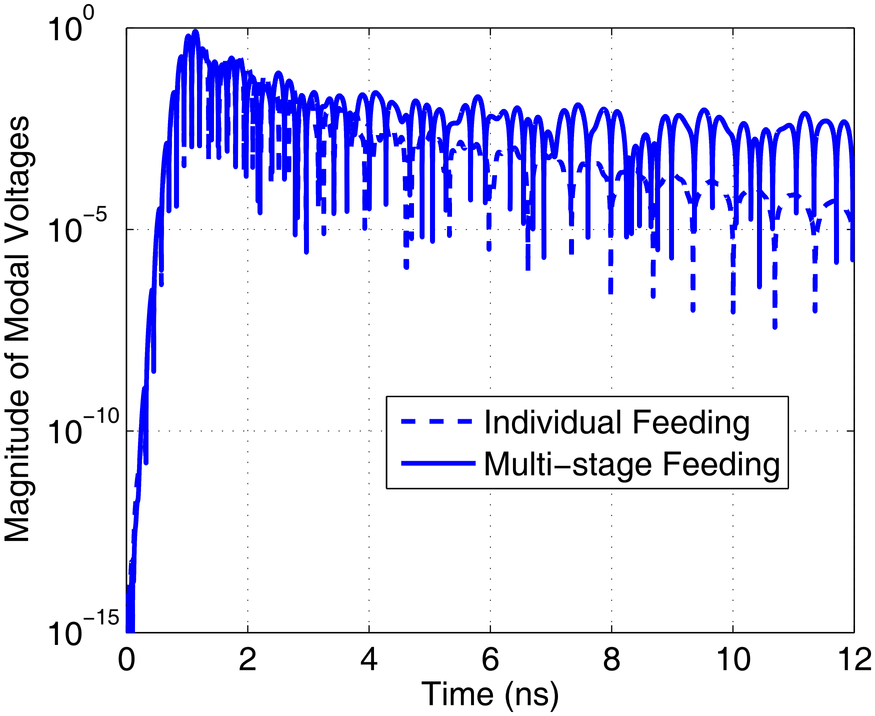

(b)

Figure 3.16: Magnitude of the time-domain modal voltages at the leftmost port ($\Delta t = 0.8$ ps) using different feeding schemes compared to those of the individual feeding case. (a) Single-stage feeding. (b) Multistage feeding. (c) Wilkinson-divider feeding.

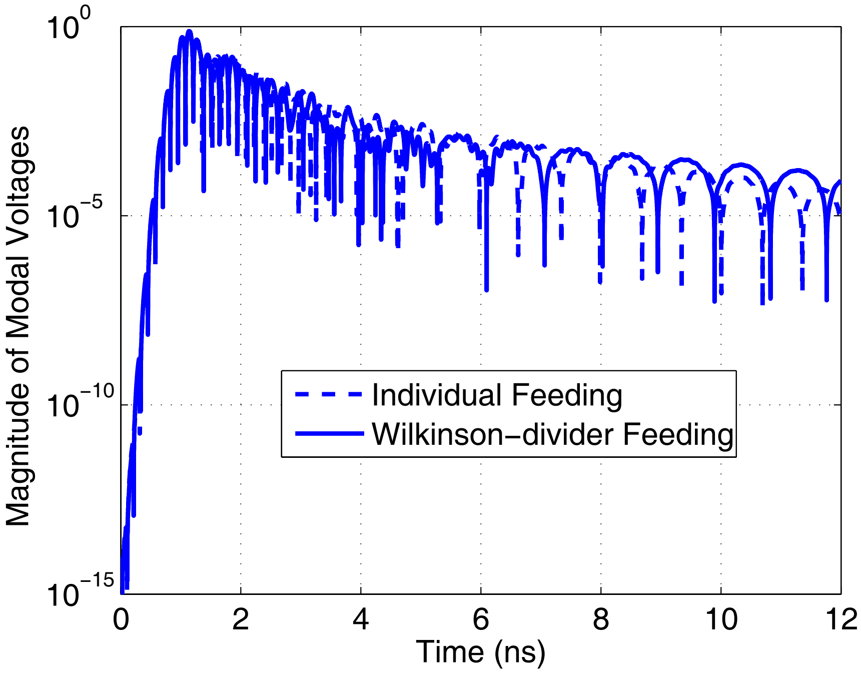

(c)

Figure 3.16: Continued.

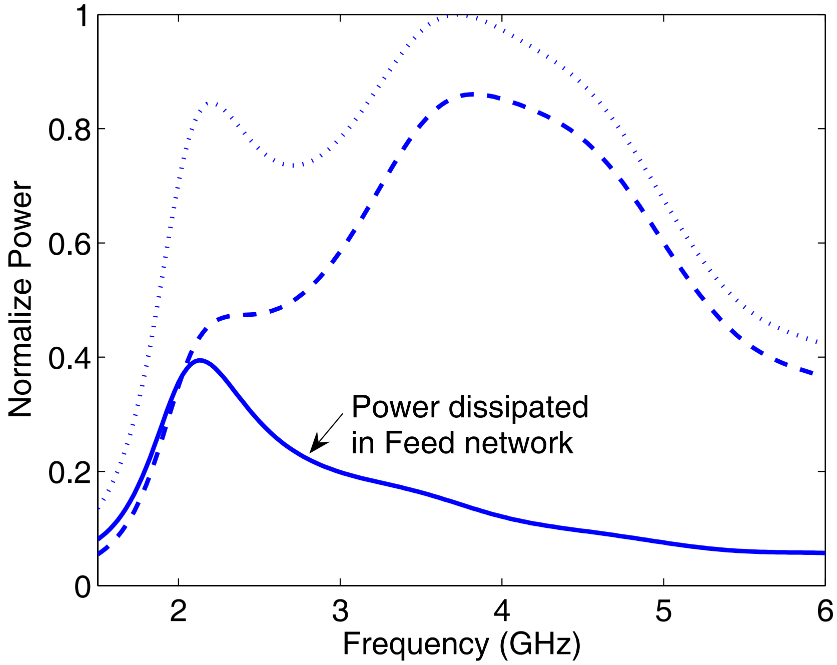

Figure 3.17: Total power delivered to the feed network (dotted line), power delivered to antennas (dashed line), and power dissipated in the feed network (solid line). All the quantities are normalized to the power available from source, i.e., $(V_0^{(+)})^2/(2Z_0)$.

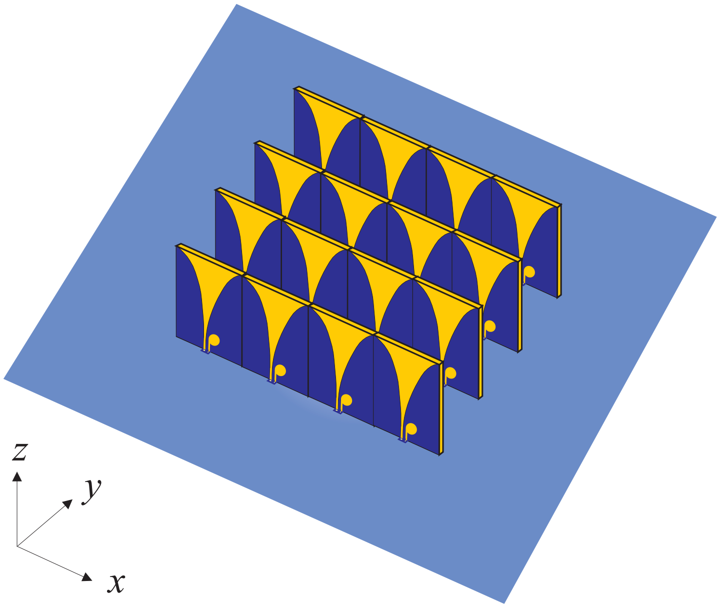

(a)

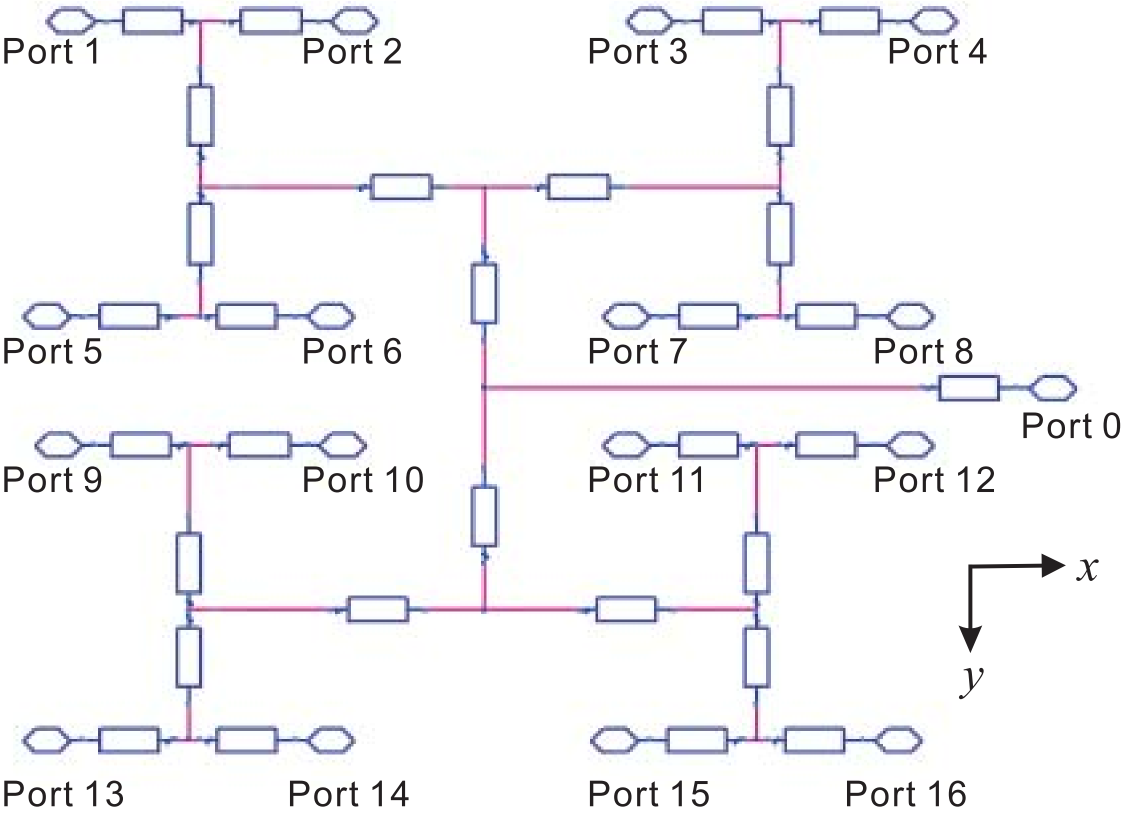
Port 1
Port 2
Port 3
Port 4
Port 5
Port 6
Port 7
Port 8
Port 0
Port 9
Port 10
Port 11
Port 12
x
y
Port 13
Port 14
Port 15
Port 16

(b)

Figure 3.18: (a) The 4×4 planar array configuration of Vivaldi antennas. (b) The multistage feed network for the 4×4 array.

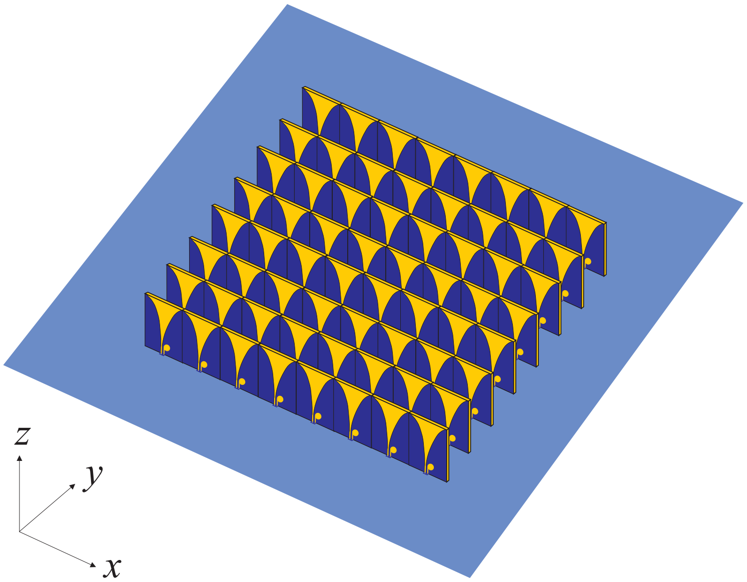

(a)

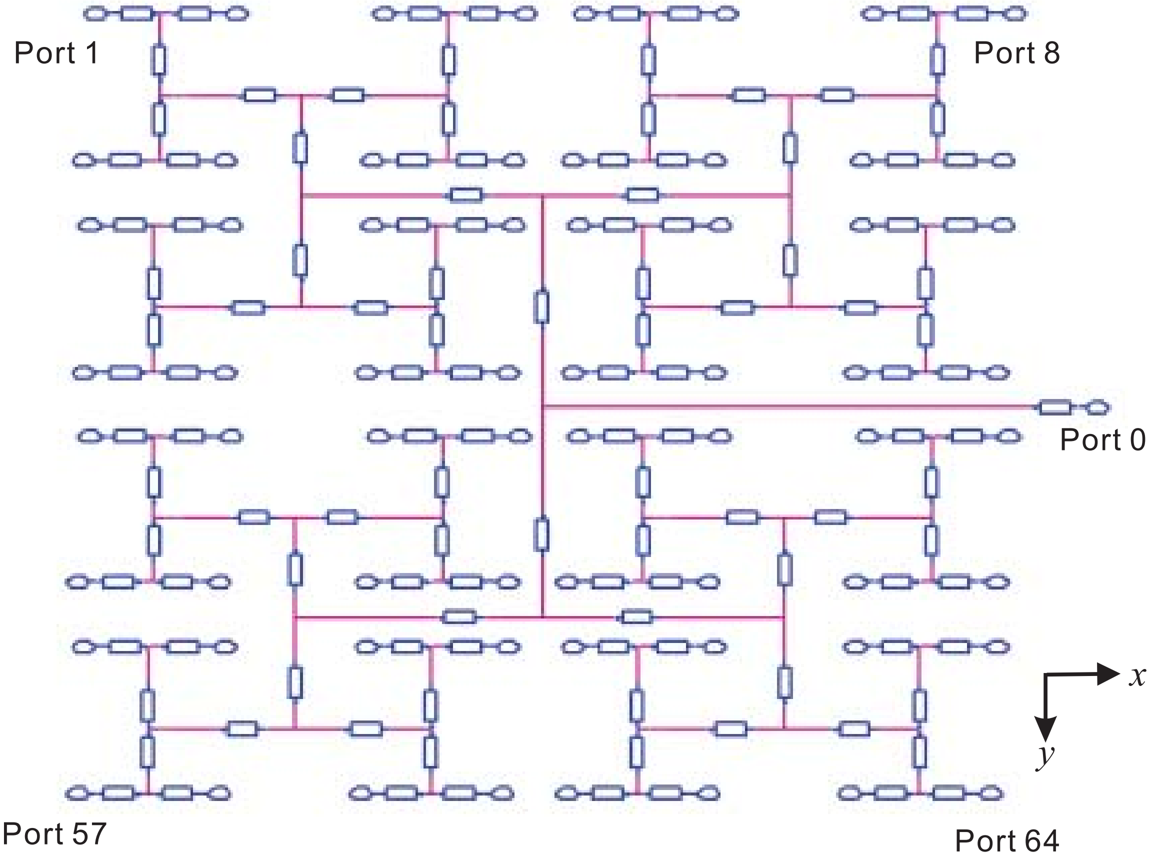
Port 1
Port 8
Port 0
Port 57
Port 64
x
y

(b)

Figure 3.19: (a) The 8×8 planar array configuration of Vivaldi antennas. (b) The multistage feed network for the 8×8 array.

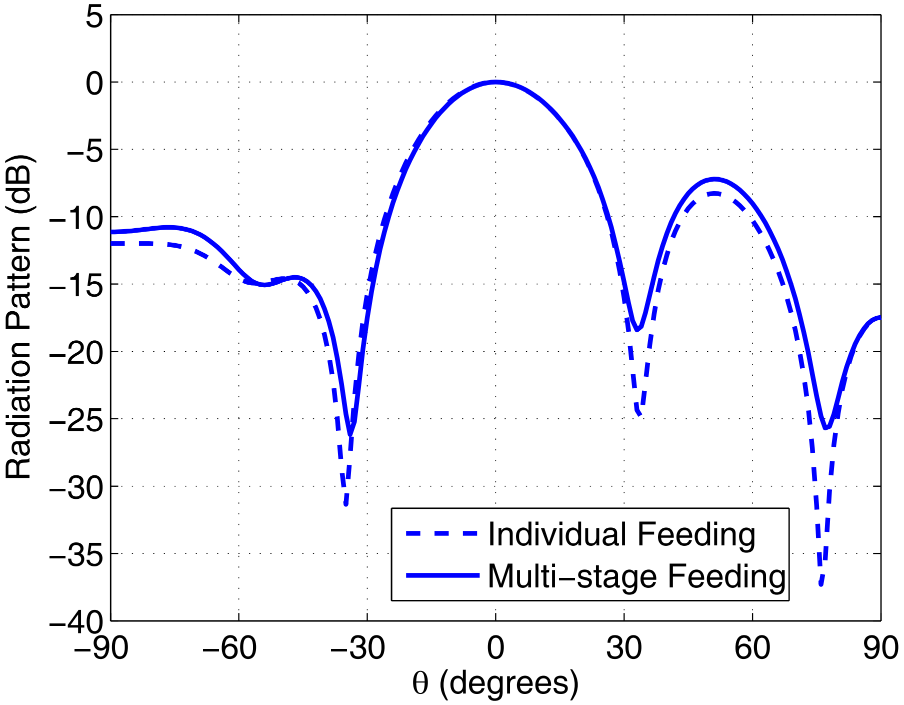

(a)

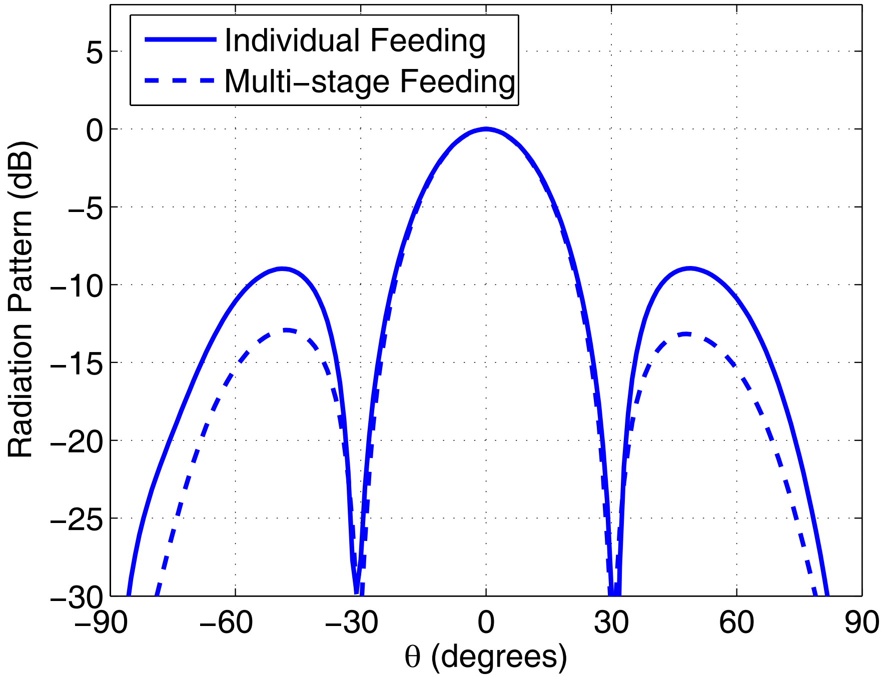

(b)

Figure 3.20: Radiation patterns of the 4×4 Vivaldi array with different feeding schemes when $\theta_s = 0^{\circ}$ and $\phi_s = 0^{\circ}$. (a) E-plane. (b) H-plane.

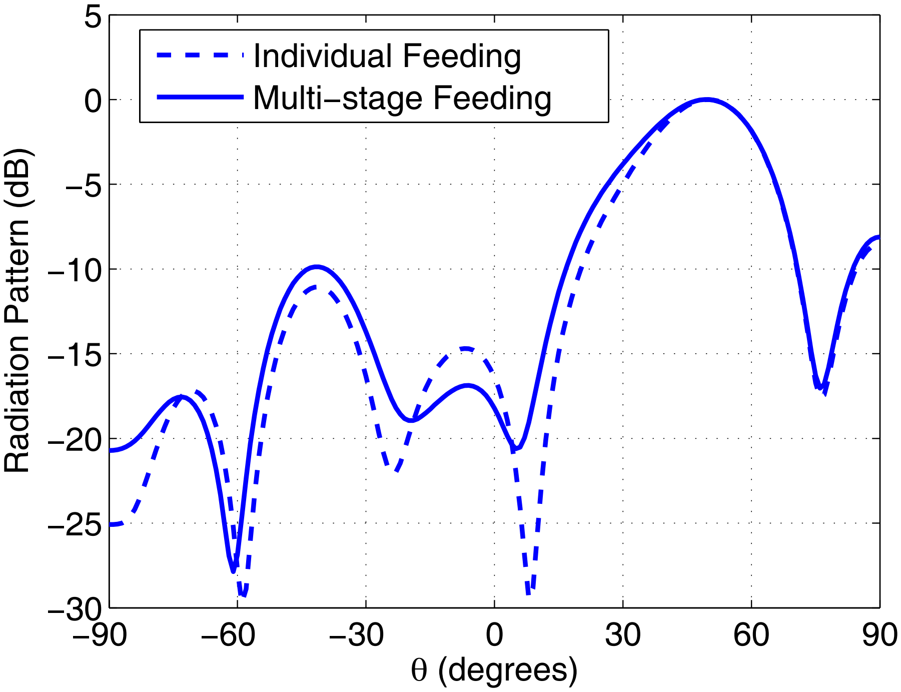

(a)

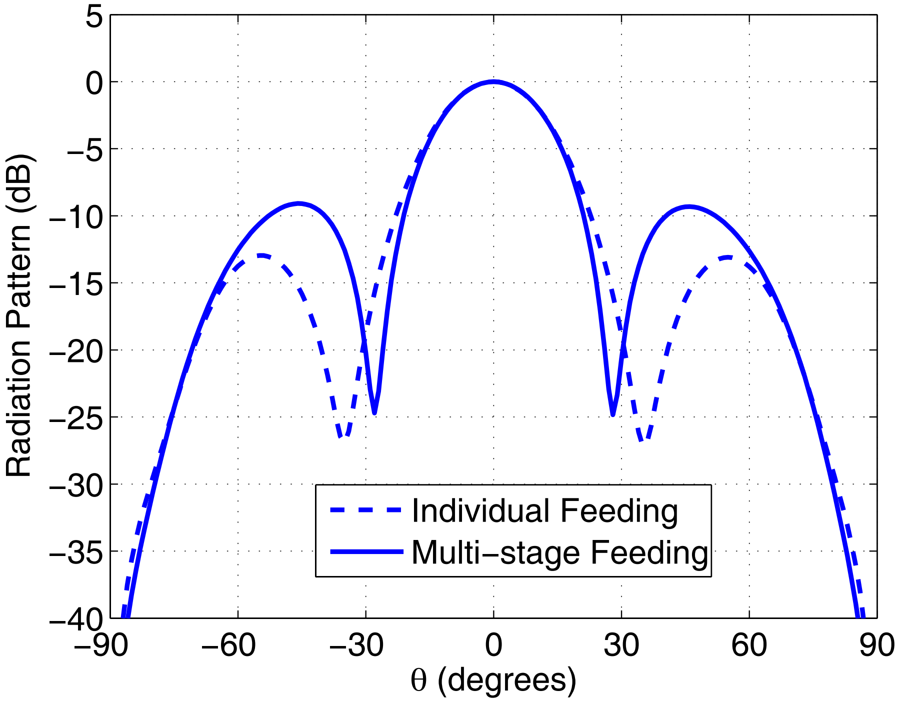

(b)

Figure 3.21: Radiation patterns of the 4×4 Vivaldi array with different feeding schemes when $\theta_s = 45^{\circ}$ and $\phi_s = 0^{\circ}$. (a) E-plane. (b) H-plane.

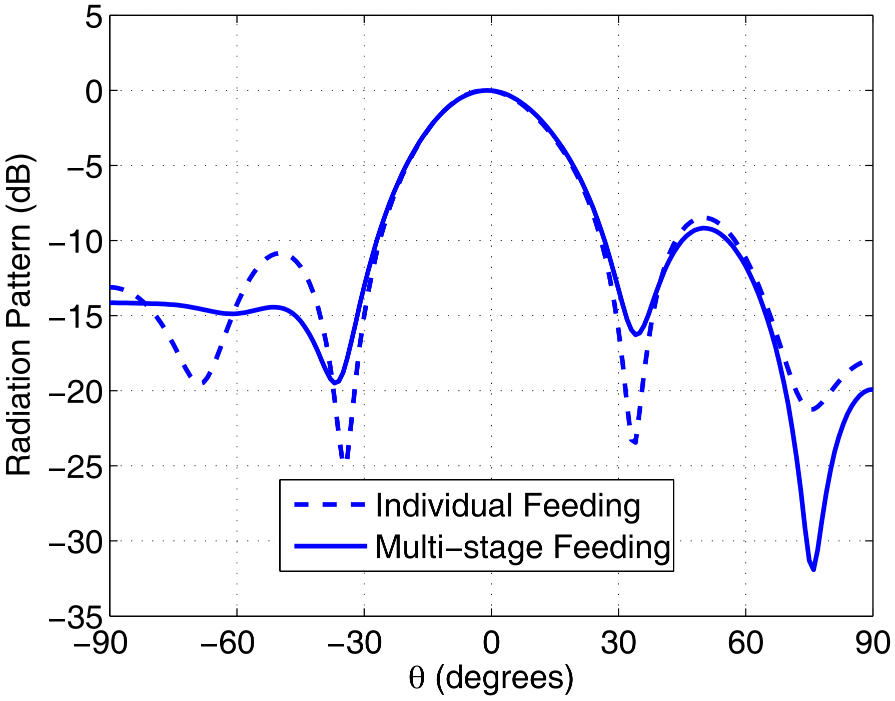

(a)

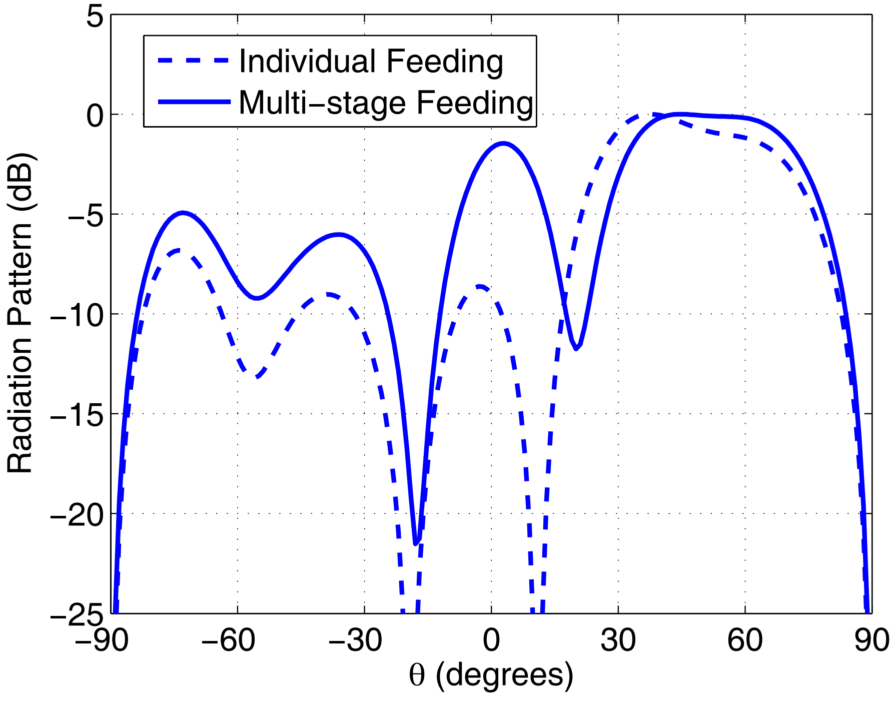

(b)

Figure 3.22: Radiation patterns of the 4×4 Vivaldi array with different feeding schemes when $\theta_s = 45^{\mathrm{o}}$ and $\phi_s = 90^{\mathrm{o}}$. (a) E-plane. (b) H-plane.

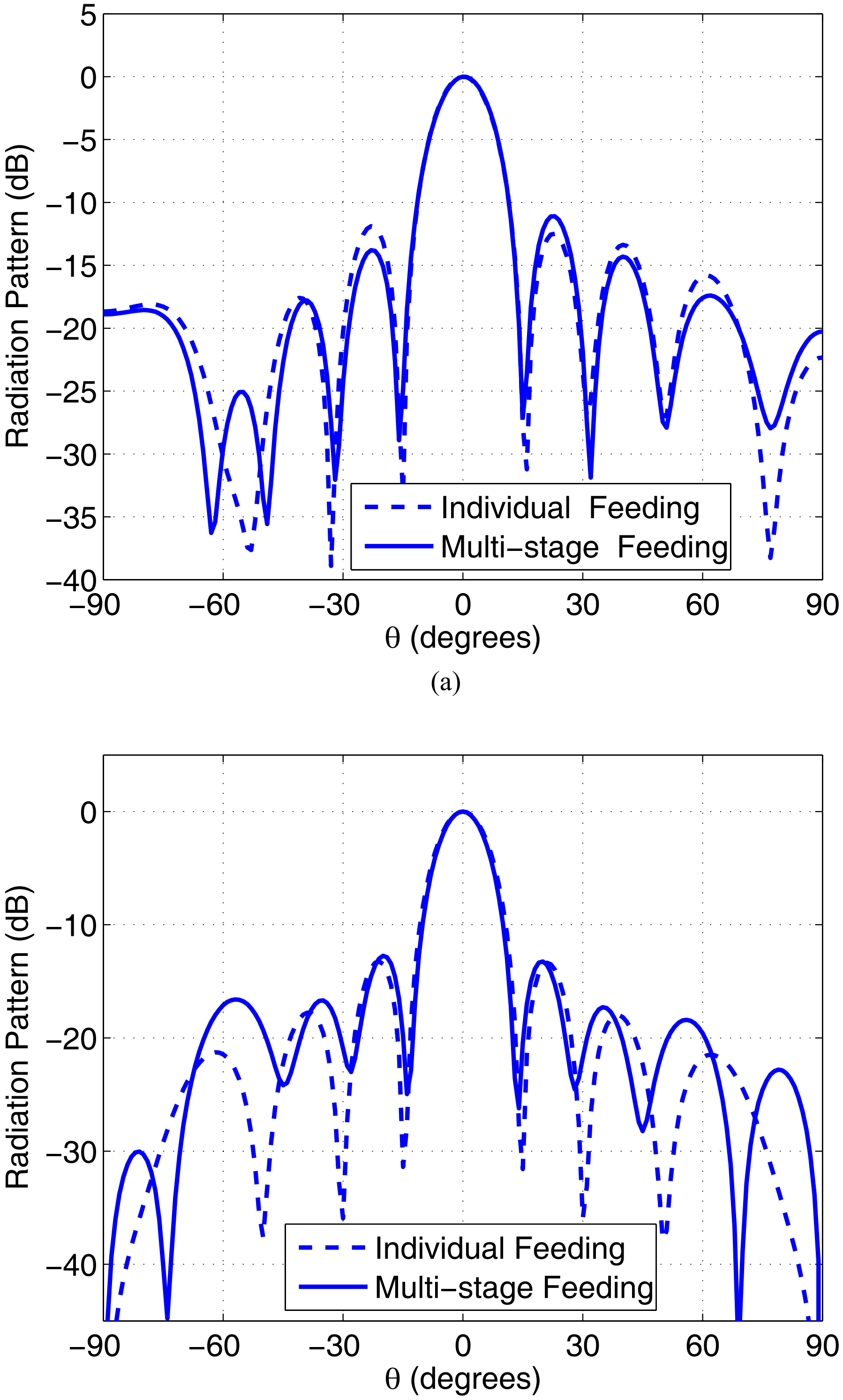

(a)

(b)

Figure 3.23: Radiation patterns of the 8×8 Vivaldi array with different feeding schemes when $\theta_s = 0^{\mathrm{o}}$ and $\phi_s = 0^{\mathrm{o}}$. (a) E-plane. (b) H-plane.

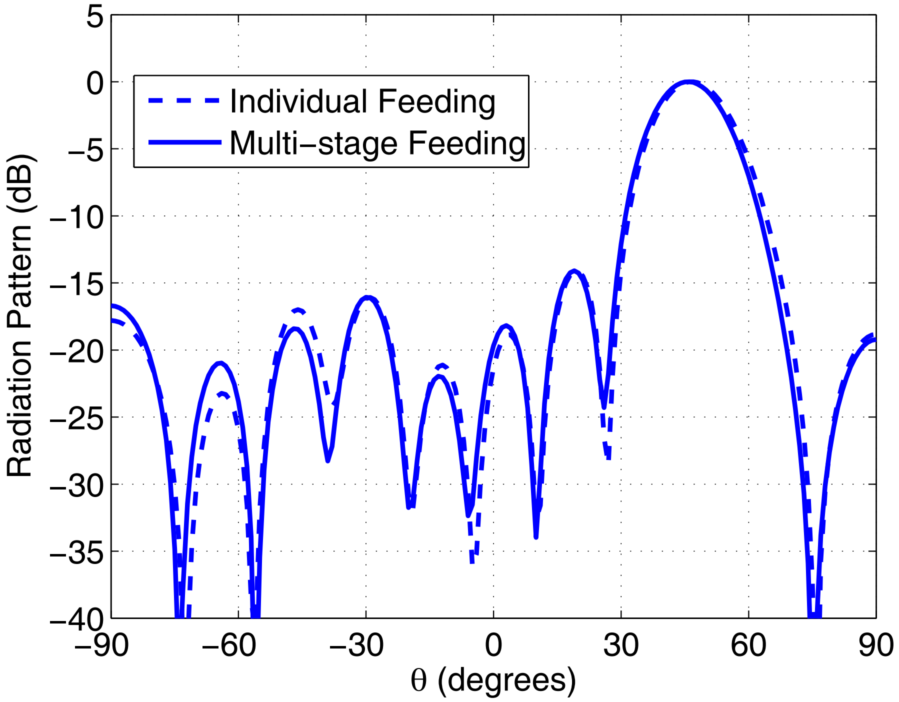

(a)

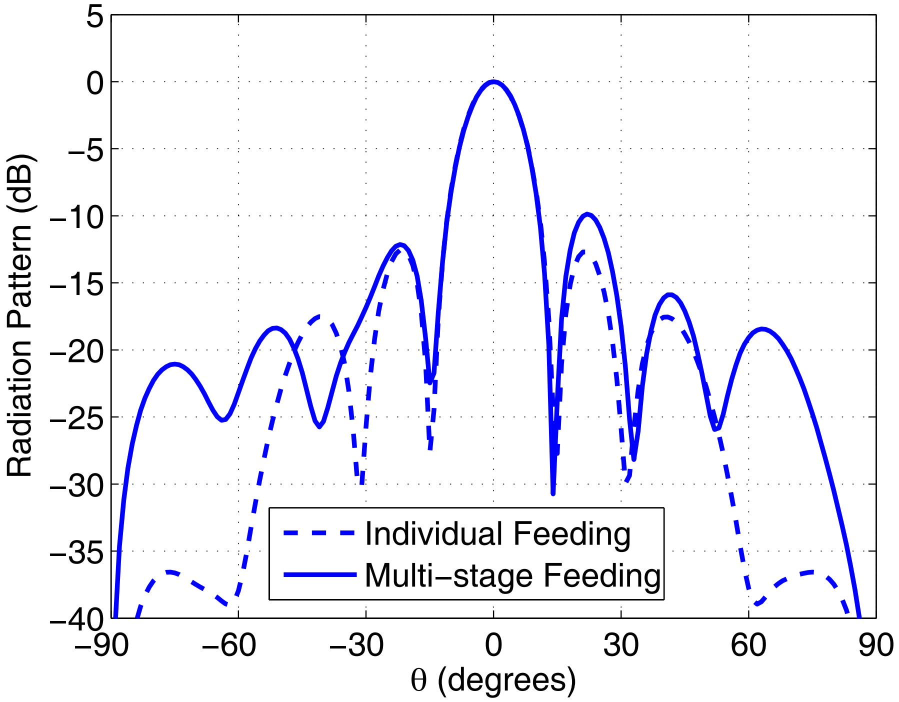

(b)

Figure 3.24: Radiation patterns of the 8×8 Vivaldi array with different feeding schemes when $\theta_s = 45^{\mathrm{o}}$ and $\phi_s = 0^{\mathrm{o}}$. (a) E-plane. (b) H-plane.

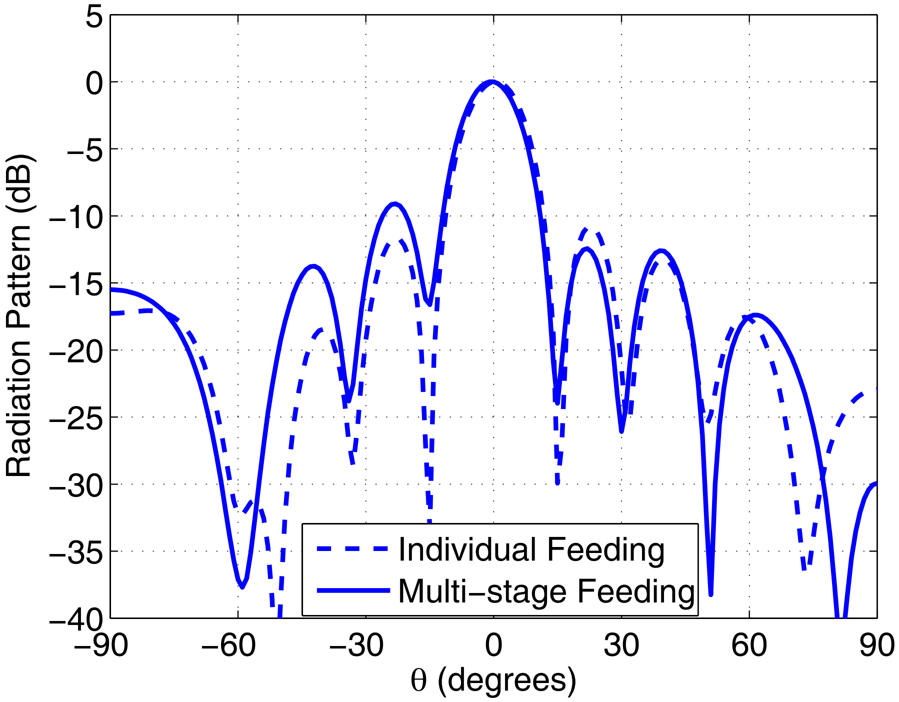

(a)

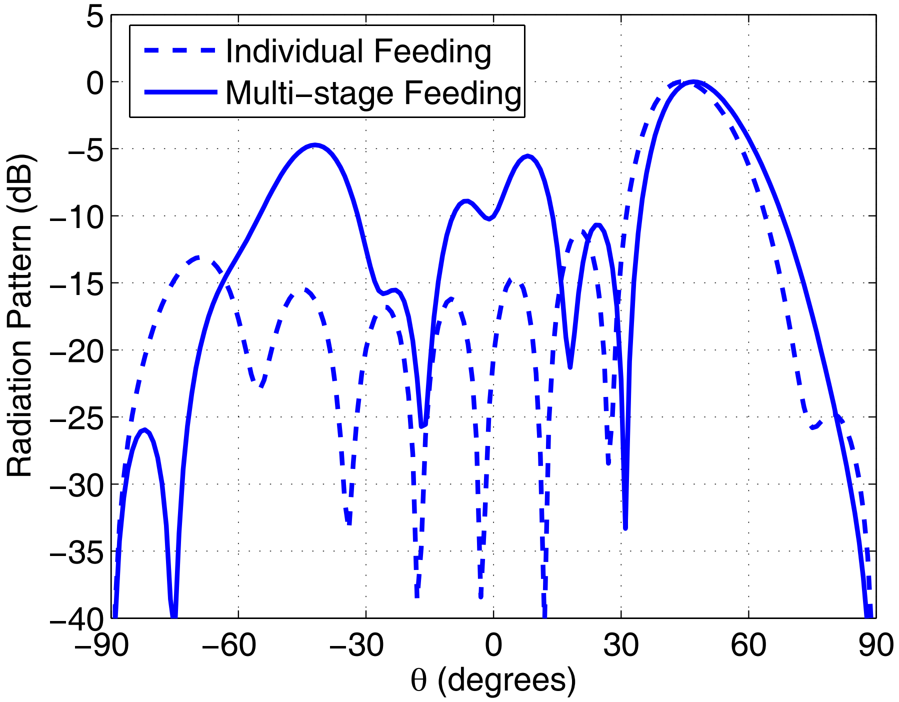

(b)

Figure 3.25: Radiation patterns of the 8×8 Vivaldi array with different feeding schemes when $\theta_s = 45^\circ$ and $\phi_s = 90^\circ$. (a) E-plane. (b) H-plane.

Table 3.1: Computational information for the simulation of the 8×1 Vivaldi array with different feeding schemes

Feed-network Type	Peak Memory (MB)	Average solution time per time step (second)
Individual feeding (no feed network)	1034	2.944
Single-stage feeding	1042	3.021
Multistage feeding	1042	3.013
Wilkinson-divider feeding	1042	2.997

Table 3.2: Computational information for the simulation of the 4×4 Vivaldi array with different feeding schemes

Feed-network Type	Peak Memory (MB)	Average solution time per time step (second)
Individual feeding (no feed network)	1043	3.184
Multistage feeding	1071	3.910

Table 3.3: Computational information for the simulation of the 8×8 Vivaldi array with different feeding schemes

Feed-network Type	Peak Memory (MB)	Average solution time per time step (second)
Individual feeding (no feed network)	1227	11.765
Multistage feeding	1313	14.517

CHAPTER 4

A HYBRID FIELD-CIRCUIT SIMULATOR BASED ON THE EXTENDED TDFEM

4.1 Introduction

Hybrid field-circuit solvers that combine a full-wave analysis and a lumped circuit simulation become indispensible for accurate characterization of complicated and mixed-scale electromagnetic devices. Consequently, circuit modeling has been incorporated into different types of time-domain full-wave simulation techniques resulting in various hybrid field-circuit simulators in the literature [42]-[57].

Considerable effort is focused on the extension of the FDTD capability to incorporate the treatment of lumped circuit elements [42]-[50]. In the context of FDTD, lumped circuit elements are treated by either assigning each of them into an edge of the FDTD grid [42], [43] or by using an algorithm based on the equivalent-source concept [44]-[46]. These techniques have been widely employed for the analysis of high-speed interconnects [47], crosstalk and package effects [48], as well as active microwave circuits such as amplifiers and mixers [49], [50].

Circuit simulations have also been hybridized with time-domain integral-equation (TDIE) solvers [51], [52]. The resulting hybrid simulators rely on the coupled TDIE-based full-wave and SPICE-like circuit simulations to track transient interactions between distributed (electromagnetic) and lumped (circuit) subsystems. To improve computational efficiency, the involved TDIE simulations are usually accelerated by fast algorithms such as the plane wave time-domain (PWTD) method [51] and the parallel time-domain adaptive integral method (AIM) [52]. These simulators have been applied to the analysis of various active and nonlinear antennas and microwave circuits, including power amplifiers and power-combining arrays.

Similar to the FDTD, early studies on the incorporation of lumped circuit elements into the TDFEM are focused on a simple approach of directly stamping their voltage-current relationships into the primary finite element matrices [53]. This technique, though straightforward, is limited to the cases that involve only linear and passive elements such as resistors, capacitors, and inductors, and thus it lacks the flexibility to include more extensive circuit networks or isolated lumped elements with more complex behavior, such as nonlinearities. Later, an approach similar to the FDTD equivalent-source method was introduced into the TDFEM framework [54]-[56]. In this approach, the circuits which are associated with certain FEM edges are treated as a separate application and the coupling between the FEM system and the circuits is modeled as an equivalent-current generator with an internal capacitive admittance at the lumped circuit port, which is then solved together with the linear/nonlinear state equations of the circuits, using either a direct call of SPICE [54] or a proper finite-difference scheme [55], [56]. This technique has been first formulated for the coupled first-order Maxwell's equations [54], [55] and then adapted to the second-order wave equations [56]. It has been successfully applied to various examples including active antennas [54], microwave amplifiers and oscillators [55], [56]. However, since this approach does not preserve the symmetry for the mutual coupling between the TDFEM and the circuit equations, it may have limited stability because the symmetry is a general requirement for achieving unconditional stability in a time-marching solution. In addition, this approach requires quite a few matrix manipulations to form the equivalent current source and the internal capacitive admittance matrix. Furthermore, it adopts a different time-discretization technique and thus a different solution scheme for the FEM unknowns associated with lumped circuits from those for the rest of the FEM unknowns. These manipulations and special treatments make it difficult to adapt an existing TDFEM code to a hybrid field-circuit solver. Recently, a circuit-oriented FEM technique has also been proposed for field-circuit coupled simulation in both frequency and time domains [57]. In this technique, an equivalent electrical network for the FEM system is formed and directly loaded into a SPICE circuit simulator together with any lumped circuit components superposed to the FEM edges.

In this chapter, a symmetric hybrid field-circuit solver based on an extended TDFEM algorithm is proposed, which was inspired by a TDIE-based field-circuit simulator [51]-[52]. The computational domain consists of distributive passive elements and active/passive lumped circuits. The FEM subsystem is formed by modeling the distributive passive elements by the standard TDFEM using the Newmark-beta scheme [1], while the lumped circuits are analyzed by a SPICE-like transient circuit solver based on the modified nodal analysis to form a circuit subsystem [58]. The coupling from the FEM subsystem to the circuit subsystem is realized by introducing an independent voltage source at each lumped port (FEM edge) whose value is determined by the TDFEM solution. On the other hand, the port currents of the circuit are computed by the circuit subsystem and become impressed current excitations along the associated FEM edges, which enable the circuit-to-FEM coupling. This hybridization of the TDFEM solver with the circuit solver results in a coupled FEM-circuit global system. Submatrices that represent mutual coupling of the FEM and circuit subsystems have been formulated into the global system. The symmetry of the mutual coupling and, thus, of the global system matrix is preserved. The resulting global FEM-circuit system is then solved at each time step by a solution algorithm adapted from the standard (quasi-) Newton algorithm.

A coupling technique similar to that in this work has been used to obtain a symmetric global system matrix where the TDFEM is hybridized with the transmission-line modeling of thin wires and thin slots [9], [59]-[60]. In those cases, the semi-discretized governing equations of subsystems are first hybridized and then discretized in time together to form the global system matrix. In this work, such a hybridization before time discretization is not available because the circuit analysis directly leads to a fully discretized circuit subsystem. The global system matrix is therefore directly assembled from the fully discretized FEM and circuit subsystems. This scheme minimizes extra matrix manipulations so that an existing TDFEM solver can be easily extended to a hybrid field-circuit solver. The proposed solver significantly extends the capability of the existing TDFEM solver to modeling more complex nonlinear and active systems.

The coupling technique above is strictly synchronous and so is referred to as a global time-stepping scheme, in the sense that it requires a common time-step size for both FEM and circuit subsystems. This seems a natural and straightforward way to hybridized the two subsystems. In contrast, a more generalized time-stepping scheme allows the signals in the different subsystems to be tracked and sampled at different time-step sizes and thus provides the freedom to choose subsystem-specific time-step sizes. It is referred to as a local or flexible time-stepping scheme later in this chapter. Compared to the global time-stepping scheme, this generalized time-stepping scheme improves the computational efficiency of the existing TDFEM-based hybrid field-circuit solver especially when the computational cost associated with the slow subsystems with a larger time-step size is much higher than that associated with the fast subsystems with a smaller time-step size.

In the following, Section 4.2 describes in detail the construction of the FEM and circuit subsystems as well as the coupling scheme and hybridization of these two subsystems, followed by a discussion of the solution schemes to efficiently solve the resulting global system of the mixed linear and nonlinear equations. The numerical examples are then presented in Section 4.3 to validate the proposed methodology and demonstrate its application and performance. The hybrid field-circuit simulation with a generalized flexible time-stepping scheme is described and validated in Section 4.4, followed by a brief summary in Section 4.5.

4.2 Formulation

4.2.1 Construction of the FEM Subsystem

The computational domain consists of both distributive passive elements and active/passive lumped circuit. The distributive passive part is modeled by the standard TDFEM described in Chapter 2, which leads to the FEM subsystem. However, because of the presence of lumped circuit elements in the distributive part, there will be an additional term in the right-hand side of (2.3) as

$$\nabla \times \frac{1}{\mu_r} \nabla \times \mathbf{E} + \frac{\varepsilon_r}{c_0^2} \frac{\partial^2 \mathbf{E}}{\partial t^2} + \mu_0 \sigma \frac{\partial \mathbf{E}}{\partial t} = -\mu_0 \frac{\partial}{\partial t}\left(\mathbf{J}^{\mathrm{im}} + \mathbf{J}^{\mathrm{CKT}}\right) \tag{4.1}$$

where $\mathbf{J}^{\mathrm{CKT}}$ denotes the impressed current excitation at the lumped ports (FEM edges) introduced by the associated lumped circuits. Following the procedure described in Chapter 2, the finite element discretization of (4.1) in the computational domain using hirachchcal vector basis function and the first-order ABC yields the following semidiscrete system:

$$\left[S\right]\{e\}+\frac{1}{c_0^2}\left[M\right]\frac{\partial^2\{e\}}{\partial t^2}+\frac{1}{c_0}\left(\left[G\right]+\left[A\right]\right)\frac{\partial\{e\}}{\partial t}=\frac{Z_0}{c_0}\left[\frac{\partial\{b^{\text{FEM}}\}}{\partial t}+\frac{\partial\{b^{\text{CKT}}\}}{\partial t}\right] \tag{4.2}$$

where the expressions for the matrix entries in $\left[S\right]$, $\left[M\right]$, $\left[G\right]$ and $\left[A\right]$ are given in (2.16)-(2.18) and (2.28), respectively, and

$$b_i^{\text{FEM/CKT}}=-\iiint_V \mathbf{N}_i\cdot\mathbf{J}^{\text{im/CKT}}dV. \tag{4.3}$$

Next, discretization of (4.2) in the time domain using the Newmark-beta scheme yields the following the updating equation:

$$\left[E_0\right]\{e\}_n=\left[E_1\right]\{e\}_{n-1}+\left[E_2\right]\{e\}_{n-2}+c_0\Delta t^2 Z_0\left(\left[\frac{\partial\{b^{\text{CKT}}\}}{\partial t}\right]_{n-1}+\left[\frac{\partial\{b^{\text{FEM}}\}}{\partial t}\right]_{n-1}\right) \tag{4.4}$$

where time index $n=1,\ 2,\ ...,\ T_{\max}$ and

$$\left[E_0\right]=\frac{c_0^2\Delta t^2}{4}\left[S\right]+\left[M\right]+\frac{c_0\Delta t}{2}\left(\left[G\right]+\left[A\right]\right) \tag{4.5}$$

$$\left[E_1\right]=-\frac{c_0^2\Delta t^2}{2}\left[S\right]+2\left[M\right] \tag{4.6}$$

$$\left[E_2\right]=-\frac{c_0^2\Delta t^2}{4}\left[S\right]-\left[M\right]+\frac{c_0\Delta t}{2}\left(\left[G\right]+\left[A\right]\right). \tag{4.7}$$

The size of the FEM solution vector $\{e\}$ is denoted as N^{FEM}.

The explicit expression of $\left[\partial\{b^{\text{CKT}}\}/\partial t\right]_{n-1}$ will be derived in Section 4.2.3 where the circuit-to-FEM coupling is described. For simplicity, in the remainder of this chapter, we ignore the sources inside the FEM domain by setting $\{b^{\text{FEM}}\}=0$.

4.2.2 Stamping Technique

Common lumped passive circuit elements such as resistors, capacitors, and inductors can be included into the TDFEM scheme by simply adding their individual values to the proper locations of the primary FEM matrices. This is referred to as the stamping technique in this dissertation. In the following, a brief derivation of this technique will be included.

The voltage V_k along an edge *k* whose direction is denoted as $\hat{l}_k$ can be computed as the negative of the line integral of the electric field vector **E** along that edge. Considering the expansion of the electric field in terms of the tangentially continuous basis functions $\mathbf{N}_k$ of the zeroth order, the following expression for V_k can be obtained:

$$V_k = -\int_{l_k} \mathbf{E} \cdot \hat{l}_k dl = -e_k \left(\int_{l_k} \mathbf{N}_k \cdot \hat{l}_k dl \right). \tag{4.8}$$

If there is a lumped element or a lumped circuit port associated with edge *k*, the current flow I_k in the lumped element (or the circuit port) is along edge *k* but with an opposite direction to $\hat{l}_k$ (shown in Fig. 4.1(a)). As an result, $\mathbf{J}^{\mathrm{CKT}} = -I_k \delta\left(\hat{l}_k\right)$ and

$$b_k^{\mathrm{CKT}} = -\iiint_V \mathbf{N}_k \cdot \mathbf{J}^{\mathrm{CKT}} dV = I_k \left(\int_{l_k} \mathbf{N}_k \cdot \hat{l}_k dV \right). \tag{4.9}$$

The voltage-current relation for a resistor with a value *R* is

$$I_k = R^{-1} V_k . \tag{4.10}$$

Substituting (4.10) into (4.9) and then into (4.2), it is found that the insertion of a lumped resistor *R* at edge *k* can be implemented by stamping the matrix $[G]$ in (4.2) as

$$G_{kk} \to G_{kk} + Z_0 R^{-1} \left(\int_{l_k} \mathbf{N}_k \cdot \hat{l}_k dl \right)^2 . \tag{4.11}$$

Using the fact that the voltage-current relation for a capacitor with a value *C* is

$$I_k = C \frac{dV_k}{dt} \tag{4.12}$$

the insertion of a lumped capacitor *C* at edge *k* can be implemented by stamping the matrix $[M]$ in (4.2) as

$$M_{kk} \to M_{kk} + Z_0 c_0 C \left(\int_{l_k} \mathbf{N}_k \cdot \hat{l}_k dl \right)^2 . \tag{4.13}$$

Similarly, the voltage-current relations for an inductor with a value L

$$I_k = L^{-1} \int V_k dt \tag{4.14}$$

can also be stamped into $\left[S\right]$ in (4.2) as

$$S_{kk} \to S_{kk} + \frac{Z_0 L^{-1}}{c_0} \left(\int_{l_k} \mathbf{N}_k \cdot \hat{l}_k dl \right)^2 . \tag{4.15}$$

Note that the time integral $\int \cdot dt$ in (4.10) cancels with the time derivative $\frac{\partial \{\}}{\partial t}$ in (4.2).

From the above, it is evident that in the case of the zeroth order edge basis function, stamping of lumped element values only affects the diagonal entries of the corresponding primary FEM matrices. The formulation can easily be extended to the case when higher order basis functions [1], [24], and [25] are employed in field expansion. Because of this, there is more than one basis function contributing to the expansion of the electric field and thus the voltage along edge k can be expressed as

$$V_k = -\int_{l_k} \mathbf{E} \cdot \hat{l}_k dl = -\sum_{p=1}^{P} e_{k_p} \left(\int_{l_k} \mathbf{N}_{k_p} \cdot \hat{l}_k dl \right) \tag{4.16}$$

if P is the number of basis functions associated with edge k. As a result, the diagonal blocks of the corresponding primary FEM matrices will be affected as, for $q, p = 1, 2, \ldots, P$

$$G_{pq} \to G_{pq} + Z_0 R^{-1} \left(\int_{l_k} \mathbf{N}_{k_q} \cdot \hat{l}_k dl \right) \left(\int_{l_k} \mathbf{N}_{k_p} \cdot \hat{l}_k dl \right) \tag{4.17a}$$

$$M_{pq} \to M_{pq} + Z_0 c_0 C \left(\int_{l_k} \mathbf{N}_{k_q} \cdot \hat{l}_k dl \right) \left(\int_{l_k} \mathbf{N}_{k_p} \cdot \hat{l}_k dl \right) \tag{4.17b}$$

$$S_{pq} \to S_{pq} + \frac{Z_0 L^{-1}}{c_0} \left(\int_{l_k} \mathbf{N}_{k_q} \cdot \hat{l}_k dl \right) \left(\int_{l_k} \mathbf{N}_{k_p} \cdot \hat{l}_k dl \right) . \tag{4.17c}$$

Similarly, the formulation above can also be extended to the case when there are multiple (more than one) edges $(\hat{l}_1, \hat{l}_2, \cdots, \hat{l}_k, \cdots, \hat{l}_K)$ associated with one lumped port (path $\hat{l}$). Again, there is more than one basis function contributing to the voltage along path $\hat{l}$ which can be expressed as the summation of voltages along all the edges $(\hat{l}_1, \hat{l}_2, \cdots, \hat{l}_k, \cdots, \hat{l}_K)$ on path $\hat{l}$,

$$V_l = -\int_l \mathbf{E} \cdot \hat{l} dl = \sum_{k=1}^{K} \left(-\int_{l_k} \mathbf{E} \cdot \hat{l}_k dl \right) = \sum_{k=1}^{K} \left(-\sum_{p=1}^{P_k} e_{k_p} \left(\int_{l_k} \mathbf{N}_{k_p} \cdot \hat{l}_k dl \right) \right) \tag{4.18}$$

where P_k is the number of basis functions associated with edge $\hat{l}_k$. The corresponding block (with a size of $\sum_{k=1}^{K} P_k$) of the primary FEM matrices will be affected as, for $q_{k'}$ = 1, 2, …, $P_{k'}$, p_k = 1, 2, …, P_k, and k = 1, 2, …, K,

$$G_{p_k q_{k'}} \to G_{p_k q_{k'}} + Z_0 R^{-1} \left(\int_{l_{k'}} \mathbf{N}_{k_{q_{k'}}} \cdot \hat{l}_{k'} dl \right) \left(\int_{l_k} \mathbf{N}_{k_{p_k}} \cdot \hat{l}_k dl \right) \tag{4.19a}$$

$$M_{p_k q_{k'}} \to M_{p_k q_{k'}} + Z_0 c_0 C \left(\int_{l_{k'}} \mathbf{N}_{k_{q_{k'}}} \cdot \hat{l}_{k'} dl \right) \left(\int_{l_k} \mathbf{N}_{k_{p_k}} \cdot \hat{l}_k dl \right) \tag{4.19b}$$

$$S_{p_k q_{k'}} \to S_{p_k q_{k'}} + \frac{Z_0 L^{-1}}{c_0} \left(\int_{l_{k'}} \mathbf{N}_{k_{q_{k'}}} \cdot \hat{l}_{k'} dl \right) \left(\int_{l_k} \mathbf{N}_{k_{p_k}} \cdot \hat{l}_k dl \right). \tag{4.19c}$$

Obviously, the stamping technique is only desired for the simplest cases. Not only is it able to handle limited types of linear circuit elements, but also each element in the circuit netlist has to be assigned to one FEM edge, so the technique lacks the capability and flexibility to process more complicated circuit networks. However, this straightforward technique is well-known for its simplicity and validity and thus can be used as a simple validation to the more advanced hybrid field-circuit solver developed in this work. In addition, the stamping technique can also be used as a supplement to the proposed hybrid field-circuit solver whenever a circuit subsystem described in Section 4.2.3 cannot or does not need to be formed.

4.2.3 Construction of the Circuit Subsystem

The circuit simulation in this work is carried out based on SPICE3 [61]. The resulting circuit solver performs a linear and nonlinear large-signal transient analysis on an arbitrary number of independent multiport circuit networks. Using the modified nodal analysis, governing circuit equations are formulated based on the circuit topologies and by applying Kirchoff's current law at all the nodes (except for the reference node) and Kirchoff's voltage law to independent loops. This analysis yields the system of equations in the time domain

$$\left[Y\right]\{V_n^{\mathrm{CKT}}\} + \mathbf{I}_n^{\mathrm{CKT,nl}}\left(\{V_n^{\mathrm{CKT}}\}\right) = \mathbf{I}_n^{\mathrm{CKT}} \tag{4.20}$$

at each time step $t = n\Delta t$, $n = 1,\ 2,\ ...,\ T_{\max}$. The time-independent admittance matrix $\left[Y\right]$ consists of contributions from linear and time-invariant circuit elements and the companion models of linear capacitors and inductors that are formulated using the trapezoidal integration rule. The vector of circuit unknowns $\{V_n^{\mathrm{CKT}}\}$ contains both node voltages and branch currents that flow through the internal supplied voltage sources, if any. Accordingly, the overall dimension of the system in (4.20), denoted as N^{CKT}, is equal to the number of nonreference nodes plus the number of independent voltage sources in the circuit netlist. The excitation vector $\mathbf{I}_n^{\mathrm{CKT}}$ holds the values of both the supplied sources and those derived from the companion models. The vector $\mathbf{I}_n^{\mathrm{CKT,nl}}\left(\{V_n^{\mathrm{CKT}}\}\right)$ represents all the contributions from the branch equations of nonlinear elements. Therefore, the number of nonlinear equations in (4.20) is proportional to the number of nonlinear circuit elements. The resulting system of equations can be solved at each time step using the multidimensional Newton-Raphson method [62].

Note that although some advanced commercial circuit simulators incorporate dynamic time-stepping control algorithms to improve the flexibility, speed, and accuracy of the solution, in this work the circuit equation system is solved by marching on in time using a constant but small time-step size (same as that in the time-domain FEM solver) throughout the entire simulation, which is common in almost all kinds of hybrid solvers. The time-step size is determined by the highest frequency of the operation frequency band in order to capture the fastest-changing signal components.

4.2.4 Coupling Scheme and Global System of Equations

The global system of equations is formed by coupling the FEM and circuit subsystems that are represented by (4.4) and (4.20), respectively. Geometrically, a circuit subsystem contains one or multiple lumped ports that reside on individual FEM edges, and thus are coupled with the FEM subsystem through the group of FEM unknowns associated with those edges. Methodologically, this mutual coupling is modeled by introducing equivalent impressed (supplied) sources to each subsystem, elaborated as follows.

As illustrated in Fig. 4.1(b), the FEM-to-circuit coupling is modeled by introducing external supplied voltage sources into the circuit subsystem at the lumped ports. The values of these external voltage sources are solely determined by the FEM unknowns associated with the edges where the lumped ports reside. By introducing these external voltage sources, (4.20) is expanded and becomes

$$\begin{bmatrix} [Y] & [B] \\ [B]^T & \mathbf{0} \end{bmatrix} \begin{Bmatrix} \{V_n^{\mathrm{CKT}}\} \\ \{I_n^{\mathrm{CP}}\} \end{Bmatrix} + \begin{Bmatrix} \mathbf{I}_n^{\mathrm{CKT,nl}}\left(\{V_n^{\mathrm{CKT}}\}\right) \\ \mathbf{0} \end{Bmatrix} = \begin{Bmatrix} \mathbf{I}_n^{\mathrm{CKT}} \\ -[C]\{e\}_n \end{Bmatrix}. \tag{4.21}$$

Here, vector $\{I_n^{\mathrm{CP}}\}$ includes currents in the external voltage sources, whose dimension is equal to the number of lumped ports, denoted as N^{CP}. Matrix $[B]$ has a size of $N^{\mathrm{CKT}} \times N^{\mathrm{CP}}$ and contains only 1's, –1's, and 0's to select the circuit nodes that are connected to the external voltage sources. Matrix $[C]$ has a size of $N^{\mathrm{CP}} \times N^{\mathrm{FEM}}$ and is formulated to compute the values of the external voltage sources from the FEM solution vector $\{e\}_n$. The nonzero entries of $[C]$ can be written as

$$C_{ki} = \int_{l_{i(k)}} \mathbf{N}_i \cdot \hat{l}_{i(k)} dl \tag{4.22}$$

where k is the index of external voltage sources and i is the index of the FEM unknown on the associated edge whose direction is denoted as $\hat{l}_{i(k)}$.

Similarly, the circuit-to-FEM coupling is modeled by introducing impressed current sources into the FEM subsystem at the FEM edges that reside at the lumped ports of the circuit subsystem. The existences of these impressed current sources are represented in (4.4) as $\left[\partial\{b^{\mathrm{CKT}}\}/\partial t\right]_{n-1}$. By observing the facts that the values of these current sources are equal to $-\{I_{n-1}^{\mathrm{CP}}\}$ and their directions are opposite to the direction of the associated edges (shown in Fig.

4.1(c)), the explicit expression for $\left[\partial\{b^{\mathrm{CKT}}\}/\partial t\right]_{n-1}$ can be derived. More specifically, the *i*th entry in $\left[\partial\{b^{\mathrm{CKT}}\}/\partial t\right]_{n-1}$, $i=1,2,...,N^{\mathrm{FEM}}$, is

$$\left[\frac{\partial\{b\}_i^{\mathrm{CKT}}}{\partial t}\right]_{n-1} = -\left(\int_{l_{i(k)}} \mathbf{N}_i\cdot(-\hat{l}_{i(k)})dV\right)\frac{\partial}{\partial t}\left\{-I_{k,n-1}^{\mathrm{CP}}\right\}. \tag{4.23}$$

If a central-difference formula is applied to approximate the time derivative, (4.23) can be written as

$$\left[\frac{\partial\{b^{\mathrm{CKT}}\}}{\partial t}\right]_{n-1} = -\frac{1}{2\Delta t}\left[C\right]^{\mathrm{T}}\left[\{I_n^{\mathrm{CP}}\}-\{I_n^{\mathrm{CP}}\}\right]. \tag{4.24}$$

Finally, substituting (4.24) into (4.4) and combining with (4.21) yields the following coupled system of equations:

$$\mathbf{F}(\mathbf{x}_n)=\mathbf{b}_n \tag{4.25}$$

where $\mathbf{x}_n=\left\{\{e\}_n \quad \{V_n^{\mathrm{CKT}}\} \quad \{I_n^{\mathrm{CP}}\}\right\}^{\mathrm{T}}$ and

$$\mathbf{F}(\mathbf{x}_n)=\begin{bmatrix}\left[E_0\right] & \mathbf{0} & \varsigma\left[C\right]^{\mathrm{T}} \\ \mathbf{0} & \varsigma[Y] & \varsigma[B] \\ \varsigma\left[C\right] & \varsigma[B]^{\mathrm{T}} & \mathbf{0}\end{bmatrix}\begin{Bmatrix}\{e\}_n \\ \{V_n^{\mathrm{CKT}}\} \\ \{I_n^{\mathrm{CP}}\}\end{Bmatrix}+\begin{Bmatrix}\mathbf{0} \\ \varsigma\mathbf{I}_n^{\mathrm{CKT,nl}}\left(\{V_n^{\mathrm{CKT}}\}\right) \\ \mathbf{0}\end{Bmatrix} \tag{4.26}$$

$$\begin{aligned}\mathbf{b}_n &= \begin{Bmatrix}\mathbf{0} \\ \varsigma\mathbf{I}_n^{\mathrm{CKT}} \\ \mathbf{0}\end{Bmatrix}+\begin{Bmatrix}\left[E_1\right]\{e\}_{n-1}+\left[E_2\right]\{e\}_{n-2} \\ \mathbf{0} \\ \mathbf{0}\end{Bmatrix}+\begin{Bmatrix}\varsigma\left[C\right]^{\mathrm{T}}\{I_{n-2}^{\mathrm{CP}}\} \\ \mathbf{0} \\ \mathbf{0}\end{Bmatrix} \\ &= \begin{Bmatrix}\mathbf{0} \\ \varsigma\mathbf{I}_n^{\mathrm{CKT}} \\ \mathbf{0}\end{Bmatrix}+\begin{bmatrix}\left[E_1\right] & \mathbf{0} & \mathbf{0} \\ \mathbf{0} & \mathbf{0} & \mathbf{0} \\ \mathbf{0} & \mathbf{0} & \mathbf{0}\end{bmatrix}\begin{Bmatrix}\{e\}_{n-1} \\ \{V_{n-1}^{\mathrm{CKT}}\} \\ \{I_{n-1}^{\mathrm{CP}}\}\end{Bmatrix}+\begin{bmatrix}\left[E_2\right] & \mathbf{0} & \varsigma\left[C\right]^{\mathrm{T}} \\ \mathbf{0} & \mathbf{0} & \mathbf{0} \\ \mathbf{0} & \mathbf{0} & \mathbf{0}\end{bmatrix}\begin{Bmatrix}\{e\}_{n-2} \\ \{V_{n-2}^{\mathrm{CKT}}\} \\ \{I_{n-2}^{\mathrm{CP}}\}\end{Bmatrix}.\end{aligned} \tag{4.27}$$

Note that to derive (4.25), all the quantities at time step *n* have been moved to the left-hand side and solved simultaneously, and (4.21) has been scaled with a constant $\varsigma=(c_0\Delta t Z_0)/2$. These simple manipulations lead to the desired symmetry in the resulting global matrix system of equations (4.25). Also, note that the third lines of (4.26) and (4.27) actually explicitly enforce the equality between the voltages over the lumped circuit ports and the voltages cross the corresponding FEM edges.

4.2.5 Solution Algorithm

The solution of the system of equations involving nonlinearity usually requires special care. Equation (4.25) can be treated as a global nonlinear system of equations of size $N^{\mathrm{FEM}} + N^{\mathrm{CKT}} + N^{\mathrm{CP}}$, which can be solved for the global solution vector $\mathbf{x}_n$ at time $t = n\Delta t$, $n = 1, 2, ..., T_{\max}$, simply by using the standard multidimensional Newton-Raphson algorithm [62]. This involves the solution of the following linearized system, at the *k*th Newton iteration of the *n*th time step:

$$\begin{bmatrix} [E_0] & \mathbf{0} & \varsigma[C]^{\mathrm{T}} \\ \mathbf{0} & \varsigma\left([Y]+[J]_{n,k}^{\mathrm{CKT,nl}}\right) & \varsigma[B] \\ \varsigma[C] & \varsigma[B]^{\mathrm{T}} & \mathbf{0} \end{bmatrix} \delta\mathbf{x}_k = \mathbf{b}_n - \mathbf{F}(\mathbf{x}_{n,k-1}) \tag{4.28}$$

where the Jacobian matrix $[J]_{n,k}^{\mathrm{CKT,nl}} = \partial\mathbf{I}_n^{\mathrm{CKT,nl}} / \partial\{V_n^{\mathrm{CKT}}\}\Big|_{\{V_{n,k-1}^{\mathrm{CKT}}\}}$ is computed via analytical formulas. However, since (4.25) is a system of mixed linear and nonlinear equations and the linear equations significantly outnumber the nonlinear equations, applying the standard Newton-Raphson algorithm to such a large matrix system in (4.25) is not an optimal solution in terms of efficiency. Furthermore, some entries of the matrix in (4.28) change for every Newton step of each time step, and thus it is very difficult to perform prefactorization of the system matrix when a direct solver is applied to solve (4.28), or to generate a satisfactory preconditioner when an iterative solver is applied. Therefore, in order to solve (4.25) in a more efficient way, we adapt the solution algorithm that was used in a hybrid field-circuit solver based on the time-domain integral equation [51], and modify this algorithm to further reduce its computational cost.

First, the linear and nonlinear circuit unknowns are separated as $\{V_n^{\mathrm{CKT}}\}$ = $\left\{\{V_n^{\mathrm{CKT,l}}\}^{\mathrm{T}} \quad \{V_n^{\mathrm{CKT,nl}}\}^{\mathrm{T}}\right\}^{\mathrm{T}}$, where $\{V_n^{\mathrm{CKT,nl}}\}$ is the nodal voltage unknowns that are involved in the expressions of $\mathbf{I}_n^{\mathrm{CKT,nl}}$. Therefore, $\mathbf{I}_n^{\mathrm{CKT,nl}}$ can be expressed as $\mathbf{I}_n^{\mathrm{CKT,nl}}(\{V_n^{\mathrm{CKT,nl}}\})$. We denote the size of $\{V_n^{\mathrm{CKT,nl}}\}$ as $N^{\mathrm{CKT,nl}}$. The Newton-Raphson method is then applied to a much smaller nonlinear system of equations $\mathbf{f}(\{V_n^{\text{CKT,nl}}\}) = \mathbf{0}$ whose dimension is equal to $N^{\text{CKT,nl}}$. Here, $\mathbf{f}(\{V_n^{\text{CKT,nl}}\}) = \mathbf{0}$ is actually a reduced equivalent system of (4.25), where only $\{V_n^{\text{CKT,nl}}\}$ is kept while other unknowns are eliminated. The matrix-reduction process (elimination of unknowns) is not done explicitly. Instead, we solve a linear matrix equation and extract the nonlinear part of the solution vector to construct $\mathbf{f}(\{V_n^{\text{CKT,nl}}\})$. The solution algorithm is stated as follows.

At $t = n\Delta t$, $n = 1, 2, ..., T_{\max}$:

1. Update the equivalent sources of linear and nonlinear capacitors and inductors and compute $\mathbf{b}_n$ in (4.27).
2. Enter the Newton iteration, for k = 1, 2, …

   2.1) Solve the following system with a natural initial guess $\{V_{n,0}^{\text{CKT,nl}}\} = \{V_{n-1}^{\text{CKT,nl}}\}$:

$$\begin{bmatrix} [E_0] & \mathbf{0} & \varsigma[C]^{\text{T}} \\ \mathbf{0} & \varsigma[Y] & \varsigma[B] \\ \varsigma[C] & \varsigma[B]^{\text{T}} & \mathbf{0} \end{bmatrix} \begin{Bmatrix} \{\tilde{e}\}_{n,k-1} \\ \{\tilde{V}_{n,k-1}^{\text{CKT}}\} \\ \{\tilde{I}_{n,k-1}^{\text{CP}}\} \end{Bmatrix} = \mathbf{b}_n - \begin{Bmatrix} \mathbf{0} \\ \varsigma \mathbf{I}_n^{\text{CKT,nl}}\left(\{V_{n,k-1}^{\text{CKT,nl}}\}\right) \\ \mathbf{0} \end{Bmatrix} \tag{4.29}$$

   2.2) Extract $\{\tilde{V}_{n,k-1}^{\text{CKT,nl}}\}$ from $\{\tilde{V}_{n,k-1}^{\text{CKT}}\}$, and compute $\mathbf{f}_{n,k-1} = \{V_{n,k-1}^{\text{CKT,nl}}\} - \{\tilde{V}_{n,k-1}^{\text{CKT,nl}}\}$.

   If $\text{norm}(\mathbf{f}_{n,k-1}) < \text{TOL}$, then $\mathbf{x}_n = \left\{\{\tilde{e}\}_{n,k-1}^{\text{T}} \quad \{\tilde{V}_{n,k-1}^{\text{CKT}}\}^{\text{T}} \quad \{\tilde{I}_{n,k-1}^{\text{CP}}\}^{\text{T}}\right\}^{\text{T}}$, and exit the Newton iteration.

   Otherwise, continue to iterate.

   2.3) Compute $\{V_{n,k}^{\text{CKT,nl}}\}$ for the next Newton iteration by solving

   $[J]_{n,k}^{\mathbf{f}} \cdot \delta\{V_{n,k}^{\text{CKT,nl}}\} = -\mathbf{f}_{n,k-1}$, and thus $\{V_{n,k}^{\text{CKT,nl}}\} = \{V_{n,k-1}^{\text{CKT,nl}}\} + \delta\{V_{n,k}^{\text{CKT,nl}}\}$.

The Jacobian matrix $[J]_{n,k}^{\mathbf{f}} = \partial\mathbf{f} / \partial\{V_n^{\text{CKT,nl}}\}\Big|_{\{V_{n,k-1}^{\text{CKT,nl}}\}}$ of size $N^{\text{CKT,nl}}$ can be computed either analytically or numerically via the forward-difference formula, but either way it requires solving (4.29) with $N^{\text{CKT,nl}}$ different right-hand sides. The derivation and proof of validity of this solution procedure have been included in Appendix B. The obvious advantage of this algorithm is that the system matrix in (4.29) is now time-independent and thus can be preassembled and prefactorized before time marching starts. Furthermore, the Newton-Raphson method is applied to an equivalent system of much smaller size than that of (4.29), and can achieve faster convergence. The drawback is that the computational cost for computing the Jacobian matrix is relatively high. However, this problem can be alleviated if the quasi-Newton methods, such as Broyden's method, are used to provide inexpensive approximations to the Jacobian matrix [62]. Therefore, we modify Step 2.3 by replacing Newton's updating formulas with the following process.

2.3) If not converged, update $\{V_{n,k}^{\mathrm{CKT,nl}}\}$ through the following steps:

a) Solve $\delta\{V_{n,k}^{\mathrm{CKT,nl}}\}$ from $\left[\tilde{J}\right]_{n,k-1}^{\mathbf{f}} \cdot \delta\{V_{n,k}^{\mathrm{CKT,nl}}\} = -\mathbf{f}_{n,k-1}$.

b) Calculate $\{V_{n,k}^{\mathrm{CKT,nl}}\} = \{V_{n,k-1}^{\mathrm{CKT,nl}}\} + \delta\{V_{n,k}^{\mathrm{CKT,nl}}\}$.

c) Compute $\mathbf{f}_{n,k}$ by solving (23), and $\delta\mathbf{f}_k = \mathbf{f}_{n,k} - \mathbf{f}_{n,k-1}$.

d) Update the approximated Jacobian matrix as

$$\left[\tilde{J}\right]_{n,k}^{\mathbf{f}} = \left[\tilde{J}\right]_{n,k-1}^{\mathbf{f}} + \frac{\left(\delta\mathbf{f}_k - \left[\tilde{J}\right]_{n,k-1}^{\mathbf{f}} \cdot \delta\{V_{n,k}^{\mathrm{CKT,nl}}\}\right) \cdot \left(\delta\{V_{n,k}^{\mathrm{CKT,nl}}\}\right)^{\mathrm{T}}}{\left(\delta\{V_{n,k}^{\mathrm{CKT,nl}}\}\right)^{\mathrm{T}} \cdot \delta\{V_{n,k}^{\mathrm{CKT,nl}}\}}. \tag{4.30}$$

The above updating process only requires solving (4.29) once to update the approximated Jacobian matrix $\left[\tilde{J}\right]^{\mathbf{f}}$ and converges superlinearly, which is found to be almost as fast as the Newton's method that converges quadratically when Δt is relatively small, but with a much smaller computational cost. An efficient implementation of the above updating scheme involves QR decomposition, which is available from [62]. The robustness of the algorithm can be greatly improved when it is combined with a line search technique.

The initial guess $\left[\tilde{J}\right]_{n,0}^{\mathbf{f}}$ at time step n can be computed using the finite difference approximation, but the converged Jacobian matrix from the previous time step $\left[\tilde{J}\right]_{n-1}^{\mathbf{f}}$ is usually a very good choice. For n = 1, we can even simply use an identity matrix. Therefore, we can minimize the number of times required to solve (4.29).

4.3 Numerical Results

In this section, the proposed hybrid field-circuit solver is applied to several numerical examples to validate the algorithm and demonstrate its accuracy and applications. In the following examples, all conductors are assumed perfect and all dielectrics are assumed linear, isotropic, nondispersive, lossless and of relative permittivity $\varepsilon(\mathbf{r})$. Extensions to more general lossy, anisotropic and dispersive dielectric materials are possible [2], and the hybrid scheme described in this chapter would remain valid and efficient. The electromagnetic structure resides in free space with permittivity ε_0 and the outer boundary is truncated by the first-order ABC. The permeability of the structure and the surrounding free space is μ_0.

It is further assumed that this field's spectrum is band-limited, i.e., essentially vanishes for frequencies $f > f_{\max}$ and that the field is zero for $t \le 0$. For the numerical examples with the dc sources for the circuit subsystem, the simulation always starts with zero initial conditions assumed for both the FEM and circuit unknowns. The dc sources are then turned on gradually in order not to violate the causality and assure the accuracy. One possible way to turn on dc sources is to multiply the final dc value V_{dc} with a three-derivative smooth window function defined as

$$f_{\mathrm{d}}(t,\tau) = \begin{cases} 0 & t \le 0 \\ 10(t/t_0)^3 - 15(t/t_0)^4 + 6(t/t_0)^5 & 0 < t < t_0 \\ 1 & t \ge t_0 \end{cases} \tag{4.31}$$

where t_0 is the time delay. The transient analysis is performed until the system reaches its steady state. Another way to handle the dc bias sources is described in Section 4.4.3. As an implicit time-marching scheme is employed, the time-step size for the global system only depends on the highest frequency of the operation frequency band. For the examples with nonlinear circuit elements involved, a smaller time step may be necessary for better convergence of the nonlinear solver which uses the converged solutions of the previous time step as an initial guess for the current time step.

4.3.1 A Terminated Coaxial Cable

To validate the proposed hybrid technique, we first consider an air-filled coaxial cable terminated with a lumped circuit, which was previously studied in [34]. The cable is 1 m long with the inner and outer conductors having radii of 4 mm and 8 mm, respectively. The cable is driven by a Norton equivalent source, which can be represented by a parallel combination of a driving current source with a $5\ \Omega$ resistor. The termination at the far end is a lumped circuit that consists of a 100 pF capacitor in series with the parallel combination of a 10 nH inductor and a $5\ \Omega$ resistor.

As mentioned in Section 4.2.2, in order to stamp the values of lumped circuit elements into the FEM primary matrices using the well-known stamping technique, each of these elements needs to be properly assigned to an FEM edge. The two end surfaces of the cable are the ones used for the assignment of the lumped elements. Considering the load end first, two cascaded edges connecting the inner and outer conductors are selected. The capacitor is assigned along one of these edges. The parallel combination of the resistor and the inductor is assigned at the other edge. A PMC boundary condition is enforced along all the remaining edges on the load-end cross-section surface. Similarly, on the cross-sectional surface associated with the driving end of the coaxial cable, a PMC condition is assigned along all edges except for one that connects the two conductors, along which the $5\ \Omega$ resistor is assigned. This edge is also chosen as the excitation port at which the driving current source will be connected, and the voltage measured at this port is used to compute the input impedance of the terminated cable.

In contrast, the simulator proposed in this chapter treats the circuit elements together as a lumped circuit. Two lumped ports are defined and each of them is assigned to one FEM edge that connects the inner and outer conductors at the driver and the load end of the coaxial cable, respectively. Naturally, the circuit nodes on the outer conductor are treated as the ground nodes in the circuit analysis. Note that in this example, the nonlinear terms in (4.25)-(4.27) vanish, and hence (4.25) can be efficiently solved by a standard linear sparse solver.

Figures 4.2(a) and (b) show the time profile of the transient voltage across the driving and load ends, respectively, computed by the proposed hybrid field-circuit solver and compared to those computed by the stamping technique. The information has also been transformed to the frequency domain. Figure 4.3 illustrates the real and imaginary parts of the computed input impedance as a function of frequency. The spectrum of the voltage across the load end (normalized to the spectrum the input current source function) is also plotted in Fig. 4.4. From the above figures, it is clear that excellent agreement is achieved between the proposed hybrid field-circuit solver and the stamping technique. Figure 4.5 records the magnitude of the port voltages up to 80,000 time steps to demonstrate the numerical stability of the proposed algorithm.

4.3.2 Microwave Amplifier

Next, a more practical example of a nonlinear metal-epitaxial-semiconductor field-effect-transistor (MESFET) amplifier circuit is considered in order to further verify the accuracy and demonstrate the application of the proposed simulator. This circuit was previously analyzed by FDTD-based [48], FETD-based [55], and PWTD and AIM accelerated TDIE-based [51]-[52] hybrid field-circuit solvers. Figures 4.6(a) and (b) show the top and front views of the amplifier circuit. Microstrip lines are mounted on a finite dielectric substrate which is backed by an equally sized ground plane. The substrate is 0.7874 mm thick, of size 17.526×16.256 mm, and of relative permittivity 2.33. On the substrate resides the microwave matching network that is connected to a packaged active device (GaAs MESFET) at the center. The large-signal circuit model of the MESFET, illustrated in Fig. 4.6(c), consists of one nonlinear capacitor and one nonlinear current source, whose values are both voltage-controlled:

$$C_{\mathrm{gs}}(V_g) = \begin{cases} \dfrac{3}{\sqrt{1 - V_{\mathrm{g}}/0.7}}\,\mathrm{pF} & V_{\mathrm{g}} < 0.35\mathrm{V} \\ 3\sqrt{2}\left(0.5 + V_{\mathrm{g}}/0.7\right)\mathrm{pF} & V_{\mathrm{g}} \geq 0.35\mathrm{V} \end{cases} \tag{4.32}$$

and

$$I_{\mathrm{ds}}(V_{\mathrm{gs}}, V_{\mathrm{d}}) = (A_0 + A_1 V_{\mathrm{gs}} + A_2 V_{\mathrm{gs}}^2 + A_3 V_{\mathrm{gs}}^3)\tanh(\alpha V_{\mathrm{d}}) \tag{4.33}$$

where $A_0 = 0.5034$, $A_1 = 0.2595$, $A_2 = -0.0542$, $A_3 = -0.0305$ and $\alpha = 1.0$. The input and output ports are both terminated with lumped 50 Ω resistors in series with the dc supplied sources V_{GG} (Port 1) and V_{DD} (Port 2). The transient expressions for the dc supplied sources are $V_{\mathrm{GG}} = -0.81 f_{\mathrm{d}}(t, 1\ \mathrm{ns})$ and $V_{\mathrm{DD}} = 18.96 f_{\mathrm{d}}(t, 1\ \mathrm{ns})$ in order to provide a dc-bias condition for this amplifier with $V_{\mathrm{GS}} = -0.81\ \mathrm{V}$ and $V_{\mathrm{DS}} = 6.4\ \mathrm{V}$. To capture the coupling between the electromagnetic fields and the lumped circuits, four lumped ports are defined at Port 1 (input), Port 2 (output), device gate terminal (G-S) and device drain terminal (D-S), respectively.

To calculate the S-parameters of the microwave amplifier, a small-signal analysis is performed. Once the system reaches its steady state, a unit amplitude modulated Gaussian pulse V_S centered at 6 GHz is added on top of the dc signal as an ac excitation while the active device still operates in the linear region. The ac responses are calculated by subtracting the steady-state (dc-only) responses from the simulated transient responses and then used to compute the S-parameters. The equivalent circuit for small-signal operation is illustrated in Fig. 4.7; the method to extract the S-parameters, particularly S_{11} and S_{21}, from the ac responses is to compute the input impedance $Z_{\mathrm{in}}(f)$ at Port 1 and the ac output voltage $\tilde{V}_{\mathrm{Port\,2}}$ and use the following formulas [63]:

$$S_{11} = \frac{Z_{\mathrm{in}}(f) - R_1}{Z_{\mathrm{in}}(f) + R_1} \tag{4.34a}$$

$$S_{21} = \frac{2F\left(\tilde{V}_{\mathrm{Port\,2}}\right)}{F\left(V_S\right)} \tag{4.34b}$$

where $F(\cdot)$ denotes a Fourier transform and $Z_{\mathrm{in}}(f)$ can be computed as

$$Z_{\text{in}}(f) = \frac{F(\tilde{V}_{\text{Port 1}})}{F(\tilde{I}_{\text{Port 1}})} = \frac{F(\tilde{V}_{\text{Port 1}})}{F(\tilde{V}_{R_1} / R_1)} . \tag{4.35}$$

The time profiles of the voltages at Port 1 (input) and Port 2 (output) are shown in Fig. 4.8. The calculated S_{11} and S_{21} are shown in Fig. 4.9 and the agreement with the results computed by other numerical algorithms [48], [52], and [55] and HP ADS [38] is seen to be good.

The nonlinear phenomena of the microwave amplifier can be analyzed by a large-signal analysis. While the dc setup is the same as in the previous case, the input AC signal now contains a single-tone excitation of 6 GHz at an input power level of 5.95 dBm. The resulting transient voltage waveforms at Terminals G-S and D-S are plotted in Fig. 4.10. The power delivered to the load can be calculated from the AC voltage across the resistor loaded at Port 2 by

$$P_{\text{L}}(f) = \left(\tilde{V}_{\text{Port 2}}(f)\right)^2 / R_2 . \tag{4.36}$$

Nonlinear phenomena cause the output power to appear at the harmonic frequencies of 6 GHz, and the output power increases as the input power level increases, which is evident in Fig. 4.11, where the output power spectrum for the first, second, and third harmonic frequencies with three different input power levels (-4.02 dBm, 5.95 dBm, and 14.00 dBm) is shown. The result agrees well with the results reported in [55]. Note that the values between harmonics are actually the numerical noises from the Fourier transform which can be further lowered by using longer time responses or proper windowing techniques.

4.3.3 Shielded Amplifier

It would be interesting to know how the packaging structure affects circuit performance when the circuit is placed in a shielding structure. Obviously, such an analysis is beyond the capability of circuit simulators such as HP ADS but can be accomplished by the method described in this chapter by including the circuit as well as the shielding structure in the hybrid TDFEM analysis. In this section, the effect of shielding structures on the performance of the same MESFET amplifier described in Section 4.3.2 is analyzed. Physically, the shielding structure forms a partially filled cavity [48]. Due to the natural resonance, the energy will be inevitably coupled back to the circuit. As a nonlinear amplifier circuit, this feedback makes the stability circles drift and may result in oscillation or instability. In order to avoid oscillation, dimensions of the packaging structure are chosen such that the resonant frequency is raised far above the frequency range of interest. For this purpose, the shielding structure is a perfectly conducting box with dimensions $17.53 \times 16.26 \times 4.72$ mm, chosen carefully so that the first resonant frequency is 11.79 GHz, which is higher than 9.0 GHz, the maximum frequency of interest. This ensures stability of the amplifier circuit and avoids any possible oscillations due to the interactions between the shielding structure and the amplifier in the transient simulation.

The side and front views of the amplifier with the shielding structure are shown in Fig. 4.12. On each of the input and output sides, there is a rectangular hole with its dimensions denoted by w and h. We explore two cases of hole dimensions: 9.27×2.36 mm (Shield 1) and 5.08×1.22 mm (Shield 2). The computed S-parameters are presented in Fig. 4.13, compared with those of the previous unshielded case. It is observed that the shields with different hole sizes have quite similar effects on the S-parameters. Specifically, the frequency of the matching dip in $|S_{11}|$ remains unchanged but the value of $|S_{11}|$ is decreased by 0.89 dB, while there is a 0.69 dB increase in $|S_{21}|$ around 6.0 GHz, which agrees with the conclusion in [48].

4.4 A Flexible Time-Stepping Scheme

4.4.1 Global Time Stepping v.s. Local Time Stepping

Like many other hybrid field-circuit solvers based on implicit full-wave methods [51], [52], [54], and [55], the TDFEM-based field-circuit solver in Section 4.2 employs a system-wide global time-step size and thus samples and couples the signals of all the subsystems in a strictly synchronous manner. Such a global time-stepping scheme is a natural choice when all the subsystems in a hybrid system have a similar requirement on their time-step sizes. This, however, is not necessarily the case in many realistic applications, where signals in subsystems have quite distinct temporal variations and require different signal-sampling rates. For such applications, numerical simulations may also require the time-step sizes of subsystems to satisfy different stability conditions. For example, when nonlinear circuit devices are present, the time-step size of a circuit subsystem has to be limited to facilitate the convergence of the nonlinear solutions. As another example, when simulating transient responses to a step change in voltage and/or current excitations, numerical oscillations can unfortunately be triggered if the trapezoidal integration rule is applied to the circuit subsystem. To overcome such a problem, we not only need to switch to the backward Euler rule, but also have to further reduce the time-step size in order to maintain the level of temporal accuracy [64]. Actually, under many circumstances the global time-stepping scheme compromises the overall computational efficiency because it simply forces the coupled transient simulation to march on in time at a time step limited by the subsystem that has the strictest restriction on the time-step size. Moreover, the global time-stepping scheme eliminates the possibility of incorporating into the circuit subsystems any nonuniform time-stepping techniques that are available in modern circuit simulation to ensure the maximum efficiency within a certain accuracy threshold, simply because the FEM subsystem requires a uniform time step. Therefore, a more flexible time-stepping scheme that allows local, subsystem-wide time-step sizes is of great interest in order to alleviate the limitation of the original global time-stepping scheme and further improve the flexibility and efficiency of the current field-circuit solver.

Indeed, the idea of utilizing local time-step sizes for different subsystems and then asynchronously coupling them in time, sometimes referred as multirate simulation, has been adopted widely in many areas. In modern circuit simulation, various advanced multirate features have already been available in the FastSPICE simulators from most commercial electronic-design-automation (EDA) software vendors (e.g., [65]). In the transient analysis of power transmission lines and interconnecting systems, use of dual or multiple time steps was proposed [66] and later evolved to a more advanced latency-exploitation technique [67]. In the community of full-wave simulations, various local time-stepping schemes have also been developed but mainly for fully explicit methods such as FDTD [68], finite volume time-domain (FVTD) [69], and more recently, discontinuous Galerkin time-domain (DGTD) [70] methods. For a hybrid field-circuit analysis, an asynchronous electromagnetic-circuit simulator based on the TDIE method was developed recently [71]. A related approach in an FDTD-based hybrid electromagnetic/SPICE simulator was described briefly in [72] for modeling the on-chip switching noise generation and coupling.

This section generalizes the strict synchronous coupling mechanism between the FEM and circuit subsystems described in Section 4.2.4 and presents a flexible time-stepping scheme for the TDFEM-based hybrid field-circuit solver. The hybrid global system consists of an FEM subsystem and several independent circuit subsystems that are connected only to the FEM subsystem. Instead of assigning a single time-step size for every subsystem, the proposed scheme adopts local, subsystem-wide time-step sizes for different subsystems and thus allows them to be updated and tracked at different sampling rates. Subsystems can then be identified as fast (with a smaller time-step size) or slow (with a larger time-step size). After the time-marching process starts, at certain time points when only fast subsystems need to be updated (referred as asynchronous time points), signals coupling from slow to fast subsystems are extrapolated based on their most recently available values. At other time points when all the subsystems are synchronized (referred as synchronous time points), subsystems are solved together in a global fashion similar to that in the original global time-stepping scheme. Because of the flexibility of allowing subsystems of different sampling rates to be coupled in time, the proposed time-stepping scheme could significantly improve the computational efficiency of the existing TDFEM-based hybrid field-circuit solver, especially when the computational cost associated with the slow subsystems is much larger than that associated with the fast subsystems. The efficiency of the hybrid field-circuit simulation with the proposed scheme could be further enhanced when the TCS technique is applied to the TDFEM part to reduce the iteration count per time step for a preconditioned iterative solution when the time-step size for the FEM subsystem becomes relatively large. Moreover, the proposed scheme paves the way for future development to incorporate into the circuit subsystems a variable or nonuniform time-stepping technique that is even more flexible.

4.4.2 A Generalized Coupling Scheme

For the FEM subsystem, the time axis is discretized uniformly into discrete time points with a subsystem-wide time-step size denoted as Δt^{FEM}. This leads to the following time-marching system for the FEM unknown vector $\{e\}_{m\Delta t^{\mathrm{FEM}}}$ at time $m\Delta t^{\mathrm{FEM}}$:

$$\begin{aligned}\left[E_0(\Delta t^{\mathrm{FEM}})\right]\{e\}_{m\Delta t^{\mathrm{FEM}}} &= \left[E_1(\Delta t^{\mathrm{FEM}})\right]\{e\}_{(m-1)\Delta t^{\mathrm{FEM}}} + \left[E_2(\Delta t^{\mathrm{FEM}})\right]\{e\}_{(m-2)\Delta t^{\mathrm{FEM}}} \\ &\quad + c_0(\Delta t^{\mathrm{FEM}})^2 Z_0\left[\partial\{b^{\mathrm{CKT}}\}/\partial t\right]_{(m-1)\Delta t^{\mathrm{FEM}}}\end{aligned} \tag{4.37}$$

where $m = 1, 2, \cdots$, is the time index for the FEM subsystem. Matrices $[E_0(\Delta t^{\mathrm{FEM}})]$, $[E_1(\Delta t^{\mathrm{FEM}})]$, and $[E_2(\Delta t^{\mathrm{FEM}})]$ are all functions of Δt^{FEM} as defined in (4.5)-(4.7), respectively.

For the lumped circuits, the time-step size is denoted as Δt^{CKT} in deriving the companion models for circuit elements [61], which yields the following circuit subsystem for the circuit unknown vector $\{V^{\mathrm{CKT}}_{n\Delta t^{\mathrm{CKT}}}\}$ at time $n\Delta t^{\mathrm{CKT}}$:

$$\left[Y(\Delta t^{\mathrm{CKT}})\right]\{V^{\mathrm{CKT}}_{n\Delta t^{\mathrm{CKT}}}\} + \mathbf{I}^{\mathrm{CKT,nl}}_{n\Delta t^{\mathrm{CKT}}}\left(\{V^{\mathrm{CKT}}_{n\Delta t^{\mathrm{CKT}}}\}\right) = \mathbf{I}^{\mathrm{CKT}}_{n\Delta t^{\mathrm{CKT}}} \tag{4.38}$$

where $n = 1, 2, \cdots$, is the time index for the circuit subsystem. The admittance matrix $\left[Y(\Delta t^{\mathrm{CKT}})\right]$ is a function of Δt^{CKT}.

Note that generally there can be more than one circuit subsystem in a global field-circuit system as long as they are independent to each other and connected only to the FEM subsystem through different lumped ports. They can possibly have all different time-step sizes, denoted as Δt^{CKT1}, $\Delta t^{\mathrm{CKT2}}, \cdots$, etc. For simplicity, in the remainder of this section, it is assumed that there is only one circuit subsystem connected to the FEM subsystem, while generalization to the case of multiple circuit subsystems is straightforward. Since the two (FEM and circuit) subsystems are marching on in time with possibly different time-step sizes, such a coupled system is sometimes referred as a dual-speed system [73].

Next, we describe the coupling schemes of the FEM and circuit subsystems that are represented by (4.37) and (4.38), respectively, at asynchronous and synchronous time points.

For a dual-speed system, at an asynchronous time point, we only update the fast subsystem. As illustrated in Fig. 4.14, if we assume that the circuit subsystem is the fast subsystem and $\Delta t^{\mathrm{FEM}} = K\Delta t^{\mathrm{CKT}}$, then for some *n*, at time $t = n\Delta t^{\mathrm{CKT}}$, only the circuit subsystem needs to be updated, and for this purpose, the signals coupling from the FEM to the circuit subsystem need to be taken into consideration. The FEM-to-circuit coupling is modeled by introducing external supplied voltage sources into the circuit subsystem at these lumped ports, whose values, denoted as $\{V_{n\Delta t^{\mathrm{CKT}}}^{\mathrm{FEM}\to\mathrm{CKT}}\}$, should be solely determined by the FEM unknowns associated with the edges where the lumped ports reside. Therefore, (4.38) is expanded and becomes

$$\begin{bmatrix} \left[Y(\Delta t^{\mathrm{CKT}})\right] & [B] \\ [B]^T & \mathbf{0} \end{bmatrix} \begin{Bmatrix} \{V_{n\Delta t^{\mathrm{CKT}}}^{\mathrm{CKT}}\} \\ \{I_{n\Delta t^{\mathrm{CKT}}}^{\mathrm{CP}}\} \end{Bmatrix} + \begin{Bmatrix} \mathbf{I}_{n\Delta t^{\mathrm{CKT}}}^{\mathrm{CKT,nl}}\left(\{V_{n\Delta t^{\mathrm{CKT}}}^{\mathrm{CKT}}\}\right) \\ \mathbf{0} \end{Bmatrix} = \begin{Bmatrix} \mathbf{I}_{n\Delta t^{\mathrm{CKT}}}^{\mathrm{CKT}} \\ \{V_{n\Delta t^{\mathrm{CKT}}}^{\mathrm{FEM}\to\mathrm{CKT}}\} \end{Bmatrix}. \tag{4.39}$$

Here, $\{I_{n\Delta t^{\mathrm{CKT}}}^{\mathrm{CP}}\}$ denotes currents in these external voltage sources, and Boolean matrix $[B]$ selects the circuit nodes connected to the external voltage sources. Assuming that this asynchronous time point, $t = n\Delta t^{\mathrm{CKT}}$, is between $(m-1)\Delta t^{\mathrm{FEM}}$ and $m\Delta t^{\mathrm{FEM}}$, then obviously, $\{V_{n\Delta t^{\mathrm{CKT}}}^{\mathrm{FEM}\to\mathrm{CKT}}\}$ cannot be obtained directly from any available FEM solutions, and some kind of extrapolation formula must be applied in order to conduct slow-to-fast conversion. For such an extrapolation-based conversion, there is usually an accuracy-stability tradeoff in the choice of the order of extrapolation. It has been studied that although overall simulation accuracy can be improved by using higher-order extrapolation formulas, this can also result in numerical instability [73]. In this work the quadratic extrapolation formula is adopted for the optimal balance between accuracy and stability. As a result, $\{V_{n\Delta t^{\mathrm{CKT}}}^{\mathrm{FEM}\to\mathrm{CKT}}\}$ can be extrapolated from the three most recent FEM solutions, i.e., $\{e\}_{(m-1)\Delta t^{\mathrm{FEM}}}$, $\{e\}_{(m-2)\Delta t^{\mathrm{FEM}}}$, and $\{e\}_{(m-3)\Delta t^{\mathrm{FEM}}}$. In the other case when the FEM subsystem is the fast subsystem and needs to be updated at asynchronous time points, the coupling from the circuit subsystems represented as $\left[\partial\{b^{\mathrm{CKT}}\}/\partial t\right]$ in (4.37) can be extrapolated in a similar fashion.

At a synchronous time point, the FEM and circuit subsystems with different time-step sizes are synchronized and thus updated together in a global fashion. Assuming such a synchronous time is $t = n\Delta t^{\mathrm{CKT}} = m\Delta t^{\mathrm{FEM}}$, then the FEM-to-circuit coupling, $\{V_{n\Delta t^{\mathrm{CKT}}}^{\mathrm{FEM}\to\mathrm{CKT}}\}$, can be computed directly as

$$\{V_{n\Delta t^{\mathrm{CKT}}}^{\mathrm{FEM}\to\mathrm{CKT}}\} = \{V_{m\Delta t^{\mathrm{FEM}}}^{\mathrm{FEM}\to\mathrm{CKT}}\} = -[C]\{e\}_{m\Delta t^{\mathrm{FEM}}} \tag{4.40}$$

where matrix $[C]$ is formulated to compute the values of the external voltage sources from the FEM solutions. On the other hand, the circuit-to-FEM coupling, represented as $\left[\partial\{b^{\mathrm{CKT}}\}/\partial t\right]_{(m-1)\Delta t^{\mathrm{FEM}}}$ in (4.37), is derived by introducing impressed current sources at the FEM edges that reside at the lumped ports of the circuit. If a central-difference formula is used, it can be approximated as

$$\left[\frac{\partial\{b^{\mathrm{CKT}}\}}{\partial t}\right]_{(m-1)\Delta t^{\mathrm{FEM}}} = -\left[C\right]^{\mathrm{T}}\left[\frac{\partial\{I^{\mathrm{CP}}\}}{\partial t}\right]_{(m-1)\Delta t^{\mathrm{FEM}}} \approx -\left[C\right]^{\mathrm{T}}\left[\frac{\{I_{n\Delta t^{\mathrm{CKT}}}^{\mathrm{CP}}\} - \{I_{(n-2K)\Delta t^{\mathrm{CKT}}}^{\mathrm{CP}}\}}{2K\Delta t^{\mathrm{CKT}}}\right]. \tag{4.41}$$

Substituting (4.41) into (4.37) and combining with (4.39) yields the coupled global system at a synchronized time t

$$\mathbf{F}_t(\mathbf{x}_t) = \mathbf{b}_t \tag{4.42}$$

where $\mathbf{x}_t = \left\{\{e\}_{m\Delta t^{\mathrm{FEM}}} \quad \{V_{n\Delta t^{\mathrm{CKT}}}^{\mathrm{CKT}}\} \quad \{I_{n\Delta t^{\mathrm{CKT}}}^{\mathrm{CP}}\}\right\}^{\mathrm{T}}$ and

$$\mathbf{F}_t(\mathbf{x}_t) = \begin{bmatrix} \left[E_0(\Delta t^{\mathrm{FEM}})\right] & \mathbf{0} & \varsigma[C]^{\mathrm{T}} \\ \mathbf{0} & \varsigma\left[Y(\Delta t^{\mathrm{CKT}})\right] & \varsigma[B] \\ \varsigma\left[C\right] & \varsigma[B]^{\mathrm{T}} & \mathbf{0} \end{bmatrix} \begin{Bmatrix} \{e\}_{m\Delta t^{\mathrm{FEM}}} \\ \{V_{n\Delta t^{\mathrm{CKT}}}^{\mathrm{CKT}}\} \\ \{I_{n\Delta t^{\mathrm{CKT}}}^{\mathrm{CP}}\} \end{Bmatrix} + \begin{Bmatrix} \mathbf{0} \\ \varsigma\mathbf{I}_{n\Delta t^{\mathrm{CKT}}}^{\mathrm{CKT,nl}}\left(\{V_{n\Delta t^{\mathrm{CKT}}}^{\mathrm{CKT}}\}\right) \\ \mathbf{0} \end{Bmatrix} \tag{4.43}$$

$$
\begin{aligned}
\mathbf{b}_t = \left\{ \begin{matrix} \mathbf{0} \\ \varsigma \mathbf{I}^{\text{CKT}}_{n\Delta t^{\text{CKT}}} \\ \mathbf{0} \end{matrix} \right\} + \left\{ \begin{matrix} \left[E_1(\Delta t^{\text{FEM}}) \right] \{e\}_{(m-1)\Delta t^{\text{FEM}}} + \left[E_2(\Delta t^{\text{FEM}}) \right] \{e\}_{(m-2)\Delta t^{\text{FEM}}} \\ \mathbf{0} \\ \mathbf{0} \end{matrix} \right\} \\
+ \left\{ \begin{matrix} \varsigma [C]^{\text{T}} \{ I^{\text{CP}}_{(n-2K)\Delta t^{\text{CKT}}} \} \\ \mathbf{0} \\ \mathbf{0} \end{matrix} \right\}.
\end{aligned}
\tag{4.44}
$$

The coupling scheme described above is illustrated in Fig. 4.14. Because the slow subsystem is now updated less frequently than in a strict global time-stepping scheme, the proposed scheme could significantly improve the overall computational efficiency of the dual-speed system, especially when the computational cost associated with the slow subsystem is much larger than that associated with the fast subsystem. Also, note that, as a special case when $\Delta t^{\text{FEM}} = \Delta t^{\text{CKT}} = \Delta t$, (4.42)-(4.44) reduce to the global system (4.25)-(4.27) with the original global time-stepping scheme.

4.4.3 Validations and Applications

The TDFEM-based hybrid field-circuit solver with the proposed time-stepping scheme is applied to several numerical examples to verify the algorithm and demonstrate its performance and applications. In the hybrid field-circuit systems of the following examples, the FEM subsystem is dominant in size. For the numerical example containing nonlinear circuit devices, there are generally two approaches to handling the dc bias sources [9]. A straightforward approach adopted in Section 4.3 is that with zero initial conditions assumed for both the FEM and circuit unknowns, the dc sources are turned on smoothly, and only after the entire system reaches its bias state is the transient analysis performed. The other approach, which is believed to be more efficient, is to localize the dc signal to the specific circuit subsystem only. A dc component is added to the signal coupling from the FEM subsystem to the circuit subsystem. The same dc component is subtracted from signals coupling back from the circuit subsystem to the FEM subsystem. This approach is adopted in this section.

We first revisit the example of the terminated coaxial cable that was previously studied in Section 4.3.1. The hybrid field-circuit system in Fig. 4.15 consists of an air-filled coaxial transmission line driven and terminated by lumped circuits. The time-step size of the FEM subsystem is denoted as Δt^{FEM}. The driving circuit at one end is labeled as circuit subsystem 1 ("Circuit 1" in Fig. 4.15) whose time-step size is denoted as Δt^{CKT1}. The termination at the other end is called circuit subsystem 2 ("Circuit 2" in Fig. 4.15) whose time-step size is denoted as Δt^{CKT2}. Table 4.1 records three test cases with different choices of time-step sizes for subsystems. Note that the first two cases (denoted as 1:1 and 2:2) actually correspond to the original global time-stepping scheme, while the 2:1 case corresponds to the proposed local time-stepping scheme in this work. Since the 1:1 case uses the smallest global time-step size, it can be used as a reference. Figure 4.16 compares the time profiles of the transient voltages at the load end for the three test cases. Good agreement is achieved. A further examination reveals that the 2:1 case has better accuracy than the 2:2 case, although they have almost the same computational cost due to the same value of Δt^{FEM} and the fact that the FEM subsystem is dominant in the hybrid system. The real and imaginary parts of the input impedance of the 1:1 and 2:1 cases are plotted in Fig. 4.17. It is clear that excellent agreement is achieved between the two results. Figure 4.18 records, for the 2:1 case, the magnitude of the voltages at the driving and load ends up to 1800 ns to demonstrate the numerical stability of the proposed algorithm.

Next, a three-port microstrip power divider is considered. A similar structure has been simulated by a full-wave-based circuit simulation method in a signal integrity analysis of high-speed interconnects [74]. The dimension and components of the system are shown in Fig. 4.19. The circuit is excited by a symmetric pulse excitation V_{in} (dashed line in Fig. 4.20) of 0.1 ns rise/fall time and a width of 0.5 ns. In order to conquer the problem of numerical oscillations triggered by the rapid change in the voltage excitation, the backward Euler rule is adopted to form circuit companion models, and Δt^{CKT} is further reduced in order to maintain the level of temporal accuracy. With the proposed time-stepping scheme, these numerical considerations do not affect the choice of the time-step size for the FEM subsystem. Figure 4.20 illustrates that Δt^{FEM} can be four times larger than that with the global time-stepping scheme, which reduces the computational cost to 1/4.

The last example is a chip-to-package interconnecting structure which was previously studied in [47] and later replicated in [71]. The hybrid field-circuit system again consists of one FEM subsystem and two circuit subsystems, and their connections are illustrated in Fig. 4.21(a). The FEM subsystem is formed by the TDFEM modeling of a microstrip of width 168 μm and length 2.016 mm on a 144 μm thick alumina substrate and of the characteristic impedance of 49 Ω as shown in Fig. 4.21(c). The FEM subsystem is connected to circuit subsystem 1 shown in Fig. 4.21(b) as its driver through lumped port 1 and to circuit subsystem 2 (not shown in Fig. 4.21) as its load through lumped port 2. Circuit subsystem 1 consists of a biased bipolar-junction-transistor (BJT) with a bias voltage source $V_{\mathrm{DC}} = 5\ \mathrm{V}$ and a bias resistor $R = 49$ Ω as well as a lumped bond-wire model with an effective inductance $L = 0.7$ nH and effective capacitance $C = 16.1$ fF. Circuit subsystem 2 is a shunt 49 Ω resistor matched to the microstrip line. In series with a source resistor $R_S = 500$ Ω, the signal voltage source V_S is a symmetric trapezoidal "fast pulse" [47] with rise and fall times of 12 ps, width of 62 ps, and voltage of 5 V. Tables 4.2 and 4.3 illustrate various test cases with different choices of time-step sizes for subsystems ($\Delta t^{\mathrm{CKT2}} = \Delta t^{\mathrm{FEM}}$ for all cases). Again, results from the simulation with the global time-stepping scheme with the smallest global time-step size (the 1:1 case) are used as a reference.

With respect to the accuracy of the simulation, Figs. 4.22(a) and 4.22(b) illustrate the simulated transient voltages at port 1 and port 2 over a time interval of 250 ps. It is shown that the results from the simulation of the proposed time-stepping scheme are practically the same as those from the reference case, and are in a reasonable agreement with those from the SPICE-only and hybrid FDTD/SPICE simulations [47]. The reference solution is also used to compute the norm-2 temporal errors of the transient voltages at port 1 for various test cases, and the results are recorded in Table 4.2. It is shown that the accuracy of a local time-stepping scheme with a smaller Δt^{CKT1} is always better than that of a global time-stepping scheme with the same Δt^{FEM} and Δt^{CKT1}, mainly because the local time-stepping schemes adopt the higher sampling rates in circuit subsystem 1.

With respect to the efficiency of the hybrid field-circuit simulation, the computational cost is related to the average Newton steps for a nonlinear solution to converge. Table 4.3 records the average Newton steps per time step for various test cases. Under the global time-stepping scheme, it is obvious that the average number of Newton steps increases as the global time-step size increases. However, for cases with the local time-stepping scheme, the number of Newton steps almost remains constant as Δt^{FEM} increases since Δt^{CKT1} is fixed, which makes these simulations more efficient. Note that a similar conclusion was also reached in [71]. The total computational cost is also related to the average iteration steps to solve a linearized problem at each Newton step at the synchronous time point. Such a linearized problem involves the FEM subsystem and thus the average iteration counts increase significantly as Δt^{FEM} increases, which makes using a larger Δt^{FEM} not very useful. The problem will be revisited in Chapter 6.

4.5 Summary

A hybrid field-circuit simulator that hybridizes the TDFEM algorithm and a circuit solver based on the modified nodal analysis is presented to perform the mixed full-wave and circuit simulation for electromagnetic devices that include both distributive portion and lumped circuits. In the proposed methodology, the distributive and passive portion of a device is modeled by the TDFEM, while the modified nodal analysis is used to construct and evaluate the circuit equations in a manner consistent with the TDFEM framework. The fully discretized FEM and circuit subsystems are coupled together and mutual-coupling matrices are introduced to capture their interactions. The resulting global system for both the FEM and circuit unknowns is solved simultaneously. An efficient and easy-to-implement solution algorithm has been developed in order to solve this global system which is typically a mixture of linear and nonlinear equations. In addition to the strict synchronous coupling mechanism, this chapter also presents a flexible time-stepping scheme which provides the flexibility to employ local, subsystem-wide time-step sizes for the FEM and circuit subsystems in order to alleviate the limitation of a strict global time-stepping scheme. It has been shown that such a flexible time-stepping scheme improves the computational efficiency of the existing TDFEM-based hybrid field-circuit solver, especially when the computational cost associated with the slow subsystems is higher than that associated with the fast subsystems.

The proposed hybrid field-circuit simulator provides a powerful and accurate CAD tool for the design of modern high-frequency devices that exhibit significant disparity in the electrical size of their geometrical features. While preserving the accuracy of the broadband characterization provided by the TDFEM, this simulator extends its capability so that lumped circuits can be handled efficiently.

4.6 Figures and Tables

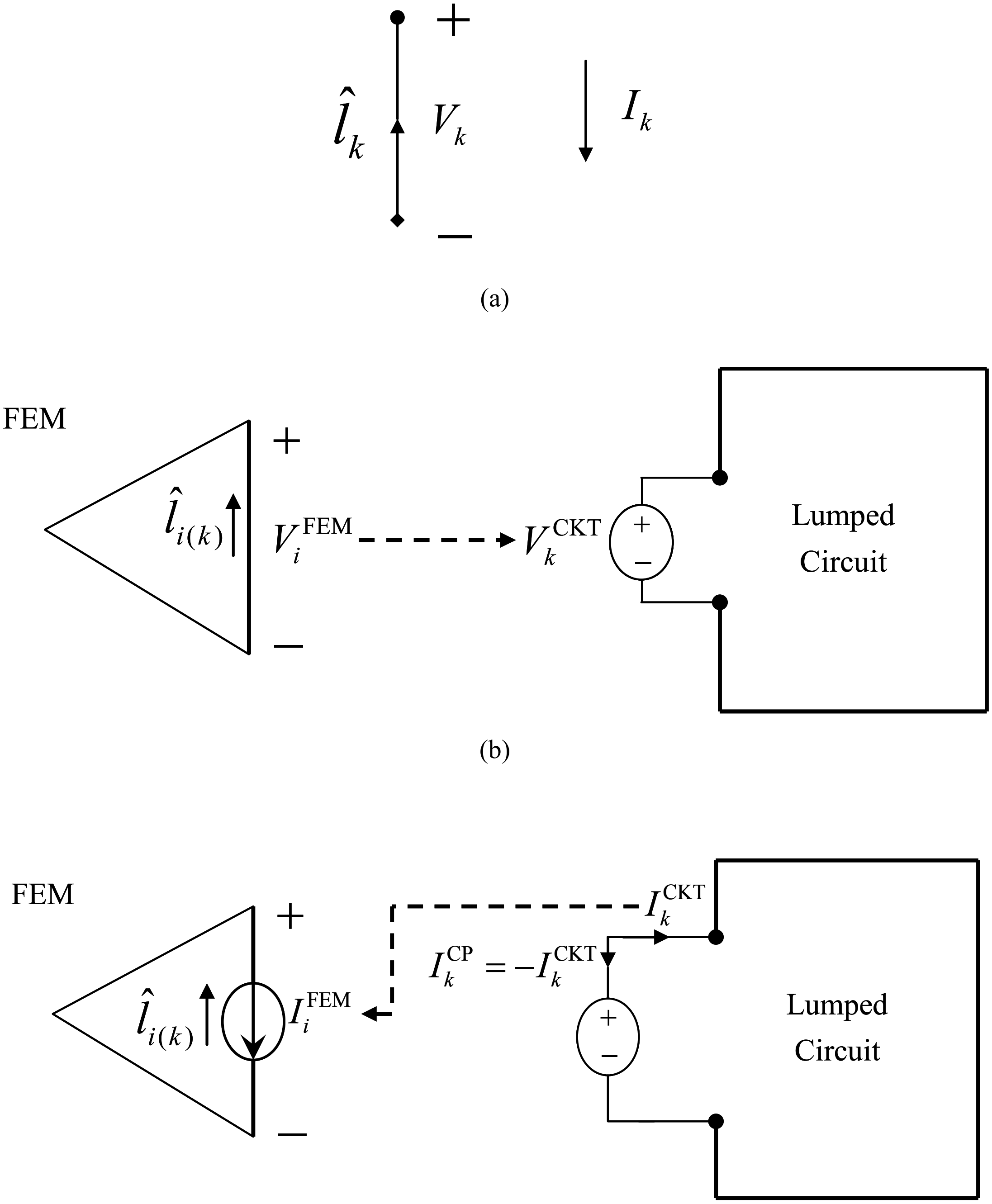
+
$\hat{l}_k$
V_k
I_k
−
FEM
+
$\hat{l}_{i(k)}$
V_i^{FEM}
V_k^{CKT}
+
−
Lumped Circuit
−
FEM
+
I_k^{CKT}
$I_k^{\text{CP}} = -I_k^{\text{CKT}}$
$\hat{l}_{i(k)}$
I_i^{FEM}
+
−
Lumped Circuit
−

(a)

(b)

(c)

Figure 4.1: Coupling between the FEM and circuit subsystems. (a) Definitions of lumped port voltages and currents. (b) FEM-to-circuit coupling. (c) Circuit-to-FEM coupling.

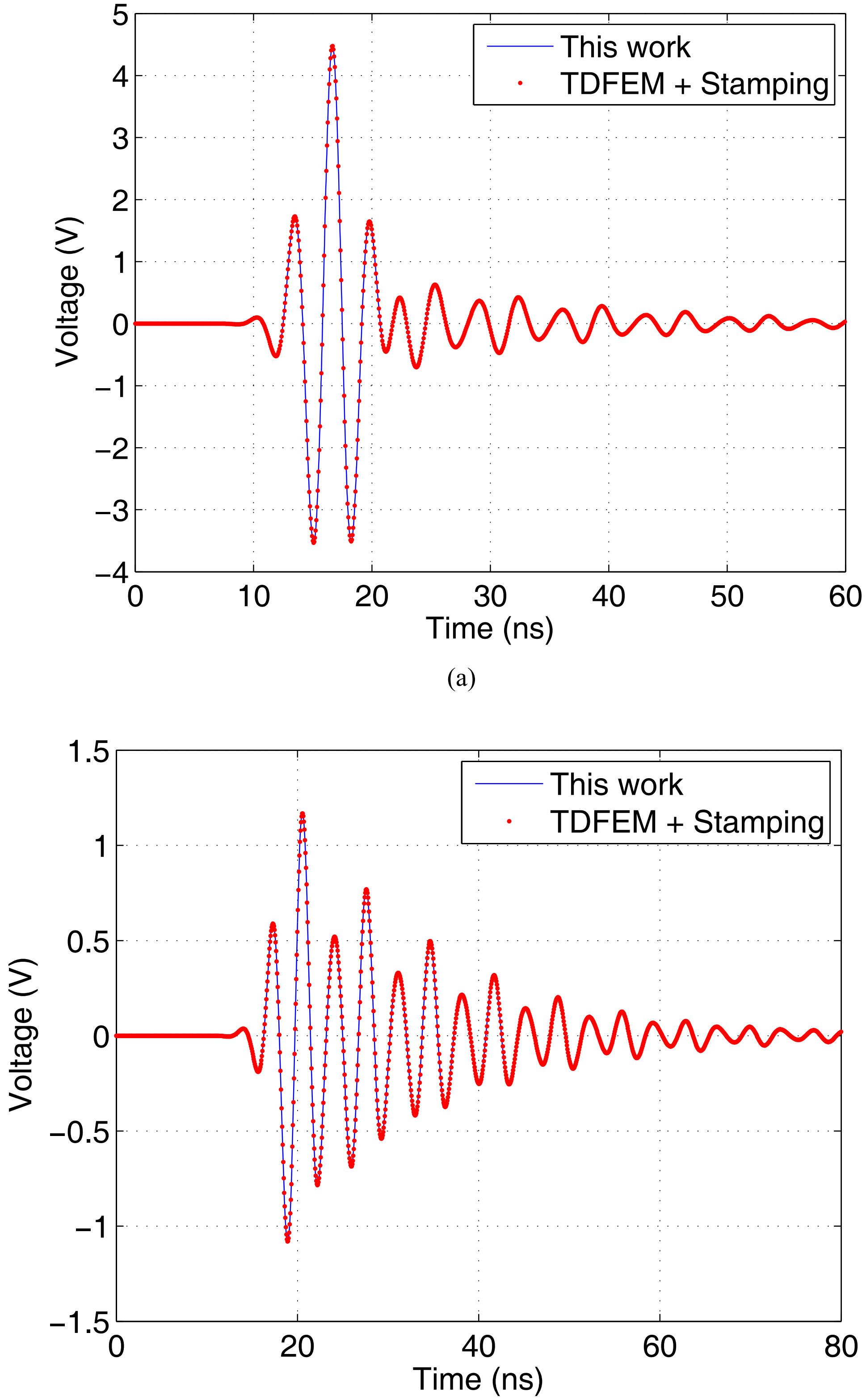

(a)

(6)

Figure 4.2: Transient voltages across (a) the driving end and (b) the load end.

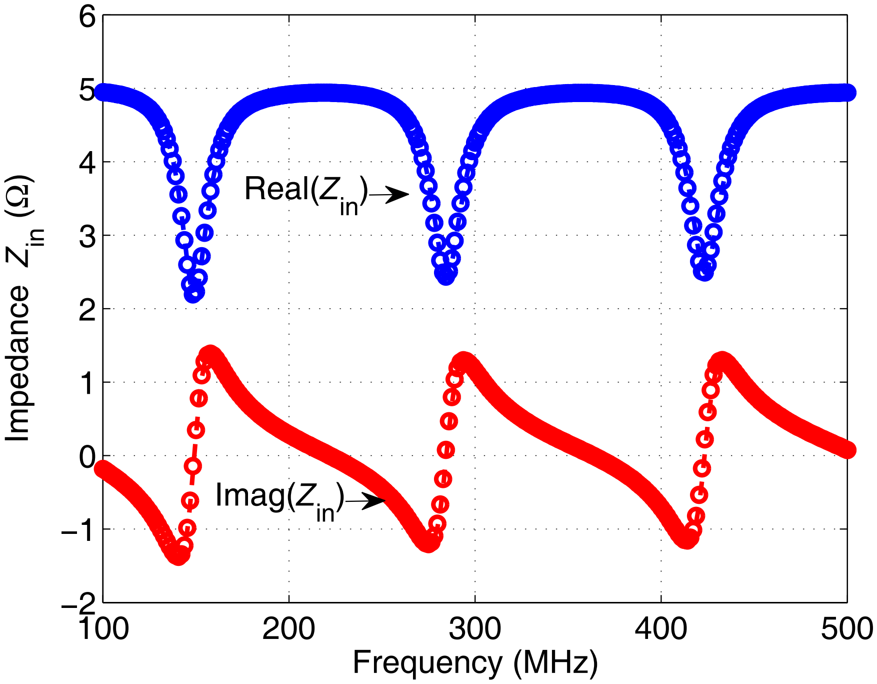

Figure 4.3: Input impedance of a terminated coaxial cable. Circle: This work. Dashed line: The stamping technique.

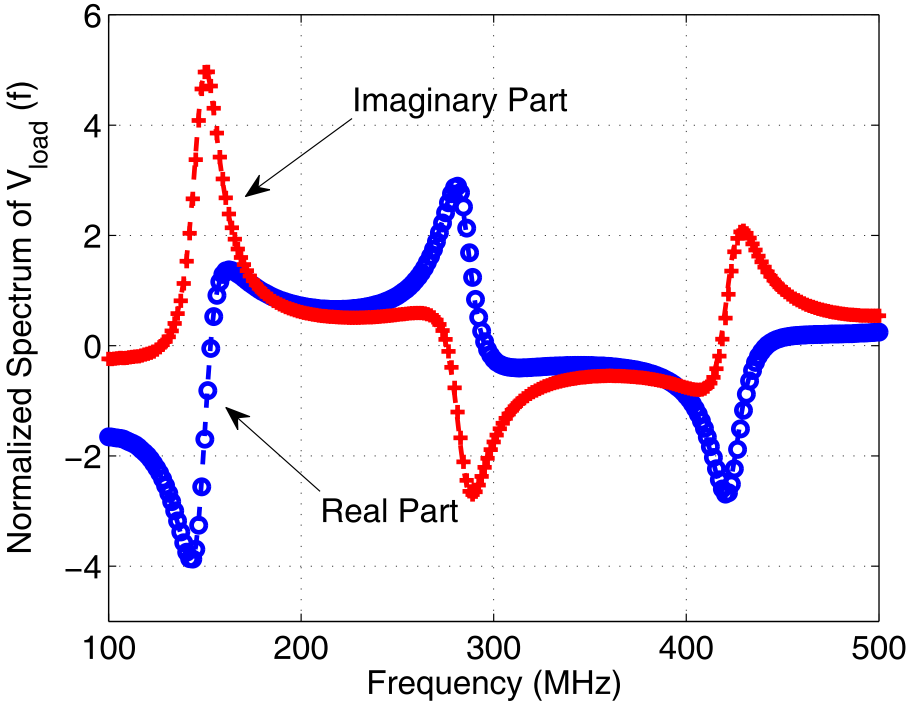

Figure 4.4: Normalized spectrum of voltages at the load end. Symbols: this work. Dashed line: the stamping technique.

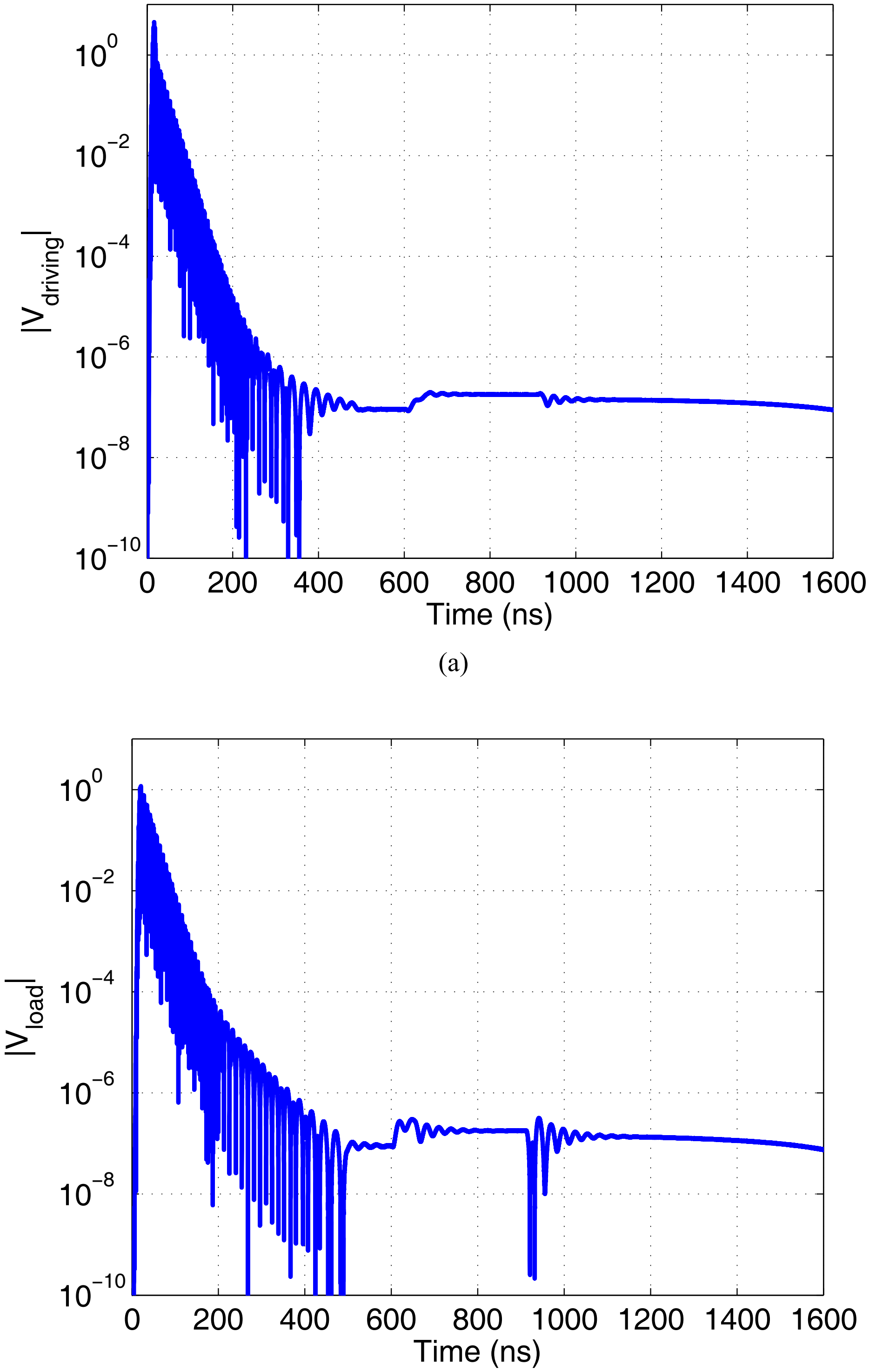

(a)

(b)

Figure 4.5: Magnitude of transient voltages at (a) the driving end and (b) the load end up to 80,000 steps $(\Delta t = 20 \text{ ps})$.

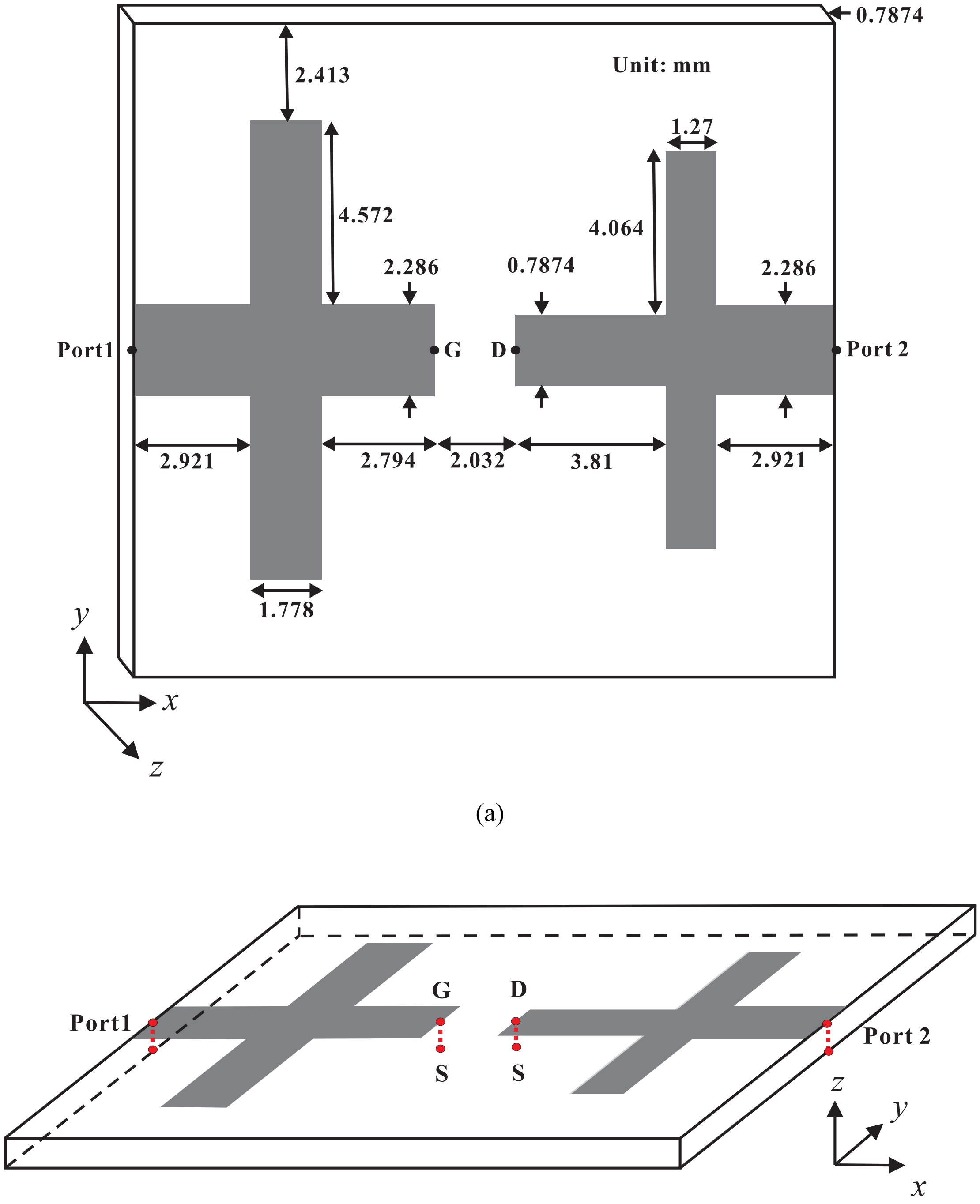
0.7874
Unit: mm
2.413
4.572
1.27
4.064
2.286
0.7874
2.286
Port1
G
D
Port 2
2.921
2.794
2.032
3.81
2.921
1.778
y
x
z
G
D
Port1
S
S
Port 2
z
y
x

(a)

(b)

Figure 4.6: MESFET microwave amplifier. (a) Top view. (b) Front view. (c) Large-signal circuit model for the MESFET.

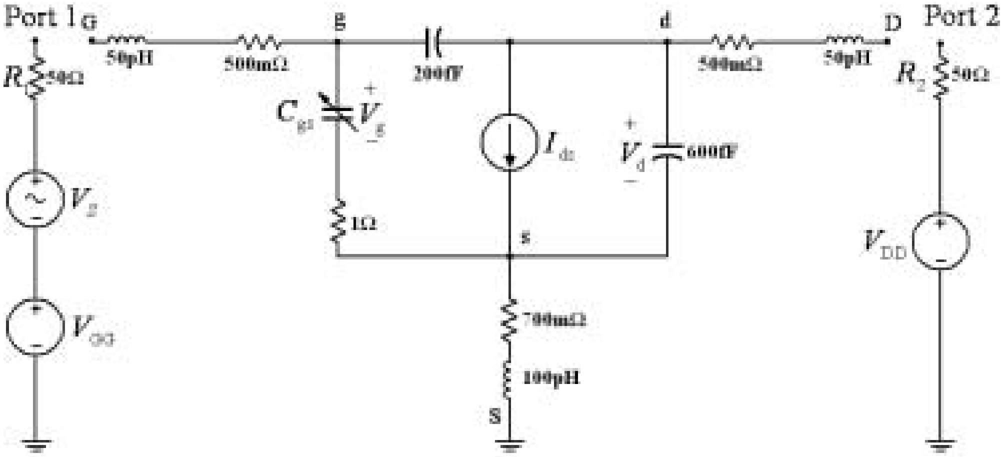
Port 1
G
50pH
500mΩ
g
200fF
d
500mΩ
50pH
D
Port 2
R_1
50Ω
C_{gs}
V_g
I_{ds}
V_d
600fF
R_2
50Ω
V_s
1Ω
s
V_{DD}
V_{GG}
700mΩ
100pH
S

(c)

Figure 4.6: Continued.

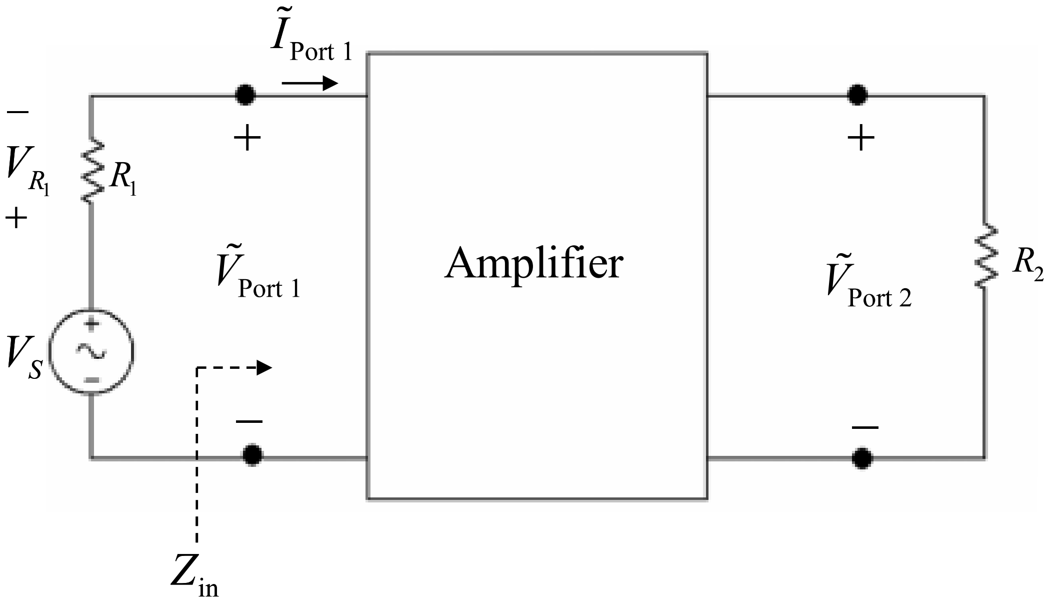
$\tilde{I}_{\text{Port 1}}$
−
V_{R_1}
+
R_1
+
$\tilde{V}_{\text{Port 1}}$
−
Amplifier
+
$\tilde{V}_{\text{Port 2}}$
−
R_2
V_S
Z_{in}

Figure 4.7: AC equivalent network for S-parameter extraction.

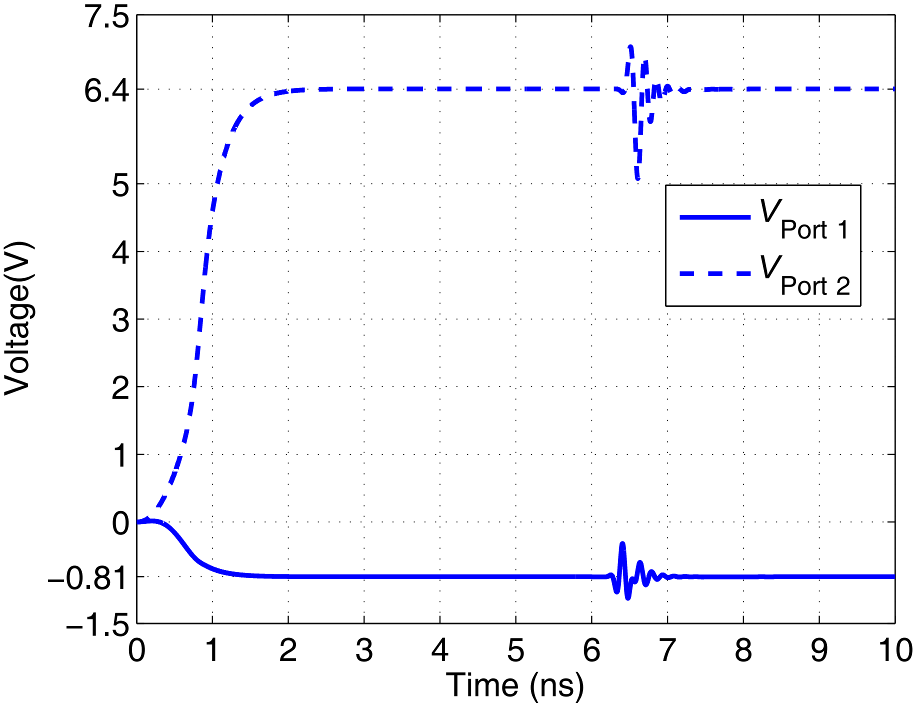

Figure 4.8: Time profiles of the voltages at Port 1(input) and Port 2 (output).

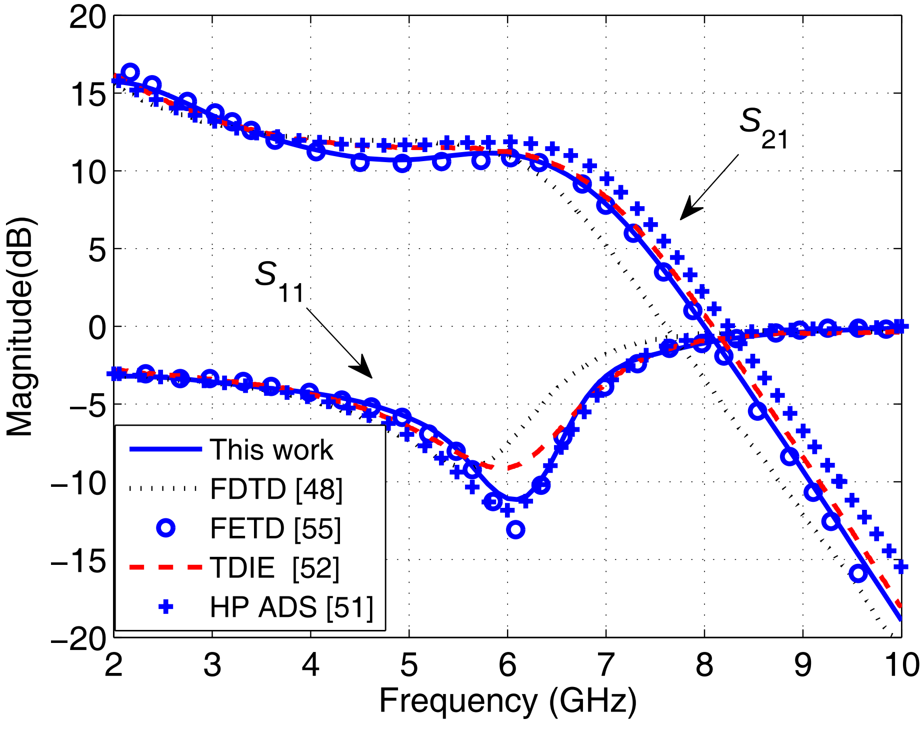

Figure 4.9: Magnitudes of S_{11} and S_{21} of the MESFET microwave amplifier.

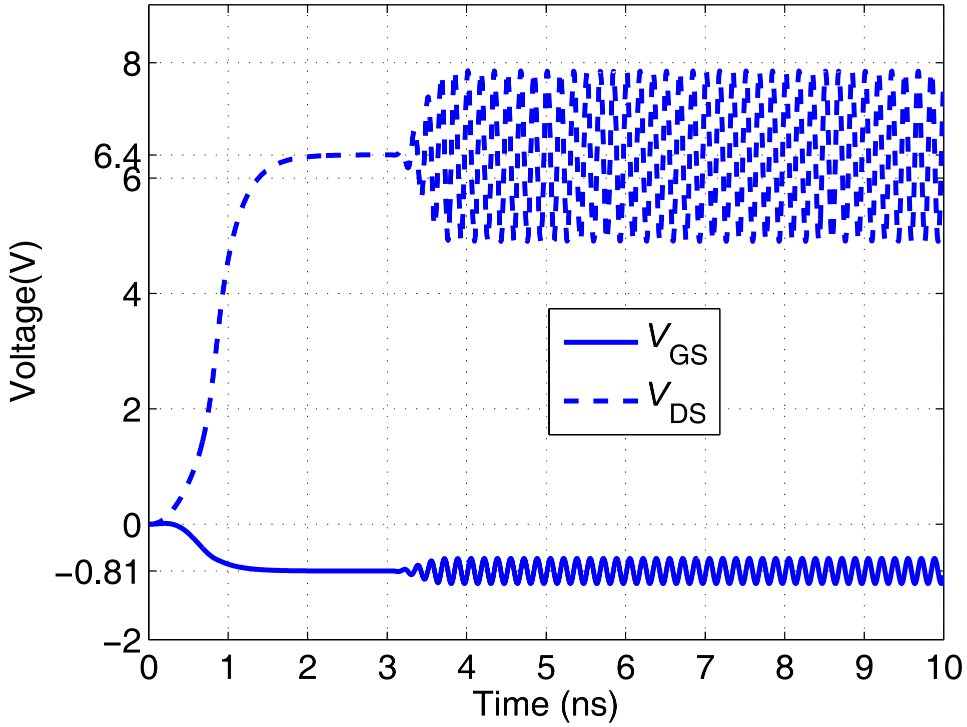

Figure 4.10: Transient voltages at the input and output terminals of the MESFET.

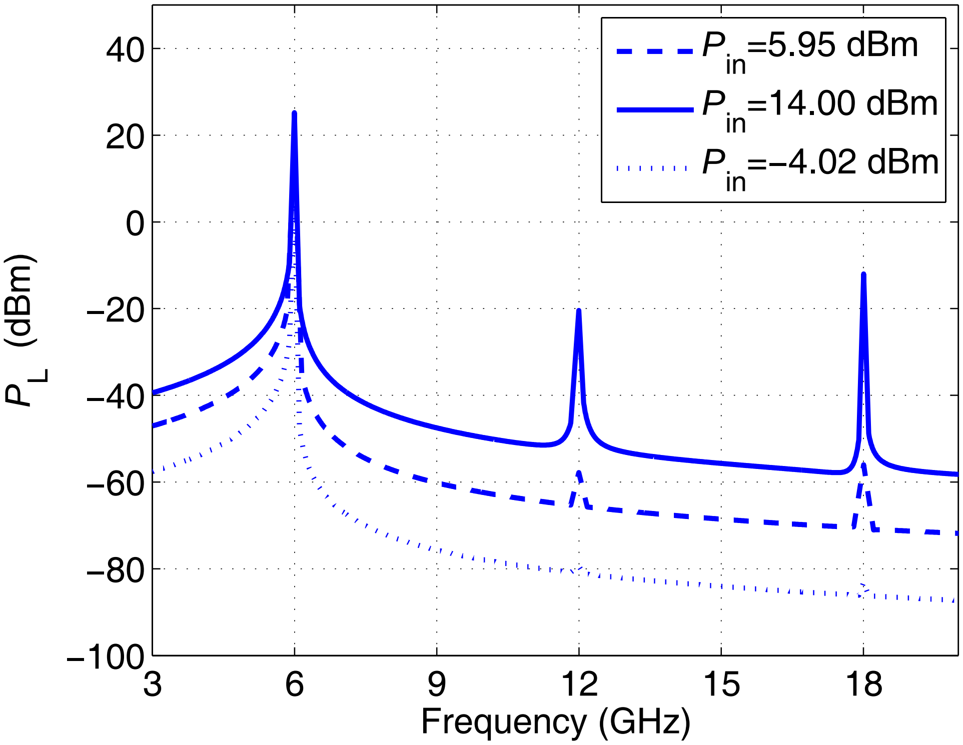

Figure 4.11: Power delivered to the load resistor using a single-tone 6 GHz excitation.

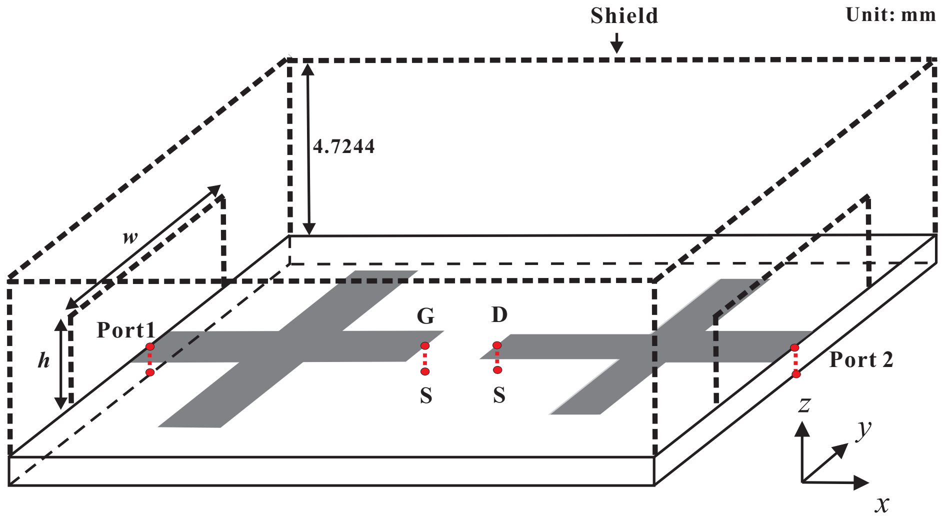
Shield
Unit: mm
4.7244
w
h
Port1
G
D
S
S
Port 2
z
y
x

Figure 4.12: Shielded MESFET microwave amplifier.

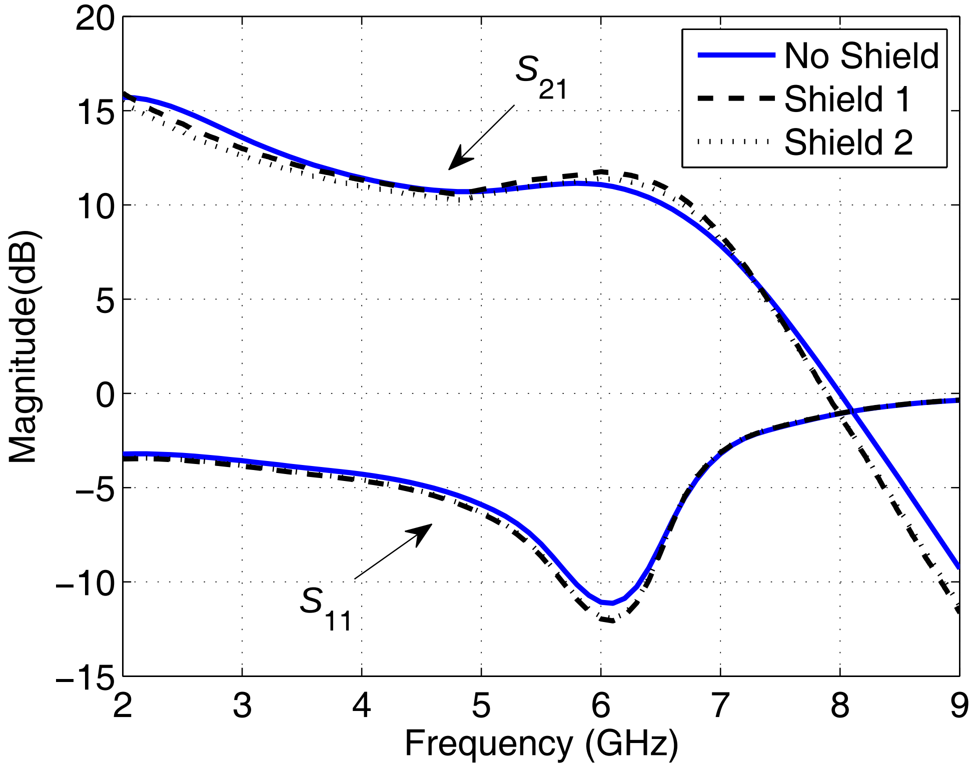

Figure 4.13: Magnitudes of S_{11} and S_{21} of the MESFET amplifier without and with shielding structures. (Shield 1: w = 9.27 mm, h = 2.36 mm. Shield 2: w = 5.08 mm, h = 1.22 mm.)

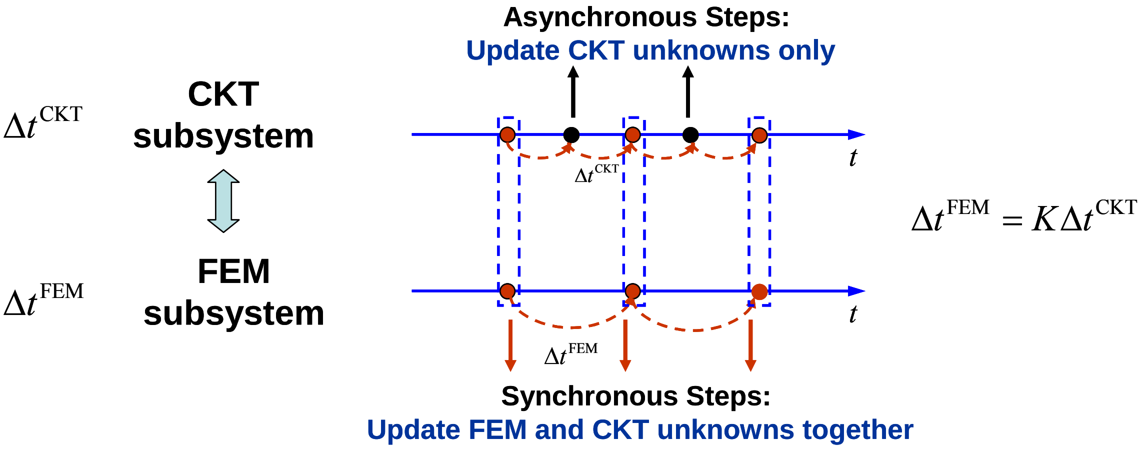
Asynchronous Steps:
Update CKT unknowns only
Δt^{CKT}
CKT subsystem
Δt^{FEM}
FEM subsystem
Δt^{CKT}
t
$\Delta t^{\mathrm{FEM}} = K\Delta t^{\mathrm{CKT}}$
Δt^{FEM}
t
Synchronous Steps:
Update FEM and CKT unknowns together

Figure 4.14: A dual-speed system at the asynchronous and synchronous steps.

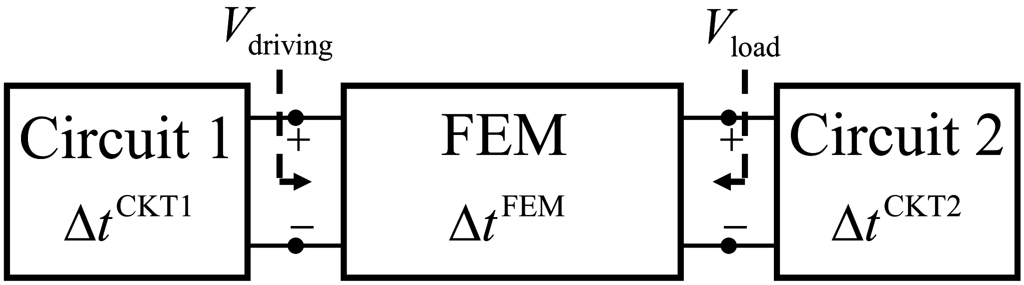
V_{driving}
V_{load}
Circuit 1
Δt^{CKT1}
+
−
FEM
Δt^{FEM}
+
−
Circuit 2
Δt^{CKT2}

Figure 4.15: Connection of the FEM and circuit subsystems in the hybrid field-circuit system.

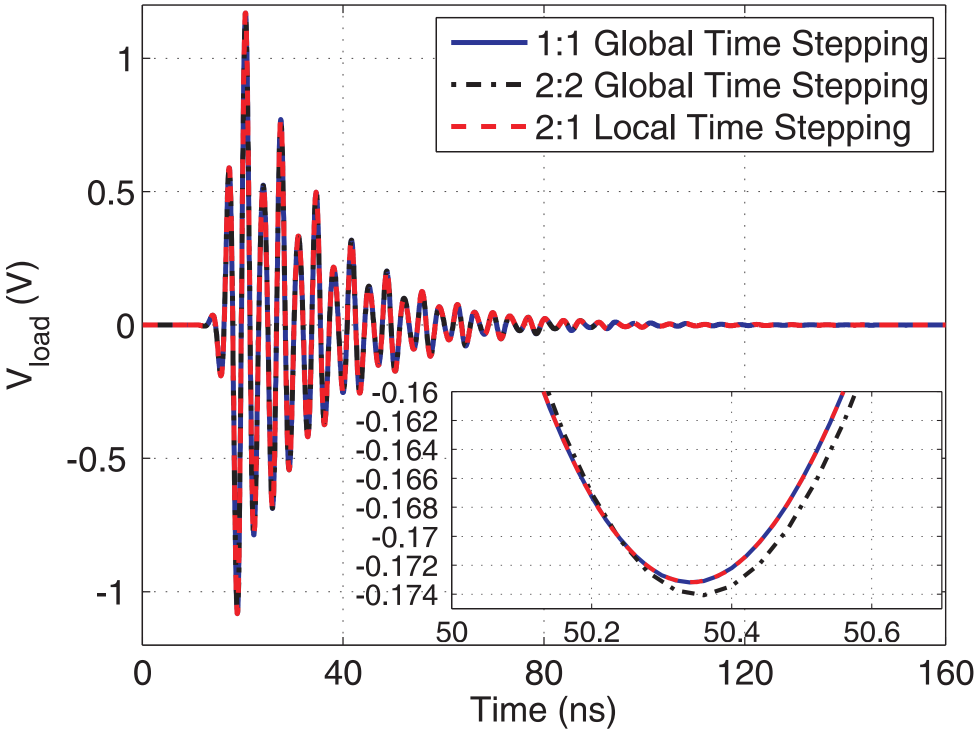

Figure 4.16: The transient voltages at the load end for the three test cases.

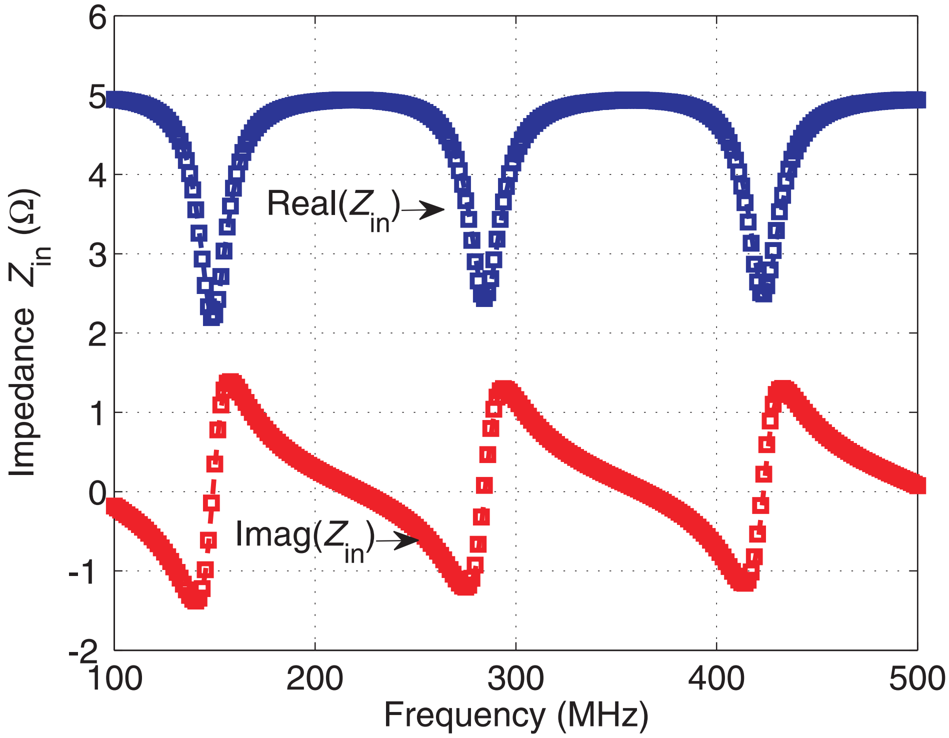

Figure 4.17: Comparison of the input impedances. Square: the 1:1 case (global time stepping). Dashed line: the 2:1 case (local time stepping).

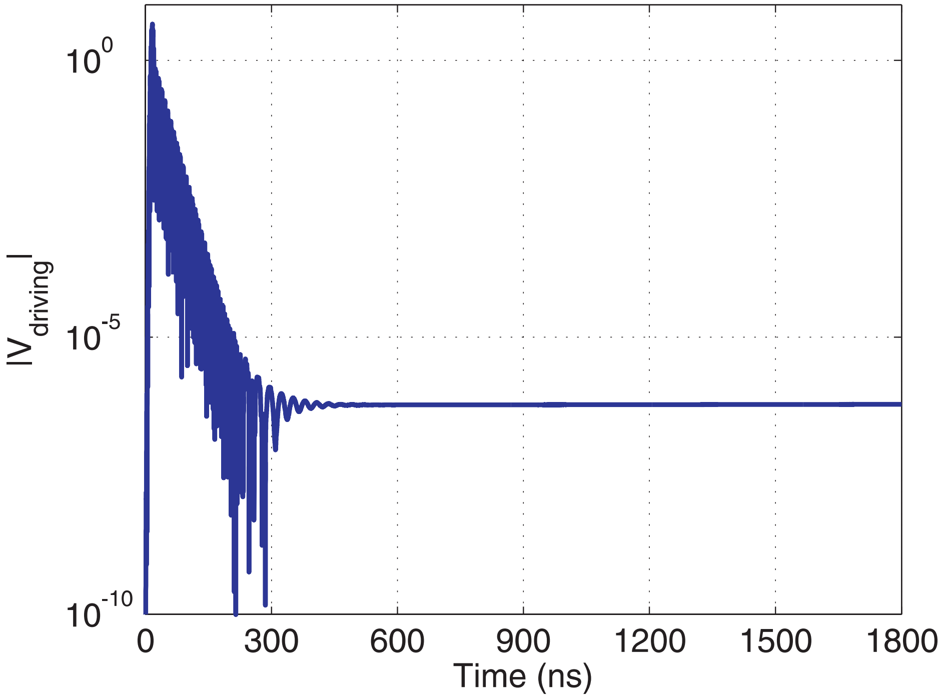

(a)

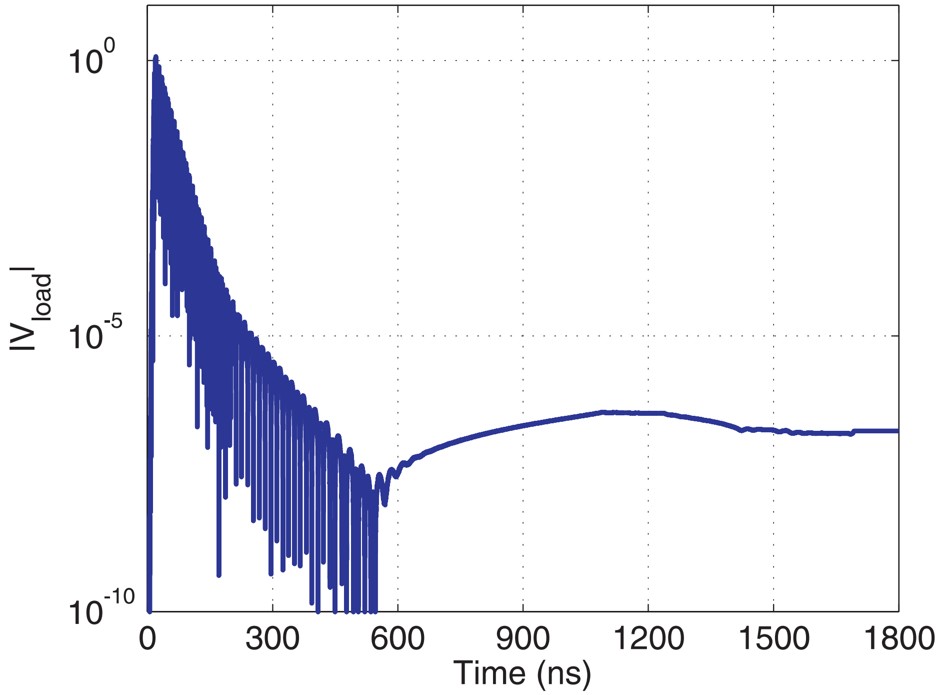

(b)

Figure 4.18: Magnitude of the transient voltages up to 1800 ns for the 2:1 case. (a) Voltage across the driving end. (b) Voltage across the load end.

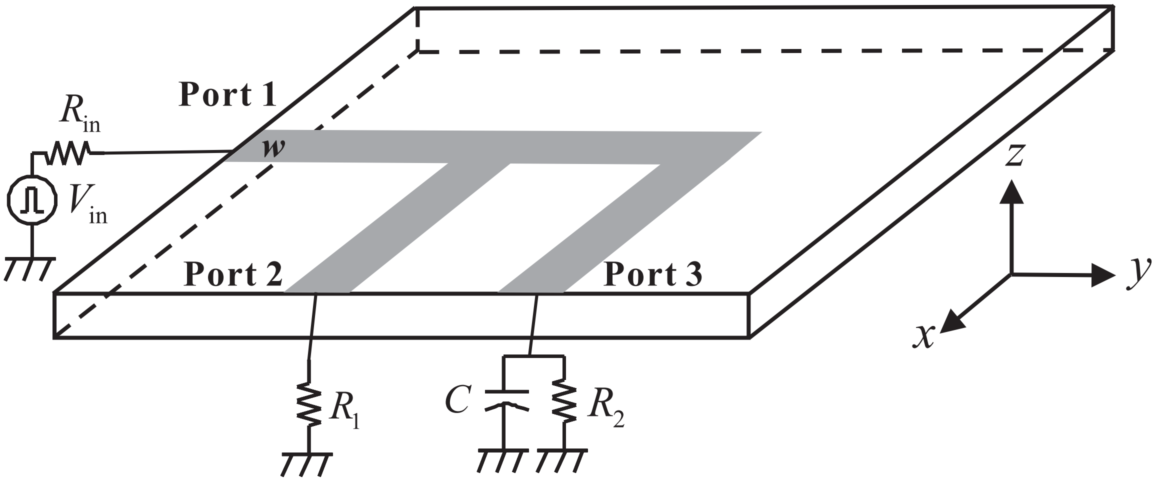

Figure 4.19: Three-port microstrip power-divider circuit. The dimensions of the circuit in the x-, y-, and z-directions are 20 mm × 20 mm × 0.5 mm and the width of the microstrip is 0.8 mm. $R_{\mathrm{in}} = 10\ \Omega$, $R_1 = R_2 = 64\ \Omega$, and $C = 5$ pF.

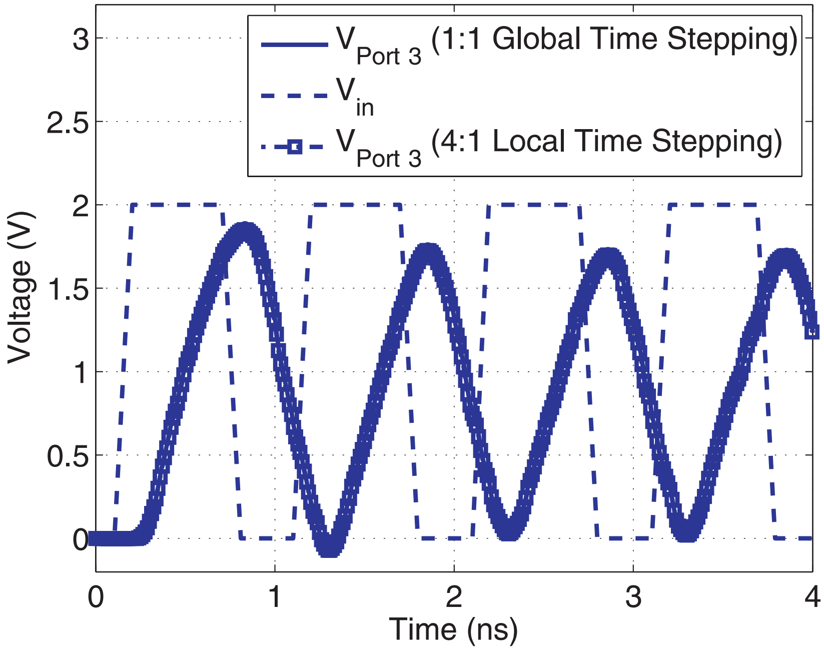

Figure 4.20: The input voltage V_{in} and the output voltage $V_{\mathrm{Port\,3}}$ recorded at Port 3. Case 1:1: $\Delta t^{\mathrm{FEM}} = \Delta t^{\mathrm{CKT}} = 0.5$ ps. Case 4:1: $\Delta t^{\mathrm{FEM}} = 4\Delta t^{\mathrm{CKT}} = 2$ ps.

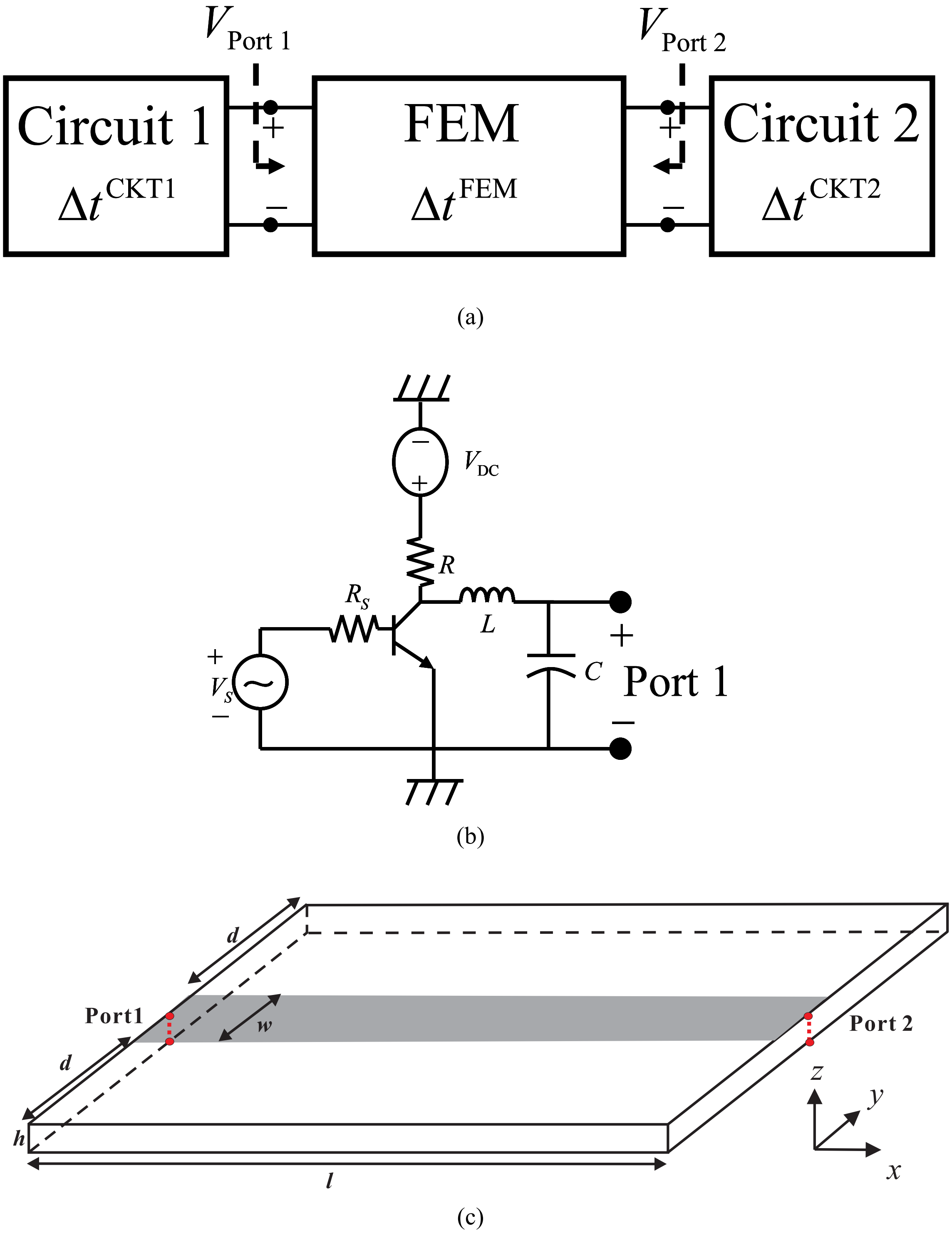
$V_{\text{Port 1}}$
$V_{\text{Port 2}}$
Circuit 1
Δt^{CKT1}
FEM
Δt^{FEM}
Circuit 2
Δt^{CKT2}
+
−
+
−
(a)
V_{DC}
R
R_S
L
C
V_S
Port 1
+
−
(b)
d
d
w
h
l
Port1
Port 2
z
y
x
(c)

Figure 4.21: A chip-to-package interconnecting structure. (a) Connection of the subsystems. (b) Circuit subsystem 1: the BJT-based driver with a bias resistor R = 49 Ω and source resistor R_S = 500 Ω. (c) The FEM subsystem.

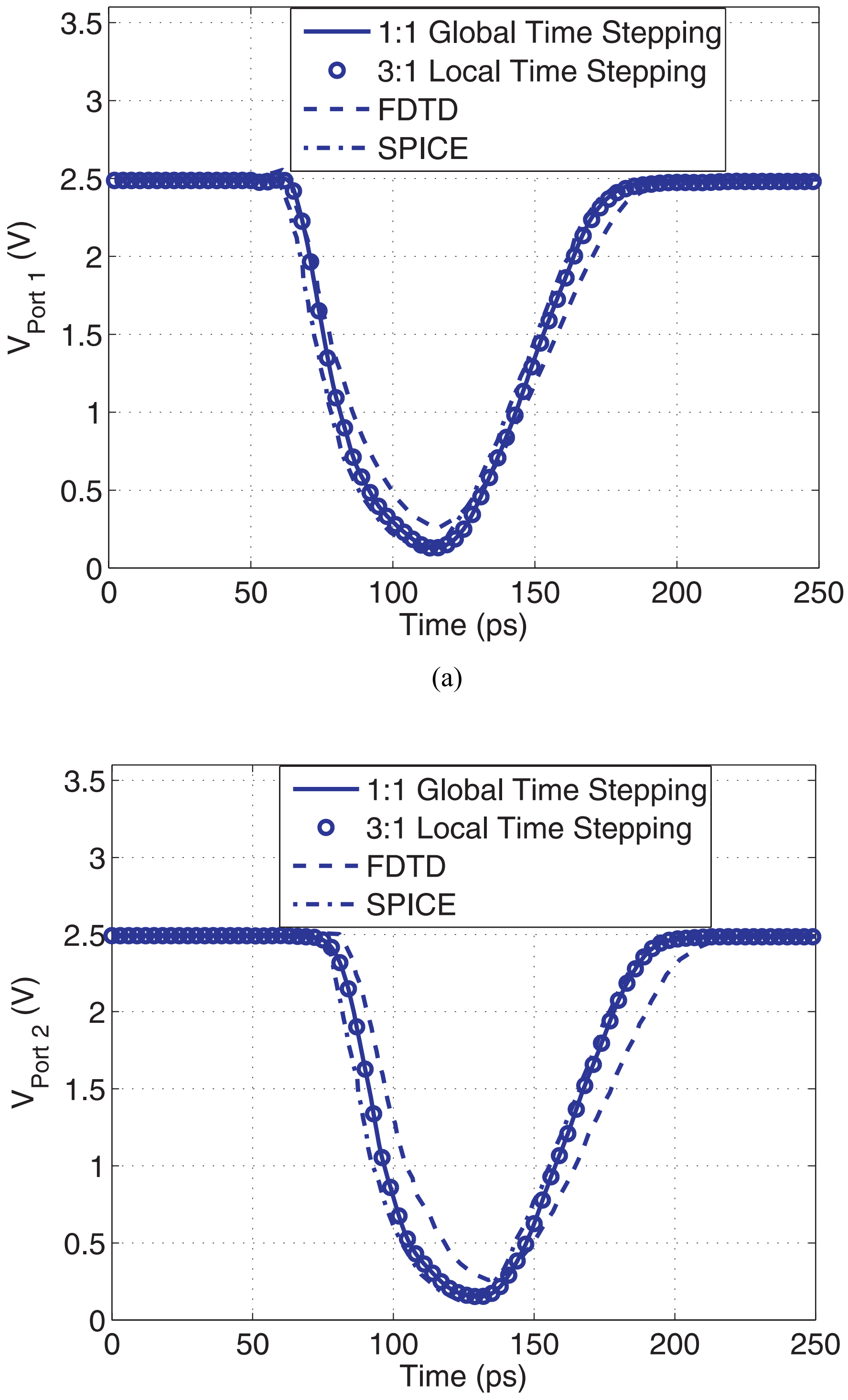

(a)

(b)

Figure 4.22: Comparison of transient voltages. (a) At Port 1. (b) At Port 2.

Table 4.1: Three test cases with different choices of time-step sizes for subsystems

Choices of time-step sizes	$\Delta t^{\mathrm{FEM}} = \Delta t^{\mathrm{CKT1}}$	Δt^{CKT2}
1:1	20 ps	20 ps
2:2	40 ps	40 ps
2:1	40 ps	20 ps

Table 4.2: Relative norm-2 error of $V_{\mathrm{Port\ 1}}$

	Global Time Stepping $\Delta t^{\mathrm{CKT1}} = \Delta t^{\mathrm{FEM}}$	Local Time Stepping $\Delta t^{\mathrm{CKT1}} = 0.25$ ps (fixed)
$\Delta t^{\mathrm{FEM}} = 0.25$ ps	reference (case 1:1)	reference (case 1:1)
$\Delta t^{\mathrm{FEM}} = 0.50$ ps	0.15e-3 (case 2:2)	0.095e-3 (case 2:1)
$\Delta t^{\mathrm{FEM}} = 0.75$ ps	0.76e-3 (case 3:3)	0.22e-3 (case 3:1)
$\Delta t^{\mathrm{FEM}} = 1.00$ ps	4.30e-3 (case 4:4)	0.94e-3 (case 3:1)

Table 4.3: Average number of Newton steps per time step

	Global Time Stepping $\Delta t^{\mathrm{CKT1}} = \Delta t^{\mathrm{FEM}}$	Local Time Stepping $\Delta t^{\mathrm{CKT1}} = 0.25$ ps (fixed)
$\Delta t^{\mathrm{FEM}} = 0.25$ ps	2.5 (case 1:1)	2.5 (case 1:1)
$\Delta t^{\mathrm{FEM}} = 0.50$ ps	3.6 (case 2:2)	2.6 (case 2:1)
$\Delta t^{\mathrm{FEM}} = 0.75$ ps	4.9 (case 3:3)	2.6 (case 3:1)
$\Delta t^{\mathrm{FEM}} = 1.00$ ps	6.3 (case 4:4)	2.7 (case 3:1)

CHAPTER 5

INCORPORATION OF MULTIPORT LUMPED NETWORKS INTO THE HYBRID FIELD-CIRCUIT ANALYSIS

5.1 Introduction

In the hybrid field-circuit solver described in the previous chapter, lumped circuit subsystems are described in detail in terms of discrete circuit elements. However, in some applications, lumped circuits might have been predesigned and characterized compactly in terms of frequency-dependent multiport network matrices. Such a compact network-matrix representation can be obtained either by measurement or simulations [75]. Even for some distributive subsystems that involve small geometrical features or strong field variations and are analyzed independently with a numerical method, multiport network-matrix representations can also be obtained by applying a model-order-reduction technique [32]-[34]. These pre-characterized network-matrix representations of subsystems are usually referred to as *lumped networks* in the literature [76]-[82]. Therefore, an accurate and efficient approach to incorporating multiport lumped networks into current simulation tools not only significantly extends the modeling capabilities of such tools but also improves their simulation efficiency especially when analyzing mixed-scale electronic systems.

In the past few years, considerable effort has been made to incorporate lumped networks into the FDTD scheme, yielding what are often referred to as lumped-network FDTD methods [76]-[82]. With the assumption that each entry of the admittance or impedance matrix of a lumped network is in a form of rational functions of the complex frequency s, the so-called lumped-network FDTD methods usually involve the following two-step procedure. First, network matrices in the Laplace domain are preprocessed and cast into proper time-stepping equations.

This is achieved either by a bilinear transform from the Laplace domain to the *Z*-domain and then to the discrete time domain [76], [77], or by utilizing the fact that the division by the state variable *s* in the Laplace domain is an integration of time [78], [79]. For simple one-port series or parallel *RLC* circuits, the piecewise linearly recursive convolution has been used to obtain the time-stepping formulas efficiently [80]. Second, the time-stepping equations obtained in the first step are solved together with the discretized Maxwell-Ampére's equation, which leads to a time-marching scheme that preserves both the second-order accuracy and the explicit nature of the conventional FDTD method. Originally proposed for one-port networks, lumped-network FDTD methods have been extended to handle general multiport networks and applied to both passive and active devices [81], [82]. In addition to the admittance and impedance matrices, other types of network matrices such as scattering matrices have also been utilized in the lumped-network FDTD methods by first converting them into admittance matrices [83]. Other than the FDTD, multiport network matrices have also been incorporated into some other simulation techniques. For example, so-called macro-elements in the form of generalized impedance matrices have been included into an efficient frequency-domain FEM analysis of waveguide components [84]. More recently, multiport admittance matrices (macromodels) have been used in conjunction with a transient field-circuit solver based on the TDIE method to perform system-level electromagnetic compatibility and interference analysis [85]. However, to the authors' knowledge, such an algorithm that incorporates the multiport lumped networks into transient analysis based on the TDFEM has neither been reported in literature nor been available in FEM-based commercial simulators.

In this chapter, we present an accurate and efficient algorithm to incorporate multiport lumped networks into the hybrid field-circuit analysis. Due to the presence of lumped networks in the computational domain, a lumped-network subsystem (in addition to the FEM and circuit subsystems) is formulated by casting its admittance matrix into the time-stepping equations whose computations can then be accelerated through recursive formulas. The lumped-network subsystem is then interfaced with the FEM subsystem through the FEM edges and the circuit subsystem through circuit nodes. The port voltages of the lumped-network subsystem are explicitly set to be the same as those computed from the FEM (or circuit) subsystem. The port currents of the lumped-network subsystem are used as impressed current excitations along the associated FEM edges (or through the related circuit nodes). Finally, all the port variables of the lumped-network subsystem are eliminated to form a global system for only the FEM and circuit unknowns. The proposed algorithm extends the capability of the existing hybrid field-circuit solver and provides a systematic and efficient scheme for incorporating lumped networks of arbitrary number of ports into the hybrid analysis, while preserving the symmetry of the global system matrix when the lumped network's admittance matrix is symmetric.

The rest of the chapter is organized as follows. Section 5.2 describes the formulation for incorporating multiport lumped networks into the hybrid solver, followed by a discussion for reducing the computational cost of time-stepping equations derived from admittance matrices. Numerical examples are presented in Section 5.3 to validate the proposed methodology and demonstrate its application and performance. Conclusions are then given in Section 5.4.

5.2 Formulation

5.2.1 Mathematical Representation

The mathematical representation of a lumped network is presented in this section. First, it is assumed that a lumped network having N^{LN} ports is represented in an $N^{\text{LN}} \times N^{\text{LN}}$ admittance matrix (other types of network matrix representation can always be converted to an admittance matrix). The admittance matrix $[\mathbf{Y}^{\text{LN}}(s)]$ relates the port current vector $\{I^{\text{LN}}(s)\}$ to the port voltage vector $\{V^{\text{LN}}(s)\}$ in the Laplace domain as $\{I^{\text{LN}}(s)\} = [\mathbf{Y}^{\text{LN}}(s)]\{V^{\text{LN}}(s)\}$, or more explicitly as

$$I_i^{\text{LN}}(s) = \sum_{j=1}^{N^{\text{LN}}} Y_{ij}^{\text{LN}}(s) V_j^{\text{LN}}(s), \qquad i = 1, 2, \cdots, N^{\text{LN}}. \tag{5.1}$$

When transformed into the time domain and discretized in time as $t = n\Delta t$, $n = 0,\ 1,\ 2,\ \cdots,\ T_{\max}$, the multiplication in (5.1) becomes discrete convolution

$$I_{i,n}^{\mathrm{LN}} = \sum_{j=1}^{N^{\mathrm{LN}}} Y_{ij,n}^{\mathrm{LN}} * V_{j,n}^{\mathrm{LN}} = \sum_{j=1}^{N^{\mathrm{LN}}} Y_{ij,0}^{\mathrm{LN}} V_{j,n}^{\mathrm{LN}} + \sum_{m=0}^{n-1} \sum_{j=1}^{N^{\mathrm{LN}}} Y_{ij,n-m}^{\mathrm{LN}} V_{j,m}^{\mathrm{LN}} . \tag{5.2}$$

In a compact form, (5.2) can be written in matrix form as

$$\{I_n^{\mathrm{LN}}\} = [Y_0^{\mathrm{LN}}]\{V_n^{\mathrm{LN}}\} + \{R_{n-1}^{\mathrm{LN}}\} \tag{5.3}$$

where $\{R_{n-1}^{\mathrm{LN}}\} = \sum_{m=0}^{n-1} [Y_{n-m}^{\mathrm{LN}}]\{V_m^{\mathrm{LN}}\}$ contains the contributions from all the previous time steps. Next, the lumped network is assumed to connect to both FEM and circuit subsystems (Fig. 5.1). Specifically, among its total N^{LN} ports, the first $N^{\mathrm{LN,\,E}}$ ports are connected to the FEM subsystem, while the remaining $N^{\mathrm{LN,\,C}} (= N^{\mathrm{LN}} - N^{\mathrm{LN,\,E}})$ ports are connected to the circuit subsystem. Accordingly, the vectors can be partitioned as $\{V_n^{\mathrm{LN}}\} = \left\{ \{V_n^{\mathrm{LN,\,E}}\}^{\mathrm{T}}\ \{V_n^{\mathrm{LN,\,C}}\}^{\mathrm{T}} \right\}^{\mathrm{T}}$, $\{I_n^{\mathrm{LN}}\} = \left\{ \{I_n^{\mathrm{LN,\,E}}\}^{\mathrm{T}}\ \{I_n^{\mathrm{LN,\,C}}\}^{\mathrm{T}} \right\}^{\mathrm{T}}$, $\{R_{n-1}^{\mathrm{LN}}\} = \left\{ \{R_{n-1}^{\mathrm{LN,\,E}}\}^{\mathrm{T}}\ \{R_{n-1}^{\mathrm{LN,\,C}}\}^{\mathrm{T}} \right\}^{\mathrm{T}}$, and $[Y_0^{\mathrm{LN}}]$ can also be partitioned as

$$[Y_0^{\mathrm{LN}}] = \begin{bmatrix} \left[Y_0^{\mathrm{EE}} \right] & \left[Y_0^{\mathrm{EC}} \right] \\ \left[Y_0^{\mathrm{CE}} \right] & \left[Y_0^{\mathrm{CC}} \right] \end{bmatrix} . \tag{5.4}$$

As a result, (5.3) can be split into two time-stepping equations for $\{I_n^{\mathrm{LN,\,E}}\}$ and $\{I_n^{\mathrm{LN,\,C}}\}$, respectively,

$$\{I_n^{\mathrm{LN,\,E}}\} = \left[Y_0^{\mathrm{EE}} \right] \{V_n^{\mathrm{LN,\,E}}\} + \left[Y_0^{\mathrm{EC}} \right] \{V_n^{\mathrm{LN,\,C}}\} + \{R_{n-1}^{\mathrm{LN,\,E}}\} \tag{5.5}$$

$$\{I_n^{\mathrm{LN,\,C}}\} = \left[Y_0^{\mathrm{CC}} \right] \{V_n^{\mathrm{LN,\,C}}\} + \left[Y_0^{\mathrm{CE}} \right] \{V_n^{\mathrm{LN,\,E}}\} + \{R_{n-1}^{\mathrm{LN,\,C}}\} . \tag{5.6}$$

Numerical schemes to couple the lumped-network subsystem described in (5.5) and (5.6) to the FEM and circuit subsystems are described in Sections 5.2.2 and 5.2.3, respectively. The global system of equations is then presented in Section 5.2.4, followed by a brief discussion about the evaluation of $\{R_{n-1}^{\mathrm{LN}}\}$.

5.2.2 Coupling to the FEM Subsystem

Consider a computational domain consisting of distributive passive elements, lumped discrete circuit, and multiport lumped networks. The finite element discretization [1, 2] of the distributive part using hierarchical vector basis function $\mathbf{N}_i$ [25] and an absorbing boundary condition yields the following semidiscrete system:

$$[S]\{e\}+\frac{1}{c_0^2}[M]\frac{\partial^2\{e\}}{\partial t^2}+\frac{1}{c_0}\big([G]+[A]\big)\frac{\partial\{e\}}{\partial t}=\frac{Z_0}{c_0}\frac{\partial\{b^{\mathrm{LN}}\}}{\partial t} \tag{5.7}$$

where $Z_0=\sqrt{\mu_0/\varepsilon_0}$, $c_0=1\big/\sqrt{\mu_0\varepsilon_0}$ and the expressions for matrices $[S]$, $[M]$, $[G]$, and $[A]$ can be found in Chapter 2. The elements of vector $\{b^{\mathrm{LN}}\}$ are given by

$$b_i^{\mathrm{LN}}=-\iiint_V \mathbf{N}_i\cdot\mathbf{J}^{\mathrm{LN}}dV \tag{5.8}$$

in which $\mathbf{J}^{\mathrm{LN}}$ denotes the current density supplied by the lumped network. The size of the FEM solution vector $\{e\}$ is denoted as N^{FEM}. Here, it is assumed that there is no internal source in the distributive part for the sake of simplicity. Otherwise, there will be an additional term in the right-hand side of (5.7) similar to (5.8) except that $\mathbf{J}^{\mathrm{LN}}$ is replaced with the current density of the internal source.

The term $\partial\{b^{\mathrm{LN}}\}/\partial t$ presents the coupling from the lumped-network subsystem to the FEM subsystem through external lumped current sources $\mathbf{J}^{\mathrm{LN}}$ at the FEM edges where the ports of the lumped network reside. The values of these lumped current sources are equal to $\{I^{\mathrm{LN,\,E}}\}$ and their directions are opposite to the direction of the associated edges. We can then obtain the explicit expression for $\partial\{b^{\mathrm{LN}}\}/\partial t$ as

$$\frac{\partial\{b^{\mathrm{LN}}\}}{\partial t}=\left[C^{\mathrm{ME}}\right]^{\mathrm{T}}\frac{\partial}{\partial t}\{I^{\mathrm{LN,\,E}}\} \tag{5.9}$$

where $\left[C^{\mathrm{ME}}\right]$ has a size of $N^{\mathrm{LN,\,E}} \times N^{\mathrm{FEM}}$ whose nonzero entries are given by

$$C_{ki}^{\mathrm{ME}} = \int_{l_{i(k)}} \mathbf{N}_i \cdot \hat{l}_{i(k)} dl \,. \tag{5.10}$$

Here, k is the port index of the lumped network and i is the index of the FEM unknown on the associated edge whose direction is denoted as $\hat{l}_{i(k)}$. If we apply a central-difference formula to approximate the time derivative, (5.9) becomes

$$\left[\frac{\partial\{b^{\mathrm{LN}}\}}{\partial t}\right]_{n-1} = \frac{1}{2\Delta t}\left[C^{\mathrm{ME}}\right]^{\mathrm{T}}\left[\{I_n^{\mathrm{LN,\,E}}\} - \{I_{n-2}^{\mathrm{LN,\,E}}\}\right]. \tag{5.11}$$

The discretization of the left-hand side of (5.7) in the time domain using the Newmark-beta method with $\beta = 1/4$ yields the updating equation

$$\left[E_0\right]\{e\}_n = \left[E_1\right]\{e\}_{n-1} + \left[E_2\right]\{e\}_{n-2} + c_0 \Delta t^2 Z_0 \left[\frac{\partial\{b^{\mathrm{LN}}\}}{\partial t}\right]_{n-1} \tag{5.12}$$

where $\left[E_0\right]$, $\left[E_1\right]$, and $\left[E_2\right]$ are defined in (4.5)-(4.7), respectively.

Another set of equations comes from the enforcement of the voltage continuity across the lumped network ports and the associated FEM edges, which can be expressed as

$$\{V_n^{\mathrm{LN,\,E}}\} = -\left[C^{\mathrm{ME}}\right]\{e\}_n \,. \tag{5.13}$$

Substituting (5.5), (5.11), and (5.13) into (5.12), we can eliminate $\{V_n^{\mathrm{LN,\,E}}\}$ to obtain the modified FEM subsystem for $\{e\}_n$ as

$$\begin{aligned}\left[\tilde{E}_0\right]\{e\}_n &= \varsigma\left[C^{\mathrm{ME}}\right]^{\mathrm{T}}\left[Y_0^{\mathrm{EC}}\right]\{V_n^{\mathrm{LN,\,C}}\} \\ &\quad + \left[E_1\right]\{e\}_{n-1} + \left[E_2\right]\{e\}_{n-2} + \varsigma\left[C^{\mathrm{ME}}\right]^{\mathrm{T}}\left[\{R_{n-1}^{\mathrm{LN,\,E}}\} - \{I_{n-2}^{\mathrm{LN,\,E}}\}\right]\end{aligned} \tag{5.14}$$

where $\varsigma = (c_0 \Delta t Z_0)/2$ and $\left[\tilde{E}_0\right]$ is the modified FEM system matrix with

$$\left[\tilde{E}_0\right] = \left[E_0\right] + \varsigma\left[C^{\mathrm{ME}}\right]^{\mathrm{T}}\left[Y_0^{\mathrm{EE}}\right]\left[C^{\mathrm{ME}}\right]. \tag{5.15}$$

5.2.3 Coupling to the Circuit Subsystem

The lumped discrete circuit elements are analyzed using the modified nodal analysis, which yields the circuit subsystem (4.20). The overall dimension of the circuit subsystem in (4.20) is denoted as N^{CKT}. The coupling from the lumped-network subsystem described in Section 5.2.1 to the circuit subsystem can be realized naturally by introducing external current flows at the circuit nodes that are connected to the ports of the lumped network [74]. The values of those current flows are equal to the corresponding port currents (entries of $\{I_n^{\mathrm{LN,\,C}}\}$) of the lumped network. If we introduce a permutation matrix $\left[B^{\mathrm{CM}}\right]$ of size $N^{\mathrm{CKT}} \times N^{\mathrm{LN,\,C}}$ that permutes each entry of $\{I_n^{\mathrm{LN,\,C}}\}$ to its corresponding branch current equations and reinforce the Kirchoff's current law, (4.20) can be modified as

$$\left[B^{\mathrm{CM}}\right]\{I_n^{\mathrm{LN,\,C}}\} + \left[Y^{\mathrm{CKT}}\right]\{V_n^{\mathrm{CKT}}\} + \mathbf{I}_n^{\mathrm{CKT,nl}}\left(\{V_n^{\mathrm{CKT}}\}\right) = \mathbf{I}_n^{\mathrm{CKT}}\,. \tag{5.16}$$

Again, the enforcement of the voltage continuity across the lumped network ports and the associated current nodes yields the following relation:

$$\{V_n^{\mathrm{LN,\,C}}\} = \left[B^{\mathrm{CM}}\right]^T \{V_n^{\mathrm{CKT}}\}\,. \tag{5.17}$$

Substituting (5.6) and (5.17) into (5.16), we can eliminate $\{V_n^{\mathrm{LN,\,C}}\}$ to obtain the modified circuit subsystem as

$$\left[\tilde{Y}^{\mathrm{CKT}}\right]\{V_n^{\mathrm{CKT}}\} + \mathbf{I}_n^{\mathrm{CKT,nl}}\left(\{V_n^{\mathrm{CKT}}\}\right) = -\left[B^{\mathrm{CM}}\right]\left[Y_0^{\mathrm{CE}}\right]\{V_n^{\mathrm{LN,\,E}}\} + \mathbf{I}_n^{\mathrm{CKT}} - \left[B^{\mathrm{CM}}\right]\{R_{n-1}^{\mathrm{LN,\,C}}\} \tag{5.18}$$

where $\left[\tilde{Y}^{\mathrm{CKT}}\right]$ is the modified circuit system matrix with

$$\left[\tilde{Y}^{\mathrm{CKT}}\right] = \left[Y^{\mathrm{CKT}}\right] + \left[B^{\mathrm{CM}}\right]\left[Y_0^{\mathrm{CC}}\right]\left[B^{\mathrm{CM}}\right]^T. \tag{5.19}$$

5.2.4 Global System of Equations

Following the coupling scheme elaborated in Section 4.2.4, the coupling of the modified FEM and circuit subsystems in (5.14) and (5.18), respectively, yields the following global system of equations for the FEM and circuit unknowns:

$$\mathbf{F}(\mathbf{x}_n) = \mathbf{b}_n \tag{5.20}$$

where $\mathbf{x}_n = \left\{ \{e\}_n \quad \{V_n^{\mathrm{CKT}}\} \quad \{I_n^{\mathrm{CP}}\} \right\}^{\mathrm{T}}$ and

$$\mathbf{F}(\mathbf{x}_n) = \begin{bmatrix} \left[\tilde{E}_0\right] & -\varsigma\left[P^{\mathrm{EMC}}\right] & \varsigma\left[C\right]^{\mathrm{T}} \\ -\varsigma\left[P^{\mathrm{CME}}\right] & \varsigma\left[\tilde{Y}^{\mathrm{CKT}}\right] & \varsigma[B] \\ \varsigma\left[C\right] & \varsigma[B]^{\mathrm{T}} & \mathbf{0} \end{bmatrix} \begin{Bmatrix} \{e\}_n \\ \{V_n^{\mathrm{CKT}}\} \\ \{I_n^{\mathrm{CP}}\} \end{Bmatrix} + \begin{Bmatrix} \mathbf{0} \\ \varsigma\mathbf{I}_n^{\mathrm{CKT,nl}}\left(\{V_n^{\mathrm{CKT}}\}\right) \\ \mathbf{0} \end{Bmatrix} \tag{5.21}$$

$$\mathbf{b}_n = \begin{Bmatrix} \mathbf{0} \\ \varsigma\mathbf{I}_n^{\mathrm{CKT}} \\ \mathbf{0} \end{Bmatrix} + \begin{bmatrix} \left[E_1\right] & \mathbf{0} & \mathbf{0} \\ \mathbf{0} & \mathbf{0} & \mathbf{0} \\ \mathbf{0} & \mathbf{0} & \mathbf{0} \end{bmatrix} \begin{Bmatrix} \{e\}_{n-1} \\ \{V_{n-1}^{\mathrm{CKT}}\} \\ \{I_{n-1}^{\mathrm{CP}}\} \end{Bmatrix} + \begin{Bmatrix} \varsigma\left[C^{\mathrm{ME}}\right]^{\mathrm{T}}\left[\{R_{n-1}^{\mathrm{LN,\,E}}\} - \{R_{n-3}^{\mathrm{LN,\,E}}\}\right] \\ -\varsigma\left[B^{\mathrm{CM}}\right]\{R_{n-1}^{\mathrm{LN,\,C}}\} \\ \mathbf{0} \end{Bmatrix}$$

$$+ \begin{bmatrix} \left[\tilde{E}_2\right] & -\varsigma\left[P^{\mathrm{EMC}}\right] & \varsigma\left[C\right]^{\mathrm{T}} \\ \mathbf{0} & \mathbf{0} & \mathbf{0} \\ \mathbf{0} & \mathbf{0} & \mathbf{0} \end{bmatrix} \begin{Bmatrix} \{e\}_{n-2} \\ \{V_{n-2}^{\mathrm{CKT}}\} \\ \{I_{n-2}^{\mathrm{CP}}\} \end{Bmatrix} \tag{5.22}$$

where

$$\left[P^{\mathrm{CME}}\right] = \left[B^{\mathrm{CM}}\right]\left[Y_0^{\mathrm{CE}}\right]\left[C^{\mathrm{ME}}\right] \tag{5.23}$$

$$\left[P^{\mathrm{EMC}}\right] = \left[C^{\mathrm{ME}}\right]^{\mathrm{T}}\left[Y_0^{\mathrm{EC}}\right]\left[B^{\mathrm{CM}}\right]^{T} \tag{5.24}$$

$$\left[\tilde{E}_2\right] = \left[E_2\right] + \varsigma\left[C^{\mathrm{ME}}\right]^{\mathrm{T}}\left[Y_0^{\mathrm{EE}}\right]\left[C^{\mathrm{ME}}\right]. \tag{5.25}$$

The definitions of matrices $\left[C\right]$ and $\left[B\right]$ can be found in Section 4.2.4. To derive (5.20), we have applied (5.5) at time step $n-2$ and again invoked the relations in (5.13) and (5.17) to completely eliminate the port variables of the lumped-network subsystem (such as $\{I_{n-2}^{\mathrm{LN,\,E}}\}$, $\{V_n^{\mathrm{LN,\,E}}\}$, and $\{V_n^{\mathrm{LN,\,C}}\}$) from the final expressions. Compared to the global system in (4.25), the overall dimension of the global system here remains the same. More importantly, the symmetry of the system matrix has been preserved as long as the admittance matrix of the lumped network itself is symmetric. However, incorporation of the multiport lumped network not only affects the diagonal blocks in the system matrix, such as $\left[\tilde{E}_0\right]$ and $\left[\tilde{Y}^{\mathrm{CKT}}\right]$, but also introduces

$-\varsigma\left[P^{\mathrm{CME}}\right]$ and $-\varsigma\left[P^{\mathrm{EMC}}\right]$ as the off-diagonal blocks that relate $\{e\}_n$ to $\{V_n^{\mathrm{CKT}}\}$ and vice versa. These off-diagonal blocks that do not exist in (4.25) represent the additional interactions between the FEM and circuit subsystems through the lumped networks that are connected to both of the subsystems.

The system of mixed linear and nonlinear equations given in (21) can be solved efficiently by applying the solution algorithm designed in Section 4.2.5. However, the overall solution efficiency can still be limited by the evaluation of the third term of $\mathbf{b}_n$ largely due to the time-consuming evaluation of the convolution. However, if $Y_{ij}^{\mathrm{LN}}(s)$ in (5.1) is given in the form of rational functions as

$$Y_{ij}^{\mathrm{LN}}(s)=\sum_{p}\frac{c_{ij,p}}{s+a_{ij,p}}+d_{ij}+se_{ij} \tag{5.26}$$

then the computational cost of $\mathbf{b}_n$ can be greatly reduced by using a recursive convolution algorithm. By invoking (5.26), after some mathematical derivations, it can be shown that the ith entry of $\{R_{n-1}^{\mathrm{LN}}\}$, denoted as $\{R_{n-1}^{\mathrm{LN}}\}_i$, can be computed as

$$\{R_{n-1}^{\mathrm{LN}}\}_i=\sum_{j=1}^{N^{\mathrm{LN}}}\sum_{p}Q_{ij,p}[n-1]+\sum_{j=1}^{N^{\mathrm{LN}}}T_{ij}[n-1] \tag{5.27}$$

where both $Q_{ij,p}[n-1]$ and $T_{ij}[n-1]$ can be updated recursively as

$$Q_{ij,p}[n-1]=e^{-a_{ij,p}\Delta t}\left(Q_{ij,p}[n-2]+c_{ij,p}\Delta t V_{j,n-1}^{\mathrm{LN}}\right) \tag{5.28}$$

$$T_{ij}[n-1]=-T_{ij}[n-2]-\frac{4}{\Delta t}e_{ij}V_{j,n-1}^{\mathrm{LN}}\,. \tag{5.29}$$

For a general case where $Y_{ij}^{\mathrm{LN}}(s)$ is given in the expressions other than (5.26), or, even more generally, when only the values of $Y_{ij}^{\mathrm{LN}}(s)$ at discrete frequency points are available (from either simulation or measurement), various rational-fitting techniques can be applied to find the rational function interpolation of the discrete data over the frequency band of interest. For instance, the Cauchy method has been used to obtain the rational approximation of measured admittance results and then incorporated into the FDTD solver [86]. In this work, we adopt the so-called VECTFIT technique [35] which is well known for its robustness, accuracy, and efficiency.

5.3 Numerical Results

To validate the accuracy and stability of the proposed formulation, we first consider the following numerical example that involves the FEM, circuit, and lumped-network subsystems. As illustrated in Fig. 5.2, a two-port lumped network (denoted as $[\mathbf{Y}^{\mathrm{LN}}(s)]$) is connected to the FEM subsystem (denoted as "FEM") and a termination circuit (denoted as "Circuit 2") through each of its ports. The lumped network is a three-pole T-type low-pass LC filter that is specified in the inset of Fig. 5.2 and the entries of $[\mathbf{Y}^{\mathrm{LN}}(s)]$ are given as

$$Y_{11}(s) = \frac{1/(L_1+L_2)}{s} + \frac{f(L_1,L_2)}{s+p} + \frac{f^*(L_1,L_2)}{s+p^*},$$

$$Y_{12}(s) = \frac{L_2}{L_1} Y_{22}(s) - \frac{1/L_1}{s},$$

$$Y_{21}(s) = \frac{L_1}{L_2} Y_{11}(s) - \frac{1/L_2}{s},$$

$$Y_{22}(s) = \frac{1/(L_1+L_2)}{s} + \frac{f(L_2,L_1)}{s+p} + \frac{f^*(L_2,L_1)}{s+p^*} \tag{5.30}$$

where $p = j\sqrt{(L_1+L_2)/(C_2L_1L_2)}$ and $f(L_1,L_2) = 0.5/L_1 - 0.5/(L_1+L_2)$. The termination circuit is a 5 nH shunt inductor. The FEM subsystem is formed by the time-domain FEM modeling of an air-filled 1 m long coaxial cable with the inner and outer perfect conductors having a radius of 4 mm and 8 mm, respectively. It is driven at the other end by an excitation circuit (denoted as "Circuit 1") represented by a driving voltage source in series with a 5 Ω resistor, which, together with the termination circuit, forms the circuit subsystem. The example is designed in such a way that there are abundant reflections, fast variations, and resonance peaks in the time and frequency domains. Therefore, the mutual coupling between the lumped-network subsystem and the other two subsystems can be fully tested. Figure 5.3 shows the time profile of the transient voltage at Ports 1 and 2 computed by the proposed technique and compared to the reference results by the method in Chapter 4 where discrete circuit elements (instead of the admittance matrix) of the lumped network are modeled directly. The normalized spectra of the port voltages are plotted in Fig. 5.4. From both plots, it is clear that excellent agreement is achieved between these two techniques and the proposed algorithm captures the fast-varying signals and resonance peaks. Figure 5.5 records the magnitude of the port voltages up to 75,000 time steps to demonstrate the numerical stability of the proposed algorithm.

Next, to demonstrate the proposed method's capability of modeling problems integrated with active devices, we simulate a microwave field-effect transistor (FET) amplifier circuit. The circuit consists of a generic JS8851-AS FET mounted over a microstrip gap whose common-source configuration and dimensions are illustrated in Fig. 5.6(a). The dielectric constant of the substrate is 2.17. Figure 5.6(b) shows a small-signal extrinsic equivalent circuit model of the FET, where its embedded intrinsic part given in [81] can be characterized by the following admittance matrix $[\mathbf{Y}^{\mathrm{LN,in}}(s)]$:

$$[\mathbf{Y}^{\mathrm{LN,in}}(s)] = \begin{bmatrix} \dfrac{sC_{\mathrm{gs}}}{1+sC_{\mathrm{gs}}R_i} + sC_{\mathrm{gd}} & -sC_{\mathrm{gd}} \\ \dfrac{G_{\mathrm{m}}}{1+sC_{\mathrm{gs}}R_i} - sC_{\mathrm{gd}} & s\left(C_{\mathrm{gd}} + C_{\mathrm{ds}}\right) + \dfrac{1}{R_{\mathrm{ds}}} \end{bmatrix} \tag{5.31}$$

where $C_{\mathrm{gs}} = 0.69$ pF, $C_{\mathrm{gd}} = 0.06$ pF, $C_{\mathrm{ds}} = 0.26$ pF, $R_i = 1.42\ \Omega$, $R_{\mathrm{ds}} = 197\ \Omega$, and $G_{\mathrm{m}} = 65$ mS. This amplifier circuit can then be simulated using the proposed algorithm in the following scheme where the admittance matrix $[\mathbf{Y}^{\mathrm{LN,in}}(s)]$ in (5.31) is directly cast into a two-port lumped-network subsystem and other circuit elements in the extrinsic FET circuit model in Fig. 5.6(b) are incorporated into the circuit subsystem. This is referred to later as the "intrinsic scheme."

Alternatively, by utilizing (5.31) and other circuit elements in Fig. 5.6(b), we can obtain an admittance matrix $[\mathbf{Y}^{\mathrm{LN,ex}}(s)]$ for the entire extrinsic FET circuit model (defined at Ports G and D in Fig. 5.6(b)) and then cast it into a two-port lumped-network subsystem. This is referred to later as the "extrinsic scheme." To analytically derive a mathematical expression for $[\mathbf{Y}^{\mathrm{LN,ex}}(s)]$ and then cast each entry into the form of (5.26) is possible but difficult and time-consuming. However, by observing the fact that it is much easier to obtain the frequency response of $[\mathbf{Y}^{\mathrm{LN,ex}}(s)]$ sampled over an arbitrary frequency band, a more effective way is to invoke the VECTFIT technique and obtain the poles and residues numerically based on the frequency samples of $[\mathbf{Y}^{\mathrm{LN,ex}}(s)]$. Note that since rational-fitting techniques [35] can easily be applied to simulated or measured results [86], our algorithm is very flexible in the sense that we do not resort to specified circuit diagrams or analytical formulas for the lumped network as long as the frequency samples of its network matrix are available. To illustrate the procedure, we first simulate the extrinsic FET circuit model and obtain 500 frequency samples of $[\mathbf{Y}^{\mathrm{LN,ex}}(s)]$ from 500 kHz to 50 GHz. These frequency samples are then used in the VECTFIT to obtain a four-pole lumped-network subsystem. Figures 5.7 and 5.8 show that the fitted admittance values agree very well with the original frequency samples in both magnitude and phase. The overall absolute fitting error is about five orders of magnitude less than the original values. This fourth-order lumped-network subsystem is then hybridized with the other two subsystems using the proposed algorithm in the time-domain simulation. The computed results of the magnitude of S_{11} and S_{21} using both intrinsic and extrinsic schemes are shown in Figs. 5.9 and 5.10, respectively. The results agree well with those computed by the FDTD [82] and the deviation from those of HP ADS is due to the lack of the full-wave capability of ADS.

5.4 Summary

This chapter presented an accurate and efficient approach for incorporating multiport lumped networks into the time-domain FEM-based hybrid field-circuit simulator to extend its capability of modeling hybrid circuits. A multiport lumped network is characterized by its admittance matrix in the Laplace domain and then cast into the time-stepping equations to form a lumped-network subsystem that relates the port currents and voltages in the discrete time domain. This lumped-network subsystem is then coupled to the FEM and circuit subsystems through their shared lumped ports, respectively. The port voltages of the lumped-network subsystem are set to be equivalent to those computed from the FEM or circuit subsystem. The port currents of the lumped-network subsystem are used as impressed current excitations for the FEM or circuit subsystem. After all the port variables of the lumped-network subsystem are eliminated, the modified FEM and circuit subsystems are individually formed and then coupled together to form a final global system for only the FEM and circuit unknowns. It has been shown that this global system of equations preserves symmetry as long as the admittance matrix of the lumped network is symmetric. To accelerate the computation of the required discrete convolution, rational-fitting techniques and recursive convolution algorithms have been applied. The validity and performance of the proposed algorithm have been demonstrated by applying it to the modeling of both passive and active microwave hybrid circuits.

With this development, the capability of the hybrid field-circuit solver has been extended significantly to the level that it is now capable of modeling transient broadband responses of electromagnetic systems involving nonlinear circuits and lumped networks, and such a capability is currently not available in any FEM-based commercial software.

5.5 Figures

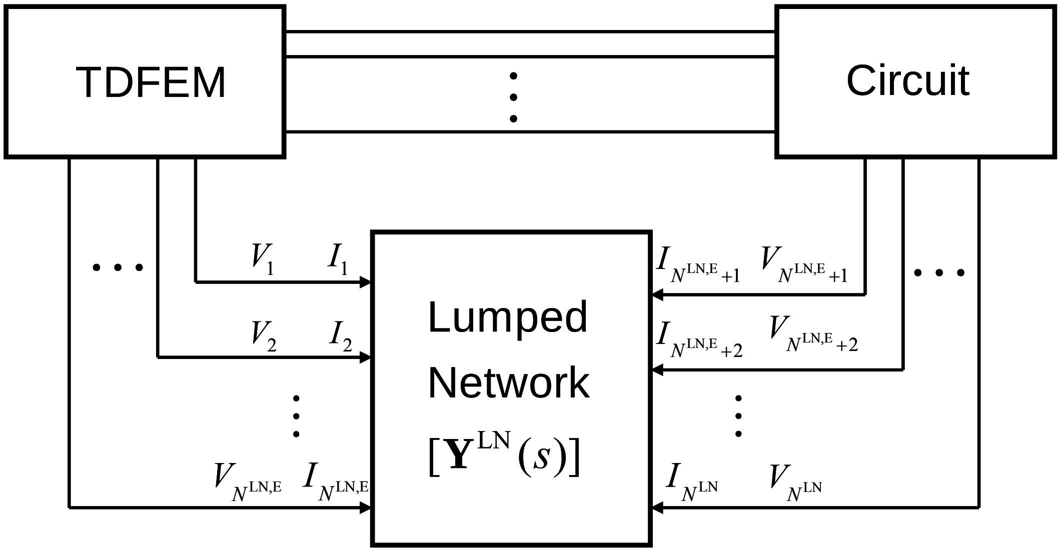
TDFEM
Circuit
Lumped
Network
$[\mathbf{Y}^{\mathrm{LN}}(s)]$
V_1
I_1
V_2
I_2
$V_{N^{\mathrm{LN,E}}}$
$I_{N^{\mathrm{LN,E}}}$
$I_{N^{\mathrm{LN,E}}+1}$
$V_{N^{\mathrm{LN,E}}+1}$
$I_{N^{\mathrm{LN,E}}+2}$
$V_{N^{\mathrm{LN,E}}+2}$
$I_{N^{\mathrm{LN}}}$
$V_{N^{\mathrm{LN}}}$

Figure 5.1: Connections of a lumped-network subsystem to FEM and circuit subsystems. Note that the superscript "LN" for "*V*"s and "*I*"s is omitted for simplicity.

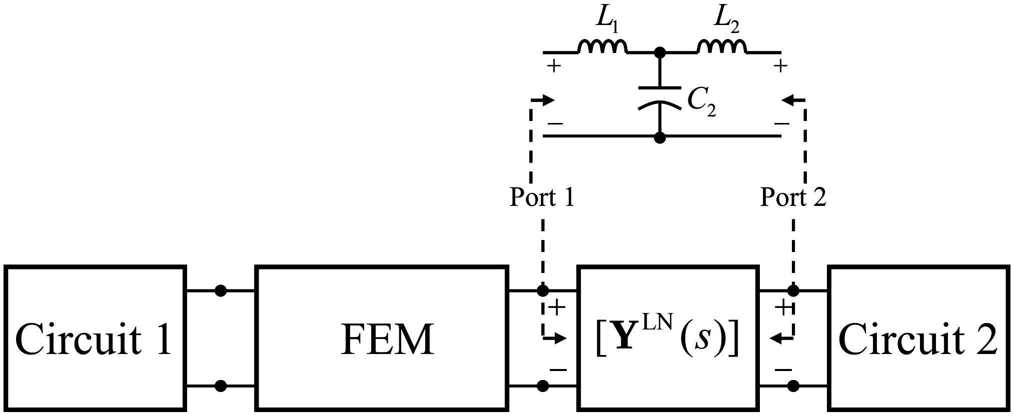
L_1
L_2
C_2
+
−
+
−
Port 1
Port 2
Circuit 1
FEM
$[\mathbf{Y}^{\mathrm{LN}}(s)]$
Circuit 2
+
−
+
−

Figure 5.2: Setup of the numerical example that hybridizes a lumped-network subsystem to FEM and circuit subsystems. L_1 = 10 nH, L_2 = 5 nH, C_2 = 100 pF.

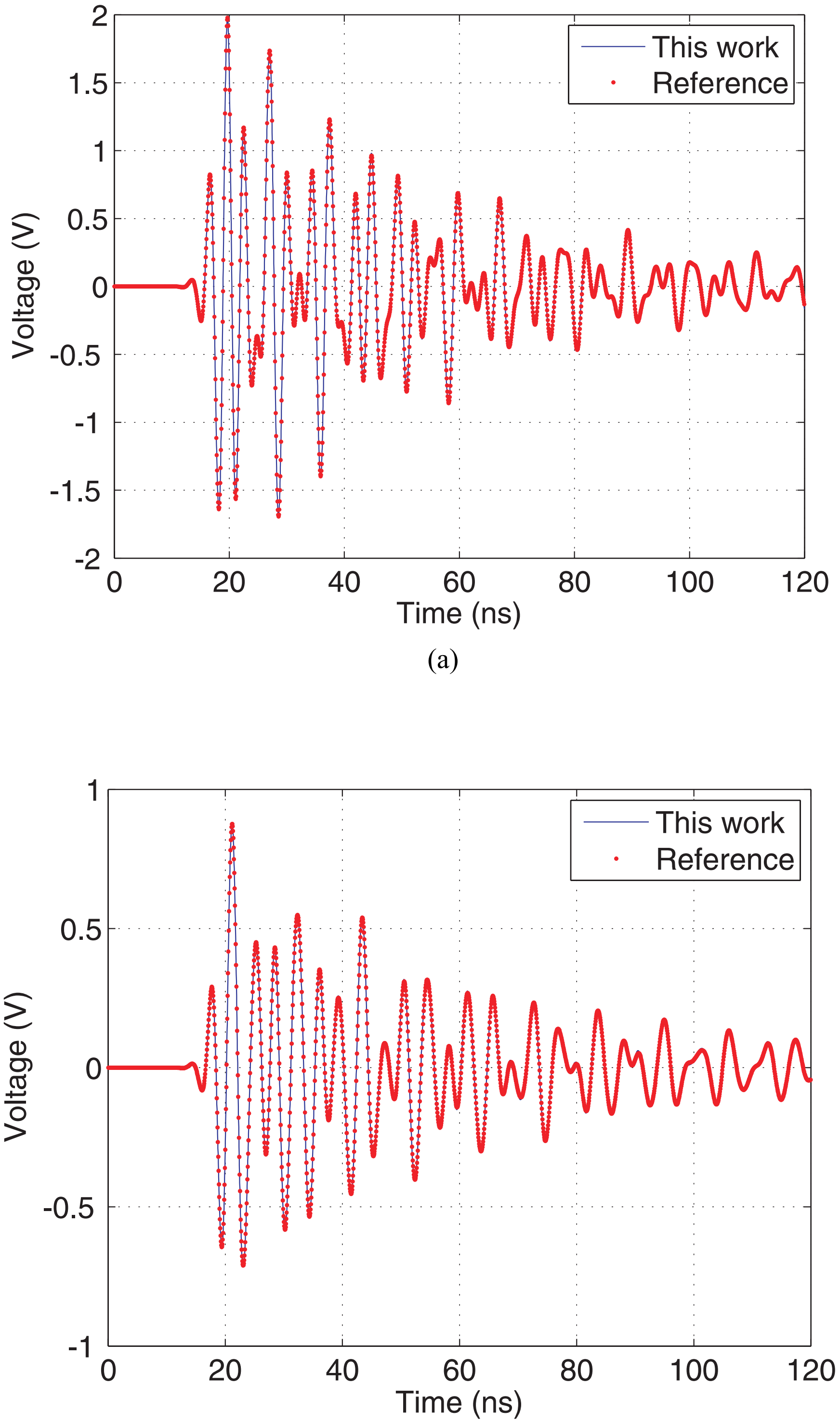

(a)

(b)

Figure 5.3: Transient voltages at the ports of the lumped network. (a) Port 1. (b) Port 2.

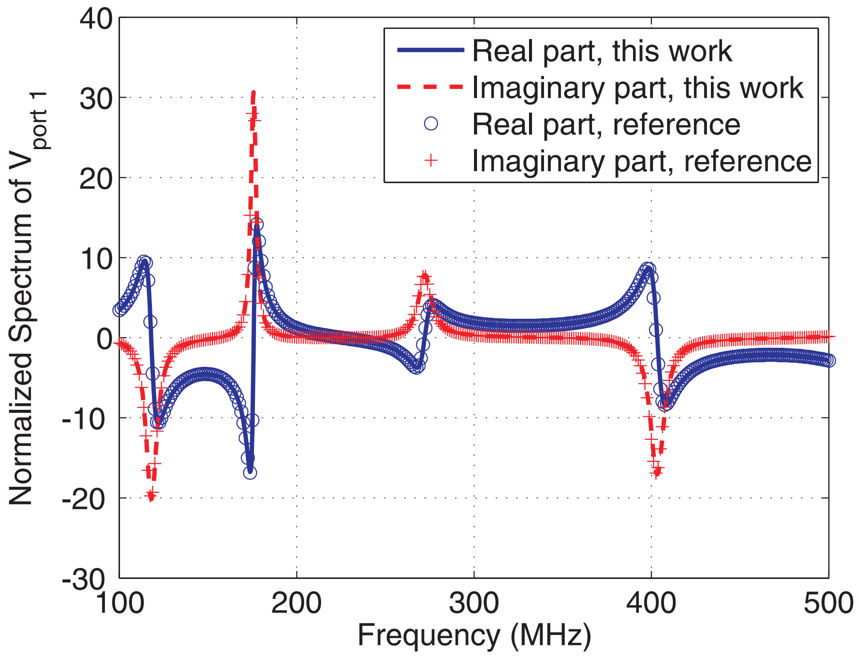

(a)

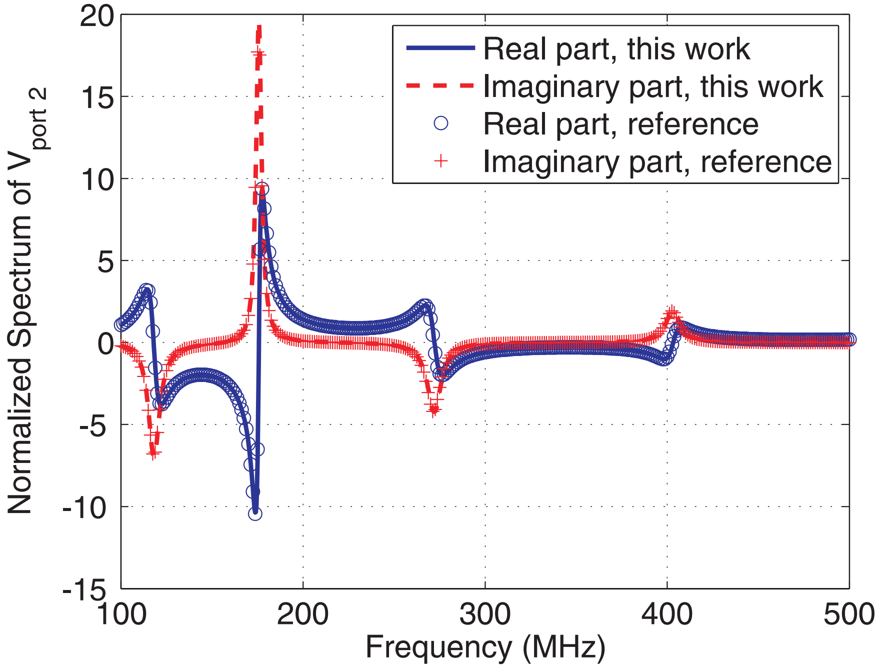

(b)

Figure 5.4: Normalized spectra of voltages at the ports of the lumped network. (a) Port 1. (b) Port 2.

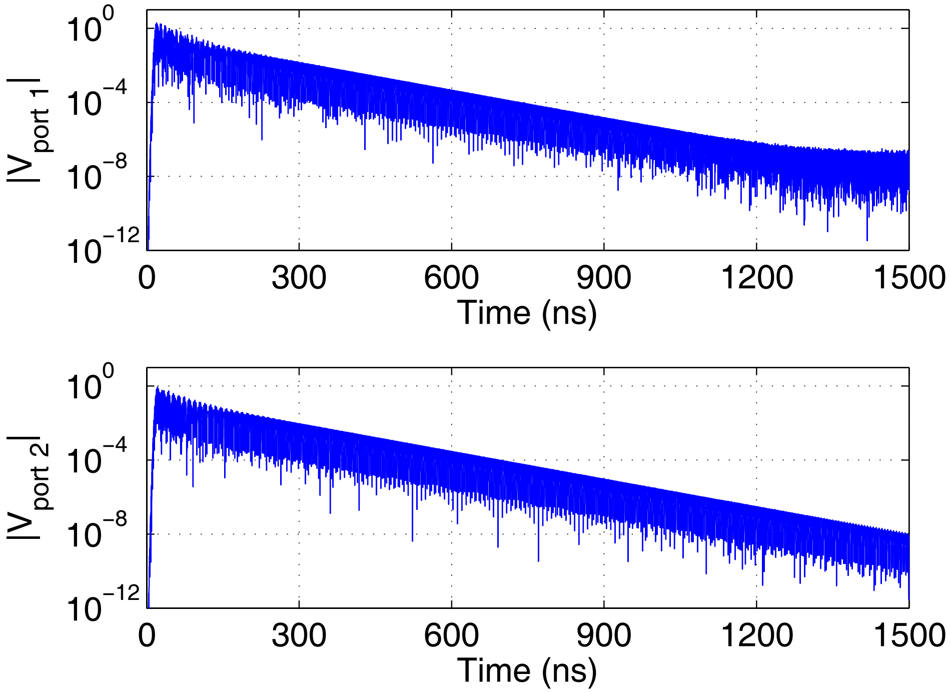

Figure 5.5: Magnitude of transient voltages at the ports of the lumped network up to 75,000 steps ($\Delta t = 20$ ps).

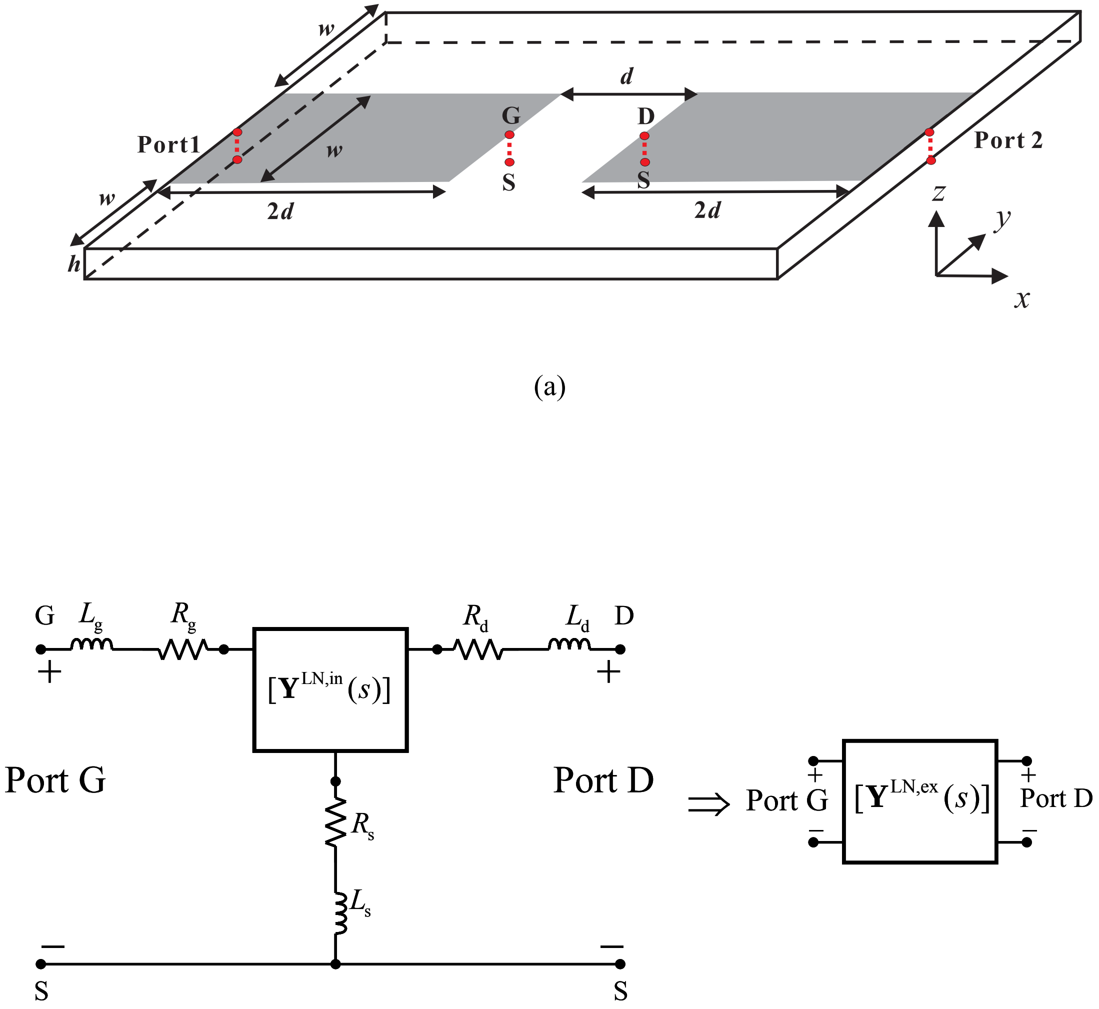
w
d
G
D
Port1
w
S
S
Port 2
w
2d
2d
z
y
h
x
G
L_g
R_g
R_d
L_d
D
+
+
$[\mathbf{Y}^{\mathrm{LN,in}}(s)]$
Port G
Port D
R_s
L_s
⇒ Port G
$[\mathbf{Y}^{\mathrm{LN,ex}}(s)]$
Port D
+
−
+
−
−
−
S
S

(a)

(b)

Figure 5.6: Microwave FET amplifier. (a) Common-source circuit configuration. (b) Small-signal extrinsic equivalent circuit model of the FET. $w = 0.79$ mm, $h = 0.254$ mm, $d = 0.5$ mm, $R_g = 1.39$ Ω, $L_g = 0.37$ nH, $R_d = 1.30$ Ω, $L_d = 0.23$ nH, $R_s = 0.76$ Ω and $L_s = 0.02$ nH. Left: intrinsic scheme. Right: extrinsic scheme.

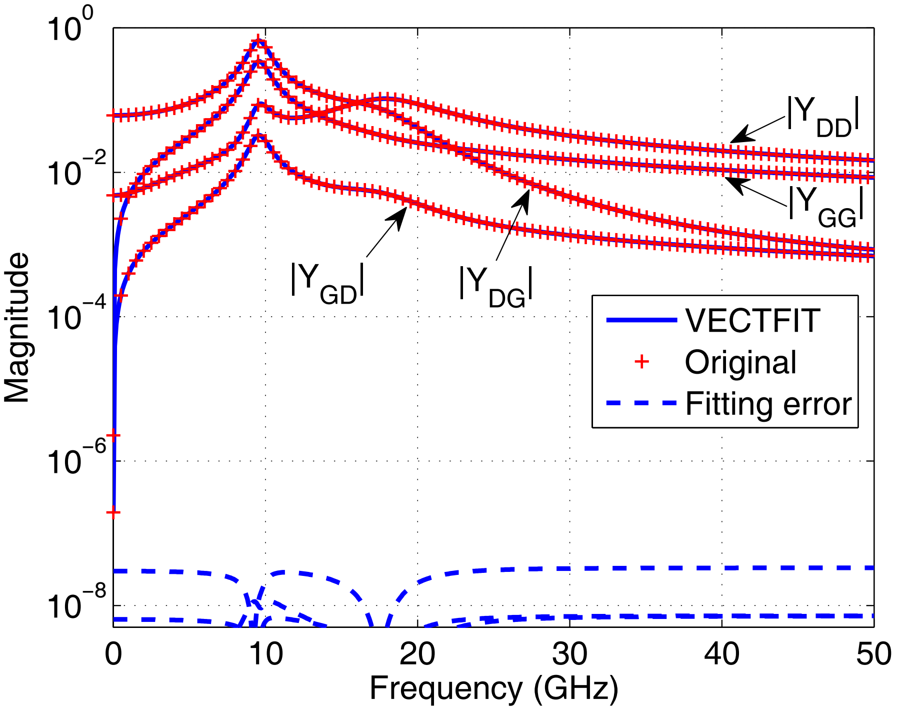

Figure 5.7: Magnitudes of the original and fitted admittance values and the fitting error.

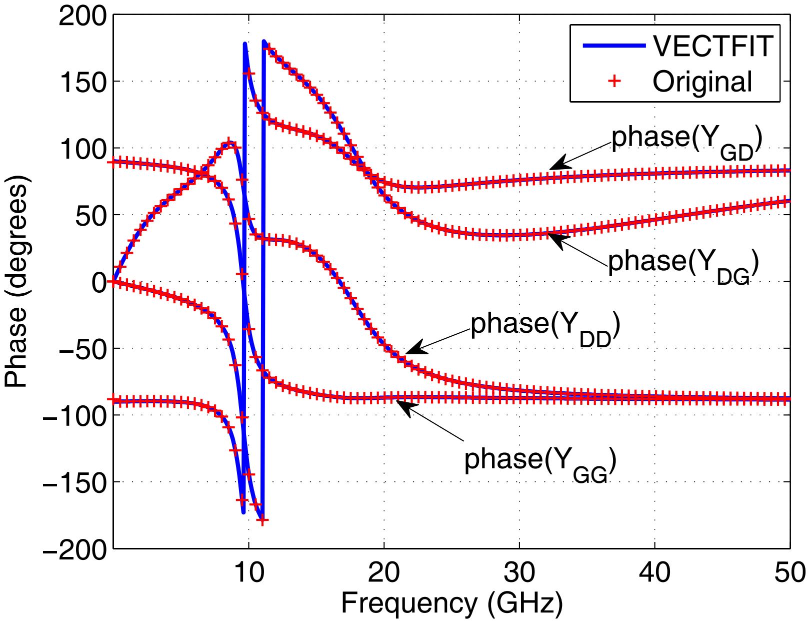

Figure 5.8: Phases of the original and fitted values of $[\mathbf{Y}^{\mathrm{LN,ex}}(s)]$ (defined at Ports G and D in Fig. 5.6(b)).

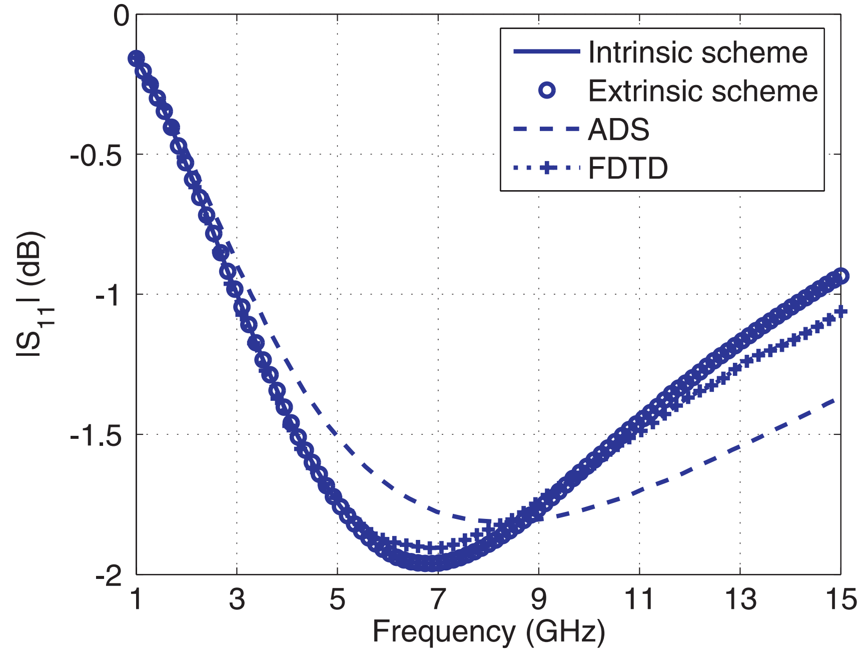

Figure 5.9: Magnitude of S_{11} of the microwave FET amplifier circuit.

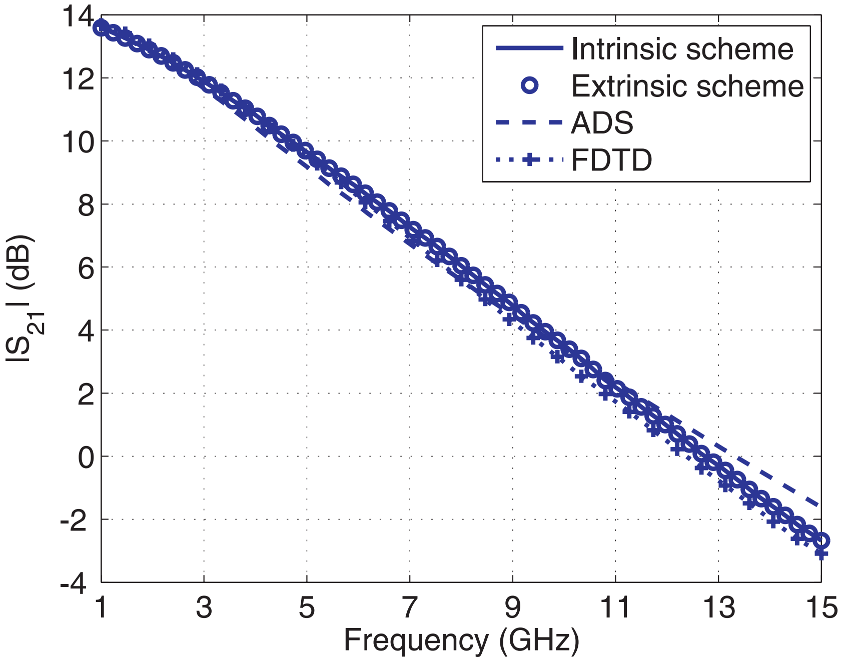

Figure 5.10: Magnitude of S_{21} of the microwave FET amplifier circuit.

CHAPTER 6

APPLICATION OF THE TREE-COTREE SPLITTING TECHNIQUE TO THE TDFEM ANALYSIS

6.1 Constraint on the Time-Step Size of the TDFEM

The TDFEM formulation in this dissertation leads to the following time-updating equation for the FEM unknowns at the *n*th time step, $\{e\}_n$:

$$\left[E_0\right]\{e\}_n = \left[E_1\right]\{e\}_{n-1} + \left[E_2\right]\{e\}_{n-2} + \frac{c_0\Delta t}{2}\left(\{b\}_n - \{b\}_{n-2}\right) \tag{6.1}$$

where $n = 1, 2, ..., T_{\max}$ is called the time index, Δt denotes the time-step size, and $[E_0]$, $[E_1]$, and $[E_2]$ are defined in (4.5)-(4.7), respectively.

The time-marching system in (6.1) is implicit and unconditionally stable in the sense that the choice of Δt is independent of the finite element mesh and solely based on the maximum frequency of interest. This seems particularly attractive for problems involving small finite elements, which would otherwise require a reduced time step to satisfy the Courant condition associated with an explicit time-marching scheme. However, a practical choice of Δt in (6.1) is often found to be largely constrained by the properties of the finite element mesh, instead of the stability consideration. This is because the application of the Newmark-beta time integration method to the wave equation can result in an ill-conditioned system matrix $[E_0]$ due to the combination of the mass and stiffness matrices. As Δt becomes larger, the system matrix becomes more ill-conditioned due to an increased weighting of the stiffness matrix; therefore, when an iterative solver is used to solve such a linear system in (6.1), the number of iterations required to obtain a specified residual will generally increase. Observing the similarity between the formulations of the frequency-domain FEM [1], [2] and the TDFEM, the constraint on the time-step size in the TDFEM is analogous to the low-frequency "breakdown" in the frequency-domain FEM; namely, if the operating frequency becomes very low, iterative solutions of the frequency-domain FEM system of equations may converge very slowly or even fail to converge. This is due to the fact that the null space of the curl operator is spanned by pure gradient bases and the dimension of the null space is equal to the unconstrained nodes in the finite element mesh. The constraint on the time-step size significantly limits the performance of the TDFEM in the cases when a large Δt is needed, for example, in low-frequency applications or when $[E_0]$ is ill-conditioned due to an extremely nonuniform mesh.

Moreover, the conventional TDFEM encounters the problem of low-frequency or late-time drift [2], due to the fact that the second-order wave equation in (6.1) supports a nontrival pure-gradient solution $-(at+b)\nabla\varphi$ when $\sigma = 0$ and $\mathbf{J}^{\text{imp}} = 0$, where φ denotes a scalar potential and *a* and *b* are constant in time [2]. Once this nonphysical static mode is excited, the solution of the TDFEM suffers a late-time linear growth. Various approaches have been proposed to suppress this phenomenon and stabilize the wave equation [87-89]. Although these methods can eliminate the late-time drift in the solution, they do not reduce the iteration count in an iterative solution when large time steps are used.

Recently, a tree-cotree splitting (TCS) algorithm has been introduced to remedy the low-frequency problem in the frequency-domain FEM [90-94] by adopting pure gradient and curl-conforming basis functions for approximating the electrostatic and magnetic-induced components of the electric field, respectively. This algorithm was developed originally for solving eddy-current problems [90] and was then applied successfully to the frequency-domain FEM analysis for waveguide structures [91, 92] and more recently, to a fast broadband analysis of high-speed circuits and interconnects [93, 94]. The TCS algorithm was also adopted to form a divergence-free constraint in order to suppress the late-time linear drift [87], a problem associated with the conventional TDFEM [2]. In this approach the TCS-based constraint equations were applied to the right-hand-side vector of the TDFEM system of equations while the TDFEM system matrix remained unchanged since the basis functions to form the system matrix were still conventional vector bases.

In this chapter, we apply the TCS algorithm to the TDFEM to alleviate the constraint on the time-step size and to improve the convergence of iterative solutions at each time step. Compared with the conventional TDFEM, application of the TCS algorithm maintains the accuracy of the TDFEM solution but significantly reduces the number of iterations per time step for a preconditioned iterative solver to converge when the time-step size becomes relatively large. In addition, because the null space of the curl operator is now represented by the pure gradient basis functions, the formulation is also free of late-time linear drift or instability.

6.2 Methodology

6.2.1 The TCS Algorithm

From Gauss's law for the magnetic flux density and Faraday's law [22], it can easily be derived that the electric field $\mathbf{E}(\mathbf{r},t)$ can be decomposed into two components as

$$\mathbf{E}(\mathbf{r},t) = -\nabla\phi(\mathbf{r},t) - \frac{\partial}{\partial t}\mathbf{A}(\mathbf{r},t) \tag{6.2}$$

where ϕ is the electric scalar potential and **A** is the magnetic vector potential. When nodal basis functions N_j and edge basis functions $\mathbf{N}_j$ are adopted to expand ϕ and **A**, respectively, (6.2) can then be written as

$$\mathbf{E}(\mathbf{r},t) = -\nabla\left[\sum\phi_j(t)N_j(\mathbf{r})\right] - \frac{\partial}{\partial t}\left[\sum a_j(t)\mathbf{N}_j(\mathbf{r})\right] = \sum e_j^g(t)\mathbf{N}_j^g(\mathbf{r}) + \sum e_j^r(t)\mathbf{N}_j^r(\mathbf{r}) \tag{6.3}$$

where $\mathbf{N}_j^g(\mathbf{r}) = \nabla N_j(\mathbf{r})$ is a pure-gradient function and $\mathbf{N}_j^r(\mathbf{r})$ denotes the conventional edge basis function. The superscript "*r*" indicates the rotational-like property of edge basis functions and thus is used to distinguish them from pure-gradient functions carrying a superscript *g*. This notation will be used throughout this chapter. Equation (6.3) suggests employing two different basis functions, $\mathbf{N}_j^g(\mathbf{r})$ and $\mathbf{N}_j^r(\mathbf{r})$, to approximate the electric- and magnetic-induced components of $\mathbf{E}(\mathbf{r},t)$, respectively. In other words, the original edge basis space can be decomposed into the irrotational and rotational-like subspaces. Mathematically, any sufficiently smooth vector field can be decomposed into an irrotational (curl-free) vector field and a solenoidal (divergence-free) vector field, a fact known as the Helmholtz decomposition. Since curl-conforming basis functions are not purely solenoidal, (6.3) actually represents an inexact Helmholtz decomposition for the edge-element approximation.

Next, we apply the TCS algorithm to the TDFEM that employs both pure-gradient and edge basis functions to expand an electric field. Similar to its application in the frequency-domain FEM, the very first step is to find a rooted spanning tree of a given finite element mesh which is also a connected graph. Starting from a root or a reference node, a spanning tree connects all other nodes in the finite element mesh through a selected group of edges called tree edges. The remaining edges are called cotree edges. When there are perfectly electrically conducting (PEC) boundaries or structures, all the PEC nodes are treated as a single node and chosen as the root. This case requires special care because any paths connecting two PEC nodes are considered as cycles and are forbidden when constructing a spanning tree. For a mesh with no PEC boundaries or structures, any node in the mesh can be chosen as a root. To maximize the performance of the TCS algorithm, the root should be chosen on the outermost boundary and those on the corners should be avoided [93, 94]. Finding a spanning tree on a given finite element mesh is actually a minimum spanning tree (MST) problem (when all links (edges) are equally weighted), which has been well studied in graph theory [95]. In this case the spanning tree is not unique. Through various numerical experiments, it is found that choosing different spanning trees would not affect the performance of the algorithm.

In this work we adopt a simplified MST algorithm [93, 94] which is summarized briefly as follows.

Initialization:

rootlist: contains all the nodes treated as root (for example, all PEC nodes).

Iterative Process:

```
While rootlist is not empty
    Extract the first node in rootlist into v.
    For all the neighboring nodes of v, denoted as Nv[i],  i = 1, 2, ⋯.
        If the following conditions 1~4 are all satisfied simultaneously, then Link{v, Nv[i]} is identified as a tree edge and add Nv[i] to the rootlist.
```

Conditions:

1. *Nv*[*i*] is not a PEC node;
2. *Nv*[*i*] is not already in the tree;
3. Link{*v*, *Nv*[*i*]} does not connect a *port* node to a node that does not belong to the same port;
4. Link{*v*, *Nv*[*i*]} is not associated with a lumped port interface.

Conditions 3 and 4 are included to facilitate the inclusion of the time-domain WPBC and lumped port interface, which will be discussed in the following subsections. Figure 6.1 illustrates a sample spanning tree on a triangular mesh.

After a spanning tree is constructed, the original edge set has been split into two groups: tree and cotree edges. The next step is to remove all the edge basis functions associated with tree edges, which can be implemented easily in any existing FEM code by excluding their contributions to the system matrix. After that, pure-gradient basis functions defined on all the nodes except for the root are added. As a result, the electric field is expanded using the modified set of basis functions as

$$\mathbf{E} = \sum_{j\in\text{free nodes}} e_j^g \mathbf{N}_j^g + \sum_{j\in\text{cotree edges}} e_j^r \mathbf{N}_j^r = \sum_j e_j^{g\cup r} \mathbf{N}_j^{g\cup r} \tag{6.4}$$

where $e_j^{g\cup r}$ and $\mathbf{N}_j^{g\cup r}$ are unified notations for convenience. Because in a spanning tree the number of tree edges is always equal to the number of nodes excluding the root, the total number of basis functions and hence the dimension of the TDFEM system matrix remain unchanged, which ensures the same level of accuracy of the TDFEM solution. With the original edge bases replaced by the modified set in (6.4), we arrive at the modified TDFEM time-marching system

$$[\tilde{E}_0]\begin{Bmatrix}\{e^r\}_n\\\{e^g\}_n\end{Bmatrix}=[\tilde{E}_1]\begin{Bmatrix}\{e^r\}_{n-1}\\\{e^g\}_{n-1}\end{Bmatrix}+[\tilde{E}_2]\begin{Bmatrix}\{e^r\}_{n-2}\\\{e^g\}_{n-2}\end{Bmatrix}+\frac{c_0\Delta t}{2}\left(\begin{Bmatrix}\{b^r\}_n\\\{b^g\}_n\end{Bmatrix}-\begin{Bmatrix}\{b^r\}_{n-2}\\\{b^g\}_{n-2}\end{Bmatrix}\right)\qquad(6.5)$$

where the expressions of the modified matrices can be derived easily. For example,

$$[\tilde{E}_0]=\begin{bmatrix}\frac{c_0^2\Delta t^2}{4}[S^{rr}]+[M^{rr}]+\frac{c_0\Delta t}{2}([G^{rr}]+[A^{rr}]) & [M^{rg}]+\frac{c_0\Delta t}{2}([G^{rg}]+[A^{rg}])\\ [M^{gr}]+\frac{c_0\Delta t}{2}([G^{gr}]+[A^{gr}]) & [M^{gg}]+\frac{c_0\Delta t}{2}([G^{gg}]+[A^{gg}])\end{bmatrix}\qquad(6.6)$$

where the superscripts *g* and *r* indicate that the testing or basis functions belong to either the pure gradient subspace or the rotational-like subspace.

6.2.2 Inclusion of the Time-Domain WPBC

Constructed based on multimodal expansion and modal orthogonality, the time-domain WPBC described in Section 2.2.4 provides a rigorous truncation boundary at a waveguide port. It has been shown that the time-domain WPBC can be written as a third-kind boundary condition in (2.30). One of the key points of implementing the time-domain WPBC in the TCS-enabled TDFEM is to evaluate the projection of modal fields onto each basis function over the port surface, or mathematically as

$$\Phi_{ipm}^{\mathrm{TEM/TE/TM}}=\iint_{S_p}\mathbf{N}_i^{g\cup r}\cdot\mathbf{e}_{(t)pm}^{\mathrm{TEM/TE/TM}}\,dS\qquad(6.7)$$

where $\mathbf{e}_{p0}^{\mathrm{TEM}}$, $\mathbf{e}_{pm}^{\mathrm{TE}}$, and $\mathbf{e}_{tpm}^{\mathrm{TM}}$ are the TEM, the *m*th TE, and the transverse component of the *m*th TM modal electric fields at the port interface, respectively. The term $\mathbf{N}_i^{g\cup r}$ denotes either a pure-gradient basis function on a non-root node or an edge basis function along a cotree edge, which has already been discussed in the preceding subsection. On the other hand, $\mathbf{e}_{p0}^{\mathrm{TEM}}$, $\mathbf{e}_{pm}^{\mathrm{TE}}$, and $\mathbf{e}_{tpm}^{\mathrm{TM}}$ are often computed numerically based on a two-dimensional finite element analysis on the waveguide port. Attention is needed to ensure the consistency of the TCS on the port mesh as well as on the mesh for the entire structure, since the former is a direct result of the latter. For example, if a tree edge connects a node on a port surface to a node that is not on the same port surface, there are no complications for the three-dimensional TDFEM analysis. However, on the port mesh there will be floating nodes that are not connected by any tree edges on the port surface, which will create complications for the two-dimensional modal calculation. For this reason, the constraint in Condition 3 needs to be included to avoid this situation.

Once a proper port mesh with a consistent TCS is constructed, the TE modes $\mathbf{e}_{pm}^{\mathrm{TE}}$ and the corresponding cutoff frequencies can be calculated through the following sparse linear eigensystem:

$$[A]\{e_t^{g\cup r}\} = k_c^2[B]\{e_t^{g\cup r}\} \tag{6.8}$$

where

$$A_{ij} = \iiint_V \frac{1}{\mu_r}(\nabla_t \times \mathbf{N}_i^{g\cup r})\cdot(\nabla_t \times \mathbf{N}_j^{g\cup r})dV \tag{6.9}$$

$$B_{ij} = \iiint_V \varepsilon_r \mathbf{N}_i^{g\cup r}\cdot \mathbf{N}_j^{g\cup r} dV\ . \tag{6.10}$$

Note that when either $\mathbf{N}_i^{g\cup r}$ or $\mathbf{N}_j^{g\cup r}$ is a pure gradient basis, the corresponding entry A_{ij} is zero. Figure 6.2 shows the field distribution of the computed TE_{10} mode of a rectangular waveguide port with and without applying the TCS algorithm.

The formulation above can also be modified into an $\mathbf{e}_t - e_z$ formulation [1, 2] to compute the TM modal fields $\mathbf{e}_{tpm}^{\mathrm{TM}}$. However, for a homogeneous port, a simpler approach to calculate $\mathbf{e}_{tpm}^{\mathrm{TM}}$ is to solve for the modal magnetic field $\mathbf{h}_{pm}^{\mathrm{TM}}$ first through a linear eigensystem similar to (6.9) with the Dirichlet boundary condition on the waveguide walls replaced by the Neumann boundary condition. It is important to point out that in the preceding subsection the spanning tree is built for the electric field formulation only and the corresponding TCS cannot be used in the magnetic field construction. Alternative approaches include building another tree based on boundary conditions for the magnetic field or simply calculating it without using the TCS. Once $\mathbf{h}_{pm}^{\mathrm{TM}}$ is obtained , $\mathbf{e}_{tpm}^{\mathrm{TM}}$ is simply given by $\hat{n}\times\mathbf{h}_{pm}^{\mathrm{TM}}$. Finally, to calculate the TEM mode $\mathbf{e}_{p0}^{\mathrm{TEM}}$, a static FEM analysis for calculating the electrostatic potential ϕ is performed which is then used in $\mathbf{e}_{p0}^{\mathrm{TEM}} = -\nabla_t \phi$. Since we do not use the TCS technique in this case, all the TCS-related information and the treatment of tree edges should be ignored.

6.2.3 Inclusion of Lumped Port Interfaces

A lumped port interface is defined as a path in a finite element mesh that connects two nodes where a lumped component is applied. Through this path, a lumped voltage can be defined and calculated from the TDFEM solution and a lumped current can be applied as excitation. As shown in Fig. 6.3, a typical lumped port interface contains one or multiple FEM edges.

Lumped port interfaces are critical in the formulation of the TDFEM-based hybrid field-circuit solver in Chapter 4 which includes simple stamping of *V-I* relations and more advanced features such as hybridization with a SPICE-like circuit simulator as well as incorporation of multiport lumped networks in Chapter 5.

The compatibility of the TCS technique with the lumped port interface is especially important for the flexible time-stepping scheme presented in Section 4.4. This time-stepping scheme removes the requirement of using a global time-step size, and provides the freedom to choose different time-step sizes for FEM and circuit subsystems. For the sake of overall computational efficiency, it would be desired that the time-step size Δt^{FEM} for the FEM subsystem (usually of a much larger size than that of the circuit subsystem) be chosen as large as possible as long as the accuracy requirement for temporal sampling is satisfied. However, the constraint on Δt^{FEM} described in Section 6.1 not only significantly limits the performance of the TDFEM, but also makes the freedom of choosing Δt^{FEM} not very useful. Introduction of the TCS technique could help alleviate this limitation.

The lumped voltage along a lumped port interface (path *l*) can be expressed as

$$V_l = -\int_l \mathbf{E} \cdot \hat{l}\, dl = -\sum_{k \in l} e_k^{g \cup r} \int_l \mathbf{N}_k^{g \cup r} \cdot \hat{l}\, dl = -\sum_{k \in l} e_k^r \int_l \mathbf{N}_k^r \cdot \hat{l}\, dl - \sum_{k \in l} e_k^g \int_l \mathbf{N}_k^g \cdot \hat{l}\, dl \tag{6.11}$$

where e_k^r and e_k^g denote the FEM unknown coefficients associated with the cotree edges and non-PEC nodes on the lumped path l, respectively. The first term of (6.11) can be calculated easily since $\mathbf{N}_k^r$ is a conventional edge basis function with a nonzero value only along edge k and thus the line integration is only calculated along that edge as

$$\int_l \mathbf{N}_k^r \cdot \hat{l} dl = \int_{\text{Edge } k} \mathbf{N}_k^r \cdot \hat{l} dl . \tag{6.12}$$

The second term contains the contribution from the pure-gradient basis function $\mathbf{N}_k^g$. If k denotes a node in the middle of path l and thus shared by two adjacent edges $l(g^-)$ and $l(g^+)$, the line integral in the second term becomes

$$\int_l \mathbf{N}_k^g \cdot \hat{l} dl = \int_{\text{Edge } l(g^+)} \mathbf{N}_k^g \cdot \hat{l} dl + \int_{\text{Edge } l(g^-)} \mathbf{N}_k^g \cdot \hat{l} dl = 0 \tag{6.13}$$

and thus has no contribution. Only the nodes at the two ends of path l have a nontrivial contribution to (6.11) as long as they are not PEC nodes. Similarly, expressions for a lumped current excitation along a lumped port interface can be derived, as well as the stamping formulas and expressions for the coupling matrix entries in the hybrid field-circuit solver.

For practical purposes, we impose Condition 4 in Section 6.2.1 to prevent any edges associated with lumped port interfaces from being selected as tree edges. Therefore, when implementing the TCS algorithm, if the path connects two PEC nodes, there is no modification related to lumped port interfaces. If any of the nodes at the two ends of the path are not on the PEC boundary, only their contributions need to be included and all the interior nodes can simply be ignored.

6.2.4 Diagonal Scaling

It is reported that when the TCS algorithm is applied to the frequency-domain FEM, the condition number of the resulting FEM system matrix decreases at low frequencies but increases at high frequencies [93]. However, after a diagonal scaling technique is applied, the TCS-enabled FEM system becomes better conditioned in both low and high frequency regions [94]. By observing that the resolution of high frequencies in the frequency-domain FEM corresponds to a small time step in the TDFEM, we can also apply the diagonal scaling technique to the TCS-enabled TDFEM system to improve its performance.

If we define two diagonal matrices $[D^L]_{ii} = [D^R]_{ii} = [E_0]_{ii}^{-1/2}$, (6.5) can be scaled as

$$\begin{aligned} [D^L][\tilde{E}_0][D^R]\{\tilde{e}^{g\cup r}\}_n &= [D^L][\tilde{E}_1][D^R]\{\tilde{e}^{g\cup r}\}_{n-1} + [D^L][\tilde{E}_2][D^R]\{\tilde{e}^{g\cup r}\}_{n-2} \\ &\quad + [D^L]\frac{c_0\Delta t}{2}\left(\{b^r\}_n - \{b^r\}_{n-2}\right) \end{aligned} \tag{6.14}$$

where $\{\tilde{e}^{g\cup r}\} = [D^R]^{-1}\{e^{g\cup r}\}$. After diagonal scaling, the system matrix $[D^L][\tilde{E}_0][D^R]$ remains symmetric while all diagonal entries become unity. Note that the above diagonal scaling technique is actually a simple preconditioner. In practical implementations there are many advanced preconditioners, such as the incomplete LU (ILU) [1], which may internally perform this diagonal scaling.

6.3 Numerical Results

In this section, several numerical examples are simulated using the TCS-enabled TDFEM to verify the implementation of the proposed formulation and demonstrate its performance and applications. All the computations were performed on a single SGI Altix 350 computer that uses Intel Itanium II 1.5 GHz processors. By using the PETSc library [96], the flexible GMRES solver with the ILU preconditioner known as ILUT [97] is adopted to solve the TDFEM system of equations with or without the TCS algorithm applied. The restart number used in the GMRES solver is set to be 30 and the reverse Cuthill-McKee (RCM) reordering technique [98] is adopted to reduce the bandwidth of the TDFEM system matrix. Reordering techniques are often critically important to the success of iterative solution techniques, particularly for geometry that is long in one direction and narrow in the other directions.

6.3.1 Performance Tests

We first consider an air-filled, 1 m long, coaxial cable with the inner and outer PEC conductors having a radius of 4 and 8 mm, respectively. The cable is driven through a lumped port interface at the driving end by a current source in parallel with a 5 Ω resistor, and terminated by a lumped port interface at the load end with a 10 nH shunt inductor. The excitation function is a Gaussian pulse with a frequency bandwidth from DC to 200 MHz. This structure is simulated by the TDFEM with and without the TCS algorithm using various time-step sizes. Figure 6.4 shows the time profile of transient voltages recorded at the driven and load ports computed by the TCS-enabled TDFEM and compared to those obtained by the conventional TDFEM. The real and imaginary parts of the input impedance are plotted in Fig. 6.5. It is clear that excellent agreement is achieved between the two results, which indicates that application of the TCS algorithm in the TDFEM maintains accuracy.

Comparisons of computational performance between the two techniques as Δt increases over a wide range are given in Figs. 6.6-6.9. For the following computations, the excitation Gaussian pulse contains frequency components from DC up to 16.75 kHz, and the drop tolerance [97] for the ILUT preconditioner is set to 10^{-6}. First, the coaxial cable is discretized into 13,100 tetrahedrons and terminated with a 5 Ω lumped resistor, and Δt increases over a range of five orders of magnitude from 50 ps to 5,000 ns. Figure 6.6 records the average number of iterations per time step when the relative convergence tolerance is set to 10^{-6} and the number of ILUT fill-ins allowed in a row equals 25 and 40, respectively (labeled in Figs. 6.6 and 6.7 as the numbers in the parenthesis). Note that increasing the fill-in provides a better, albeit more expensive, preconditioner due to an increased memory requirement as well as a larger number of floating-point operations per iteration. In Fig. 6.6, it is shown that to a limited extent a better preconditioner helps to reduce the iteration count. However, without applying the TCS algorithm, the number of iterations still increases significantly with increasing Δt. For example, even if a better preconditioner is applied, as Δt approaches 200 ns the number of iterations per time step for this case exceeds 1,000 (not shown in Fig. 6.6), which makes the standard simulation of limited practical utility. However, by applying the TCS algorithm, the number of iterations per time step remains small, and this is accomplished without further augmenting the memory requirements for the preconditioner.

It is evident in Fig. 6.6 that as Δt increases over such a wide range, the average number of iterations per time step required by the TCS algorithm remains nearly constant, independent of which preconditioner is applied. The significant reduction in the iteration count that is obtained by applying the TCS algorithm also leads to a significant speedup in the overall computation time. Figure 6.7 records the total solution time versus Δt for the two techniques when the excitation pulse contains frequency components up to 16.75 kHz. In this simulation, the required total time to reach the steady state is 500 μs. When the time-step size is chosen as 50 ps, 10^7 time steps are then needed to complete the time marching. As the time-step size increases, the number of required time steps correspondingly decreases. At 5,000 ns, we need only 100 time steps to complete the time marching. However, without TCS the iteration count per time step increases significantly with an increased time-step size, and consequently, this increase in the iteration count per time step quickly offsets the effect of a decreased number of required time steps. That is why the total solution time for the traditional TDFEM formulation initially decreases, but eventually increases rapidly as Δt increases. With the TCS applied, since the iteration counts almost remain a constant, the total solution time decreases linearly as Δt increases even up to 5,000 ns. As a result, the total solution time is reduced significantly from over 12,000 minutes to only a few seconds.

Next, the coaxial cable is discretized with approximately 272,000 tetrahedrons, terminated at both ends using the time-domain WPBC and excited by the same Gaussian pulse described above, which has a bandwidth from DC to 16.75 kHz. Similar performance of the TCS on the reduction of the number of iterations and total solution time is observed in Figs. 6.8 and 6.9, respectively, when Δt increases over a range of four orders of magnitude from 500 ps to 5,000 ns, the relative convergence tolerance is set to 10^{-4}, and the number of ILUT fill-ins allowed in a row equals 250. Note that the test case is so challenging for the conventional TDFEM that without the TCS the time-step size is constrained to very small values.

The number of iterations is usually related to the condition number of the matrix. Figure 6.9

shows the condition number of the TDFEM system as a function of Δt before and after diagonal scaling is applied for the previous example with 13,100 tetrahedrons. As can be seen, before diagonal scaling, the condition number of the system matrix obtained with the TCS algorithm is increased slightly; however, when combined with a simple diagonal scaling (internally done within the construction of the ILU preconditioner) the TCS algorithm yields a system matrix with a condition number that is usually several orders of magnitude lower than that of the other cases shown in Fig. 6.10.

6.3.2 Practical Examples

To further verify the implementation and test the performance, the TDFEM combined with the TCS algorithm is applied to more practical examples. The following examples exhibit a significant geometrical complexity as well as abundant simulation features, which include PEC boundaries, the first-order ABC, the time-domain WPBC, and near-to-far calculations [1, 2]. Simulation of these examples is challenging in the sense that the dimension of radiation apertures or radiation boundaries is significantly larger than that of the feed region. In addition, in order to accurately compute the input impedance or *S* parameters, the mesh density around the feed region need to be very high [2], and therefore, the finite element discretization results in an extremely nonuniform mesh.

The dimensions and parameters of an ultrawideband (UWB) Vivaldi antenna are given in Fig. 6.11. A stripline is used to feed the antenna, which is modeled as a TEM port. The transient modal voltage at the input wave port is plotted in Fig. 6.12. The *S* parameters at the input waveport and the radiation patterns in the *xz* plane at two different frequencies are displayed in Figs. 6.13 and 6.14, respectively. The excellent agreement between the conventional TDFEM and TCS-enabled TDFEM indicates that application of the TCS algorithm maintains the accuracy of results even with high geometrical and modeling complexities. Moreover, due to the extremely nonuniform FEM meshes, without the TCS algorithm a very small time-step size that grossly oversamples the time signals has to be used to expedite the convergence at each time step. By using the TCS, we can adopt a time-step size larger than the oversampled ones and achieve a speedup factor up to 3.1 when measured in the total simulation time, while still maintaining the level of the accuracy.

The next example is a coaxial-fed circular waveguide antenna, which is known as the Vlasov antenna. The geometrical information of the Vlasov antenna is available in [2, 11]. The dimensions of the geometrical features of the antenna vary from a few millimeters in the feed region to 561.5 mm at the radiating aperture. The total number of unknowns is nearly 1 million. The TCS-enable TDFEM is able to solve the problem in 1,058 minutes with a peak memory requirement of approximately 3.4 GB. The average number of iterations per time step is about 8. The computed return loss at the coaxial port is plotted in Fig. 6.15 and agrees well with reference data by VOLMAX [99]. It is reported that applying the conventional TDFEM to the entire structure is rather difficult [11, 12]. When an iterative solver is used, the number of iterations per time step becomes quite large [11]. With the same settings for the iterative solver and the preconditioner, the average number of iterations reaches 35. When a direct solver is applied, the peak memory requirement reaches 16 GB [12].

To show that the TCS technique helps improve the efficiency of the hybrid field-circuit simulation with the local time-stepping scheme in Chapter 4.4, we revisit the chip-to-package interconnecting examples. It has been pointed out that the total computational cost is partly related to the average iteration steps to solve a linearized problem at each Newton step at the synchronous time point. Such a linearized problem involves the FEM subsystem, and thus the average iteration counts increase significantly as Δt^{FEM} increases. To show this, we consider the same structure excited by a "slow pulse" [47] with rise and fall times, and width, that are ten times larger than the previous values, and we maintain Δt^{CKT1} equal to 2 ps and increase the Δt^{FEM} from 2 ps to 50 ps. Without the application of the TCS techniques, the average iteration count increases from 4 to over 17. In contrast, when the TCS is applied, the average iteration count remains around 4 to 5.

6.3.3 Suppression of the Late-Time Linear Drift and Instability

To demonstrate that the use of the TCS algorithm and the introduction of pure gradient basis functions help suppress the late-time linear drift associated with the conventional TDFEM, we consider a lossless cubical PEC cavity with a side length of 0.8 m and a lumped current excitation placed at the center of the cavity. The excitation current has a profile of a Gaussian pulse with 99% of the power in a frequency band from DC to 200 MHz. Figure 6.16 shows the lumped voltage recorded by integrating the electric fields along the FEM edges through which the lumped current excitation is applied. Without the TCS algorithm, the nonphysical linear drift in the traditional solution of this type of application is evident after 50,000 time steps. In contrast, the TDFEM combined with the TCS successfully suppresses the emergence of the nonphysical linear drift.

Another important test of the low-frequency stability of the proposed method is the computation of late-time responses to single-tone sinusoid excitations of extremely low frequency. Although a Gaussian excitation in the previous examples has frequency content down to DC, the energy is actually distributed across a broad frequency range. On the other hand, because sinusoidal excitation has essentially all its energy at the single frequency (with the exception of turn-on transients), it may more readily and more obviously expose any potential issues in the time-domain simulations. Here we revisit the test geometry for Figs. 6.5 and 6.6, which is now excited by tapered single-tone sinusoid signals of 10 Hz and 1 Hz, respectively. For the ILUT preconditioner, the drop tolerance is set to 10^{-6}, and the number of ILUT fill-ins allowed in a row equals 40. Table 6.1 records the maximum time to which the TCS-enabled TDFEM simulation can march on before the results are tampered by the accumulated iterative solution errors. Such accumulated solution errors can be suppressed by reducing the relative residue tolerance. With the help of the TCS, the TDFEM simulation can easily go up to a few thousand cycles under the single-tone excitation of extremely low frequency. For both 10 Hz and 1 Hz cases, the time-step sizes correspond to 40 points per period, which is 3~4 orders of magnitude larger that the maximum time-step size Δt in Fig. 6.5, while the average iteration count per time step is still around 7.

6.4 Summary

This chapter described the application of the TCS algorithm to the TDFEM analysis to reduce the number of iterations per time step and accelerate the time-marching process by adopting a larger time-step size within the requirement of the temporal sampling rate.

The conventional TDFEM formulation using edge basis functions leads to an unconditionally stable time-marching scheme such that, ideally, the time-step size is solely dependent on the temporal variation of the field. However, when an iterative solver is applied to solve the TDFEM system, the number of iterations per time step increases significantly as the time-step size increases. This additional constraint on the time-step size limits the efficiency and performance of the TDFEM in many practical applications.

Decomposition of the electric field into the electrostatic and magnetic-induced components suggests the use of both pure gradient and edge basis functions to expand the electric field in the TDFEM, which is enabled by the TCS algorithm performed on the edge set of a three-dimensional finite element mesh. The FEM edge set is then split into tree and cotree edges, and the edge basis functions associated with tree edges are replaced by an equal number of pure gradient basis functions defined on non-root nodes. It is found that after special care is exercised, use of the TCS algorithm is compatible with important advanced features in the TDFEM, such as the time-domain WPBC and lumped port interfaces for hybrid field-circuit simulations. Compared with the conventional TDFEM, it was shown that the use of the TCS algorithm maintains the accuracy of the TDFEM solution and can significantly reduce the iteration count per time step for a preconditioned iterative solver to converge, which is particularly important when the time-step size is desired to be relatively large for problems containing low-frequency components or highly nonuniform meshes. It was also demonstrated that the TCS algorithm and introduction of pure gradient basis functions in the TDFEM can effectively suppress the late-time linear drift and instability.

6.5 Figures and Tables

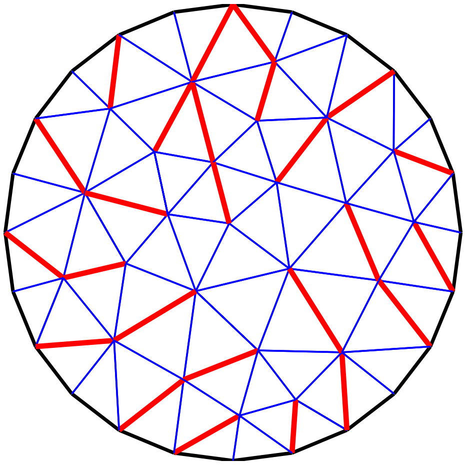

Figure 6.1: A sample TCS on the mesh of a circular waveguide. Tree edges are represented by thick lines. Edges on the outermost boundary are PEC edges.

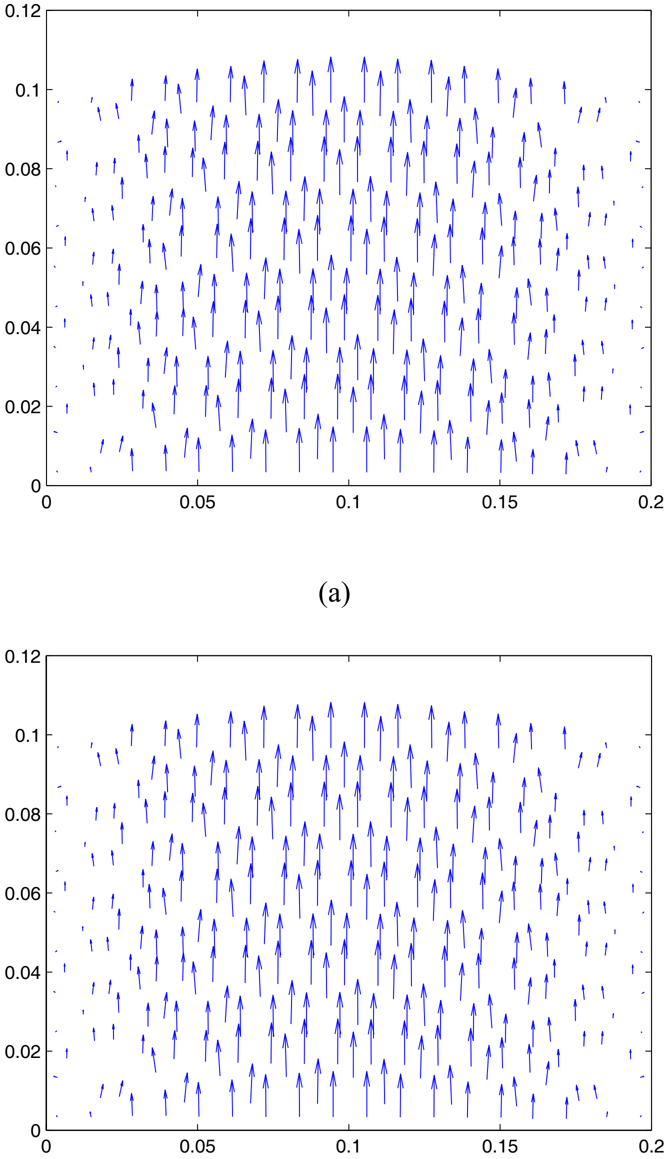

(a)

(b)

Figure 6.2: Field distribution of the computed TE_{10} mode of a rectangular waveguide port with and without the application of the TCS algorithm. Left: without the TCS. Right: with the TCS.

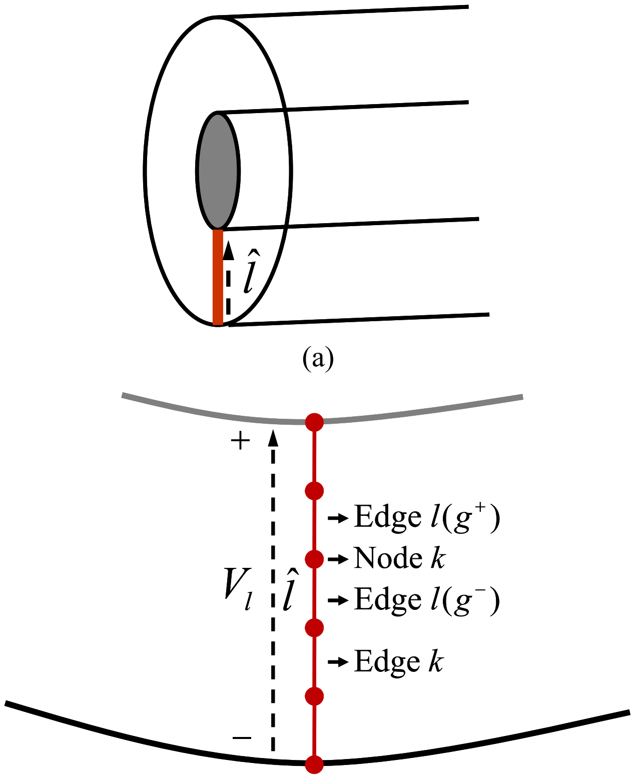
$\hat{l}$
+
V_l
$\hat{l}$
−
Edge $l(g^+)$
Node k
Edge $l(g^-)$
Edge k

(a)

(b)

Figure 6.3: A typical lumped port interface contains one or multiple FEM edges.

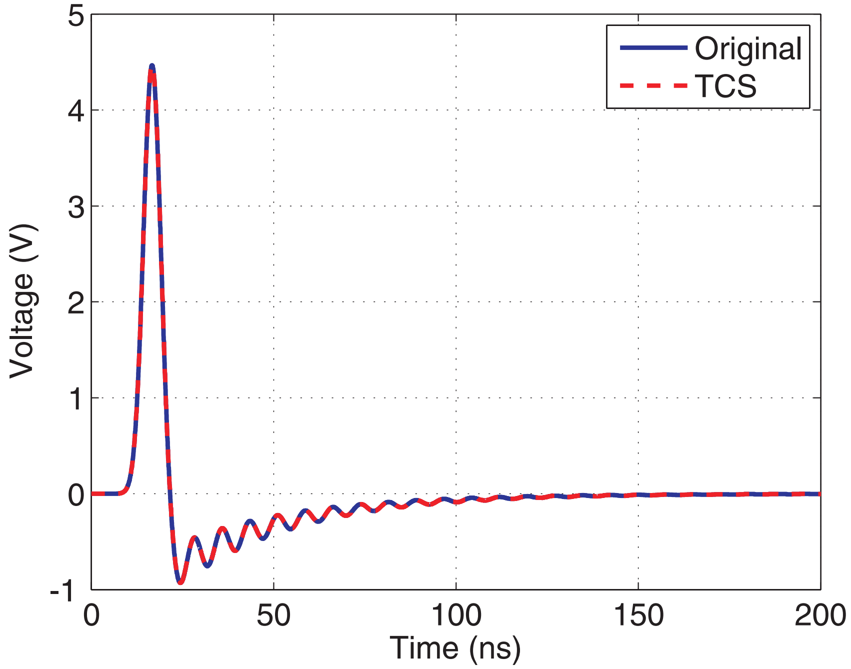

(a)

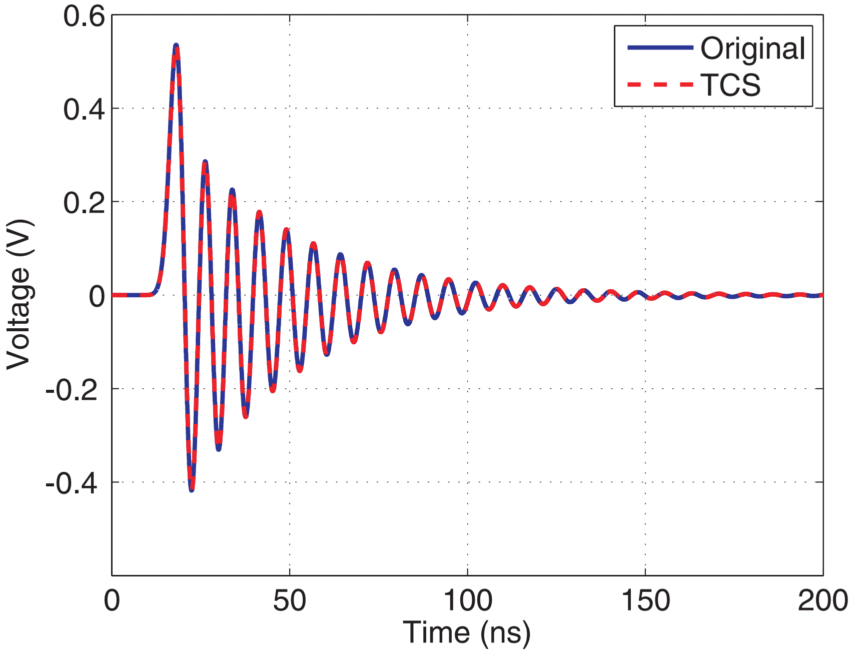

(b)

Figure 6.4: Transient voltages recorded at the lumped port interface across (a) the driven end and (b) the load end.

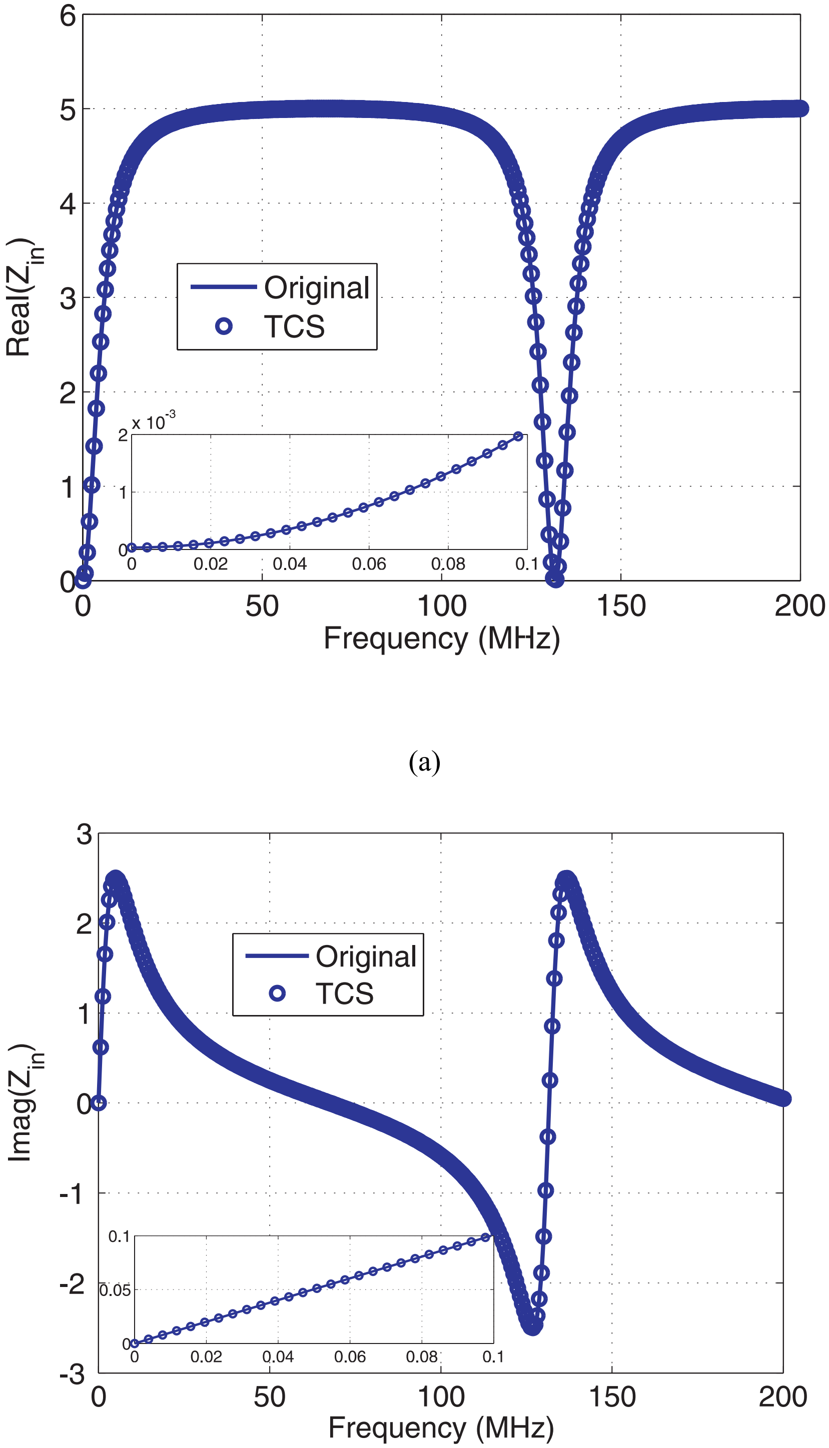

(a)

(b)

Figure 6.5: Computed input impedance with or without the application of the TCS algorithm. (a) Real part. (b) Imaginary part. Inserts: enlarged at the low-frequency region.

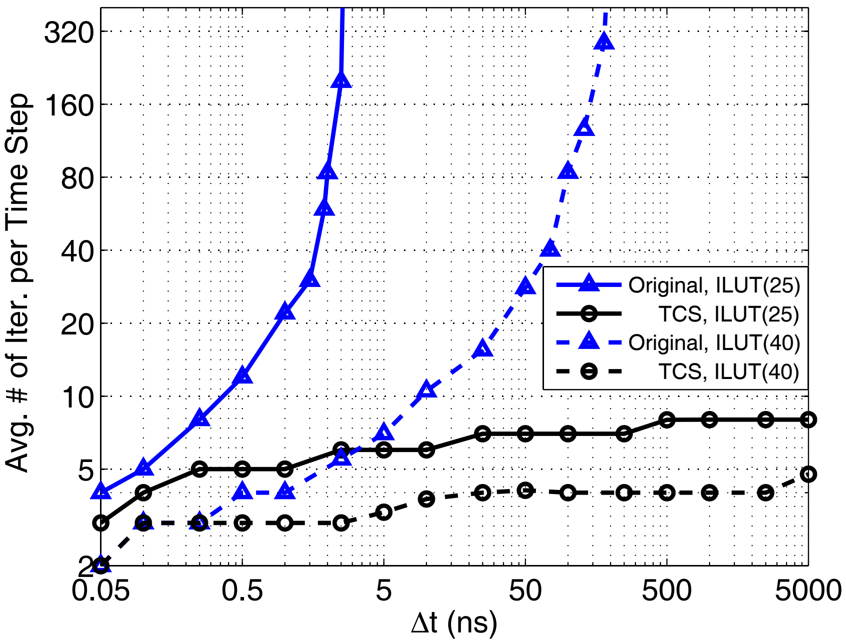

Figure 6.6: Average number of iterations per time step for the case of lumped port interfaces.

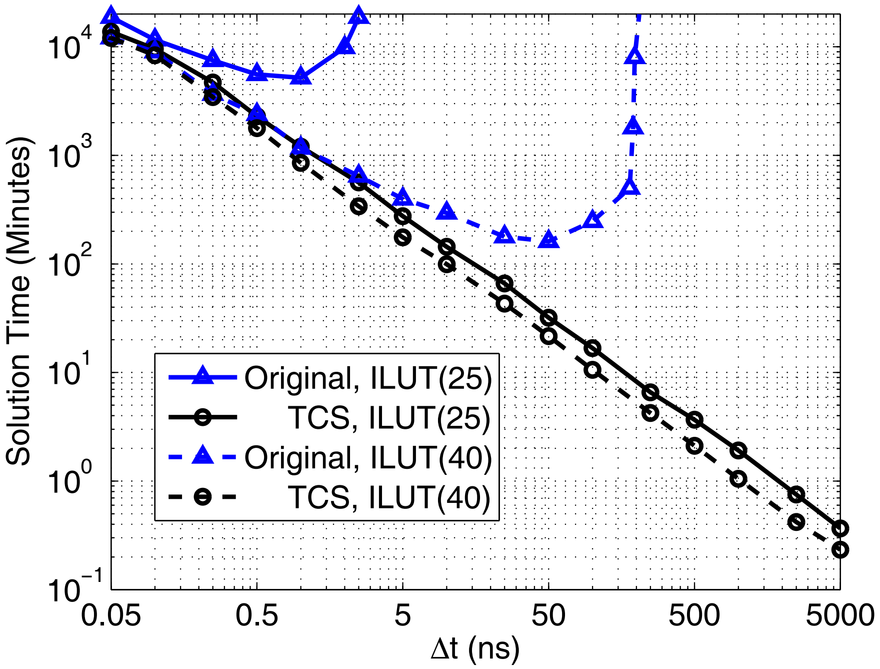

Figure 6.7: Total solution time for the case of lumped port interfaces. The required total time to reach the steady state is 500 μs, which corresponds to 10^7 time steps when $\Delta t = 50$ ps, and 100 time steps when $\Delta t = 5{,}000$ ns.

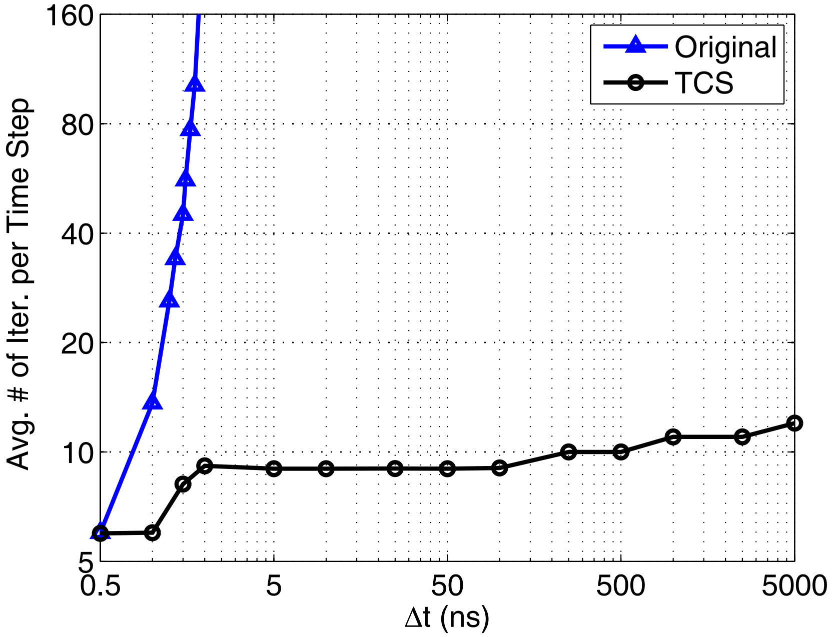

Figure 6.8: Average number of iterations per time step for the case of wave ports.

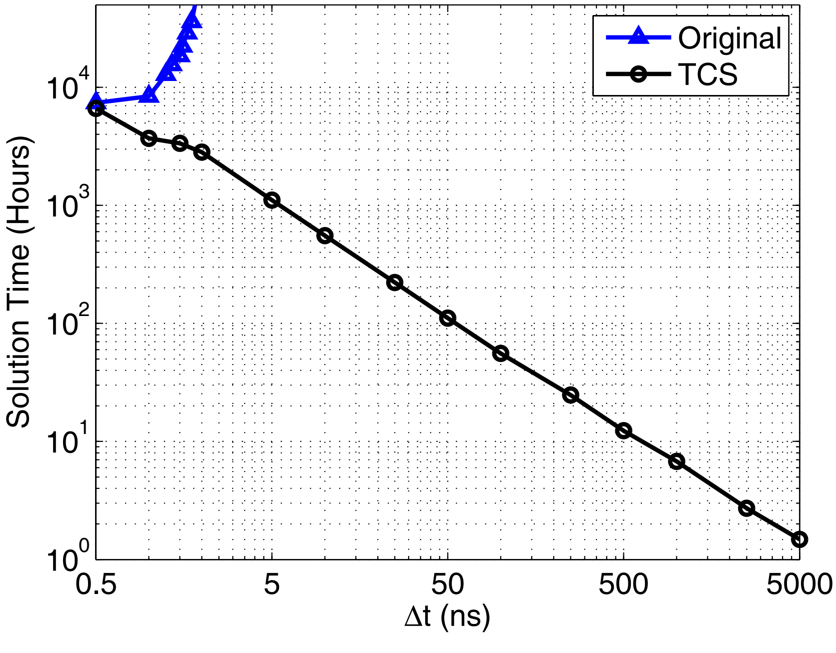

Figure 6.9: Total solution time for the case of wave ports. The required total time to reach the steady state is 500 μs, which corresponds to 10^6 time steps when $\Delta t = 500$ ps, and 100 time steps when $\Delta t = 5{,}000$ ns.

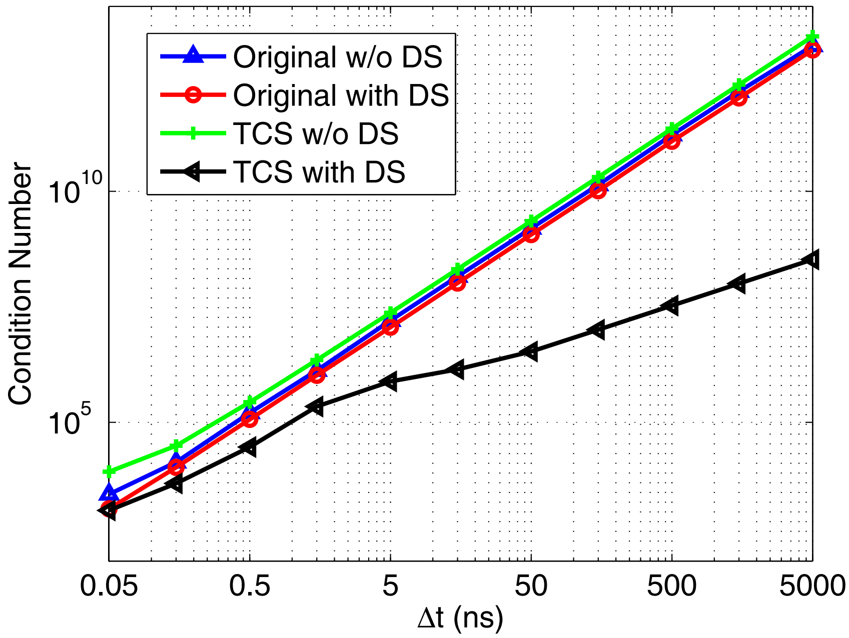

Figure 6.10: Condition number of the system matrices of the two techniques with and without diagonal scaling (DS).

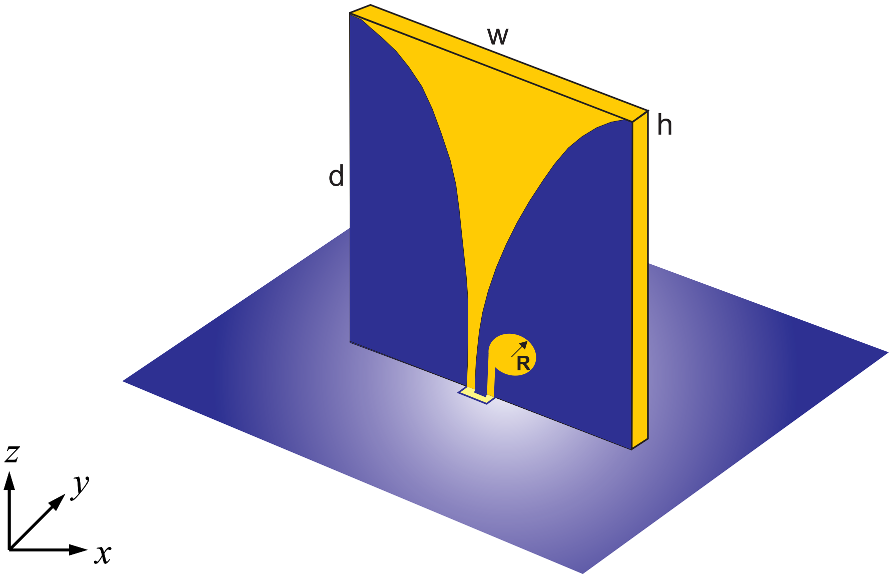

Figure 6.11: Geometry of a Vivaldi antenna. Dimensions: w = 40 mm, d = 55 mm, R = 5 mm, h = 1.5 mm. The relative permittivity of the stub is 3.0. Stripline width τ_s = 2 mm.

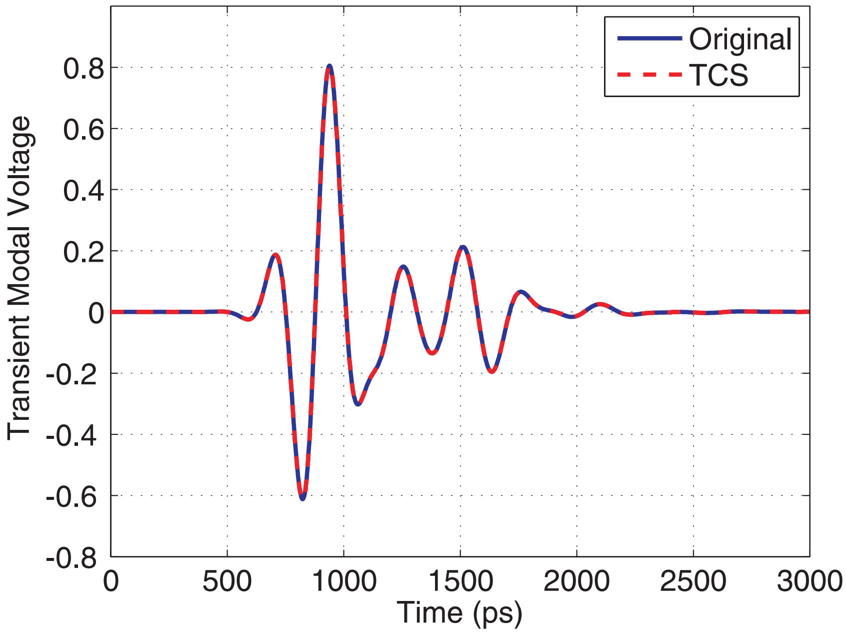

Figure 6.12: Transient modal voltage recorded at the input wave port for a Vivaldi antenna.

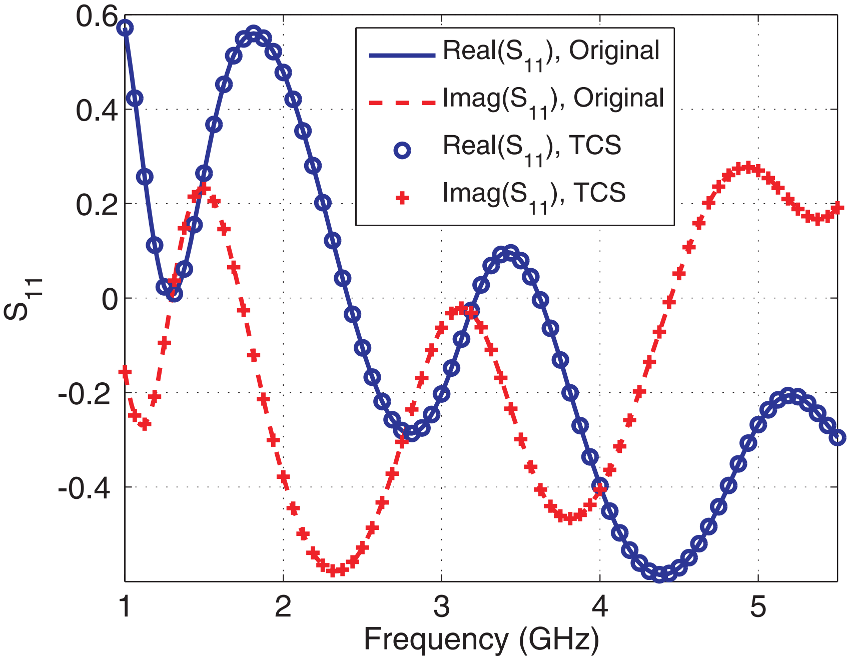

Figure 6.13: Real and imaginary parts of S_{11} at the TEM port for a Vivaldi antenna.

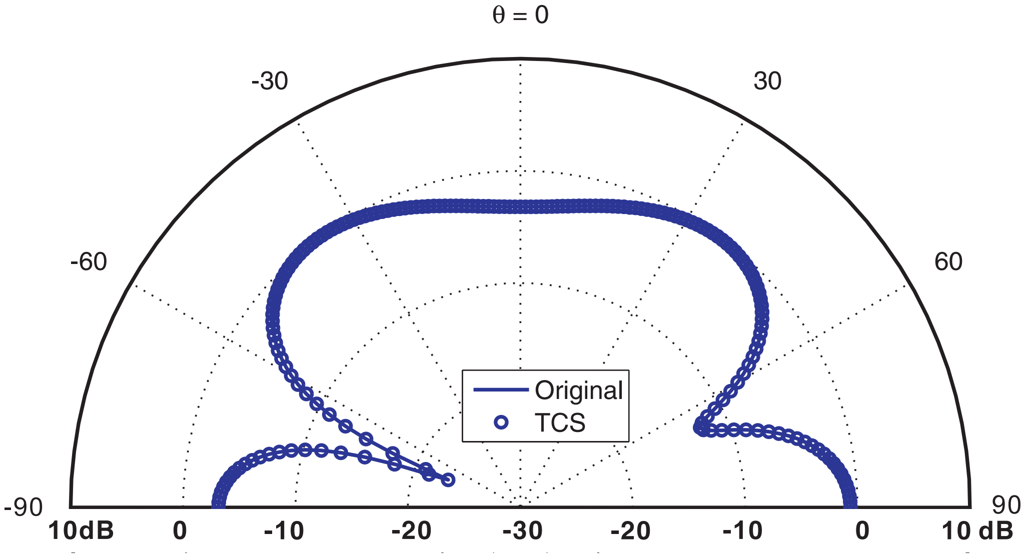

(a)

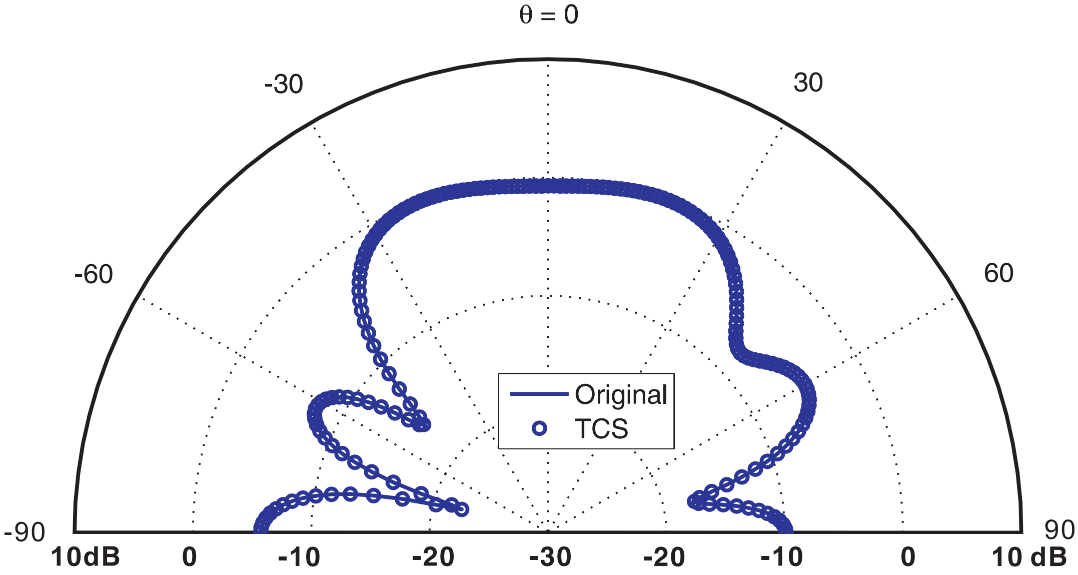

(b)

Figure 6.14: Radiation patterns in the *xz* plane for the Vivaldi antenna. (a) At 3.25 GHz. (b) At 5.50 GHz.

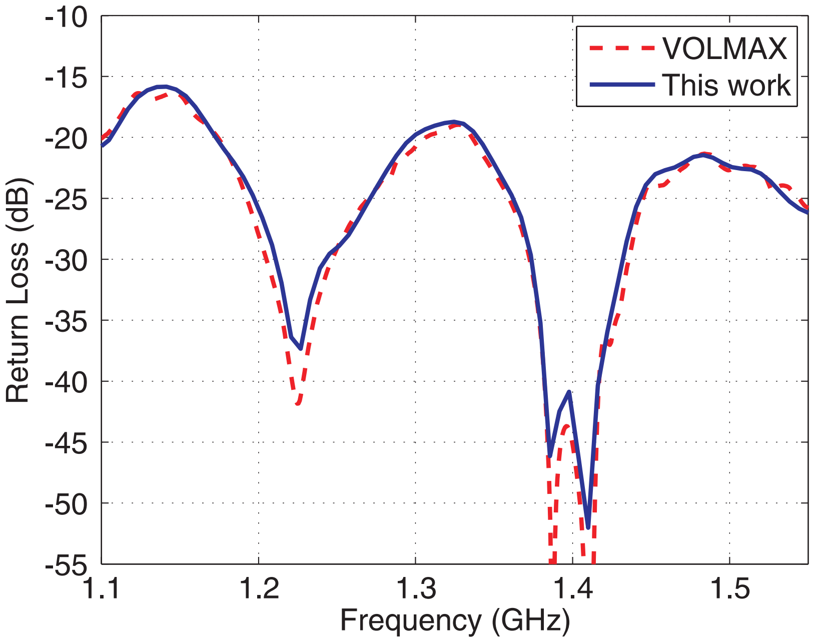

Figure 6.15: Computed return loss at the coaxial port of a Vlasov antenna.

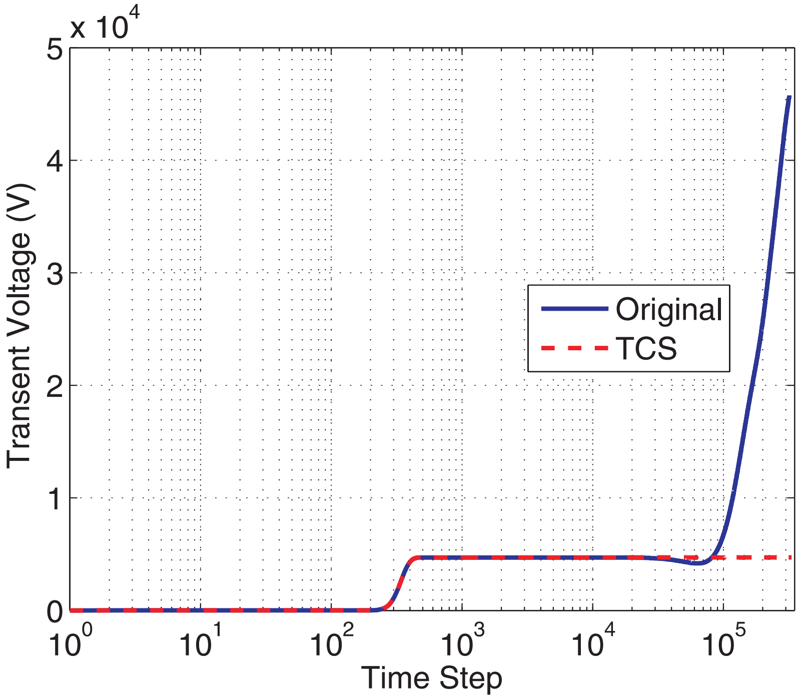

Figure 6.16: Temporal voltage along the FEM edges associated with lumped current excitation.

Table 6.1 : Maximum time that the TCS-enabled TDFEM can reach under single-tone excitations

Frequency of excitation	Relative tolerance	Time-step size	Maximum time
10 Hz	10^{-6}	2.5 ms	510 s
10 Hz	10^{-8}	2.5 ms	>2,200 s
1 Hz	10^{-8}	25.0 ms	>8,900 s

CHAPTER 7

CONCLUSIONS AND FUTURE WORK

This dissertation is mainly devoted to the development of numerical algorithms for incorporating the feed-network and circuit modeling into the time-domain finite element analysis of a wide variety of electromagnetic devices including antenna arrays and microwave circuits. This chapter draws conclusions and sheds light on possible future research work that would further extend the capability of numerical algorithms developed in this dissertation.

It is pointed out that incorporating the feed-network modeling into antenna array analysis and accurately capturing the interactions between the antenna elements and the feed network is necessary and important in the simulation of an antenna system. An accurate and efficient algorithm to achieve this goal is proposed and presented. The feed network and the antennas are separated by a set of well-defined waveport interfaces. The antennas are simulated by the TDFEM combined with the time-domain WPBC, while the feed network is cast into a rational function macromodel based on its scattering matrix enabling a computationally efficient, recursive convolution scheme in transient analysis. The bidirectional decomposition of the fields as well as the port voltages and port currents enables the exchange of information between the antenna elements and the feed network to occur through the incident and reflected modal voltages/currents at properly defined port interfaces. No instability is introduced in this coupled analysis provided that the frequency range of validity of the feed-network macromodel is properly selected and its passivity over the frequency bandwidth of interest is enforced. The proposed approach also works seamlessly in a domain decomposition formulation for the simulation of large and complex antenna arrays. The validity, efficiency, and stability of the proposed method are demonstrated through its application to antenna arrays fed by various feed networks. The proposed approach significantly extends the current antenna modeling capability to the system level without significantly increasing the simulation complexity.

Next, for complicated electromagnetic devices that include both distributive and lumped subsystems, this dissertation presents a methodology such that lumped circuit modeling can be incorporated into the TDFEM analysis, which results in a hybrid field-circuit solver to perform the mixed full-wave and circuit simulation. In the proposed methodology, The FEM subsystem is formed by modeling the distributive passive portion using the Newmark-beta scheme, while the lumped circuits are analyzed by a SPICE-like transient circuit solver to generate a circuit subsystem that is constructed and discretized in a manner consistent with the TDFEM framework. The FEM and circuit subsystems are coupled together through the lumped ports. The coupling from the FEM subsystem to the circuit subsystem is realized by introducing an independent voltage source at each lumped port (its associated FEM edges) whose value is determined by the TDFEM solution. The resulting port current response computed by the circuit subsystem becomes an impressed current excitation for the FEM subsystem at the lumped port, which enables the circuit-to-FEM coupling. The resulting global system for both the FEM and circuit unknowns is solved by an efficient solution algorithm carefully designed for a global system of mixed linear and nonlinear equations when there are nonlinear circuit devices present. The proposed field-circuit simulator provides a powerful and accurate CAD tool for the design of modern high-frequency devices that exhibit significant disparity in the electrical size of their geometrical features.

The versatility, capability, and efficiency of the hybrid field-circuit simulators developed in this dissertation have been further extended and enhanced in several aspects. First, in modern mixed-scale circuit systems, a lumped circuit might have been predesigned and characterized compactly in terms of a frequency-dependent admittance matrix which is often referred to as a *lumped network*. An advanced algorithm is also proposed for systematically and efficiently incorporating multiport lumped networks into the hybrid field-circuit solver. The Laplace-domain admittance matrices are cast into the time-domain stepping equations for port voltages and currents to form a lumped-network subsystem which is then interfaced with the FEM and circuit subsystems through shared ports. While its port voltages are determined by the FEM and circuit subsystems, its port currents are treated as external current excitations. All the lumped-network port variables are then eliminated from the final expressions to again form a global system for only the FEM and circuit unknowns. Incorporating lumped networks into the current simulation tool will not only significantly extend its current modeling capabilities but also improve the simulation efficiency, especially when analyzing mixed-scale electronic systems. With the enhanced circuit modeling capability for both lumped discrete elements and lumped networks, the full strength of the advanced hybrid TDFEM algorithm could be further explored with numerical examples that involve large and complex mixed-scale electromagnetic devices. Second, the TCS technique has been applied to the TDFEM analysis of electromagnetic problems to accelerate the time-marching process. The FEM edge set is split into tree and cotree edges, and the edge basis functions associated with tree edges are replaced by an equal number of pure gradient basis functions defined on non-root nodes. Use of the TCS algorithm is compatible with the time-domain WPBC and lumped port interfaces for hybrid field-circuit simulation. It is shown that application of the TCS to the TDFEM analysis maintains the solution accuracy while significantly reducing the iteration count per time step for a preconditioned iterative solution when the time-step size becomes relatively large. As a result, it allows adoption of a larger time-step size within the requirement of the temporal sampling rate to achieve a faster time-marching process with a marginal additional cost. It also helps suppress the late-time linear drift or instability associated with the conventional TDFEM. Lastly, the original TDFEM-based hybrid field-circuit solver utilizes a common time-step size for the FEM and circuit subsystems. In some applications where both fast- and slow-varying subsystems are present, use of a system-wide common time step compromises the computational efficiency in the sense that it always forces the coupled transient simulation to march on in time at the smallest time step limited by any subsystem that has the strictest restriction on the time-step size. A flexible time-stepping scheme has been developed to enable a multirate simulation in this hybrid field-circuit simulation through a generalized coupling scheme between the FEM and circuit subsystems in order to adopt different time-step sizes for fast- and slow-varying subsystems. Because of the ability to allow different sampling rates for different subsystems, the proposed time-stepping scheme can significantly improve the computational efficiency of the TDFEM-based hybrid field-circuit solver, especially when the computational cost associated with slow subsystems is higher than that associated with fast subsystems. Various numerical examples are presented to validate the algorithms and demonstrate the accuracy and applications of these advanced features of the hybrid field-circuit solver.

Through years of development, the TDFEM has been demonstrated as a powerful transient simulation technique and has been widely acknowledged as a promising candidate to meet the future challenges in the electromagnetic simulations and EDA industry. In this dissertation, various modeling techniques have been hybridized with the TDFEM in order to develop co-simulation schemes for efficient and accurate analysis of large and complicated electronic systems with mixed-scale and multiphysics features. Through this procedure, the modeling capability and versatility of the TDFEM has been significantly extended and enhanced, which has been demonstrated through various numerical examples. In order to further enhance the modeling capability of the current hybrid solver, one possible future work is to incorporate the lumped thin wire model [9], [59], [100], and [101] into the TDFEM framework. Thin wires represent a special geometry that has an extremely small transverse dimension but is electrically large in the longitudinal dimension. An advantage of introducing the thin wire model is that it greatly relaxes the mesh density around a physical conducting wire and hence reduces the modeling complexity and makes simulation much more efficient. Armed with the capability of thin wire modeling, the hybrid solver can possibly be applied to simulate even more complicated realistic electronic systems similar to those in [102]. Moreover, considering that currently the lumped circuits are modeled by a SPICE-like circuit simulation program developed in this research, another possible topic for future work is to incorporate into the circuit modeling part of this work more advanced circuit simulation techniques. For instance, a variable time-stepping scheme has been widely adopted in many commercial software packages. With this technique, the time-step size is neither fixed beforehand nor uniform, but changing along the time-marching process, corresponding to any temporal changes of the signals in the circuits. When the signals change slowly, the time-step size will be adapted to a larger value for a better efficiency. When the signals start to change faster and a large time-step produces an error level over a certain threshold, the time-step size will automatically be reduced. This technique has brought a lot benefit in achieving maximum efficiency within a certain accuracy threshold, and fortunately the flexible time-stepping scheme developed in this dissertation has paved a way for incorporation of such a technique. Finally, an ultimate way to further enhance the circuit modeling part of the hybrid solver may be to directly connect the TDFEM program to the public-domain SPICE programs such as Berkeley SPICE3 [61]. Although this requires a lot of work on the interfacing of two different codes, once done, many advanced features and device models that are already in the SPICE library will be directly available for the hybrid field-circuit simulation.

APPENDIX A
DERIVATION OF THE UPDATING EQUATIONS

The feed network is assumed to have *N*+1 ports with port indices from 0 to *N*. We rewrite (3.21) in a compact matrix form as

$$\left\{\mathbf{V}^{(-)}(s)\right\} = \overline{\mathbf{S}}(s) \cdot \left\{\mathbf{V}^{(+)}(s)\right\} . \tag{A.1}$$

When all the entries of $\overline{\mathbf{S}}(s)$ are approximated by rational functions shown in (3.22), we obtain a macromodel $\tilde{\overline{\mathbf{S}}}(s)$ in the following state-space format:

$$\tilde{\overline{\mathbf{S}}}(s) = \overline{\mathbf{C}} \cdot (s\overline{\mathbf{I}} - \overline{\mathbf{A}})^{-1} \cdot \overline{\mathbf{B}} + \overline{\mathbf{D}} . \tag{A.2}$$

The number of the common poles in the rational approximations is N_k, with pole indices from 1 to N_k. The matrix $\overline{\mathbf{I}}$ is an identity matrix. The matrix $\overline{\mathbf{A}}$ is a diagonal matrix whose entries contain poles of the rational approximation

$$\overline{\mathbf{A}} = \begin{bmatrix} \overline{\mathbf{A}}_0 & & & \\ & \overline{\mathbf{A}}_1 & & \\ & & \ddots & \\ & & & \overline{\mathbf{A}}_N \end{bmatrix} \tag{A.3}$$

with diagonal submatrices

$$\overline{\mathbf{A}}_0 = \overline{\mathbf{A}}_1 = \cdots = \overline{\mathbf{A}}_N = \begin{bmatrix} a_1 & & & \\ & a_2 & & \\ & & \ddots & \\ & & & a_{N_k} \end{bmatrix} . \tag{A.4}$$

The matrix $\overline{\mathbf{B}}$ contains only 1’s and 0’s

$$\bar{\mathbf{B}} = \begin{bmatrix} \{\mathbf{U}\}_0 & & & \\ & \{\mathbf{U}\}_1 & & \\ & & \ddots & \\ & & & \{\mathbf{U}\}_N \end{bmatrix} \tag{A.5}$$

with column vectors $\{\mathbf{U}_0\} = \{\mathbf{U}_1\} = \cdots = \{\mathbf{U}_N\}$ of length N_k, whose entries are all equal to 1. The matrix $\bar{\mathbf{C}}$ includes the residues of the rational fits of the elements $\tilde{S}_{ij}(s)$

$$\bar{\mathbf{C}} = \begin{bmatrix} \{\mathbf{C}_{00}\} & \{\mathbf{C}_{01}\} & \cdots & \{\mathbf{C}_{0N}\} \\ \{\mathbf{C}_{10}\} & \{\mathbf{C}_{11}\} & \cdots & \{\mathbf{C}_{1N}\} \\ \vdots & \vdots & \ddots & \vdots \\ \{\mathbf{C}_{N0}\} & \{\mathbf{C}_{N1}\} & \cdots & \{\mathbf{C}_{NN}\} \end{bmatrix} \tag{A.6}$$

with row vectors $\{\mathbf{C}_{ij}\} = [c_{ij,1}\ c_{ij,2}\ \cdots\ c_{ij,N_k}]$. Finally, the matrix $\bar{\mathbf{D}}$ contains all the constants in the rational approximations in (28), if any,

$$\bar{\mathbf{D}} = \begin{bmatrix} d_{00} & d_{01} & \cdots & d_{0N} \\ d_{10} & d_{11} & \cdots & d_{1N} \\ \vdots & \vdots & \ddots & \vdots \\ d_{N0} & d_{N1} & \cdots & d_{NN} \end{bmatrix}. \tag{A.7}$$

Invoking (A.2), (A.1) becomes

$$\begin{aligned} \left\{\mathbf{V}^{(-)}\right\} = \bar{\tilde{\mathbf{S}}} \cdot \left\{\mathbf{V}^{(+)}\right\} &= \bar{\mathbf{C}} \cdot (s\bar{\mathbf{I}} - \bar{\mathbf{A}})^{-1} \cdot \bar{\mathbf{B}} \cdot \left\{\mathbf{V}^{(+)}\right\} + \bar{\mathbf{D}} \cdot \left\{\mathbf{V}^{(+)}\right\} \\ &= \bar{\mathbf{C}} \cdot \left\{\mathbf{T}_\mathrm{V}(s)\right\} + \bar{\mathbf{D}} \cdot \left\{\mathbf{V}^{(+)}(s)\right\} \end{aligned} \tag{A.8}$$

with

$$\left\{\mathbf{T}_\mathrm{V}(s)\right\} = (s\bar{\mathbf{I}} - \bar{\mathbf{A}})^{-1} \cdot \bar{\mathbf{B}} \cdot \left\{\mathbf{V}^{(+)}(s)\right\}. \tag{A.9}$$

Its time-domain form is readily obtained as

$$\left\{\mathbf{T}_\mathrm{V}(t)\right\} = \exp\left(\bar{\mathbf{A}}\Delta t\right) u(t) * \bar{\mathbf{B}} \cdot \left\{\mathbf{V}^{(+)}(t)\right\} \tag{A.10}$$

where $\exp(\cdot)$ indicates a matrix exponential, and $u(t)$ denotes the unit step function. After time discretization, the time convolution above can be evaluated using the following recursive formula:

$$\left\{\mathbf{T}_\mathrm{V}\right\}^{n+1} = \bar{\mathbf{E}}_1 \cdot \left\{\mathbf{T}_\mathrm{V}\right\}^n + \bar{\mathbf{E}}_2 \cdot \bar{\mathbf{B}} \cdot \left\{\mathbf{V}^{(+)}\right\}^n \tag{A.11}$$

where $\bar{\mathbf{E}}_1 = \exp(\bar{\mathbf{A}}\Delta t)$ and $\bar{\mathbf{E}}_2 = (\exp(\mathbf{A}\Delta t) - \mathbf{I}) \cdot (\mathbf{A}^{-1})$. Based on (A.8), once $\left\{\mathbf{T}_{\mathrm{V}}\right\}^{n+1}$ is obtained, $\left\{\mathbf{V}^{(-)}\right\}^{n+1}$ can be computed as

$$\left\{\mathbf{V}^{(-)}\right\}^{n+1} = \bar{\mathbf{C}} \cdot \left\{\mathbf{T}_{\mathrm{V}}\right\}^{n+1} + \bar{\mathbf{D}} \cdot \left\{\mathbf{V}^{(+)}\right\}^{n}. \tag{A.12}$$

APPENDIX B

DERIVATION AND PROOF OF VALIDITY OF THE SOLUTION ALGORITHM

Equation (4.25) along with (4.26) and (4.27) is a system (size of *N*) of mixed linear and nonlinear equations. Therefore, at each time step, a system of equations in the following generalized form needs to be solved:

$$\mathbf{F}(\mathbf{x}) = \begin{bmatrix} [A] & [B] \\ [C] & [D] \end{bmatrix} \begin{bmatrix} \{x^{\mathrm{l}}\} \\ \{x^{\mathrm{nl}}\} \end{bmatrix} + \begin{bmatrix} \mathbf{0} \\ \mathbf{I}^{\mathrm{nl}}(\{x^{\mathrm{nl}}\}) \end{bmatrix} - \begin{bmatrix} \{b^{\mathrm{l}}\} \\ \{b^{\mathrm{nl}}\} \end{bmatrix} = \mathbf{0} \tag{B.1}$$

where submatrices [*A*], [*B*], [*C*], and [*D*], and right-hand-side subvectors $\{b^{\mathrm{l}}\}$ and $\{b^{\mathrm{nl}}\}$ are predetermined and invariant at Newton steps. The unknown vector is separated into two groups so that $\{x^{\mathrm{l}}\}$ (size of N^{nl}) represents the unknowns associated with pure linear equations and $\{x^{\mathrm{nl}}\}$ (size of $N^{\mathrm{nl}} = N - N^{\mathrm{nl}}$) presents the remaining unknowns involved with nonlinear expressions compactly as $\mathbf{I}^{\mathrm{nl}}(\{x^{\mathrm{nl}}\})$.

It can be derived easily that the system in (B.2) is equivalent to (B.1) by eliminating $\{x^{\mathrm{l}}\}$, which results in a nonlinear system only with respect to $\{x^{\mathrm{nl}}\}$

$$\mathbf{f}(\{x^{\mathrm{nl}}\}) = \{x^{\mathrm{nl}}\} + [E]\mathbf{I}^{\mathrm{nl}}(\{x^{\mathrm{nl}}\}) - [E](\{b^{\mathrm{nl}}\} - [C][A]^{-1}\{b^{\mathrm{l}}\}) = \mathbf{0} \tag{B.2}$$

where $[E] = ([D] - [C][A]^{-1}[B])^{-1}$ is the inversion of the Schur complement of [*A*].

If the Newton-Raphson method is applied to (B.2) instead of (B.1), then at the *k*th Newton iteration, given an initial guess $\{x_{k-1}^{\mathrm{nl}}\}$, we need to first compute $\mathbf{f}_{k-1} = \mathbf{f}(\{x_{k-1}^{\mathrm{nl}}\})$ and check convergence. However, instead of explicitly computing $\mathbf{f}_{k-1} = \mathbf{f}(\{x_{k-1}^{\mathrm{nl}}\})$ through (B.2), we first solve the following intermediate linear system:

$$\begin{bmatrix} [A] & [B] \\ [C] & [D] \end{bmatrix} \begin{bmatrix} \{\tilde{x}^{\mathrm{l}}\} \\ \{\tilde{x}^{\mathrm{nl}}\} \end{bmatrix} = \begin{bmatrix} \{b^{\mathrm{l}}\} \\ \{b^{\mathrm{nl}}\} \end{bmatrix} - \begin{bmatrix} \mathbf{0} \\ \mathbf{I}^{\mathrm{nl}}(\{x_{k-1}^{\mathrm{nl}}\}) \end{bmatrix} \tag{B.3}$$

where $\begin{bmatrix} \{\tilde{x}^{\mathrm{l}}\}^{\mathrm{T}} & \{\tilde{x}^{\mathrm{nl}}\}^{\mathrm{T}} \end{bmatrix}^{\mathrm{T}}$ is a intermediate solution vector. We then compute $\{x_{k-1}^{\mathrm{nl}}\} - \{\tilde{x}^{\mathrm{nl}}\}$. It is easy to verify that $\{x_{k-1}^{\mathrm{nl}}\} - \{\tilde{x}^{\mathrm{nl}}\} = \mathbf{f}(\{x_{k-1}^{\mathrm{nl}}\}) = \mathbf{f}_{k-1}$.

Another important step in applying the Newton-Raphson method to (B.2) is to find the $\delta\{x_k^{\mathrm{nl}}\}$ such that the Newton updating can be perform as $\{x_k^{\mathrm{nl}}\} = \{x_{k-1}^{\mathrm{nl}}\} + \delta\{x_k^{\mathrm{nl}}\}$. This involves the computation of the Jacobian matrix $[J]^{\mathbf{f}}\big|_{\{x_{k-1}^{\mathrm{nl}}\}}$ of (B.2). Explicitly, $[J]^{\mathbf{f}}\big|_{\{x_{k-1}^{\mathrm{nl}}\}}$ can be computed from (B.2) as

$$[J]^{\mathbf{f}}\Big|_{\{x_{k-1}^{\mathrm{nl}}\}} = \frac{\partial \mathbf{f}(\{x^{\mathrm{nl}}\})}{\partial\{x^{\mathrm{nl}}\}}\bigg|_{\{x_{k-1}^{\mathrm{nl}}\}} = \bar{\mathbf{I}} + [E]\frac{\partial \mathbf{I}^{\mathrm{nl}}(\{x^{\mathrm{nl}}\})}{\partial\{x^{\mathrm{nl}}\}}\bigg|_{\{x_{k-1}^{\mathrm{nl}}\}} \tag{B.4}$$

where $\bar{\mathbf{I}}$ is the identity matrix. The second term $[E]\frac{\partial \mathbf{I}^{\mathrm{nl}}(\{x^{\mathrm{nl}}\})}{\partial\{x^{\mathrm{nl}}\}}\bigg|_{\{x_{k-1}^{\mathrm{nl}}\}}$ can be obtained column by column by solving

$$\begin{bmatrix} A & B \\ C & D \end{bmatrix} \begin{bmatrix} w \\ y_j \end{bmatrix} = \begin{bmatrix} 0 \\ c_j \end{bmatrix} \tag{B.5}$$

where c_j and y_j are the *j*th columns of $\frac{\partial \mathbf{I}^{\mathrm{nl}}(\{x^{\mathrm{nl}}\})}{\partial\{x^{\mathrm{nl}}\}}\bigg|_{\{x_{k-1}^{\mathrm{nl}}\}}$ and $[E]\frac{\partial \mathbf{I}^{\mathrm{nl}}(\{x^{\mathrm{nl}}\})}{\partial\{x^{\mathrm{nl}}\}}\bigg|_{\{x_{k-1}^{\mathrm{nl}}\}}$, respectively. This leads to solving (B.5) N^{nl} times per Newton step. Note that even if $[J]^{\mathbf{f}}\big|_{\{x_{k-1}^{\mathrm{nl}}\}}$ can also be updated using forward difference approximation, this leads to the same computation cost. We have successfully avoided modifying the system matrix at each Newton step because now both (B.3) and (B.5) have a predetermined system matrix and can be solved by linear solvers. However, when N^{nl} is large and (B.5) cannot be solved very efficiently, the above way to find $[J]^{\mathbf{f}}\big|_{\{x_{k-1}^{\mathrm{nl}}\}}$ can become a bottleneck.

Alternatively, quasi-Newton methods, such as Broyden's method, provide an inexpensive approximation of $[J]^{\mathbf{f}}\big|_{\{x_{k-1}^{\mathrm{nl}}\}}$ without solving a system (B.5) so many times and thus significantly reduce the computational cost.

REFERENCES

[1] J. M. Jin, *The Finite Element Method in Electromagnetics*, 2nd ed. New York, NY: Wiley, 2002.

[2] J. M. Jin and D. J. Riley, *Finite Element Analysis of Antennas and Arrays*. Hoboken, NJ: Wiley, 2009.

[3] R. F. Harrington, *Field Computation by Moment Methods*. New York, NY: Macmillan, 1968; reprinted by IEEE Press, 1993.

[4] A. Taflove and S. Hagness, *Computational Electrodynamics: The Finite Difference Time Domain Method*, 3rd ed. Boston, MA: Artech House 2005.

[5] R. Courant, “Variational methods for the solution of problems of equilibrium and vibrations,” *Bull. Amer. Math. Soc.,* vol. 49, no. 1, pp. 1-23, 1943.

[6] H. Ali and G. Costache, “Finite-element time-domain analysis of axisymmetrical radiators,” *IEEE Trans. Antennas Propagat.*, vol. 42, no. 2, pp. 272-275, Feb. 1994.

[7] C. Geuzaine, B. Meys, V. Beauvois, and W. Legros, “An FETD approach for the modeling of antennas,” *IEEE Trans. Magn.*, vol. 36, no. 4-1, pp. 251-254, July 2000.

[8] D. Jiao and J. M. Jin, “Time-domain finite-element simulation of cavity-backed microstrip patch antennas,” *Microwave Opt. Tech. Lett.*, vol. 32, no. 4, pp. 892-896, Feb. 2002.

[9] F. Edelvik, G. Ledfelt, and D. Riley, “An unconditionally stable subcell model for arbitrarily oriented thin wires in the FETD method,” *IEEE Trans. Antennas Propagat.*, vol. 51, no. 8, pp. 1797-1805, Aug. 2003.

[10] Z. Lou and J. M. Jin, “An accurate waveguide port boundary condition for the time-domain finite-element method,” *IEEE Trans. Antennas Propagat.*, vol. 53, no. 9, pp. 3014-3023, Sep. 2005.

[11] Z. Lou and J. M. Jin, “Modeling and simulation of broad-band antennas using the time-domain finite element method,” *IEEE Trans. Antennas Propagat.*, vol. 53, no. 12, pp. 4099-4110, Dec. 2005.

[12] Z. Lou and J. M. Jin, “A novel dual-field time-domain finite-element domain decomposition method for computational electromagnetics,” *IEEE Trans. Antennas Propagat*, vol. 54, no. 6, pp. 1850-1862, June 2006.

[13] Z. Lou and J. M. Jin, “A dual-field domain-decomposition method for the time-domain finite-element analysis of large finite arrays,” *J. Comput. Physics*, vol. 222, no. 1, pp. 408-427, March 2007.

[14] T. Rylander, F. Edelvik, A. Bondeson, and D. Riley, “Advances in hybrid FDTD-FE techniques,” in *Computational Electrodynamics: The Finite Difference Time Domain Method*, 3rd ed. A. Taflove and S. Hagness, Eds. Boston, MA: Artech House 2005.

[15] A. E. Yilmaz, Z. Lou, E. Michielssen, and J. M. Jin, “A single boundary, implicit, and FFT-accelerated time-domain finite element-boundary integral solver,” *IEEE Trans. Antennas Propagat*, vol. 55, no. 5, pp. 1382-1397, May 2007.

[16] D. Jiao, “Advanced time-domain finite element method for electromagnetic analysis,” Ph.D. dissertation, University of Illinois at Urbana-Champaign, Urbana, IL, 2001.

[17] Z. Lou, “Time-domain finite element simulation of large antennas and antenna arrays,” Ph.D. dissertation, University of Illinois at Urbana-Champaign, Urbana, IL, 2006.

[18] K.-L. Wu, M. Spenuk, J. Litva, and D.-G. Fang, “Theoretical and experimental study of feed network effects on the radiation pattern of series-fed microstrip antenna arrays,” *IEE Proc. H: Microwave, Antennas Propag.,* vol. 138, no. 3, pp. 238-242, June 1991.

[19] C. F. Wang, F. Ling, and J. M. Jin, “A fast full-wave analysis of scattering and radiation from large finite arrays of microstrip antennas,” *IEEE Trans. Antennas Propagat.*, vol. 46, no. 10, pp. 1467-1474, Oct. 1998.

[20] F. Ling, C. F. Wang, and J. M. Jin, “An efficient algorithm for analyzing large-scale microstrip structures using adaptive integral method combined with discrete complex image method,” *IEEE Trans. Microwave Theory Tech.*, vol. 48, no. 5, pp. 238-242, May 2000.

[21] M. Timm, “Open architecture solves large 3D puzzles,” *Microwaves & RF*, vol. 41, no. 5, pp. 144-155, May 2002.

[22] C. A. Balanis, *Advanced Engineering Electromagnetics*. New York, NY: Wiley, 1989.

[23] N. Newmark, “A method of computation for structural dynamics,” *J. Eng. Mech. Div.*, vol. 85, pp. 67-94, July 1959.

[24] R. D. Graglia, D. R. Wilton, and A. F. Peterson, “Higher order interpolatory vectorbases for computational electromagnetics,” *IEEE Trans. Antennas Propagat.*, vol. 45, pp. 329-340, Mar. 1997.

[25] J. Webb, “Hierarchal vector basis functions of arbitrary order for triangular and tetrahedral finite elements,” *IEEE Trans. Antennas Propagat.*, vol. 47, pp. 1244-1253, Aug. 1999.

[26] S. Gedney and U. Navsariwala, “An unconditionally stable finite element time-domain solution of the vector wave equation,” *IEEE Microwave Guided Wave Lett.*, vol. 5, pp. 332-334, Oct. 1995.

[27] J. Lee, R. Lee, and A. Cangellaris, “Time-domain finite-element methods,” *IEEE Trans. Antennas Propagat.*, vol. 45, pp. 430-442, Mar. 1997.

[28] D. Jiao and J. M. Jin, “A general approach for the stability analysis of the time-domain finite-element method for electromagnetic simulations,” *IEEE Trans. Antennas Propagat.,* vol. 50, pp. 1624-1631, Nov. 2002.

[29] J. Liu, J. M. Jin, E. K. N. Yung, and R. S. Chen, “A fast three-dimensional higher-order finite element analysis of microwave waveguide devices,” *Microwave Opt. Tech. Lett.*, vol. 32, pp. 344-352, Mar. 2002.

[30] D. A. White, “Orthogonal vector basis functions for time domain finite element solution of the vector wave equation,” *IEEE Trans. Magn.*, vol. 35, pp. 1458-1461, 1999.

[31] D. Jiao and J. M. Jin, “Three-dimensional orthogonal vector basis functions for time-domain finite element solution of vector wave equations,” *IEEE Trans. Antennas Propagat.,* vol. 51, pp. 59-65, Jan. 2003.

[32] Y. Zhu and A. C. Cangellaris, “A new finite element model for reduced order electromagnetic modeling,” *IEEE Microwave Wireless Comp. Lett.*, vol. 11, pp. 211-213, May 2001.

[33] Y. Zhu and A. C. Cangellaris, “Finite element-based model order reduction of electromagnetic devices,” *International Journal of Numerical Modeling: Electronic Networks, Devices and Fields*, vol. 15, no. 1, pp. 73-92, Jan. 2002.

[34] H. Wu and A. Cangellaris, "Model-order reduction of finite-element approximations of passive electromagnetic devices including lumped electrical-circuit models," *IEEE Trans. Microwave Theory Tech.*, vol. 52, no. 9, pp. 2305-2313, Sep. 2004.

[35] B. Gustavsen and A. Semlyen, "Rational approximation of frequency domain responses by vector fitting," *IEEE Trans. Power Delivery*, vol. 14, no. 3, pp. 1052- 1061, July 1999.

[36] D. J. Riley, C. D. Turner, L. D. Bacon, and J. D. Kotulski, "Numerical modeling tools for transient electromagnetic problems," Sandia National Laboratories, Albuquerque, NM, Tech. Rep. SAND90-0519, Apr. 1990.

[37] HSPICE, Synopsys, Inc., Mountain View, CA, http://www.synopsys.com/Tools/Verification/ AMSVerification/CircuitSimulation/HSPICE/Pages/default.aspx.

[38] Agilent Advanced Design System (ADS), Agilent Technologies, Inc., Santa Clara, CA, http://eesof.tm.agilent.com/products/ads_main.html.

[39] S. Grivet-Talocia, "Passivity enforcement via perturbation of Hamiltonian matrices," *IEEE Trans. Circuits Systems I: Fundamental Theory and Applications*, vol. 51, no. 9, pp. 1755-1769, Sept. 2004.

[40] B. Gustavsen and A. Semlyen, "Enforcing passivity for admittance matrices approximated by rational functions," *IEEE Trans. Power Systems*, vol. 16, no. 1, pp. 97-104, Feb. 2001.

[41] E. Wilkinson, "An N-way hybrid power divider," *IRE Trans. Microwave Theory Tech.*, vol. 8, no.1, pp. 116-118, Jan. 1960.

[42] W. Sui, D. A. Christensen, and C. H. Durney, "Extending the two-dimensional FDTD method to hybrid electromagnetic systems with active and passive lumped elements," *IEEE Trans. Microwave Theory Tech.*, vol. 40, pp. 724-730, Apr. 1992.

[43] M. Piket-May, A. Taflove, and J. Baron, "FDTD modeling of digital signal propagation in 3-D circuits with passive and active loads," *IEEE Trans. Microwave Theory Tech.*, vol. 42, pp. 1514-1523, Aug. 1994.

[44] V. A. Thomas, M. E. Jones, M. Piket-May, A. Taflove, and E. Harrigan, "The use of SPICE lumped circuits as sub-grid models for FDTD analysis," *IEEE Microwave Guided Wave Lett.*, vol. 4, pp. 141-143, May 1994.

[45] C.-N. Kuo, R.-B. Wu, B. Houshmand, and T. Itoh, “Modeling of microwave active devices using the FDTD analysis based on the voltage source approach,” *IEEE Microwave Guided Wave Lett.*, vol. 6, pp.199-201, May 1996.

[46] C.-N. Kuo, B. Houshmand, and T. Itoh, “FDTD analysis of active circuits with equivalent current source approach,” in *IEEE AP-S Int. Symp. Dig.*, Newport Beach, CA, June 1995, pp. 1510-1513.

[47] Y. Tsuei, A. C. Cangellaris, and J. L. Prince, “Rigorous electromagnetic modeling of chip-to-package (first-level) interconnections,” *IEEE Trans. Comp., Hybrids, Manufact. Technol.*, vol. 16, pp. 876-883, Dec. 1993.

[48] C.-N. Kuo, B. Houshmand, and T. Itoh, “Full-wave analysis of packaged microwave circuits with active and nonlinear devices: An FDTD approach,” *IEEE Trans. Microwave Theory Tech.*, vol. 45, pp. 819-826, May 1997.

[49] K.-P. Ma, B. Houshmand, Y. Qian, and T. Itoh, “Global time-domain full-wave analysis of microwave circuits involving highly nonlinear phenomena and EMC effects,” *IEEE Trans. Microwave Theory Tech.*, vol. 47,no. 6, pp. 859-866, June 1999.

[50] M. Chen, W. R. Deal, B. Houshmand, and T. Itoh, “Global time-domain full-wave analysis of microwave FET oscillators and self-oscillating mixers,” in *IEEE MTT-S Int. Microwave Symp. Dig.*, Baltimore, MD, June 1998, pp. 1135-1138.

[51] K. Aygün, B. C. Fisher, J. Meng, and E. Michielssen, “A fast hybrid field-circuit simulator for transient analysis of microwave circuits,” *IEEE Trans. Microwave Theory Tech.*, vol. 52, no. 2, pp. 573-583, Feb. 2004.

[52] A. E. Yılmaz, J.-M. Jin, and E. Michielssen, “A parallel FFT accelerated transient field-circuit simulator,” *IEEE Trans. Microwave Theory Tech.*, vol. 53, no. 9, pp. 2851-2865, Sep. 2005.

[53] M. Feliziani and F. Maradei, “Modeling of electromagnetic fields and electrical circuits with lumped and distributed elements by the WETD method,” *IEEE Trans. Magn.*, vol. 35, no. 3, Part 1, pp. 1666-1669, May 1999.

[54] K. Guillouard, M. F. Wong, V. F. Hanna, and J. Citerne, “A new global time-domain electromagnetic simulator of microwave circuits including lumped elements based on finite-element method,” *IEEE Trans. Microwave Theory Tech.*, vol. 47, pp. 2045-2049, Oct. 1999.

[55] S. Chang, R. Coccioli, Y. Qian, and T. Itoh, "A global finite-element time-domain analysis of active nonlinear microwave circuits," *IEEE Trans. Microwave Theory Tech.*, vol. 47, pp. 2410-2416, Dec. 1999.

[56] H.-P. Tsai, Y. Wang, and T. Itoh, "An unconditionally stable extended (USE) finite-element time-domain solution of active nonlinear microwave circuits using perfectly matched layers," *IEEE Trans. Microwave Theory Tech.*, vol. 50, pp. 2226-2232, Oct. 2002.

[57] M. Feliziani and F. Maradei, "Circuit-oriented FEM: Solution of circuit-field coupled problems by circuit equations," *IEEE Trans. Magn.*, vol. 38, no. 2, pp. 965-968, Mar. 2002.

[58] C. Ho, A. E. Ruehli, and P. A. Brennan, "The modified nodal approach to network analysis," *IEEE Trans. Circuits Syst.*, vol. CAS-22, pp. 504-509, June 1975.

[59] F. Edelvik and D. J. Riley, "An unconditionally stable subcell model for arbitrarily oriented thin wires in the FETD method," in *Proc. IEEE Antennas Propagat. Soc. Int. Symp.*, vol. 2, July 2002, pp. 186-189.

[60] F. Edelvik and T. Weiland, "Stable modeling of arbitrary thin slots in the finite element time-domain method," *Int. J. Numer. Model.*, vol. 17, pp. 365-383, June 2004.

[61] T. L. Quarles, "The SPICE3 implementation guide," Univ. of California, Berkeley, CA, Tech. Rep. ERL-M89/44, April 1989.

[62] W. H. Press, S. A. Teukolsky, W. T. Vetterling, and B. P. Flannery, *Numerical Recipes: The Art of Scientific Computing*, 3rd ed. New York, NY: Cambridge Univ. Press, 2007.

[63] G. Gonzales, *Microwave Transistor Amplifiers*, 2nd ed. Upper Saddle River, NJ: Prentice Hall, 1997.

[64] B. K. Johnson, "Numerical oscillations in EMTP-like programs," lecture notes, ECE524: Transients in Power Systems, University of Idaho, Spring 2008.

[65] *HSIM Reference Manual*, Synopsys, Inc., 2009, http://www.synopsys.com.

[66] A. Semlyen and F. d. Leon, "Computation of electro-magnetic transients using dual or multiple time steps," *IEEE Trans. Power Syst.*, vol. 8, no. 3, pp. 1274-1281, Aug. 1993.

[67] F. A. Moreira and J. R. Martí, "Latency techniques for time-domain power system transients simulation," *IEEE Trans. Power Syst.*, vol. 20, no. 1, pp. 246-253, Feb. 2005.

[68] F. Collino, T. Fouquet, and P. Joly, “Conservative space-time mesh refinement methods for the FDTD solution of Maxwell’s equations,” *J. Comput. Phys.*, vol. 211, no. 1, pp. 9-35, Jan. 2006.

[69] C. Fumeaux, D. Baumann, P. Leuchtmann, and R. Vahldieck, “A generalized local time-step scheme for efficient FVTD simulations in strongly inhomogeneous meshes,” *IEEE Trans. Microwave Theory Tech.*, vol. 52, no. 3, pp. 1067-1076, March 2004.

[70] E. Montseny, S. Pernet, X. Ferrieres, and G. Cohen, “Dissipative terms and local time-stepping improvements in a spatial high order discontinuous Galerkin scheme for the time-domain Maxwell’s equations,” *J. Comput. Physics*, vol. 227, no. 14, pp. 6795-6820, July 2008.

[71] A. E. Yılmaz, J. M. Jin, and E. Michielssen, “A TDIE-based asynchronous electromagnetic-circuit simulator,” *IEEE Microw. Wireless Compon. Lett.*, vol. 16, no. 3, pp. 122-124, Mar. 2006.

[72] J.-Y. Ihm, I. J. Chung, G. Manetas, and A. C. Cangellaris, “Comprehensive models for the investigation of on-chip switching noise generation and coupling,” in *Proc. IEEE Int. EMC Symp.*, vol. 2, Aug. 2005, pp. 666-671.

[73] R. M. Howe, “Accuracy and stability tradeoffs in multi-rate simulation,” in *Proc. SPIE*, vol. 4367, pp. 113-126, *Enabling Technology for Simulation Science V*, A. F. Sisti and D. A. Trevisani Eds., 2001.

[74] E. P. Li, E. X. Liu, L. W. Li, and M. S. Leong, “A coupled efficient and systematic full-wave time-domain macromodeling and circuit simulation method for signal integrity analysis of high-speed interconnects,” *IEEE Trans. Adv. Packag.*, vol. 27, no. 1, pp. 213-223, Feb. 2004.

[75] A. Odabasioglu, M. Celik, and L. T. Pileggi, “PRIMA: Passive reduced-order interconnect macromodeling algorithm,” *IEEE Trans. Computer-Aided Design*, vol. 17, pp. 645-653, Aug. 1998.

[76] J. A. Pereda, F. Alimenti, P. Mezzanotte, L. Roselli, and R. Sorrentino, “A new algorithm for the incorporation of arbitrary linear lumped networks into FDTD simulators,” *IEEE Trans. Microw. Theory Tech.*, vol. 47, no. 6, pp. 943-949, Jun. 1999.

[77] H. E. A. El-Raouf, W. Yu, and R. Mittra, “Application of the Z-transform technique to modeling linear lumped loads in the FDTD,” *Proc. Inst. Elect. Eng. Microwave, Antennas, Propag.*, vol. 151, no. 1, pp. 67-70, Feb. 2004.

[78] J.-Y. Lee, J.-H. Lee, and H.-K. Jung, “Linear lumped loads in the FDTD method using piecewise linear recursive convolution method,” *IEEE Microwave Wireless Compon. Lett.*, vol. 16, no. 4, pp. 158-160, Apr. 2006.

[79] T.-L. Wu, S.-T. Chen, and Y.-S. Huang, “A novel approach for the incorporation of arbitrary linear lumped network into FDTD method,” *IEEE Microwave Wireless Compon. Lett.*, vol. 14, no. 2, pp. 74-76, Feb. 2004.

[80] Z. Shao and M. Fujise, “An improved FDTD formulation for general linear lumped microwave circuits based on matrix theory,” *IEEE Trans. Microwave Theory Tech.*, vol. 53, no. 7, pp. 2261-2266, Jul. 2005.

[81] O. Gonzalez, J. A. Pereda, A. Herrera, and A. Vegas, “An extension of the lumped-network FDTD method to linear two-port lumped circuits,” *IEEE Trans. Microwave Theory Tech.*, vol. 54, no. 7, pp. 3045-3051, Jul. 2006.

[82] C.-C. Wang and C.-W. Kuo, “An efficient scheme for processing arbitrary lumped multiport devices in the finite-difference time-domain method,” *IEEE Trans. Microwave Theory Tech.*, vol. 55, no. 5, pp. 958-965, May 2007.

[83] X. Ye and J. L. Drewniak, “Incorporating two-port networks with S-parameters into FDTD,” *IEEE Microwave Wireless Compon. Lett.*, vol. 11, no. 2, pp. 77-79, Feb. 2001.

[84] Y. Zhu and A. C. Cangellaris, “Macro-elements for efficient FEM simulation of small geometric features in waveguide components,” *IEEE Trans. Microwave Theory Tech.*, vol. 48, no. 12, pp. 2254-2260, Dec. 2000.

[85] A. E. Yılmaz, “Parallel FFT-accelerated time-domain integral equation solvers for electromagnetic analysis,” Ph.D. dissertation, University of Illinois at Urbana-Champaign, Urbana, IL, 2005.

[86] O. González, J. A. Pereda, A. Herrera, A. Grande, and Á. Vegas, “Combining the FDTD method and rational-fitting techniques for modeling active devices characterized by measured S-parameters,” *IEEE Microwave Wireless Compon. Lett.*, vol. 17, no. 7, pp. 477-479, July 2007.

[87] N. V. Venkatarayalu, M. N. Vouvakis, Y.-B. Gan and J.-F. Lee, “Suppressing linear time growth in edge element based finite element time domain solution using divergence free constraint equation,” in *Proc. IEEE Antennas Propagat. Soc. Int. Symp.*, July 2005, pp. 193-196.

[88] W. A. Artuzi, Jr., "Improving the Newmark time integration scheme in finite element time domain methods," *IEEE Microw. Wireless Compon. Lett.*, vol. 15, no. 12, pp. 898-900, Dec. 2005.

[89] R. A. Chilton and R. Lee, "The discrete origin of FETD-Newmark late time instabiliy, and a correction scheme," *J. Comput. Physics*, vol. 224, no. 2, pp. 1293-1306, June 2007.

[90] R. Albanese and G. Rubinacci, "Solution of three dimensional eddy current problems by integral and differential methods," *IEEE Trans. Magn.*, vol. 24, pp. 98-101, Jan. 1988.

[91] S. C. Lee, J. F. Lee, and R. Lee, "Hierarchical vector finite elements for analyzing waveguiding structures," *IEEE Trans. Microwave Theory Tech.*, vol. 51, no. 8, pp. 1897-1905, Aug. 2003.

[92] J. F. Lee and D. K. Sun, "p-Type multiplicative Schwarz (pMUS) method with vector finite elements for modeling three-dimensional waveguide discontinuities," *IEEE Trans. Microwave Theory Tech.*, vol. 52, no. 3, pp. 864-870, March 2004.

[93] S. H. Lee and J. M. Jin, "Application of the tree-cotree splitting for improving matrix conditioning in the full-wave finite-element analysis of high-speed circuits," *Microwave Opt. Tech. Lett.*, vol. 50, no. 6, pp. 1476-1481, June 2008.

[94] S. H. Lee, "Efficient finite element electromagnetic analysis for high-frequency/high-speed circuits and multiconductor transmission lines," Ph.D. dissertation, University of Illinois at Urbana-Champaign, Urbana, IL, 2009.

[95] B. Chazelle, "A minimum spanning tree algorithm with inverse-Ackermann type complexity," *J. ACM*, vol. 47, no. 6, pp. 1028-1047, Nov 2000.

[96] S. Balay, W. Gropp, L. C. McInnes, and B. Smith, *PETSc Users Manual*, Argonne National Laboratory, April 2001.

[97] Y. Saad, *Iterative Methods for Sparse Linear Systems*. Boston, MA: PWS Publishing Company, 1996.

[98] E. Cuthill and J. McKee, "Reducing the bandwidth of sparse symmetric matrices," in *Proc. 24th Nat. Conf. ACM*, 1969, pp. 157-172.

[99] D. J. Riley and C. D. Tuner, “VOLMAX: a solid-model-based, transient, volumetric Maxwell solver using hybrid grids,” *IEEE Antennas Propag. Mag.*, vol. 39, no. 1, p. 2033, Feb. 1997.

[100] F. Edelvik, “A new technique for accurate and stable modeling of arbitrarily oriented thin wires in the FDTD method,” *IEEE Trans. Electromagn. Compat.*, vol. 45, no. 2, pp. 416-423, May 2003.

[101] S. H. Lee and J.-M. Jin, “Fast reduced-order finite-element modeling of lossy thin wires using lumped impedance elements,” *IEEE Trans. Advanced Packag.*, accepted for future publication.

[102] H. Bağcı, A. E. Yılmaz, J. M. Jin, and E. Michielssen, “Fast and rigorous time-domain EMC/EMI analysis of electrically large complex structures loaded with coaxial cables,” *IEEE Trans. EMC*, vol. 49, no. 2, pp. 361-381, May 2007.

AUTHOR’S BIOGRAPHY

Rui Wang was born in 1982 in Chengdu, Sichuan, China. He received the B.E. degree in electrical engineering from the University of Science and Technology of China, Hefei, China, in 2004, and the M.S. degree in electrical engineering from the University of Illinois at Urbana-Champaign (UIUC), in 2006. He is currently working toward the Ph.D. degree in electrical engineering at UIUC.

Since 2004, he has been a Research Assistant with the Center for Computational Electromagnetics, UIUC. His research interests include numerical simulation of antennas and microwave devices, time-domain FEM, and hybrid methods. Mr. Wang was the recipient of the 2008 Ernest A. Reid Fellowship Award and the 2009 Yuen T. Lo Outstanding Research Award, both presented by the Department of Electrical and Computer Engineering, UIUC. He was also the recipient of the 2009 Best Student Paper Award presented at the 25th Review of Progress in Applied Computational Electromagnetics (ACES), Monterey, CA.